

Hind, David Martin (2015) Current derivative estimation for sensorless motor drives. PhD thesis, University of Nottingham.

Access from the University of Nottingham repository:

<http://eprints.nottingham.ac.uk/28679/1/David%20Hind%20Thesis.pdf>

Copyright and reuse:

The Nottingham ePrints service makes this work by researchers of the University of Nottingham available open access under the following conditions.

- Copyright and all moral rights to the version of the paper presented here belong to the individual author(s) and/or other copyright owners.
- To the extent reasonable and practicable the material made available in Nottingham ePrints has been checked for eligibility before being made available.
- Copies of full items can be used for personal research or study, educational, or not-for-profit purposes without prior permission or charge provided that the authors, title and full bibliographic details are credited, a hyperlink and/or URL is given for the original metadata page and the content is not changed in any way.
- Quotations or similar reproductions must be sufficiently acknowledged.

Please see our full end user licence at:

http://eprints.nottingham.ac.uk/end_user_agreement.pdf

A note on versions:

The version presented here may differ from the published version or from the version of record. If you wish to cite this item you are advised to consult the publisher's version. Please see the repository url above for details on accessing the published version and note that access may require a subscription.

For more information, please contact eprints@nottingham.ac.uk

**Current Derivative
Estimation for Sensorless
Motor Drives**

David Martin Hind, MEng

**Thesis submitted to the University of
Nottingham for the degree of Doctor of
Philosophy**

APRIL 2015

Abstract

The work presented in this thesis aims to improve the performance of the Fundamental PWM sensorless control technique by proposing a new way to estimate current derivatives in the presence of high frequency oscillations. The Fundamental PWM technique offers performance across the entire speed range (including zero speed). The method requires current derivative measurements when certain PWM (Pulse Width Modulation) active and null vectors are applied to the machine. However the switching action of the active devices in the inverter and the associated large dv/dt result in current and current derivative waveforms being affected by high frequency oscillations which prevent accurate measurement of the current derivative. Other approaches have allowed these oscillations to decay before attempting to take a derivative measurement. This requires that the PWM vectors are applied to the machine for a time sufficient to allow the oscillations to decay and a derivative measurement to be made (the minimum pulse width). On some occasions this time is longer than the time a vector would have normally been applied for (for example when operating at low speed) and the vectors must be extended and later compensated. Vector extension introduces undesirable current distortion, audible noise, torque ripple and vibration.

In this thesis the high frequency oscillations and their sources are investigated and a method of using Artificial Neural Networks to estimate current derivatives using only a short window of the transient current response is proposed. The method is able to estimate the derivative directly from phase current measurements affected by high frequency oscillations and thus allows a reduction in the minimum pulse width to be achieved (since it is no longer necessary to wait for the oscillations to fully decay) without the need for dedicated current derivative sensors. The performance of the technique is validated with experimental results.

Acknowledgements

The work presented in this thesis would not have been possible without the help, support and influences of others. I would sincerely like thank my primary supervisor, Professor Mark Sumner, who has guided me throughout this work and has always shown faith in me. I would also like to thank my secondary supervisor, Professor Chris Gerada, who gave me the opportunity to undertake a PhD and has also been a valuable source of advice. I would like to thank my examiners, Dr Dave Atkinson (Newcastle University) and Professor Jon Clare (The University of Nottingham). I would also like to thank my many friends within the PEMC group, in particular Marco Degano, Jorge Espina, James Borg Bartolo, Richard Davies, Andrew Goodman and Edward Christopher who have been there with help, advice, practical assistance and friendly conversation along the way.

I would also like to thank my predecessors who worked on Sensorless control prior to me. They include Kamal Subhi Saleh, Yahan Hua, Quing Gao and Yu Duan. Their hard work and advice helped me gain an understanding of the area and what was required to advance the technology.

Finally I would like to thank my family who have been very patient with me through this period in my life. Without them this would not have been possible.

Contents

Abstract	i
Acknowledgements	ii
Contents.....	iii
List of Figures	ix
List of Tables.....	xvii
Chapter 1	1
Introduction	1
1.1 Background.....	1
1.2 Scope of the Thesis and Overall Objectives	3
1.3 Thesis Overview	6
Chapter 2.....	9
Sensorless Control Techniques	9
2.1 Introduction	9
2.2 Mathematical Methods	10
2.2.1 Model Based Adaptive Reference System (MRAS).....	10
2.2.2 Observer Techniques	12
2.2.3 The Extended Kalman Filter	13
2.2.4 Mathematical Methods Conclusions.....	13
2.3 Saliency Tacking Techniques	14
2.3.1 Introduction.....	14
2.3.2 High Frequency Injection Methods	20
2.3.2.1 Continuous Injection in the $\alpha\beta$ Frame	20
2.3.2.2 d-axis Injection	21
2.3.3 Test Pulse Methods	21

2.3.3.1	INFORM.....	22
2.3.3.2	Fundamental PWM Technique.....	23
2.4	The Narrow Vector Problem	26
2.4.1	Introduction.....	26
2.4.2	SVPWM Pulse Width Extensions.....	29
2.4.3	Current Distortion Introduced as a Result of Extending Vectors – An Investigative Demonstration	33
2.4.4	Narrow Vector Problem Conclusions	35
2.5	Appearance of the Current Derivatives	35
2.6	Accuracy Requirements of a Current Derivative Estimation/Calculation System.....	38
2.7	Hybrid Sensorless Solutions.....	40
Chapter 3	42
High Frequency Parasitic Effects in a Variable Speed Drive		42
3.1	Introduction	42
3.2	Modelling of the High Frequency Behaviour of a Drive System.....	43
3.3	Motor Modelling in the High Frequency Range	44
3.3.1	Introduction.....	44
3.3.2	Motor Model Development.....	45
3.3.3	Finding the Model Parameters	50
3.4	Cable Modelling in the High Frequency Range	57
3.4.1	Introduction.....	57
3.4.2	Finding the Model Parameters	59
3.5	Time Domain Simulation Results.....	63
3.6	Effects of Supply Cable Length.....	65
3.7	High Frequency Behaviour Due to the Drive.....	69
3.8	Influences of Inverter Non-linearities.....	70
3.9	Conclusions	76

Chapter 4.....	78
Current Derivative Estimation in the Presence of HF Oscillations.....	78
4.1 Introduction	78
4.2 Removing or Reducing the High Frequency Content in the Transient Current Response.....	79
4.2.1 Use of EMI Filters	79
4.2.2 Variation of the IGBT Gate Impedance.....	80
4.2.3 Injection of Low Magnitude Test Pulses	81
4.3 Use of Mathematical Techniques	83
4.3.1 Introduction.....	83
4.3.2 Work by Other Researchers in the Field.....	84
4.4 Estimation of the Current Derivative Using Curve Fitting Methods..	87
4.4.1 Introduction.....	87
4.4.2 Curve Fitting to a First Order Linear Approximation.....	88
4.4.3 Curve Fitting to a Single Exponentially Decaying Sinusoid Approximation	90
4.4.4 Straight Line Approximation Following Moving Average Filtering.....	93
4.4.5 Straight Line Approximation Following Dominant Sinusoid Component Cancellation and Low Pass Filtering of Waveform	95
4.5 Difficulties Associated with Mathematical Curve Fitting Methods...	98
Chapter 5.....	100
Derivative Estimation Using Artificial Neural Networks	100
5.1 Introduction	100
5.2 Artificial Neural Networks and Their General Operation	102
5.3 Use of Neural Networks in Sensorless Control Applications.....	104
5.4 Estimation of Current Derivatives Using Neural Networks.....	105
5.4.1 Training a Neural Network for Derivative Estimation	105

5.4.2 Data Normalisation	107
5.5 Simulation Results	108
5.5.1 Phase A, First Active Vector	108
5.5.2 Phase A, Second Active Vector	112
5.5.3 Phase A, Null Vector	115
5.5.4 Phases B and C.....	118
5.6 Conclusions	118
Chapter 6.....	120
Hardware and Practical Implementation	120
6.1 Introduction	120
6.2 Permanent Magnet Motor.....	121
6.3 Power Electronics	122
6.4 DSP and FPGA Control Platform.....	123
6.4.1 Modifications to DSP/FPGA Control Platform	124
6.4.1.1 Modifications to the PWM	124
6.4.1.2 Trigger Signal	124
6.4.1.3 New Period Signal	125
6.4.1.4 Sector	126
6.4.1.5 Encoder Output.....	126
6.4.1.6 V/F Operation Handshaking Signals	126
6.5 Implementation of the Proposed Technique in Hardware	127
6.5.1 Introduction.....	127
6.5.2 FPGA Platform	128
6.5.3 Signal Measurement and High Speed Data Acquisition.....	129
6.5.4 Current Measurement.....	132
6.5.5 Justification of the Use of Low Bandwidth Current Sensors.....	133
6.6 FPGA Design.....	138
6.6.1 Introduction.....	138

6.6.2 Linear Feedback Shift Register (LFSR)	140
6.6.3 ADC Sampling Controller	140
6.6.4 Least Squares Curve Fit Calculator	144
6.6.5 ANN Controller	144
6.6.6 Artificial Neural Network Implementation.....	145
6.6.7 SD Card Controller	148
6.6.8 Position Estimation Based on Derivative Estimates.....	150
6.6.9 Output State Machine	151
6.6.10 Storing Results in the FPGA's On-board Memory for Offline Processing	152
6.7 Training of the Neural Network in Matlab.....	152
6.8 Conclusions	154
Chapter 7.....	155
Experimental Results.....	155
7.1 Introduction	155
7.2 Single ANN	156
7.3 Triple ANN.....	157
7.4 Operating Point Variation.....	168
7.5 Low Speed Performance Limitations	173
7.6 Minimum Pulse Width Reduction	174
7.7 Conclusions	185
Chapter 8.....	187
Conclusions, Discussions and Suggestions of Future Work.....	187
8.1 Conclusions and Discussions.....	187
8.2 Future Work.....	194
8.2.1 Improved High Frequency Simulation Model.....	194
8.2.2 Alternative Neural Networks	194

8.2.3 Improved Training Data.....	195
8.2.4 Improvements to the Present Implementation	195
8.2.5 ANN Online Adaptive Learning	196
8.2.6 Hybrid Derivative Estimate Techniques	196
8.2.7 Use the Derivative Estimates to Produce a Position Estimate that can be used for Closed Loop Control	197
8.2.8 Improvements to the Derivative Estimation Performance of the ANN at Low Speed and Under Low Load.....	197
8.2.9 Use ANN Derivative Estimation Technique to Track Saliency in an Induction Machine	198
8.3 Publications	199
Appendix A	200
Appendix B	205
Bibliography.....	255

List of Figures

Figure 2.1 MRAS sensorless control scheme where the rotor flux is the estimated parameter	10
Figure 2.2 Voltage model implemented using a feedback integrator to cancel the effect of integrator drift [13, 14]	11
Figure 2.3 Simplified diagram of the rotor flux and speed adaptive observer	12
Figure 2.4 Rotor construction configurations of a permanent magnet motor [23]: (a) surface mount, (b) Inset and (c) Interior	16
Figure 2.5 Magnetic saturation due to the main flux and leakage flux in a surface mounted permanent magnet machine [23, 30]	17
Figure 2.6 Saturation points due to leakage flux [30].....	18
Figure 2.7 Test vectors applied under INFORM [22].....	22
Figure 2.8 Illustrates the timing of the derivative measurements with respect to the PWM waveforms applied to the machine	24
Figure 2.9 current response (a) and current derivative response (b) to inverter switching	27
Figure 2.10 phase current response under a narrow vector. The high frequency oscillations under the first active vector do not have time to settle before the second active vector is applied	28
Figure 2.11 The locations on the SVPWM plane where voltage vector extensions are required [42].....	29
Figure 2.12 An ideal PWM output waveform for sector 1, $t_1 - t_7$ are the vector times.....	29
Figure 2.13 A case where vector extension is required for the first active vector only, with the original vector length being $> t_{\min}/2$	31
Figure 2.14 A case where vector extension is required for the first active vector only, with the original vector length being $< t_{\min}/2$	32

Figure 2.15 THD of the phase current waveform according to speed (electrical frequency) and minimum pulse width (t_{min})	34
Figure 2.16 Current derivatives under the first (a) and second (b) SVPWM active vectors. The SVPWM sector (c) is also shown	36
Figure 2.17 Equivalent circuit for phase A of a PM motor	37
Figure 2.18 The THD + N (Total Harmonic Distortion + Noise) of the position vector when random noise is added to the derivative waveforms obtained using the two current sample method	39
Figure 3.1 main parasitic impedances in a standard drive setup [54]	43
Figure 3.2 HF motor models proposed by a) [62], b) [60], c) [56] and d) [63]	47
Figure 3.3 Measurement Setup to Determine Differential Mode Parameters	50
Figure 3.4 Measurement Setup to Determine Common Mode Parameters	51
Figure 3.5 The common mode (red) and differential mode (black) impedance responses captured from a 4 kW ASEA induction machine. Also highlighted are the key points that are used to find high frequency model component parameters	52
Figure 3.6 Comparison of the simulated and the experimentally captured common mode impedance response	55
Figure 3.7 Comparison of the simulated and the experimentally captured differential mode impedance response.....	55
Figure 3.8 Configuration used to simulate high and low frequency behaviour [55, 57, 68].....	56
Figure 3.9 the standard transmission line model of a cable [70-72].....	57
Figure 3.10 expanded high frequency models of the power cable per-unit length. (a) includes the effects of dielectric losses [60], while (b) includes skin and proximity effects [63].....	58
Figure 3.11 Short (a) and open (b) circuit frequency responses of a 1m length of 5 core shielded cable.....	59
Figure 3.12 A comparison of the measured and simulated open circuit (a) and short circuit (b) impedance responses.....	62

Figure 3.13 Simulated and experimental current transients are compared for their high frequency content	63
Figure 3.14 FFTs of the transients shown in Figure 3.13. (a) is FFT of the experimental transient while (b) is FFT of the simulated transient	64
Figure 3.15 shows the difference in current transients between short (a) (24m in this case) and long (b) (125m) cable lengths. The transient for the short cable length is dominated by a 1 MHz component, see (c), while the transient corresponding to the long cable length is dominated by a component at approximately 250 kHz, see (d). It is clear that the transient for the short cable length, (a), decays much quicker than the case for a long cable length, (c)	66
Figure 3.16 shows the effect on the dominant frequency component of increasing the supply cable length (results obtained through simulation and show a similar behaviour to that observed in [63]).....	67
Figure 3.17 Parasitic components present in an IGBT module [74].....	69
Figure 3.18 Effect of current level on device switching behaviour.....	73
Figure 3.19 Additional Capacitances to be considered in the drive [54, 75, 78]	74
Figure 3.20 the effects on voltage and current transients of additional parasitic capacitances added in parallel with active switching devices to capture non-linear switching behaviour	75
Figure 4.1 An illustration of how reduced amplitude test pulses result in smaller transient current responses and hence a smaller current ripple is introduced [22].....	82
Figure 4.2 An illustration of the effects of filtering the sampled current waveform. The ideal (red) waveform is shown, as is a realistic representation (blue) where a 1 MHz exponentially decaying sin wave is superimposed. This wave is filtered and shown (black), the filter cut off frequency is 250 kHz. The frequency of the ideal triangle wave is 100 kHz. Notice the delay due to the phase shift and the rounding of the wave around the peaks due to the removal of the triplen harmonics which form the triangle wave	89

Figure 4.3 Experimentally measured transient current waveform (red) and corresponding underlying gradient (black). Also included are low pass filtered versions of the transient current waveform (blue and green) to show the non-symmetrical contributions made by the lower frequency components.....	90
Figure 4.4 Experimental waveform and approximation based on (Eqn 4.1) ...	91
Figure 4.5 Experimental waveform and moving average filtered waveform, a wave fitted to the moving average result is also shown.....	93
Figure 4.6 Experimental waveform and resulting period moving average filtered waveform, a wave fitted to the moving average result is also shown which provides the gradient estimation	94
Figure 4.7 The experimental current waveform is shown along with a waveform with dominant exponentially decaying sinusoid component removed; a wave fitted to this result is also shown which provides the gradient estimation. N.B. filtered and fitted waveforms are identical	96
Figure 5.1 The structure of a feed-forward neural network. The inter connections between the inputs and hidden layer neurons and also between the hidden layer neurons and output layer neuron are weighted (I=input, B= bias and O=output)	103
Figure 5.2 The proposed method for obtaining training data for the neural network	106
Figure 5.3 Data normalisation required pre and post neural network [105]..	107
Figure 5.4 The estimated first active vector derivatives from the ANN are shown with the derivatives calculated from a least squares fit for comparison. In (a) the transients supplied to the ANN had been seen during the training process while in (b) the transients supplied to the ANN had not be used previously.....	110
Figure 5.5 The instantaneous error of the ANN estimated first active vector derivatives compared to the least squares fit results	111
Figure 5.6 The estimated second active vector derivatives from the ANN are shown with the derivatives calculated from a least squares fit for comparison. In (a) the transients supplied to the ANN had been seen during the training	

process while in (b) the transients supplied to the ANN had not be used previously.....	113
Figure 5.7 The instantaneous error of the ANN estimated second active vector derivatives compared to the least squares fit results.....	114
Figure 5.8 The estimated null vector derivatives from the ANN are shown with the derivatives calculated from a least squares fit for comparison. In (a) the transients supplied to the ANN had been seen during the training process while in (b) the transients supplied to the ANN had not be used previously.	116
Figure 5.9 The instantaneous error of the ANN estimated null vector derivatives compared to the least squares fit results.....	117
Figure 6.1 A diagram illustrating the layout of the overall system	121
Figure 6.2 an illustration of the positions of the new period and trigger signals with respect to the PWM waveforms.....	125
Figure 6.3 Front view of the Terasic DE3 board with key hardware features highlighted. Image courtesy of Terasic [108].....	128
Figure 6.4 Front and Back view of the Terasic AD/DA board. Image courtesy of Terasic [109].....	130
Figure 6.5 The AD8138 produces a differential output from a single ended input centred on the mid-point of the supply voltage (V_{oc}).....	131
Figure 6.6 ADC Interface board designed “in house” at the University of Nottingham. The board uses high speed op-amps to provide single-ended to differential conversion at the input and vice-versa at the output.....	132
Figure 6.7 Current Sensing Board designed to measure and scale the three phase motor currents	133
Figure 6.8 Working principle of the LEM closed loop hall effect current sensor. Image courtesy of LEM [114]	134
Figure 6.9 LEM current sensor bode plot. Image adapted from [114]	135
Figure 6.10 Lecroy Vs LEM current sensors. (a) shows the time domain response captured by the sensors while (b) and (c) show the frequency domain responses of the Lecroy and LEM sensors respectively	137

Figure 6.11 An illustrative diagram showing how the main components are connected within the FPGA design.....	139
Figure 6.12 ADC Controller operational flow diagram when in “Run” mode	142
Figure 6.13 ADC Controller operational flow diagram when in “Train” mode	143
Figure 6.14 ANN controller operational flow diagram	145
Figure 6.15 Artificial Neural Network operational flow diagram	147
Figure 6.16 SD Card Controller operation flow diagram when writing to the SD card.....	149
Figure 6.17 SD Card Controller operation flow diagram when reading from the SD card.....	150
Figure 6.18: Position estimator operational flow diagram.....	151
Figure 7.1 ANN estimated first active vector derivatives for each phase when using only one ANN trained with data collected from phase A only. Derivative results obtained from the two current sample method are shown for reference	157
Figure 7.2 First null vector estimates of the ANN plotted with measured values from a Rogowski coil and a result obtained from the two current sample method (a). Using the two current sample results as a reference, the error of the ANN estimate is calculated and also shown in (b). The distribution of error amplitude is also shown in (c)	160
Figure 7.3 First active vector estimates of the ANN plotted with measured values from a Rogowski coil and a result obtained from the two current sample method (a). Using the two current sample results as a reference, the error of the ANN estimate is calculated and also shown in (b). The distribution of error amplitude is also shown in (c)	161
Figure 7.4 Second active vector estimates of the ANN plotted with measured values from a Rogowski coil and a result obtained from the two current sample method (a). Using the two current sample results as a reference, the	

error of the ANN estimate is calculated and also shown in (b). The distribution of error amplitude is also shown in (c)	163
Figure 7.5 Second null vector estimates of the ANN plotted with measured values from a Rogowski coil and a result obtained from the two current sample method (a). Using the two current sample results as a reference, the error of the ANN estimate is calculated and also shown in (b). The distribution of error amplitude is also shown in (c)	164
Figure 7.6 the frequency content of the position vectors for both the two current sample method (a) and the ANN method (b) is shown above, these were calculated using the derivatives shown in Figure 7.2 - 7.5 (a).....	167
Figure 7.7 Relative second harmonic strength found from ANN estimates. The ANN was trained using data captured at 30Hz, no load and 30Hz, 44% load	169
Figure 7.8 Surface plots illustrating the performance of the ANN and two current sample methods at various speeds and loads. For these tests the minimum pulse width was maintained at 17 μ s.....	170
Figure 7.9 Saturation saliency component amplitude found from derivatives obtained from the ANN method, (a), and the two current sample method, (b), at various speeds and loads	172
Figure 7.10 Current transient and a corresponding derivative estimate from the ANN (red) and derivative measurements using the two current sample method with a 10 μ s delay between sample points (black), a 3 μ s delay between sample points (pink).....	174
Figure 7.11 shows the relative second harmonic strength (a) and the amplitude of the second harmonic component (b) for ANN derivative estimates found under reduced pulse widths. Notice that under no load the relative second harmonic strength is poor due to the high harmonic content.....	176
Figure 7.12 Comparison of the vector derivative estimates by the ANN when applying 3 μ s and 17 μ s minimum pulse widths.....	180

Figure 7.13 Comparison of the harmonic contents of P_β derived from (a) ANN with $3\mu\text{s } t_{\text{min}}$, (b) two current sample method with $3\mu\text{s } t_{\text{min}}$, (c) ANN with $17\mu\text{s } t_{\text{min}}$ and (d) two current sample method with $17\mu\text{s } t_{\text{min}}$	182
Figure 7.14 Comparison of the vector derivative estimates from the ANN, two current sample method and Rogowski coil when a $3\mu\text{s}$ minimum pulse width is applied	184

List of Tables

Table 2.1 Position scalars for each of the active vectors (and corresponding null vectors) when operating a star connected machine [40, 41].....	25
Table 2.2 The voltages applied to each phase, in each sector of the SVPWM plane for both first active and second active vectors	38
Table 3.1 Model parameters found from (Eqn 3.1) – (Eqn 3.12)	54
Table 3.2 calculated component values for the high frequency cable model ..	61
Table 3.3 the stages involved in switching an inverter leg and how the parasitic capacitances of the devices effect switching	71
Table 6.1 Permanent magnet motor parameters [106].....	122

Chapter 1

Introduction

1.1 Background

Variable frequency drives are now commonplace in industrial applications and with the realisation of the negative environmental effects of burning fossil fuels they are certain to become even more common in future motive applications.

The most basic control technique of all those employed in variable frequency drives using AC machines is open loop control. Open loop control offers a simple solution but provides poor dynamic performance and suffers from speed droop when a load torque is applied. Whilst this is perfectly acceptable in many applications, there are many others where this is not acceptable and closed loop control is needed. Closed loop control systems have relied on shaft mounted encoders or resolvers to provide a rotor position measurement which can be used for control. These mechanical speed feedback devices work very well, but their reliability can be an issue, especially when operating in harsh environments, which can undermine the robustness and reliability of the entire drive system leading to potentially costly downtime. Other disadvantages include the additional cost, increased manufacture time since they must be calibrated and on small machines they represent a significant proportion of the entire physical package size.

These drawbacks have contributed towards a large research focus on sensorless control techniques. Such techniques rely on electrical measurements only to estimate the rotor position allowing closed loop control of the machine without the need to have a mechanical speed sensor. Many sensorless approaches exist, each of which has its own merits and weaknesses. Of the sensorless techniques, mathematical model approaches face issues at low speed where measurements from the machine become small and are badly affected by noise which prevents these methods from being able to operate at zero speed. Parameter sensitivity and variation also introduces errors while the inverter itself affects the performance by introducing non-linear behaviour through variations in the applied dv/dt . Saliency tracking methods seek to track inductance variations brought about by the variation in the effective air gap length.

The saliency tracking techniques when considered from a general point of view (as in Chapter 2) can be applied to both permanent magnet machines and induction machines. The difference lies in the saliencies that are being tracked and their sources. For example, the saturation saliency in permanent magnet machines is due to the rotor magnets while in an induction machine it is due to the fundamental wave. Geometric effects in permanent magnet machines arise from magnet placement while in induction machines it is due to rotor design (rotor slot opening width, number of rotor bars etc).

Saliency tracking techniques are able to operate at zero speed and are immune to parameter sensitivities but often require additional signals to be applied to the machine either by adding these to the fundamental output of the inverter or by directly modifying the PWM (pulse width modulation) sequence itself, both of which introduce current distortion, torque ripple and audible noise.

One particular saliency tracking technique, the Fundamental PWM technique, makes use of the current derivative response of the machine to

pulses applied under normal SVPWM (Space Vector PWM) to track the machine saliency. This is in theory an ideal solution as the removal of the need to add special test pulses or HF (high frequency) signals also removes their negative side effects (current distortion, torque ripple, vibration and audible noise) and the technique is able to operate across the entire speed range. However additional sensors in the form of current derivative sensors are often required and the technique is limited by high frequency oscillations appearing in the current and current derivative waveforms due to parasitic impedances in the motor and cabling responding to the large dv/dt applied during switching.

These oscillations are responsible for the major limitation affecting the Fundamental PWM technique – the Narrow Vector Problem, as they prevent immediate measurement of the current derivative and result in an enforced delay until measurement of the current derivative becomes possible. The PWM vector being applied to the machine must also be maintained throughout this delay; in many cases this means extending the PWM vector length beyond the time originally intended. This delay is known as the minimum vector time (t_{min}) and extending short vectors to the minimum vector time introduces undesirable current distortion into the response.

1.2 Scope of the Thesis and Overall Objectives

This thesis aims to investigate the minimum vector problem and propose new methods to reduce this limitation thus providing a sensorless technique that can operate across the entire speed range with minimal current distortion, torque ripple and audible noise. It will be seen that the parasitic impedances that cause the high frequency oscillations in the current response cannot be eradicated and so will always produce some unwanted ringing

which prevents one from overcoming the problem completely. In this work methods to extract the current derivative from the transient phase current waveform while the high frequency oscillations are still present are explored. This offers two distinct advantages:

- 1) If the derivative can be estimated before the oscillations have decayed then the minimum vector time can be significantly reduced therefore reducing the current distortion imposed by vector extensions.

- 2) Extracting the derivative from the phase current response removes the need to have additional dedicated derivative sensors in the drive as the standard current sensors found in a normal drive can be used instead.

It should be noted that the phase current has previously been used to estimate the derivative but a significant minimum vector length was required to allow a detectable change in the current to occur [1]. In this work a new approach which uses the phase current and an artificial neural network to estimate the current derivative in a shorter time than has previously been possible is proposed. The Narrow Vector Problem is far from straightforward to solve as there are significant variations in the shape of the transient responses seen. The transient current response is highly dependent on the dv/dt of the inverter which varies according to the conducting device and operating condition of the inverter.

A target for the accuracy of the derivatives estimated by the proposed technique is specified in this work. A maximum increase of 10% in the THD+N (Total Harmonic Distortion + Noise) when compared to derivatives found through existing methods has been defined as the acceptable limit in Chapter 2.

Noting the above arguments a number of objectives may be set out which include:

- To understand the sources of main parasitic impedances which cause the high frequency phenomena seen in the transient current and current derivative responses following inverter switching
- To understand the non-linear switching behaviour of the inverter, its effects on the transient current response and appreciate when and how this effects the current derivative response
- To propose solutions which either have zero or a minimal effect on the fundamental operation of the inverter
- To investigate new methods of extracting the current derivative from a transient current response in a reduced time, in the presence of high frequency oscillations. The maximum acceptable increase in the THD + N of the estimated derivatives (compared to derivatives obtained using existing methods) is limited to 10%.
- To identify the saturation saliency component using the estimated derivatives in a time frame that is at least comparable to existing methods.
- To implement proposed solutions in hardware in order to demonstrate their effectiveness in a real time situation.

1.3 Thesis Overview

The following gives a brief outline of the material contained in this thesis

Chapter 2 summarizes the common sensorless approaches beginning with mathematical model based approaches. The saliencies (and their origins) that exist in induction machines and permanent magnet machines are introduced before moving on to generally describe saliency tracking techniques. The Fundamental PWM technique and its main limitation, the Narrow Vector Problem, are described in detail as it is this area that this research is aimed at improving. The appearance of the current derivative waveforms that are of interest is introduced and an acceptable level of accuracy for a derivative estimation system is defined.

Chapter 3 discusses the sources of the parasitic impedances that give rise to the oscillations seen in the current response following a switching event of the inverter. Electrical models which are able to reproduce the high frequency behaviour are investigated and simulation results are presented and compared with those obtained through experimental investigation. Discrepancies in the shape of the current transients following switching at low current are highlighted and the reasons behind the anomaly are identified and discussed; namely the non-linear switching behaviour of the inverter due to the parasitic capacitance of the switching devices. Simulation results are then presented with these parasitic capacitances included to replicate the low current behaviour.

Chapter 4 introduces a number of methods implemented by researchers previously which lessen the high frequency current oscillations. These methods mostly aim to reduce the dv/dt of the inverter phase(s) following switching. While this does reduce the current oscillations it also has the effect of reducing the high frequency content of the voltage waveform applied to the

machine. The leakage inductances respond to this high frequency content allowing the position to be identified. The derivative response reduces and switching losses are increased.

Since it is desirable to have a solution which has a minimal effect on the operation of the drive, non-intrusive techniques are investigated which make use of current sensors (therefore removing the need for special current derivative sensors). These involve sampling the current transient (including the high frequency oscillations) at high speed to capture the response to a reasonable resolution – this is often referred to as oversampling. Work by other researchers is introduced before a mathematical curve fitting approach is explored. Many variations on the curve fitting approach are presented, however an accurate estimate of the current derivative could not be achieved when using only a small portion of the current transient. This is due to the limited bandwidth of the current sensor, the non-linear switching behaviour of the inverter and difficulties in identifying key contributions in the response beyond the dominant high frequency component.

Chapter 5 introduces the idea of using an artificial neural network (ANN) as a pattern recognition tool to associate current transients with their steady state derivatives. This method offers a way of dealing with both the non-linear switching behaviour of the inverter and the limited bandwidth of the current transducer. Artificial neural networks require training and so a methodology to achieve this is discussed before results obtained using a neural network implemented in Matlab supplied with experimental current transient data are presented.

Chapter 6 presents the experimental system. The hardware configuration, control platform and FPGA (Field-Programmable Gate Array) development board (used to implement the proposed technique) are described. Some of the FPGA design methodology is also described.

Chapter 7 presents a set of experimental results achieved using the proposed technique. The derivative estimates from the neural network are compared with derivative measurements obtained using the two current sample method (which measures the change in phase current amplitude over a set time window to give di/dt) and those measured directly using a Rogowski coil. The performance of the neural network approach at various speeds and loads is analysed to see what effects these factors have on the ability of the ANN to accurately estimate the derivatives and ultimately identify the saturation saliency component. Finally the performance of the technique with a narrowed pulse width is investigated. The results show that although there is degradation in the accuracy of the derivative estimates, they offer an improvement over the traditional two current sample and derivative sensor techniques when operating under narrow pulse widths.

Chapter 8 discusses the findings of the research and suggests further work that could be undertaken in this research area based on the findings of this study.

Chapter 2

Sensorless Control Techniques

2.1 Introduction

Sensorless control techniques are particularly attractive to industry as they offer closed loop control without the need for a shaft mounted mechanical encoder or resolver. This has a number of advantages including a reduction in production time and costs, smaller overall physical size of the machine (this is particularly the case for small frame size machines where an encoder is a significant proportion of the overall size) and increased reliability and robustness given the tendency of encoders and resolvers to fail under harsh conditions. This Chapter will briefly introduce the main sensorless techniques that exist today and are applicable to both permanent magnet and induction machines. Sensorless techniques can be divided into two categories; mathematical model based methods which generally rely on measuring electrical inputs of the machine and supplying these to a mathematical model from which a speed estimate is obtained while saliency tracking techniques make use of the machines anisotropic properties. As each technique is discussed the associated shortcomings will also be highlighted. With the various techniques introduced, the main focus will be directed towards the Fundamental PWM technique and the main limitation that effects this technique, the Narrow Vector Problem, which this work will aim to alleviate.

2.2 Mathematical Methods

2.2.1 Model Based Adaptive Reference System (MRAS)

The MRAS approach is one of the simplest closed loop sensorless techniques known. It relies on two mathematical models of the machine. One which depends on rotor speed (the adaptive model) and one which is independent of rotor speed (the reference model). The models both estimate the same parameter with rotor flux being common [2-4], Back-EMF [5] and reactive power [6] have also been used. The cross product of the model outputs is taken and the rotor speed is adjusted such that the adaptive model output is changed to drive the cross product result to zero at which point the estimated rotor speed will match the actual rotor speed [2, 3]. The adaptive mechanism is designed according to the hyper-stability concept which guarantees convergence and suitable dynamic characteristics [7].

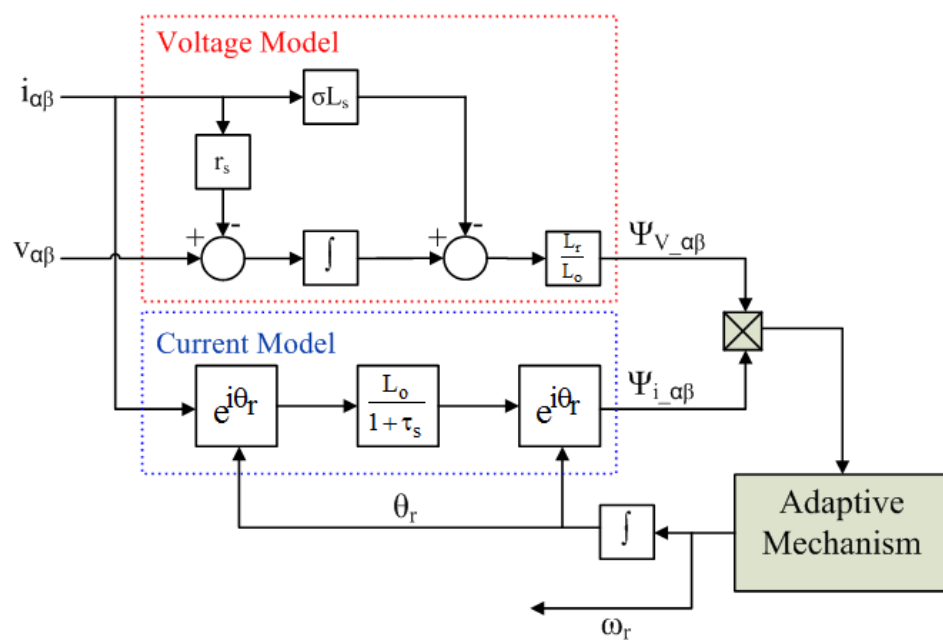


Figure 2.1 MRAS sensorless control scheme where the rotor flux is the estimated parameter

Performance of MRAS systems at high speed is excellent. However they perform poorly at low speeds where the sampled values supplied to the models are difficult to accurately measure and have a low signal to noise ratio. Parameter sensitivity is also an issue as parameters need to be accurately defined. There is often a need to calibrate a drive to determine the exact values of the model parameters (instead of simply using datasheet and calculated values). Heating during operation causes a change in the resistances used in the design with a key parameters being the stator and rotor resistances, this in turn affects the stator and rotor time constants. Many tracking techniques have been proposed to limit the effects of changes in stator and rotor resistance by tracking the variation online [8-12]. In addition, effects from the inverter itself start to become significant at low speed and should be compensated. For example the power device voltage drop is considerable when compared to the voltage supplied to the machine [13]. These methods also require the use of integrators which introduce drift due to noise in the measurements or imperfect AC quantities. It is reported that low pass filters can replace the integrator but low speed behaviour will be affected due to the phase shift introduced [2, 13]. An alternative is to use a feedback integrator which identifies the drift component in the output and feeds a cancellation term back into the integrator [13, 14]. The feedback integrator modification to the voltage model is illustrated in Figure 2.2.

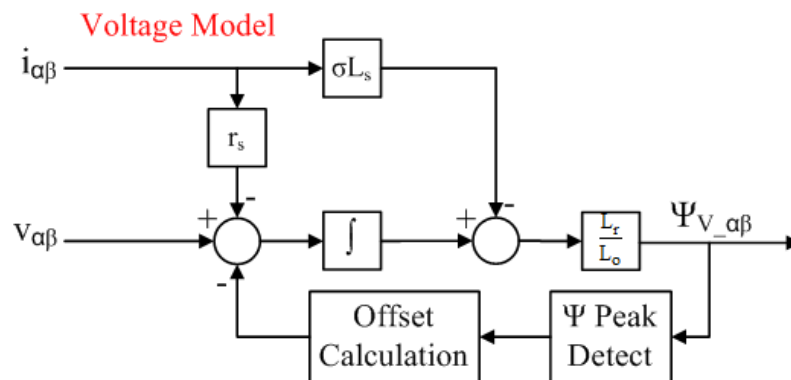


Figure 2.2 Voltage model implemented using a feedback integrator to cancel the effect of integrator drift [13, 14]

The feedback integrator well but can be difficult to start since the identification of the drift component usually relies on knowledge of peak AC values (hence one full period of the flux waveform is required).

2.2.2 Observer Techniques

Observers feature a state space model of the machine operating in parallel with the actual machine itself. The concept involves supplying measured values to the model and then estimating state variables that can be compared with a measured value from the machine. In [15-19] the estimated state variables of an induction machine model were the stator current and rotor flux. The state space model includes the rotor speed. This is the unknown parameter of interest and is varied through an adaptive mechanism until the state space model output matches the measured value of the machine. The model was supplied with stator voltage measurements in the stationary reference frame. Design of the adaptive mechanism according to the Lyapunov criterion and careful selection of the gain values used ensures stability [16]. Figure 2.3 gives a general overview of an observer based design. More details regarding the implementation can be found in [15-19].

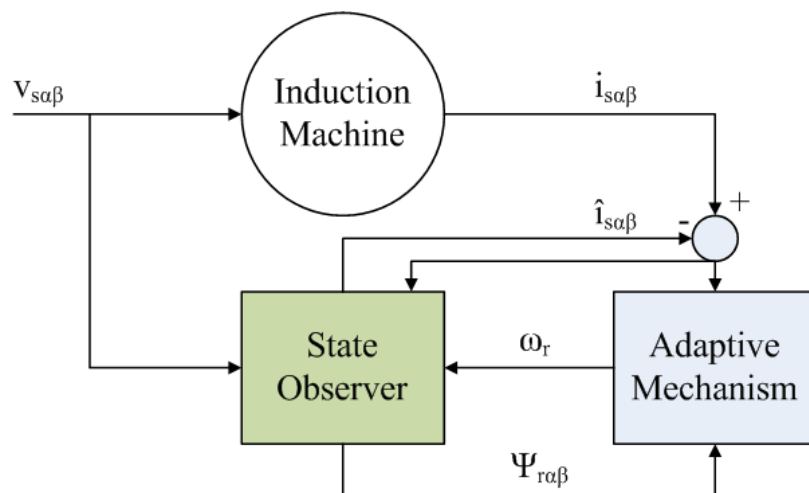


Figure 2.3 Simplified diagram of the rotor flux and speed adaptive observer

Observer techniques suffer from stability problems at low and zero speed operation. Also accurate definition of parameters is important and parameter tracking/identification is often required to overcome changes due to heating.

2.2.3 The Extended Kalman Filter

Where measurements are affected by noise the Kalman filter, a variation on the standard observer based methods, is seen as a good way to estimate state variables. When the rotor speed is considered as a state variable the system becomes non-linear and an extended Kalman filter must be used which involves linearizing the system about a set operating point [20, 21]. The system estimates the error covariance and uses this to predict states. The implementation of the algorithm is a recursive one and as a result adds a significant computation burden. The performance of the system in the presence of random noise however is very good.

2.2.4 Mathematical Methods Conclusions

The mathematical techniques described all share the common characteristic of performing very well at high speed but poorly at low and zero speed. This limitation restricts their use in many applications since variable speed drives must start from zero speed and often need to be able to operate at or close to zero speed. This has led to a concentration of research effort on an alternative type of approach called saliency tracking which will now be discussed.

2.3 Saliency Tracking Techniques

2.3.1 Introduction

With the zero and low speed limitations of the mathematical modelling techniques, saliency tracking techniques have received significant attention in recent years. These techniques take advantage of the machines anisotropy which can either be natural or intentionally introduced. The anisotropic properties of the machine can be tracked even when operating at zero speed and the influence parameter dependence (which affects the mathematical model methods) is removed. The work presented in this research is implemented using a permanent magnet machine, but the saliency tracking techniques described are equally applicable to both permanent magnet machines and induction machines. Before describing the saliency tracking methods, the saliencies that exist in permanent magnet machines and induction machines are briefly described. Several saliencies have been identified and can be successfully tracked in induction machines, these include:

- Saturation saliency due to fundamental wave excitation [22-25]. The main flux has an associated orthogonal leakage flux which causes magnetic saturation around the affected stator windings. This directly affects the leakage inductance of affected stator windings. The stator leakage inductance is modulated as the saturation moves around the stator. The effect is similar to saturation saliency due to the magnets in permanent magnet machines (which will be described in more detail later).
- Rotor slotting saliency exists due to the variation in magnetic coupling between the stator windings and rotor slot openings as the rotor slots pass the stator windings [22, 23, 25-27]. Each stator winding has a leakage flux associated with it which passes through the surface of the rotor (for explanation purposes assume that this flux does not couple with the rotor

bars). The rotor slots cause a variation in the effective air gap seen by the leakage flux. The two extremes are; 1) rotor and stator slots aligned – in this case the leakage flux will be at a minimum as the aligned rotor slot affects the leakage flux path (resulting in maximum air gap length). 2) Stator and rotor slots misaligned by half a rotor slot pitch – in this case the leakage flux is at a maximum as adjacent rotor slots have no effect on the leakage flux path. The variation in leakage flux modulates the stator leakage inductance which allows detection of the effect. The number of saliency cycles per rotor revolution will be equal to the number of rotor slots. This technique requires the use of a rotor with open or semi closed rotor slots.

- Saliency can be intentionally introduced by designing the rotor with asymmetries introduced around its circumference. In [28] the width of the rotor slot openings were varied to cause a variation in the leakage inductance while in [29] a double cage rotor was used which incorporated a resistance variation in the wire used in the outer cage (achieved by varying the copper gauge). These methods can offer a more robust position signal by being independent of load but obviously require the use of a specially designed rotor.

When considering permanent magnet machines there are two main saliencies which naturally exist; geometric and saturation saliencies.

Geometric saliencies arise from the magnet placement in the rotor construction. Three common arrangements exist; these are illustrated in Figure 2.4 [23]. The magnets themselves have a relative permeability close to one meaning that the magnets appear as air gap to the flux. The main flux due to the permanent magnets is aligned with the d-axis. An increase in the effective air gap seen by the d axis leads to a reduction in the d axis inductance compared to the q axis inductance. The surface mount arrangement shown in Figure 2.4 (a), from the point of view of the rotor and effective air gap, is symmetrical and has a no geometric saliency. The configuration shown in

Figure 2.4 (b) has some saliency due to the rotor iron interpoles while the construction shown in Figure 2.4 (c) is a highly salient one. In addition to the salient nature of this design, the magnets themselves are better protected against centrifugal forces as they are contained within the rotor. This also offers better thermal protection thus reducing the risk of de-magnetisation. They are however more difficult to construct [23].

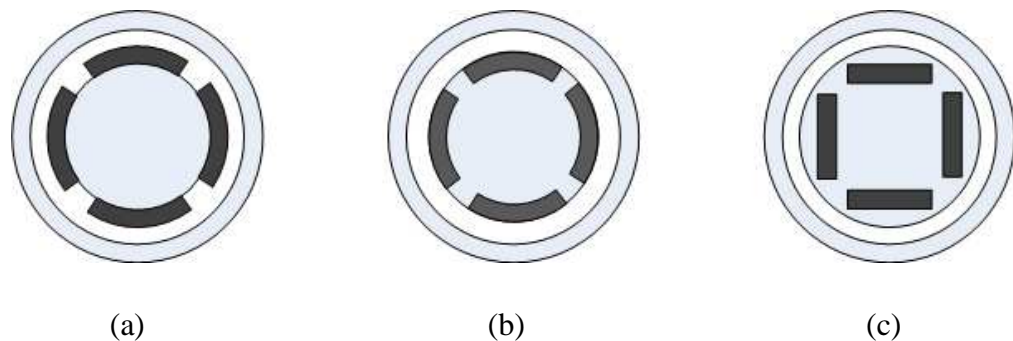


Figure 2.4 Rotor construction configurations of a permanent magnet motor [23]: (a) surface mount, (b) Inset and (c) Interior

The other saliency that exists in permanent magnet machines is known as saturation saliency. The flux in the machine causes local saturation of the iron, therefore reducing its permeability. This reduces the inductance of any conductors passing through the stator's saturated region. There is a large saturation due to the main flux. Saturation also exists due to the leakage flux which occurs orthogonally to the main flux. This is illustrated in Figure 2.5 which shows the ideal no load case [23, 30].

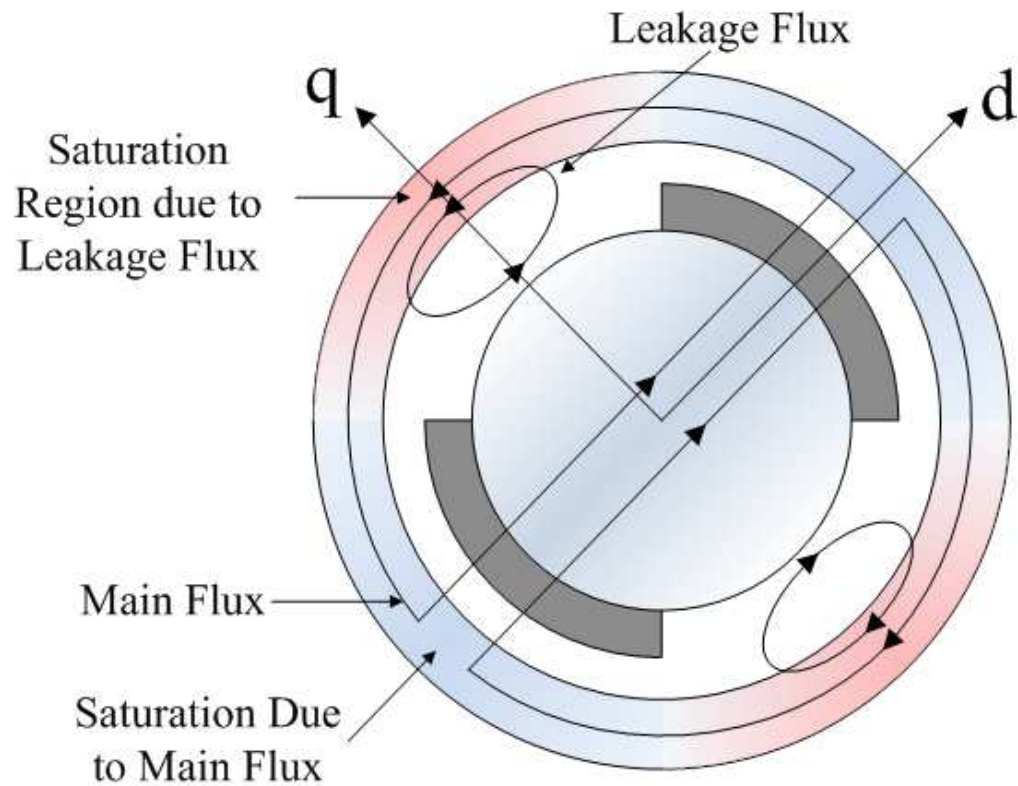


Figure 2.5 Magnetic saturation due to the main flux and leakage flux in a surface mounted permanent magnet machine [23, 30]

Under normal unloaded conditions the main flux causes a large saturation aligned to the d-axis. The resulting effective air gap due to the main flux is large [31]. The leakage flux saturation affects are aligned to the q-axis, hence saturation due to the leakage flux causes a reduction in the q-axis leakage inductance compared to the d-axis leakage inductance. The leakage inductances are almost unaffected by the saturation due to the main flux [32]. The saturation caused by the leakage flux occurs in the stator yoke and the teeth as shown in Figure 2.6 [30].

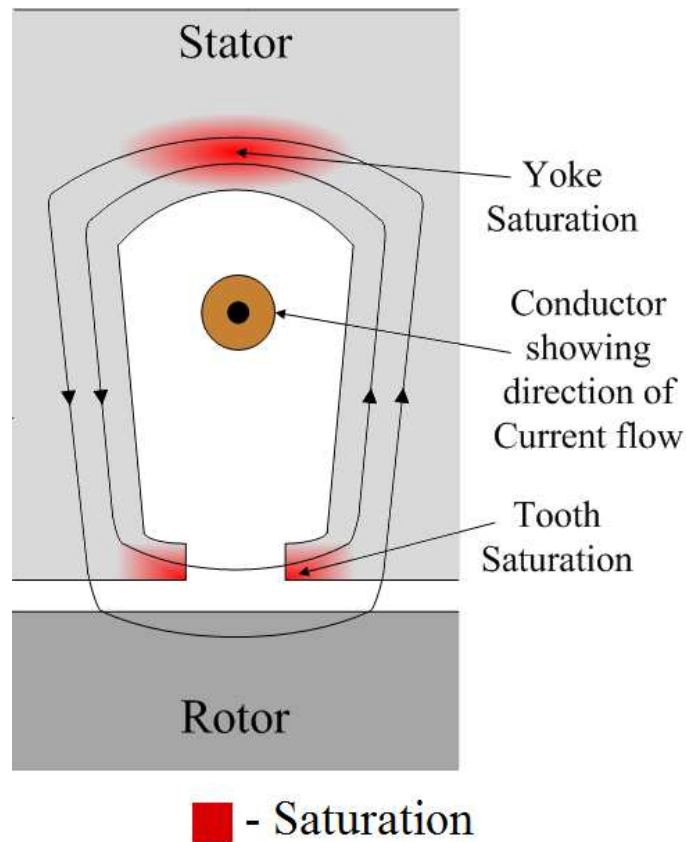


Figure 2.6 Saturation points due to leakage flux [30]

The saturation results in a reduction in the permeability of the iron surrounding the stator windings. This causes a reduction of the stator leakage inductances of the windings traversing the saturated iron. By tracking the variation in spatial leakage inductance around the machine the rotor position can be established. The stator leakage inductances themselves are positionally dependant and can be described by equations 2.1 - 2.3 [33].

$$l_{\sigma a} = l_o + \Delta l. \cos(n_{an}\theta_{an}) \quad (\text{Eqn 2.1})$$

$$l_{\sigma b} = l_o + \Delta l. \cos\left(n_{an}\left(\theta_{an} - \frac{2\pi}{3}\right)\right) \quad (\text{Eqn 2.2})$$

$$l_{\sigma c} = l_o + \Delta l \cdot \cos\left(n_{an}\left(\theta_{an} - \frac{4\pi}{3}\right)\right) \quad (\text{Eqn 2.3})$$

Where l_o is the average inductance, Δl is the inductance amplitude variation due to the saliency, n_{an} is the number saliency peaks per shaft rotation (=2 for saturation saliency).

In order to track the variation in stator inductance a high frequency voltage signal is applied to the machine and the resulting current response is measured to track the impedance variation. This high frequency signal generates a flux which is not able to flow through the main flux path and so the leakage effects dominate the response (providing the effects of resistance voltage drop and back-EMF are cancelled) [23, 31].

When load is applied to the machine the q-axis current introduces a flux in the q-axis which has the effect of shifting the resultant main flux away from the d-axis. The resulting position estimate is aligned to the resultant flux and not the true d-axis of the machine and so compensation is required to remove the phase shift effects of q-axis flux on the position estimate [23, 30, 34]. Naturally the level of compensation needed depends on the magnitude of I_q and hence load.

Saliency tracking methods themselves can be further split into two groups depending on the way the high frequency signal is applied; one group of methods have a high frequency signal added or “injected” into the demand signals applied to the machine while the other group of methods make use of the inherent high frequency content of transient vectors applied to the machine under PWM. For transient vector methods, in most cases additional vectors are applied to the machine that would not be applied under normal PWM operation in order to obtain the necessary measurements required for position estimation.

2.3.2 High Frequency Injection Methods

High frequency signal injection techniques work by adding a high frequency signal to the reference vector that is output by the inverter under normal operation. The high frequency signal itself is added during the implementation of the classic vector control equations and can either be added as a current [35] or as a voltage [28]. Voltage injection is more common since the bandwidth of the current controller will limit the frequency that can be injected. Injecting a lower frequency results in a larger torque ripple. The leakage inductances are modulated by the machine saliencies. This can be detected in the response to the high frequency signal [36]. Different high frequency signals have been applied to the machine in literature. A number of these will now be briefly discussed.

2.3.2.1 Continuous Injection in the $\alpha\beta$ Frame

This method adds a high frequency signal to the reference vector in the stationary $\alpha\beta$ reference frame. This is commonly injected as a voltage and so is added to the output of the current controller. The injected component can have a frequency of a few hundred Hz to a few kHz [37]. The high frequency current response of the machine consists of a positive sequence component and a negative sequence component both of which rotate at the injection frequency but in opposing directions. The negative sequence component also includes the saliency information which can be isolated to find the rotor position [28, 29]. A common approach to achieving this is to use a heterodyne demodulation strategy [28, 29].

This technique works well and its implementation is simple but the injected signal has components in both the flux and torque axis and so induces substantial torque ripple and audible noise.

2.3.2.2 d-axis Injection

This method seeks to improve the performance obtained from the $\alpha\beta$ injection technique by injecting a signal which only has a component in the flux axis [38], therefore reducing the torque ripple and audible noise seen in the response. The signal is injected into the rotating dq reference frame. The true dq orientation is not known so the injected signal is applied to an estimated dq frame. In [38] a measurement frame was defined as being 45° offset from the estimated frame. Theoretically, if the estimated frame is aligned with the actual dq frame of the machine then the d and q axis impedances measured in the 45° offset frame should have the same magnitude (assuming the impedances are symmetrical along the d or q axis). Any difference between the d and q axis impedances can be used as an error signal to drive the estimated dq axis onto the real dq axis allowing an accurate position estimate to be obtained [38].

2.3.3 Test Pulse Methods

An alternative to adding high frequency signals to the fundamental output of the inverter is to use the voltage vectors themselves applied by the PWM strategy since they have intrinsic high frequency content. Two approaches will be discussed here: the INFORM method and the Fundamental PWM technique. The latter has been designed to make use of the voltage vectors applied during normal PWM operation meaning that ideally no modifications need to be made to the vectors applied to the machine. In reality this is not the case and reasons behind this will be explained.

2.3.3.1 INFORM

The INFORM (Indirect Flux Detection by Online Reactance Measurement) method [33] uses additional test pulses applied during the null vector of a SVPWM period to measure the current derivatives which are modulated by the saliency and so contain position information. Three pulses must be applied in order to obtain the necessary measurements to construct a position vector and cancel the effects of back EMF and stator resistance voltage drop. For each of the pulses applied an equal but opposite pulse is immediately applied to cancel the effect of the initial pulse. As a result the net effect in terms of the additional voltage applied to the machine over a PWM period is zero. However the current does experience some additional distortion which leads to an increase in the THD (Total Harmonic Distortion) of the current and torque ripple. Figure 2.5 illustrates a typical INFORM pulse train. The additional switching of the phases increases switching losses. Also, the starting position for all three phases in the null vector is $+V_{DC}$, this means that it is necessary to switch multiple phases simultaneously. This can lead to $2V_{DC}$ being applied to the motor windings which will cause a reduction in the lifetime of the winding insulation [22].

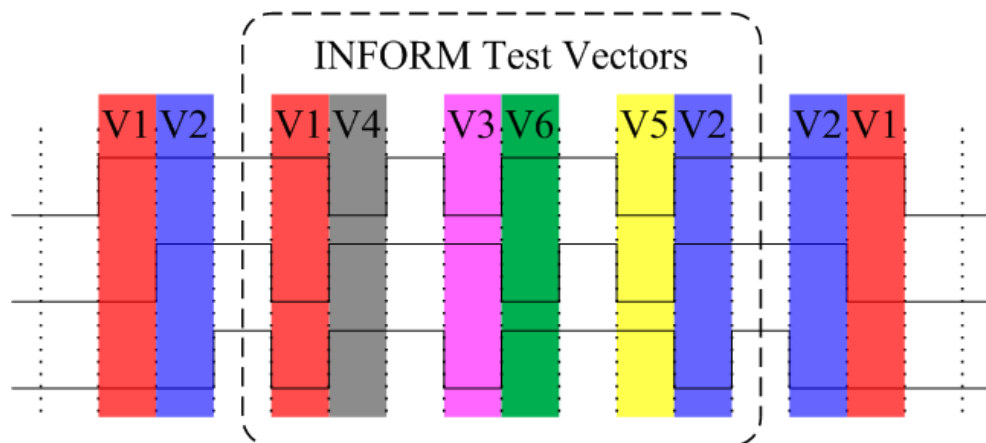


Figure 2.7 Test vectors applied under INFORM [22]

This method suffers from a limitation known as the minimum vector problem. The problem will be discussed in more detail later in this chapter but a brief description is that following a change in the switching state of the inverter high frequency oscillations are seen in the phase current and current derivative responses and these oscillations must be allowed to decay before a measurement of the derivative can be taken. As the oscillations can usually be guaranteed to have decayed after a certain amount of time, this time is the minimum time that a pulse must be applied to the machine for when a derivative measurement is required. It naturally follows that the opposite (compensation) pulse applied immediately after must also be applied for the same amount of time to fully compensate the change in the volts-seconds applied to the machine. As a result, the minimum pulse width limitation, apart from increasing current distortion, means that it is not always possible to have all three test pulses (and their necessary compensating pulses) in the same null vector. In [39] this was addressed by spreading the three test pulses over three consecutive PWM periods. However the mathematical derivation of the position vector equations assumes there is little change in the machines state between measurements. This assumption implies a limitation on the machines operating range as at high speed there is a significant change in position between each of the measurements.

2.3.3.2 Fundamental PWM Technique

The Fundamental PWM technique is another saliency tracking technique that uses test pulses applied to the machine in order to measure the modulation of the current derivative due to the leakage inductance and therefore track the machine saliency. The approach is designed to make use of the vectors applied under normal SVPWM meaning that no modifications to the standard PWM waveform in the form of additional test or compensation pulses are required [40, 41]. The method is theoretically able to work across

the entire speed range and is applicable to both induction machines and permanent magnet machines. The need to apply opposite test vectors, as with the INFORM method, in order to cancel the effects of back EMF and stator resistance voltage drop is removed by making use of the null vectors [41].

In terms of the implementation, ideally, all that is required is the sampling of current derivatives under certain active and null PWM vectors. Figure 2.8 illustrates the timing of the derivative sampling with respect to the PWM waveforms.

Once obtained, the derivative results are then used to calculate the position scalars P_a , P_b and P_c . The SVPWM sector in which the voltage reference lies determines which current derivatives should be measured and the results are easily utilised to obtain a position estimate.

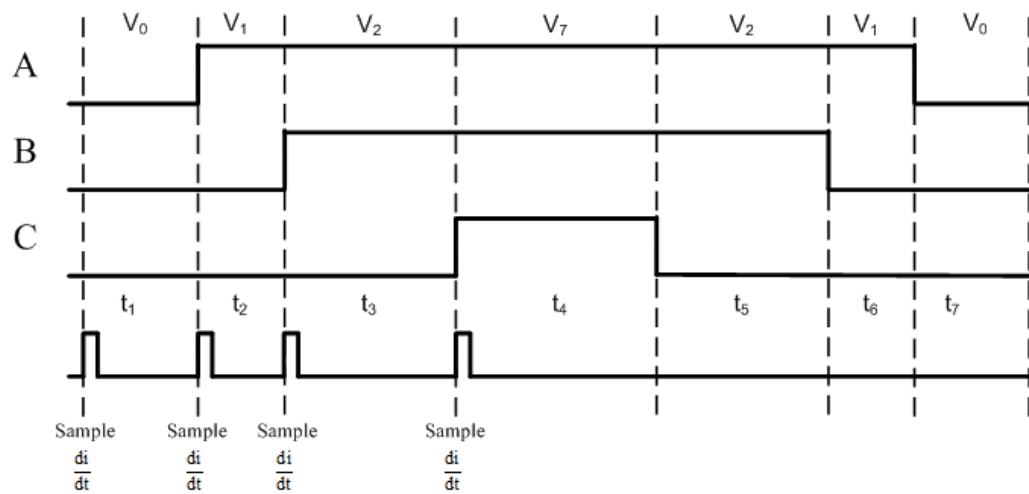


Figure 2.8 Illustrates the timing of the derivative measurements with respect to the PWM waveforms applied to the machine

The table of position scalar equations for a star connected machine is given in Table 2.1. Details regarding the derivation of the equations shown and the constant, c , referred to in Table 2.1, as well as information regarding the calculation of a position estimate based on the position scalars can be found in Appendix A. A similar set of equations can be derived for a delta connected machine.

SVPWM Vectors	Pa	Pb	Pc
V1 & V0	$2 - c \left(\frac{di_{aV1}}{dt} - \frac{di_{aV0}}{dt} \right)$	$-1 - c \left(\frac{di_{cV1}}{dt} - \frac{di_{cV0}}{dt} \right)$	$-1 - c \left(\frac{di_{bV1}}{dt} - \frac{di_{bV0}}{dt} \right)$
V2 & V7	$-1 + c \left(\frac{di_{bV2}}{dt} - \frac{di_{bV7}}{dt} \right)$	$-1 + c \left(\frac{di_{aV2}}{dt} - \frac{di_{aV7}}{dt} \right)$	$2 + c \left(\frac{di_{cV2}}{dt} - \frac{di_{cV7}}{dt} \right)$
V3 & V0	$-1 - c \left(\frac{di_{cV3}}{dt} - \frac{di_{cV0}}{dt} \right)$	$2 - c \left(\frac{di_{bV3}}{dt} - \frac{di_{bV0}}{dt} \right)$	$-1 - c \left(\frac{di_{aV3}}{dt} - \frac{di_{aV0}}{dt} \right)$
V4 & V7	$2 - c \left(\frac{di_{aV4}}{dt} - \frac{di_{aV7}}{dt} \right)$	$-1 + c \left(\frac{di_{cV4}}{dt} - \frac{di_{cV7}}{dt} \right)$	$-1 + c \left(\frac{di_{bV4}}{dt} - \frac{di_{bV7}}{dt} \right)$
V5 & V0	$-1 - c \left(\frac{di_{bV5}}{dt} - \frac{di_{bV0}}{dt} \right)$	$-1 - c \left(\frac{di_{aV5}}{dt} - \frac{di_{aV0}}{dt} \right)$	$2 - c \left(\frac{di_{cV5}}{dt} - \frac{di_{cV0}}{dt} \right)$
V6 & V7	$-1 + c \left(\frac{di_{cV6}}{dt} - \frac{di_{cV7}}{dt} \right)$	$2 - c \left(\frac{di_{bV6}}{dt} - \frac{di_{bV7}}{dt} \right)$	$-1 + c \left(\frac{di_{aV6}}{dt} - \frac{di_{aV7}}{dt} \right)$

Table 2.1 Position scalars for each of the active vectors (and corresponding null vectors) when operating a star connected machine [40, 41]

Superficially the Fundamental PWM technique appears to offer an ideal solution by making use of the vectors that would be applied to the machine with or without the addition of a sensorless control implementation. It simply involves sampling the necessary current derivatives, from which a position estimate may be obtained. The implementation of this approach in terms of the vectors applied to the machine and the responses that must be measured are confined to a single PWM period. In practice measurement of the current derivatives following inverter switching is prevented by high frequency oscillations appearing in the both the current and current derivative waveforms. These oscillations impose a limitation on the Fundamental PWM

technique known as the Narrow Vector Problem. This research is aimed at reducing this limitation which will now be described in detail.

2.4 The Narrow Vector Problem

2.4.1 Introduction

For the Fundamental PWM technique to work, an accurate measurement of the current derivative is required under certain SVPWM vectors. Taking an accurate measurement of the current derivative is not always possible however, as following a change in the switching state of the inverter; the current waveform contains high frequency oscillations (up to the MHz range). These oscillations, whose source and behaviour are investigated in Chapter 3, initially prevent an accurate derivative measurement from being made, but decay to the point where a derivative measurement can be made after a short amount of time. The length of time is dependent on the drive setup and is determined by the frequency content of the current or current derivative transient response following switching; this will be discussed further in Chapter 3. Figure 2.9 shows a typical current (a) and current derivative (b) response of a machine following the switching of an inverter output phase. The derivative response was captured using a commercial di/dt sensor built by PEM UK. The response has been filtered and amplified by the inbuilt signal processing circuitry of the sensor which has removed some of the high frequency content. In this instance the PWM vector times were large enough to allow the transient oscillations to decay, after which a current derivative measurement could be made.

Allowing the oscillations to decay before taking a measurement is acceptable but it requires that all vectors applied to the machine (under which

a derivative measurement is required) are sufficiently long enough to allow time for the oscillations to decay leading to a minimum PWM vector time threshold often called the minimum pulse width, t_{\min} .

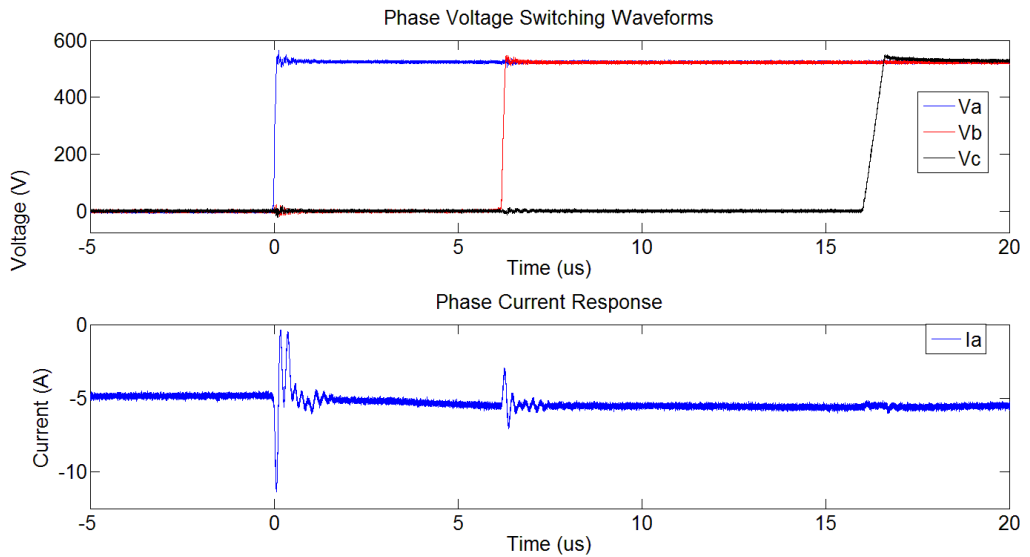


Figure 2.9 (a)

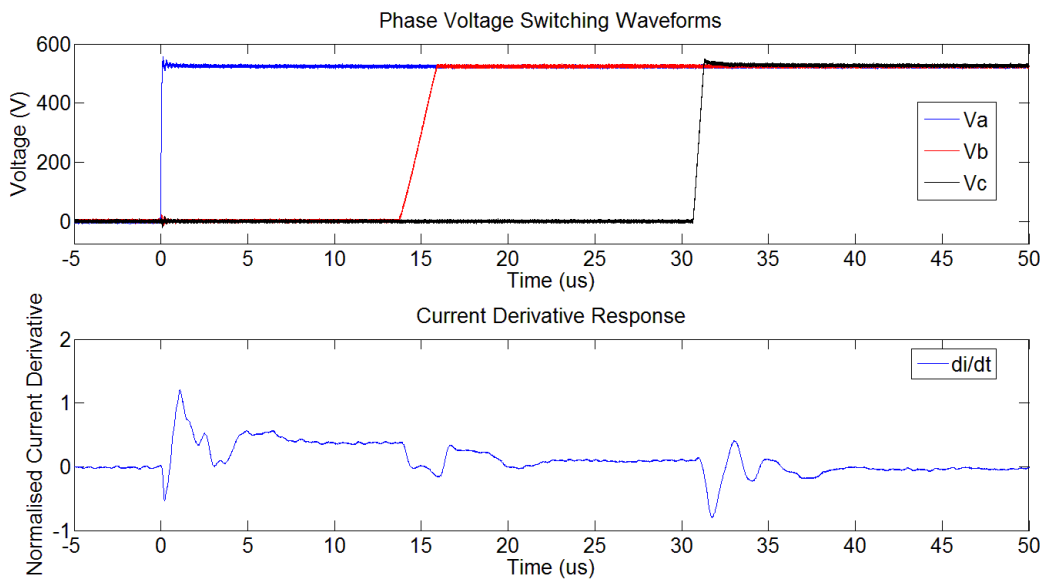


Figure 2.9 (b)

Figure 2.9 current response (a) and current derivative response (b) to inverter switching

A problem arises when the vector time is less than the minimum pulse width and there is not a sufficient amount of time available to allow the oscillations to decay and a derivative measurement to be made. Figure 2.10 shows an example where the vector time for the first active vector is less than the minimum pulse width threshold. It is clear that in this situation an accurate current derivative measurement cannot be obtained under this vector.

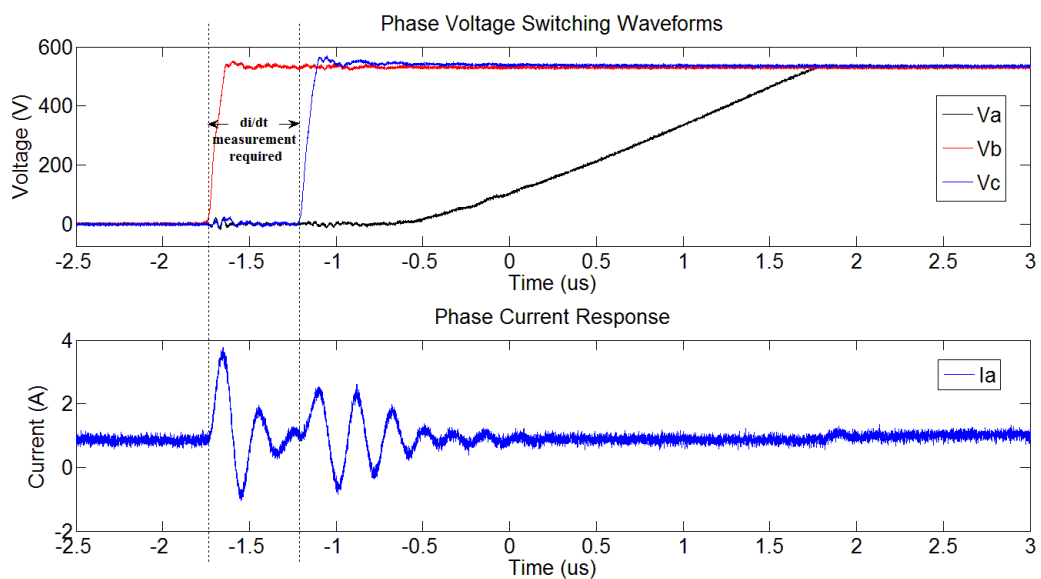


Figure 2.10 phase current response under a narrow vector. The high frequency oscillations under the first active vector do not have time to settle before the second active vector is applied

Minimum pulse width violations occur at low voltage references and when crossing SVPWM boundaries, some vectors must be extended to ensure that the minimum pulse width threshold is not breached. Figure 2.11 illustrates the areas in the SVPWM plane where pulse width extensions are required [42].

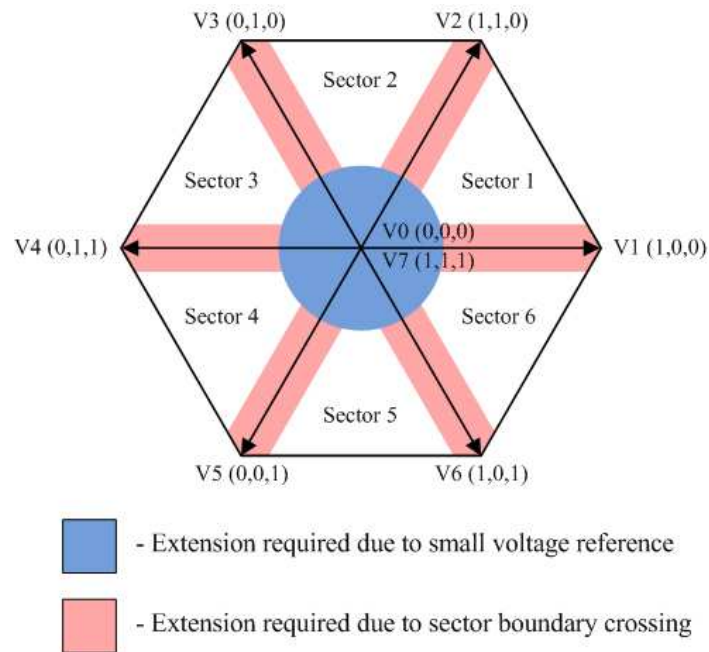


Figure 2.11 The locations on the SVPWM plane where voltage vector extensions are required [42]

2.4.2 SVPWM Pulse Width Extensions

Under normal (ideal) SVPWM operation the demand PWM vectors are applied in a symmetrical manner during the PWM period as illustrated in Figure 2.12.

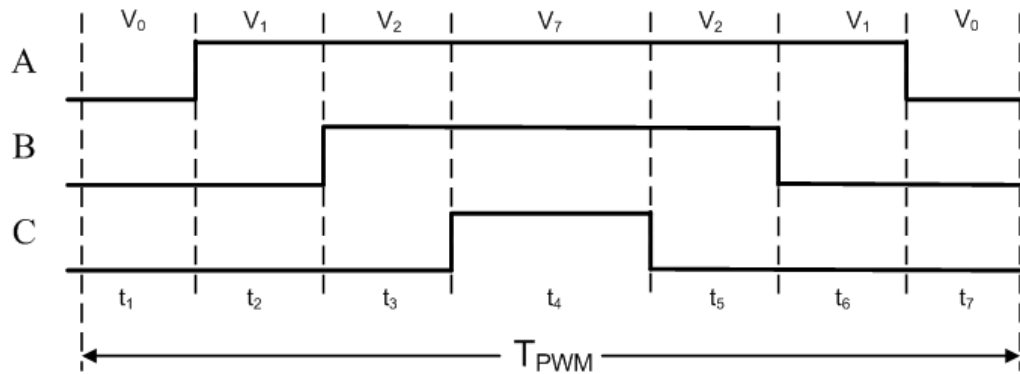


Figure 2.12 An ideal PWM output waveform for sector 1, $t_1 - t_7$ are the vector times

When it is necessary to extend vector(s) due to an original demand vector (under which a derivative measurement is required) being less than the minimum pulse width (t_{\min}) there are two possibilities that exist. To illustrate these scenarios it will be assumed that the first active vector time, t_2 , is less than the minimum pulse width threshold:

i) $t_2 < t_{\min}$ but $t_2 \geq t_{\min}/2$

If a PWM demand vector is less than the minimum pulse width threshold but still greater than half the minimum pulse width threshold then the minimum pulse width threshold can be met in one half of the PWM period (thereby allowing a derivative measurement to be made) by applying the vector asymmetrically, e.g. if the first active vector is too short it can be applied for a longer period in the first half of the PWM period than in the second half. Whenever a vector is extended to satisfy the minimum pulse width criteria, additional current distortion is introduced. This scenario is illustrated in Figure 2.13.

ii) $t_2 < t_{\min}$ and $t_2 < t_{\min}/2$

If the demand vector is less than half the minimum pulse width threshold then the pulse extension to t_{\min} will result in an increase in the volt-seconds being applied to the machine for a given vector. This must be compensated, usually by applying a different vector from the SVPWM plane, one which would not normally be applied in the sector the voltage reference lies in as illustrated in Figure 2.14. This ensures that the reference voltage vector that was originally intended is maintained in each PWM period.

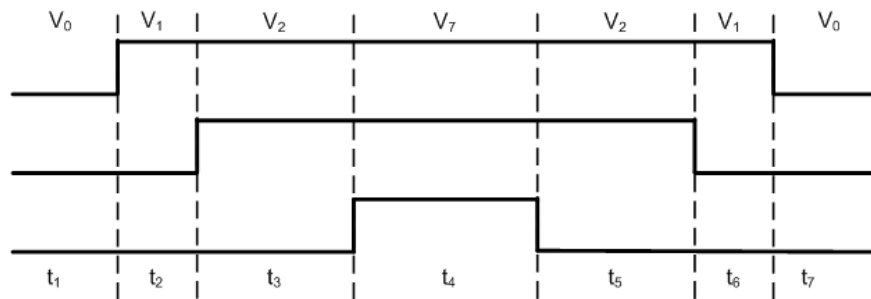


Figure 2.13 (a) PWM vectors before extension applied to t_2

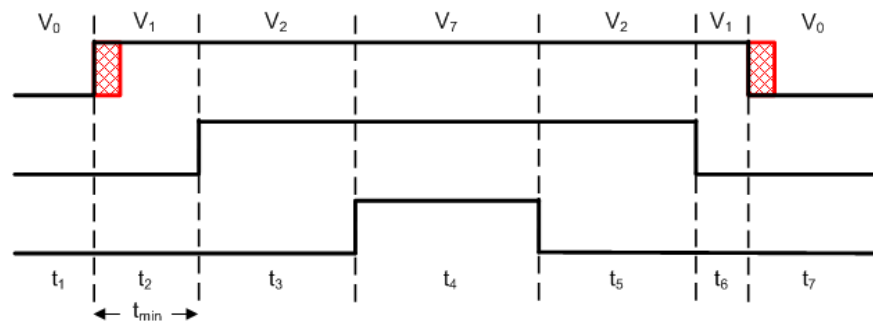


Figure 2.13 (b) PWM vectors after extension applied to t_2 , now $t_2 = t_{min}$

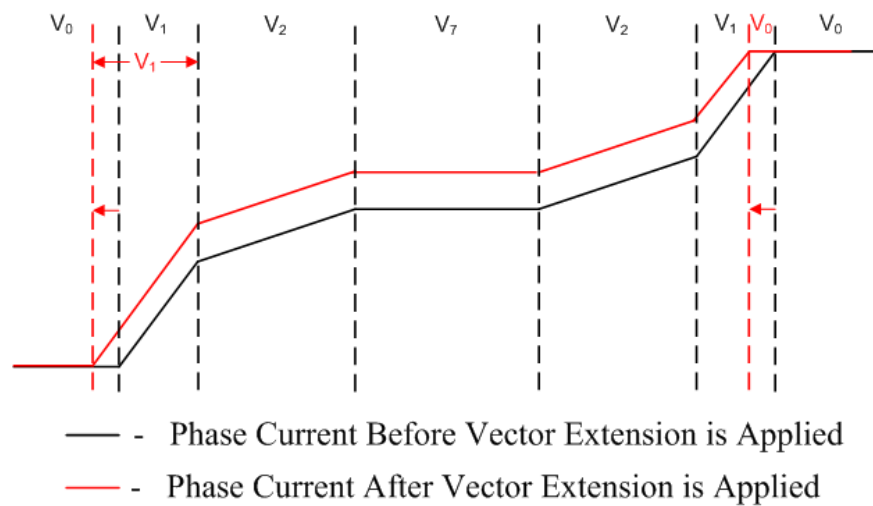


Figure 2.13 (c) Typical phase current illustrating the effects of extending a vector, the difference between the normal (black) and extended vector case (red) is the current distortion introduced

Figure 2.13 A case where vector extension is required for the first active vector only, with the original vector length being $> t_{min}/2$

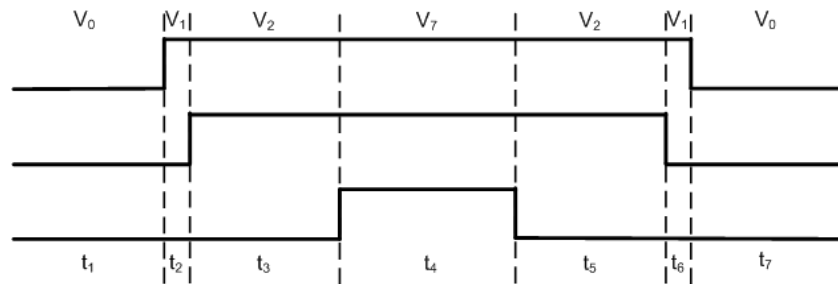


Figure 2.14 (a) PWM vectors before extension applied to t_2

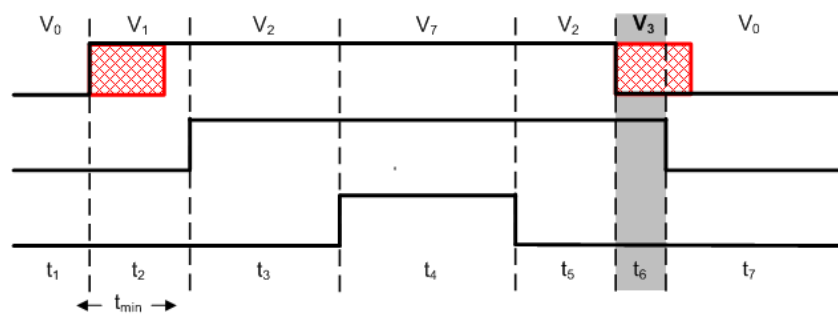


Figure 2.14 (b) PWM vectors after extension applied to t_2 , now $t_2 = t_{min}$, V_3 is now applied in the second half of the PWM period to compensate the extension of V_1

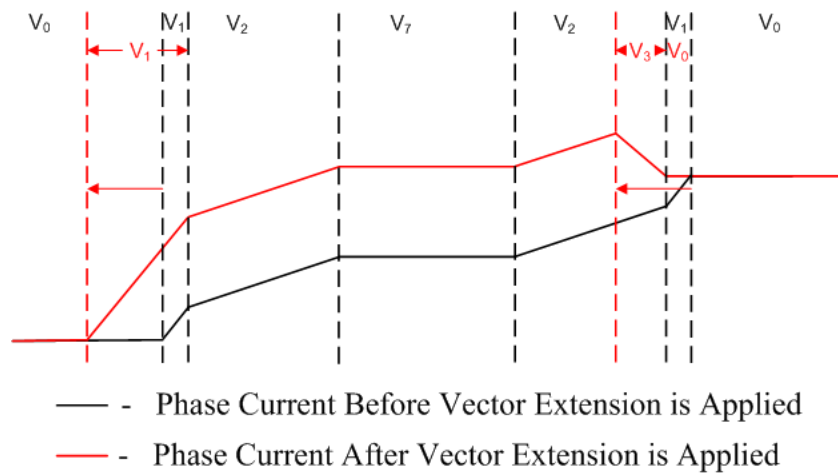


Figure 2.14 (c) Typical phase current illustrating the effects of extending a vector, the difference between the normal (black) and extended vector case (red) is the current distortion introduced

Figure 2.14 A case where vector extension is required for the first active vector only, with the original vector length being $< t_{min}/2$

It is clear that a narrower pulse requires a larger extension and therefore results in a larger current distortion being introduced which significantly effects harmonic performance. A number of compensation approaches have been published [23, 43, 44] some of which introduce less distortion than others by compensating as close to the extension as possible. But whenever extensions are implemented, distortion of the current waveform is unavoidable.

2.4.3 Current Distortion Introduced as a Result of Extending Vectors – An Investigative Demonstration

In order to highlight the level of current distortion introduced by extending vectors a number of experimental measurements were taken using different minimum pulse width thresholds at different speeds. Vector extensions were compensated using the methodology described in (2.4.2). The experimental rig described in Chapter 6 was used to collect the results. Some loading of the machine was required as the results were collected using a permanent magnet machine which only has a small fundamental current component at low loads. The choice of loading value used was arbitrary; a value of 50% load was selected. Under each speed five different minimum pulse widths were applied to the PWM and a measure of the total harmonic distortion (THD) of the phase current waveform was taken according to Eqn 2.4.

$$I_{\text{THD}} = \left(\frac{\sqrt{\sum_{n=2}^{10} (I_n^2)}}{I_1} \right) \cdot 100\% \quad (\text{Eqn 2.4})$$

The THD of the phase current waveform can be plotted according to the speed and minimum pulse width threshold as shown in Figure 2.15.

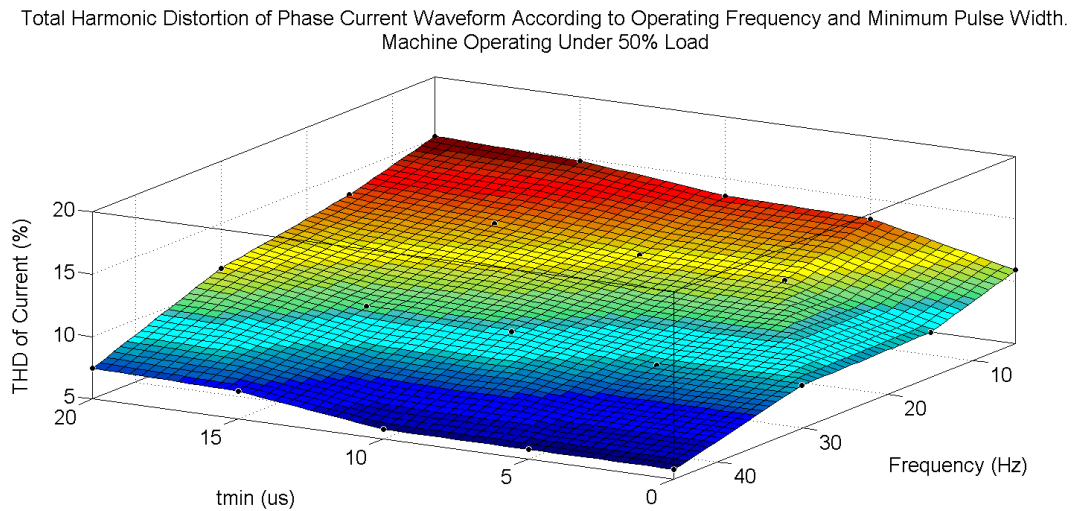


Figure 2.15 THD of the phase current waveform according to speed (electrical frequency) and minimum pulse width (t_{min})

Figure 2.15 illustrates the problem well. Firstly it can clearly be seen that an increase in the t_{min} value generally results in an increase in the THD. Secondly a reduction in speed also causes an increase in THD. This is because the low speed region corresponds to the blue region in Figure 2.11, where narrow pulse widths naturally occur on both active vectors. This means that even a small t_{min} value will cause a large number of vector extensions to be required. The bigger the t_{min} value the larger the distortion introduced. Conversely, at high speed a small value of t_{min} has little effect since the majority of the PWM vectors will already be longer than the t_{min} threshold. It should be noted that at low fundamental frequencies the THD per fundamental period is increased as there are an increased number of PWM periods (per fundamental period) where current distortion could be introduced. While collecting the results it was observed that the fundamental current component remained the same (as expected) and the increase in THD was mainly due to an increase in the 5th and 7th harmonic components as the t_{min} value was increased for each speed.

2.4.4 Narrow Vector Problem Conclusions

The Narrow Vector Problem is one of the remaining major limitations affecting the implementation of the Fundamental PWM technique. It will be seen in Chapter 3 that the oscillations seen in the current and current derivative waveforms arise due to parasitic impedances in the motor, drive and cabling. Since these effects cannot be removed oscillations will always be present following switching and hence narrow vectors will need to be extended to allow derivative measurements to be made, at the expense of the additional current distortion introduced. This problem is worsened at higher switching frequencies where vectors are generally shorter and so will require extending on a more frequent basis. The problem cannot be removed. However, it has been established that the current distortion (and associated torque ripple, vibration and audible noise) introduced is significantly reduced with a shorter minimum pulse width threshold. If an estimate of the current derivative can be made in a reduced time (ideally before the high frequency oscillations have decayed) then the minimum pulse width threshold can be reduced. This is the basis of the work proposed in this thesis.

2.5 Appearance of the Current Derivatives

It is pertinent to introduce and explain the current derivative waveforms seen under the SVPWM active vectors which must be measured in order to track saliency. The waveforms displayed in Figure 2.16 were obtained using the experimental setup detailed in Chapter 6. Figure 2.16 (a) shows current derivative waveforms sampled under the first active vector for phases A, B and C while Figure 2.16 (b) shows similar waveforms sampled under the second active vector. Figure 2.16 (c) shows the SVPWM sector.

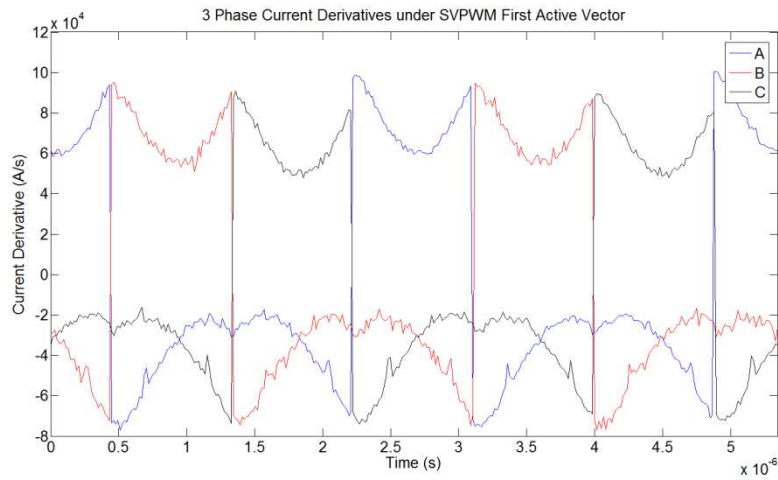


Figure 2.16 (a) Current derivatives under first active vector

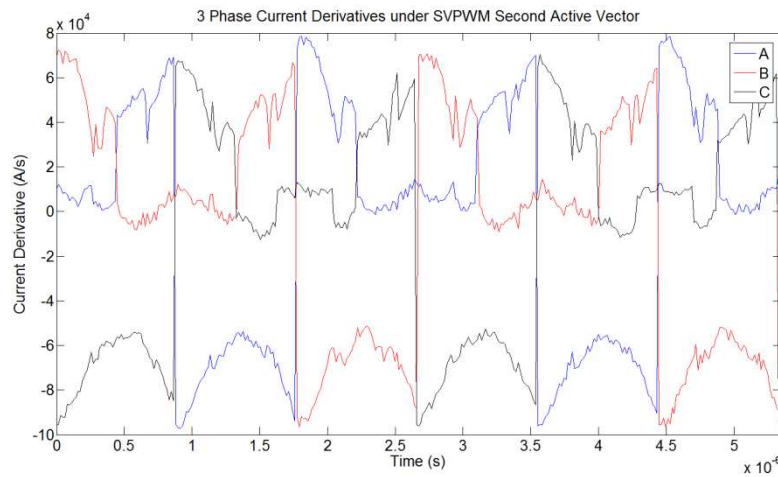


Figure 2.16 (b) Current derivatives under second active vector

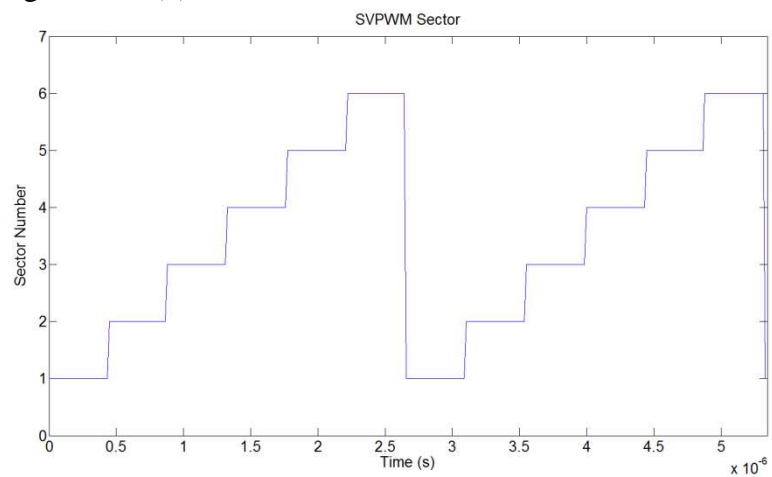


Figure 2.16 (c) SVPWM sector

Figure 2.16 Current derivatives under the first (a) and second (b) SVPWM active vectors. The SVPWM sector (c) is also shown

When inspecting the first active vector derivatives of Figures 2.16 (a) it is clear that (for each phase) for one third of the fundamental period the derivatives have positive amplitude while for the remaining two thirds of the fundamental period they have negative amplitude. Similarly, in the case of the second active vector derivatives, the derivatives have positive amplitude for two thirds of the fundamental period and negative amplitude for the remaining one third of the fundamental period. This can be explained by using the motor equivalent circuit illustrated in Figure 2.17 [22].

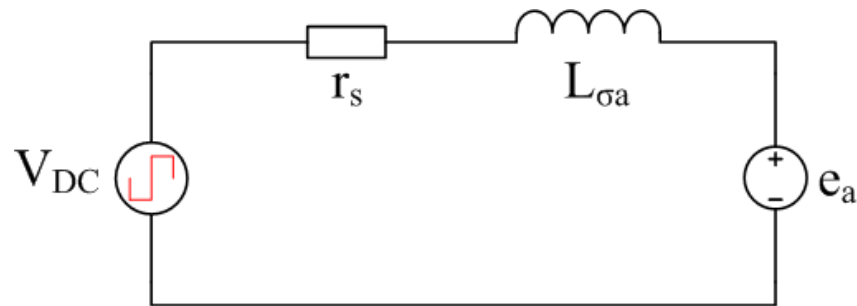


Figure 2.17 Equivalent circuit for phase A of a PM motor

Where V_{DC} is the applied DC link voltage, r_s is the stator resistance, $L_{\sigma a}$ is the leakage inductance and e_a is the back EMF. If the back EMF and stator resistance are neglected (this is valid since the back EMF has small amplitude at low speeds and the stator resistance voltage drop is small compared to the DC link voltage) then Eqn 2.5 describes applied voltage.

$$V_{DC} = L_{\sigma a} \frac{di}{dt} \quad (\text{Eqn 2.5})$$

Hence the current derivative (di/dt) depends on the applied DC link voltage and the leakage inductance (which is modulated by the motor saliencies). Table 2.2 shows the voltages applied to the motor by the inverter

under the first active and second active SVPWM vectors. It is clear from Table 2.2 that for phase A, under the first active vector, $+V_{DC}$ is applied for one third of the fundamental period (under sectors one and six), hence a positive derivative is expected. While $-V_{DC}$ is applied for two thirds of the fundamental period (under sectors two to five), hence a negative derivative is expected. This expectation matches the observations made in Figure 2.16. Similar conclusions can be drawn for the second active vector.

	Sector \ Phase	1	2	3	4	5	6
	First Active Vector	A	$+V_{DC}$	$-V_{DC}$	$-V_{DC}$	$-V_{DC}$	$-V_{DC}$
B		$-V_{DC}$	$+V_{DC}$	$+V_{DC}$	$-V_{DC}$	$-V_{DC}$	$-V_{DC}$
C		$-V_{DC}$	$-V_{DC}$	$-V_{DC}$	$+V_{DC}$	$+V_{DC}$	$-V_{DC}$
Second Active Vector	A	$+V_{DC}$	$+V_{DC}$	$-V_{DC}$	$-V_{DC}$	$+V_{DC}$	$+V_{DC}$
	B	$+V_{DC}$	$+V_{DC}$	$+V_{DC}$	$+V_{DC}$	$-V_{DC}$	$-V_{DC}$
	C	$-V_{DC}$	$-V_{DC}$	$+V_{DC}$	$+V_{DC}$	$+V_{DC}$	$+V_{DC}$

Table 2.2 The voltages applied to each phase, in each sector of the SVPWM plane for both first active and second active vectors

2.6 Accuracy Requirements of a Current Derivative Estimation/Calculation System

The current benchmark in terms of the accuracy of measured current derivative values is set by dedicated current derivative sensors, such as Rogowski coils. Standard current sensor implementations (where the derivative is estimated using two current measurements taken over a pre-defined time window – referred to as the two current sample approach in this work) have also been demonstrated and perform well provided a large minimum pulse width is set. Using the experimental setup described in Chapter 6, a $17\mu\text{s}$ minimum pulse width was found to be adequate for

measurement of the derivative when using both Rogowski coils and standard current sensors. The target of the new derivative calculation/estimation approach investigated in this work is to match the derivative measurement performance of these existing methods without the need to have the same large minimum pulse widths. In order to gauge what is an acceptable level of performance for a current derivative calculation/estimation approach, random noise has been added to derivatives measured using the two current sample approach. The THD + N (Total Harmonic Distortion + Noise) of the resulting position vector (calculated using the derivatives) was measured and is displayed in Figure 2.18. The peak amplitude of the derivatives used to calculate the position vector was 1×10^5 .

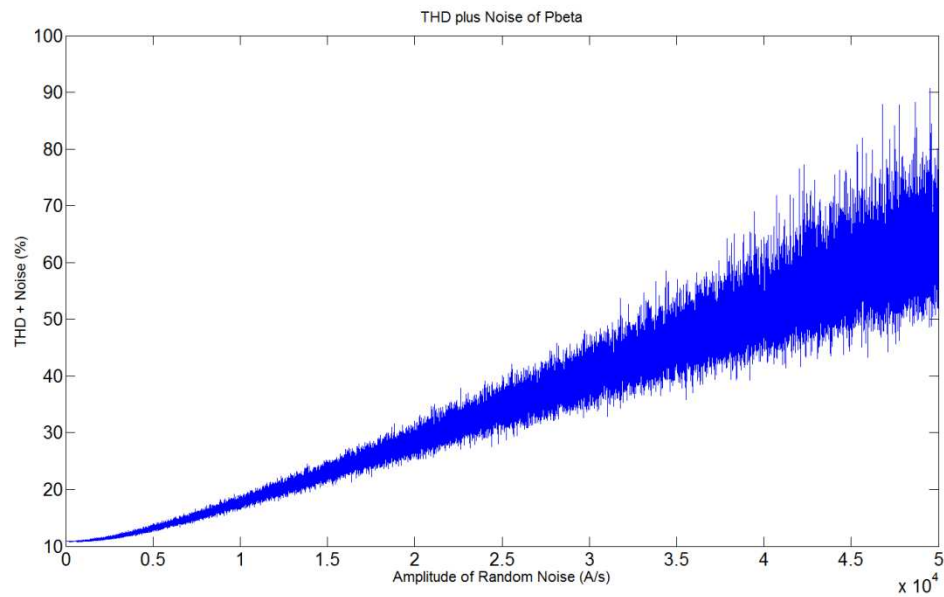


Figure 2.18 The THD + N (Total Harmonic Distortion + Noise) of the position vector when random noise is added to the derivative waveforms obtained using the two current sample method

It was important to include the noise contribution in the distortion measurement as this would not be truly reflected in a standard THD measurement but practically would make it difficult to cleanly isolate the

saliency component that is of interest using standard methods such as synchronous filtering [22, 23]. From the results shown in Figure 2.18 it is clear that as the amplitude of the noise added to the derivatives is increased, the position vector (and therefore the position estimate that would arise) is adversely affected. If a limit of 10% is set on the maximum allowable THD+N distortion (compared to the results obtained using the two current sample method), then the amplitude of the noise that is acceptable in the derivative estimates/calculations is $\pm 1.315e^4$ A/s (according to Figure 2.18).

Hence a target of this work will be to produce a derivative estimate that falls within $\pm 1.315e^4$ A/s of the value obtained from the two current sample method whilst only using a small time window to allow a reduction in the minimum pulse width to be achieved.

2.7 Hybrid Sensorless Solutions

Hybrid approaches combine more than one sensorless technique in order to achieve a better overall performance. This represents the best possibility for a generally applicable sensorless approach that can operate reliably across the entire speed range. Typically a hybrid solution will employ a saliency tracking technique at zero and low speed and a mathematical model approach for medium to high speed operation [45-53]. The two different approaches complement each other well. Saliency tracking methods can provide reliable low speed operation while at higher speeds mathematical model based methods can be used. This also allows the saliency tracking technique to be disabled if desired at higher speed. This can be advantageous since stopping the injection of a high frequency signal or the modification of the switching waveforms will significantly reduce the torque ripple and current distortion seen in the machines response.

With regards to the Fundamental PWM technique, at high speed it is the null vectors that become narrow and hence could require extension. Also, the technique cannot work in the over-modulation region as it requires that two active vectors and null vectors are applied [45]. Hence at high speed it would be beneficial to have a mathematical model based technique that could be relied upon to give an accurate position estimate.

The difficulties associated with hybrid solutions are the added complexity of implementing two techniques, the additional computation power required and how to achieve the crossover of the speed and angle value used for control from the different techniques.

Chapter 3

High Frequency Parasitic Effects in a Variable Speed Drive

3.1 Introduction

In order to allow investigation to take place into possible ways to reduce the minimum vector limitation, a detailed and thorough understanding of the sources of the high frequency current phenomena is required. It is widely known and accepted that the high frequency ringing observed in the phase current waveforms is due to parasitic capacitances and inductances that exist in the motor drive and cabling and the large dv/dt seen by these impedances when switching the active devices in the inverter. In order to reduce these high frequency effects (which can also cause problems with EMI) these impedances should be minimised through careful and considered design and construction techniques and if possible the dv/dt applied should be reduced. Figure 3.1 shows a simple drive schematic including some parasitic components. The main parasitic components illustrated are W) the capacitance to ground via the heat-sink, X) switching device parallel capacitance, Y) the loss and inductance of the supply cable, the capacitive coupling of the phases and the capacitance to ground via the shielding, Z) The turn to turn capacitance and the phase to frame capacitance of the windings.

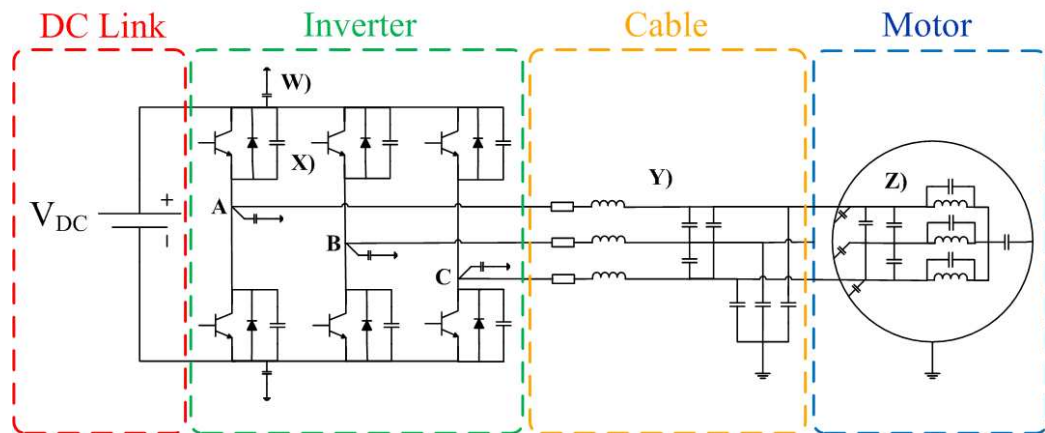


Figure 3.1 main parasitic impedances in a standard drive setup [54]

A complete and detailed description of the causes and locations of these parasitic impedances is lacking generally in the research literature. This is to some extent because the parasitic impedances are so diverse that to list them all and detail their quantitative effect on the machine response would be extremely difficult. It is however possible to pick some of the key contributing components which when included in a simulation model will produce a result which closely matches the real result.

3.2 Modelling of the High Frequency Behaviour of a Drive System

The parasitic impedances present in the drive system give rise to the high frequency behaviour that is of interest. Establishing the origins of these parasitic components and gaining a measure of the impedances themselves however is a complicated task. It is well known that noise conduction paths can be categorised into one of two types – common mode and differential mode [55]. Common mode conduction paths occur when there is a path through which current may flow between a conductor and ground while

differential mode paths exist when current paths are present between conductors. In a drive system the differential mode currents flow between capacitively coupled conductors and back through the inverter and DC link which completes the loop. There are many sources of these paths; many of the components in a drive system are grounded for safety reasons and provide common mode paths e.g. inverter heat-sink, cable shielding and motor frame. Insulation materials act as a dielectric material leading to capacitive coupling between conductors which again creates noise paths. Most of these couplings only become an issue at high frequency, in this work the frequency range of interest is 10 kHz to 30 MHz [56]. The following sections will describe the key contributors to the parasitic impedance network from the perspective of the motor and cabling and describe the simulation models that already exist in literature to allow investigation into high frequency behaviour. Later it will be seen that in order to capture the non-linear switching behaviour of the inverter some of the parasitic capacitances in the inverter itself must be included in any simulation model.

3.3 Motor Modelling in the High Frequency Range

3.3.1 Introduction

The creation of a high frequency motor and cabling model is achieved by producing an electrical model which has an identical frequency response in the MHz range to that of the actual motor and cabling being modelled. Such models are generally designed on a per phase basis and are capable of accurately characterising the frequency response in the 10 kHz to 30 MHz range [56]. Finding an appropriate model and extracting parameters for the

components within the model is a non trivial task and a number of methods exist to enable this. One such method is the Finite Element Method where the material properties and geometries (which can be difficult to obtain) of the machine being modelled are entered into modelling software which can then predict the parasitic impedance values for a given electrical model [57]. Another approach, the analytical approach, involves solving electrical circuit equations to find model parameters [58]. This method is more complex and although the resulting models can produce accurate results, they hold little physical meaning being constructed from several RLC branches that imitate the frequency response. Another alternative approach, the asymptotical method, was used in this work and is based on experimental measurement of the frequency response from which model parameters can then be derived. The components in the models proposed by previous investigations have been attributed to real physical quantities and effects in the motor or cabling. The component values in the models when using the asymptotical approach are found from equations which take their inputs from asymptotes of the frequency response as well as the maxima and minima values in the experimental frequency response.

3.3.2 Motor Model Development

Historically research into the high frequency behaviour of inverters coupled to motors began in the mid 1990's when it was realised that the EMI of such a setup was significant and could have a negative effect on neighbouring devices [59]. Initially the focus was directed towards understanding the EMI sources and producing simulation models to facilitate improvements in the EMC of drives. To this end, the models proposed were used as a tool to assist in the design of EMC filters [55, 58-60]. Many early high frequency models required a compromise between accuracy in the simulated results and a reasonable simulation run time, especially since any

motor model usually forms part of a larger system model rather than simply being simulated individually. Some models were not suitable at all for time domain simulations since many early models were made up of several segments placed in series to try and capture the distributed effects of the windings [55, 61]. This led to models which had high component counts and also made calculating model parameters difficult, while others were not capable of simulating both common mode and differential mode behaviour [60, 62]. With modern computing capability constantly improving, the run time restriction became less of a concern and models have more recently been designed for both frequency and time domain simulation and have incorporated both common mode and differential mode effects. This has led to more complex but more accurate models.

Many different models have been proposed in the literature. In this work the model proposed in [63] was adopted. The principle reasons behind this decision were that the model was based on the culmination of many years worth of research by many different authors, the relative ease of model parameter extraction and also because in [63] a corresponding cable model had been successfully used to investigate the effects of cable length – something which has a heavy influence on the high frequency content of the current waveform and is therefore extremely relevant to this research. The selected model proposed in [56, 63] is of a lumped parameter type. This will cause some loss in accuracy since some of the effects (such as turn to turn capacitance and winding to ground capacitance) are clearly distributed effects. However this reduction in accuracy has been proven to have a minimal detrimental effect in the final results [54, 62]. Only the stator windings are considered in the high frequency analysis since the high frequency flux does not penetrate the rotor or stator laminations [64]. The models which have been proposed in the literature have been based on evolution, with each new model incorporating an improvement compared to the previous effort. Figure 3.2 (a) – (d) illustrates the development of the chosen model which will now be introduced and discussed.

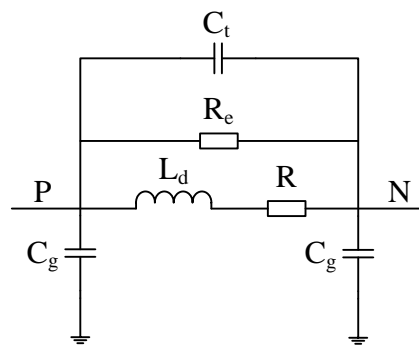


Figure 3.2 (a)

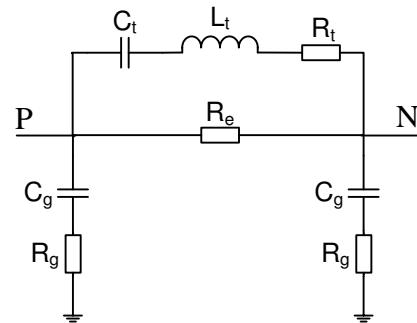


Figure 3.2 (b)

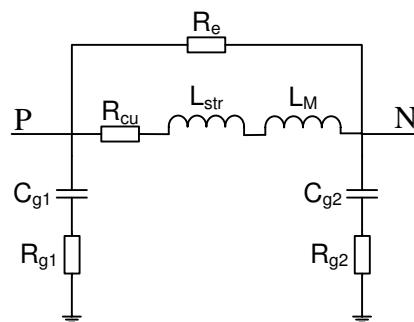


Figure 3.2 (c)

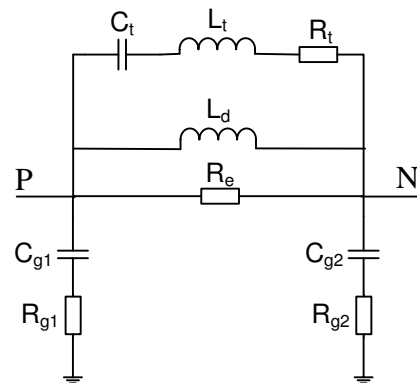


Figure 3.2 (d)

Figure 3.2 HF motor models proposed by a) [62], b) [60], c) [56] and d) [63]

The models in Figure 3.2 (a) and (b) were not suitable for common and differential mode simulation owing to the way that the frequency response measurements were made. Also, splitting the winding to frame capacitance into two separate capacitance values (as in Figures 3.2 (c) and (d) allows the common mode and differential mode responses to be more accurately modelled [65]. The models in Figure 3.2 (a) and (b) however, form a foundation for later models and are therefore relevant in the derivation of the model used in this work.

The model proposed in Figure 3.2 (a) was one of the first to be designed to simulate both high and low frequency behaviour of the machine simultaneously in the time domain [62]. The lumped parameter model consisted of a resistance and inductance to represent the low frequency resistance and stator leakage inductance (R and L_d). Connected in parallel branches to this there is a resistance to represent the eddy current loss in the magnetic core (R_e) and a capacitance for the turn to turn capacitive coupling (C_t). Finally there is a capacitive coupling between the winding and ground at both the phase and neutral ends of the winding (C_g). In this model this capacitance is given the same value at each end of the winding. The damping of the high frequency oscillations in the current was attributed to the impedance of the cable and input impedance of the machine. Initially the model failed to accurately model the damping of these current oscillations so a resistance was added in series with C_g at the phase input end to increase the damping performance.

This model was adopted and used to produce the model illustrated in Figure 3.2 (b) [60]. The model featured some key additions including a resistance between the winding neutral and ground (R_g). The parallel turn to turn branch also now included a resistance (R_t) and inductance (L_t) which would be present in the high frequency path. These additional components meant that a second resonance point in the experimental result was now captured by the simulation. A parallel branch containing the dynamic dq model was suggested to capture the low frequency behaviour.

An intermediate model not shown here was proposed by Weber [66] and was based on [59, 60, 62, 64]. The purpose of the work was to try and design a model library that could be used to simulate the high frequency behaviour of a given motor. The conclusion was that for accurate simulation performance each motor should be modelled individually. It is however of interest since it provided the basis for the work in [56, 63] which were the first models to be designed for simulating common mode and differential behaviour and could be used for both time and frequency domain simulation.

These models were not aimed at being able to capture low frequency behaviour. The component count of the model was relatively low and the parameter extraction techniques were simple and described in detail.

The initial model illustrated in Figure 3.2 (c) [56], consisted of the winding to ground capacitances (C_{g1} and C_{g2}) and resistances (R_{g1} and R_{g2}) as in Figure 3.2 (b) [60] but in line with the real machine, these were given different values (where as in [60] they were treated as equal). R_{cu} represented the copper loss and could be neglected for high frequency simulation and therefore analysis in the frequency domain but at low frequencies acted to limit the current and so was necessary for time domain simulation. The inductances represent the stray inductance (L_{str}) and an inductance incorporating the inductive coupling between the phases (L_M). Once again iron loss was included in the form of a parallel resistance (R_e) but turn to turn effects were not included. The model produced good results but there was a resonance point not captured by the proposed model and so an additional capacitance and resistance were added in parallel with the phase coupled inductance, L_M . The values for these components were found by trial and error and had no physical meaning. The additional resonance provided by these additional components resulted in an improved correlation between the simulated and experimental results.

Finally the model proposed in Figure 3.2 (d) [63] was based entirely on Figure 3.2 (c). However the additional resonance point which was identified in [60] as being due to the turn to turn impedance was included. The additional un-attributable resistance and capacitance in [56] were replaced with a parallel branch containing the turn to turn impedance components (C_t , L_t and R_t). The method for finding these additional component values was documented in a similar way to [60].

This resulted in a complete model for time and frequency domain simulation including both common and differential mode behaviour with a low component count where each component could be associated with the real physical effects of the machine and each component value was simple to find.

The model was accurate up to very high frequencies (> 30 MHz) at which point the impedances of the measuring equipment would begin to affect the measured response and so effects observed in the response could not be attributed to the machine [56]. It should be noted that some accuracy is lost by stipulating that the model must be suitable for time domain simulation as some of the parameters should in reality have some frequency dependence, for example R_e in Figure 3.2 (d) which represents iron loss. As the frequency is increased the cross sectional area decreases due to diffusion [56].

3.3.3 Finding the Model Parameters

The method proposed in [56] was used to find the parameters for use in the motor model. This requires two measurements of the machine's frequency response – one of the common mode response and one of the differential mode response. The measurements are taken with the motor at standstill and all supply cabling detached. To measure the impedance of the differential path of a three phase machine, two of the three phases are connected together as shown in Figure 3.3. The frequency response is then measured using an impedance analyser or RLC meter across the two shorted phases and third phase

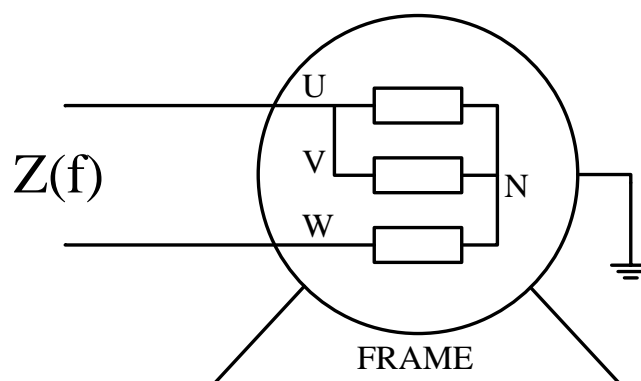


Figure 3.3 Measurement Setup to Determine Differential Mode Parameters

To measure the impedance of the common mode path all three phases of the stator windings are connected together and the response is measured between the input of the three phases and the motor frame, as shown in Figure 3.4.

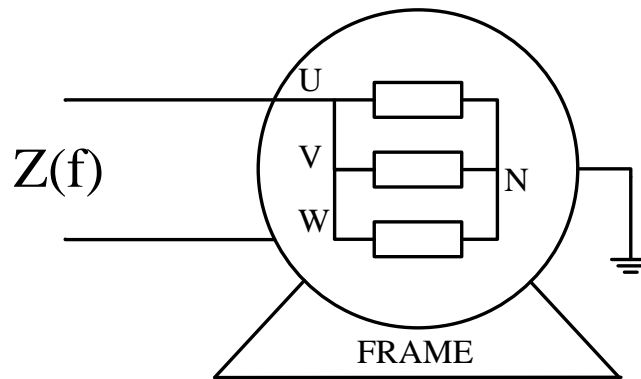


Figure 3.4 Measurement Setup to Determine Common Mode Parameters

Figure 3.5 shows the common mode and differential mode impedance responses for an ASEA 4 kW induction machine measured using a HP Agilent 4194 Impedance analyser. To increase the accuracy of the results the logarithmic steps (100-1000, 1000-10000, 10000-100000...) of the measurement were broken up and carried out separately when taking measurements.

The following derivation of the HF model parameters is based on [63]. Refer to Figure 3.2 (d) for the schematic of the model used. There are a number of points in the common and differential mode impedance response which are used to find the model parameters and these are marked on the plots in Figure 3.5.

The points marked C_{HF} , C_{total} and L_{DM} in Figure 3.5 are the points from which asymptotes are taken to find the value for each of the respective impedances. The asymptotes are assumed to have a gradient of 20dB/decade, capacitances are found from $C = \frac{1}{2\pi fZ}$ while inductances are calculated using

$$L = \frac{Z}{2\pi f}$$

Impedance Magnitude Response for Common and Differential Mode Paths

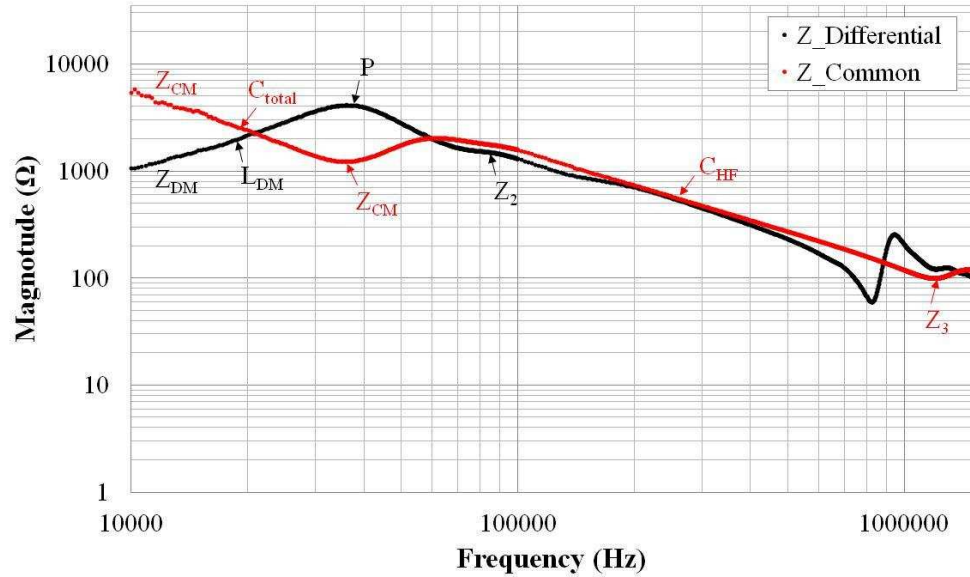


Figure 3.5 The common mode (red) and differential mode (black) impedance responses captured from a 4 kW ASEA induction machine. Also highlighted are the key points that are used to find high frequency model component parameters

Once C_{HF} , C_{total} and L_{DM} have been obtained the equations for the derivation of the electrical component values given in (Eqn 3.1) to (Eqn 3.12) can be used to find the remaining component values [63].

$$C_{g1} = \frac{1}{3} C_{HF} \quad (\text{Eqn 3.1})$$

$$C_{g2} = \frac{1}{3} (C_{total} - C_{HF}) \quad (\text{Eqn 3.2})$$

$$L_{CM} = (12\pi^2 C_{g2} f_{z1}^2)^{-1} \quad (\text{Eqn 3.3})$$

$$R_e \approx \frac{2}{3} |Z_p| \quad (\text{Eqn 3.4})$$

$$R_{g1} = \frac{2}{3} |Z_{z3}| \quad (\text{Eqn 3.5})$$

$$R_e = \frac{2}{3} |Z_{z1}| \quad (\text{Eqn 3.6})$$

$$L_d = L_{CM} + \frac{4}{9} L_{DM} \quad (\text{Eqn 3.7})$$

$$R_{g2} \approx \frac{1}{3} |Z_{z1}| \quad (\text{Eqn 3.8})$$

$$C_t \approx \frac{1}{6} (C_{g1} + C_{g2}) \quad (\text{Eqn 3.9})$$

$$L_{zu} = 3(16\pi^2 C_{g1} f_{z3}^2)^{-1} \quad (\text{Eqn 3.10})$$

$$R_t = |Z_{z2}| \cos(\theta_{z2}) \quad (\text{Eqn 3.11})$$

$$L_t = \frac{1}{C_t} \left(\frac{1}{2\pi f_{z2}} \right)^2 \quad (\text{Eqn 3.12})$$

By using the impedance responses of the ASEA machine (Figure 3.5) and equations (Eqn 3.1) to (Eqn 3.12) the electrical parameters shown in Table 3.1 were calculated

Parameter	Value
C_{g1}	30.47 pF
C_{g2}	16.52 pF
R_e	6.47 k Ω
R_{g1}	11.66 Ω
R_{g2}	398.69 Ω
L_t	504.42 μ H
C_t	7.83 pF
R_t	2.88 k Ω
L_d	486.66 μ H
L_{zu}	6.525 μ H

Table 3.1 Model parameters found from (Eqn 3.1) – (Eqn 3.12)

The Model in Figure 3.2 (d) was implemented using Matlab Simulink and the parameters in Table 3.1. Figure 3.6 shows the common mode impedance response of the model in the frequency domain with the experimentally derived response also shown for comparison. The results show that the model produces reasonable approximation.

Figure 3.7 shows the differential mode response of the model implemented in simulink compared with the actual measured response of the machine. Again the result from the model is a reasonable approximation to the measured response with the resonant points occurring at the correct frequencies.

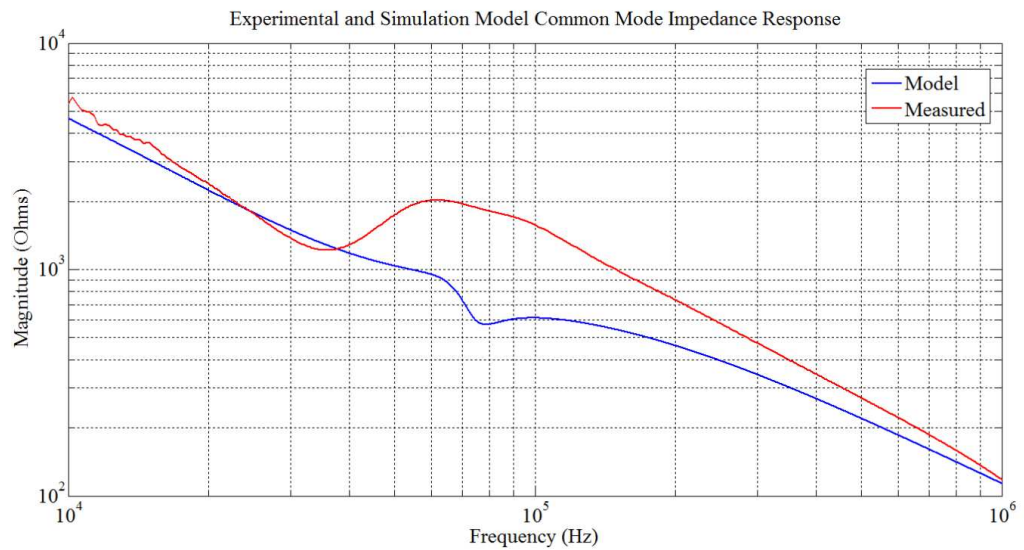


Figure 3.6 Comparison of the simulated and the experimentally captured common mode impedance response

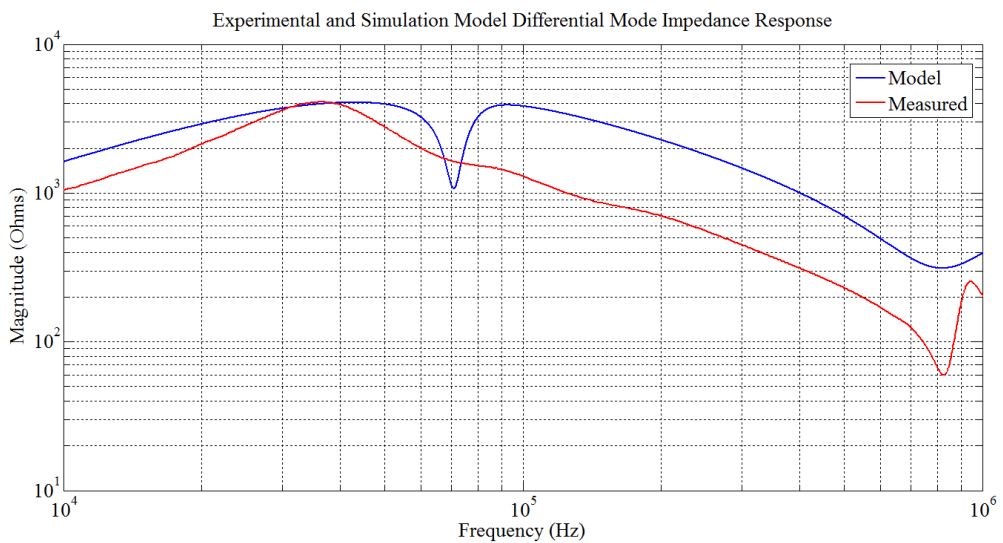


Figure 3.7 Comparison of the simulated and the experimentally captured differential mode impedance response

In literature the result is often refined at this point (by modifying the electrical model parameters using trial and error) in order to acquire an improved approximation. Previously a Genetic algorithm has been used to refine the result and obtain a better fit between the simulation and

experimental results [67]. In this research the result was refined to a small degree through trial and error. This yielded a closer match for the differential mode response, but was a compromise since the common mode response was adversely affected. However it was the time domain response that was of interest and this was found to have good correlation with experimental data, in terms of its high frequency content, even before the model parameters were modified.

In the case that low frequency behaviour of the machine must also be considered two principal methods are suggested for incorporating the high frequency model into simulation. The simpler of these is to run the high frequency model in parallel with a low frequency simulation [55, 57, 68] with both models being supplied from the same source as illustrated in Figure 3.8. The high frequency models have a low impedance at the fundamental frequency, so filters are placed at the input of the high frequency models to block fundamental components [55]. This simulation approach was used in this research owing to its simplicity and the lack of a need to obtain a single accurate response across the entire frequency range (since it is only the high frequency content that is of interest).

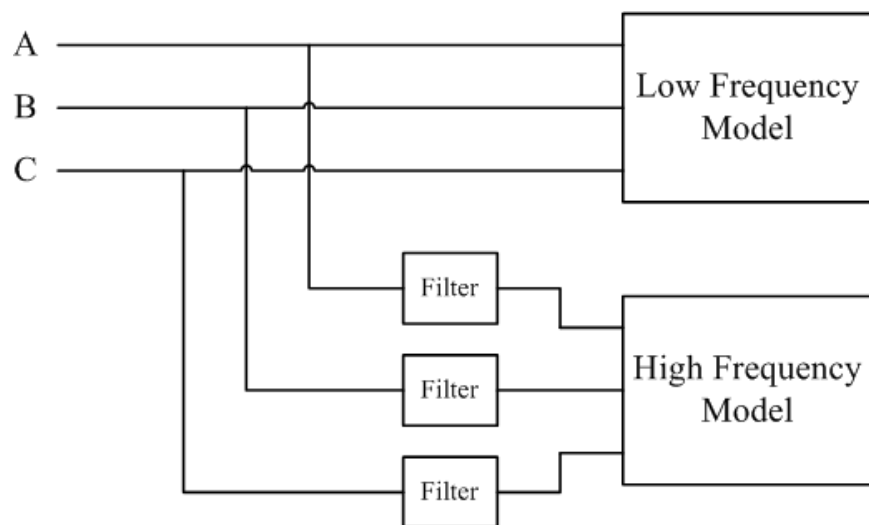


Figure 3.8 Configuration used to simulate high and low frequency behaviour [55, 57, 68]

An alternative method involved modifying the IEEE standard 112 per phase equivalent circuit to include the high frequency parameters [60, 62, 69]. This approach was not used in this work as the inclusion of low frequency behaviour into the results was not required; hence the merging of the low and high frequency models would have unnecessarily increased the complexity of the model.

3.4 Cable Modelling in the High Frequency Range

3.4.1 Introduction

Similar models to those proposed for motors have been proposed for predicting the high frequency behaviour of motor supply cabling. The cable modelled is of a shielded multi-core/conductor type and is modelled per unit metre. The cable conductors each have an associated inductance and loss across their length and are coupled through the dielectric insulating material between the conductors. A number of cable models have been proposed, Figure 3.9 shows the most commonly adopted model, based on a standard transmission line model, it is a second order per unit metre model and has few components [70-72].

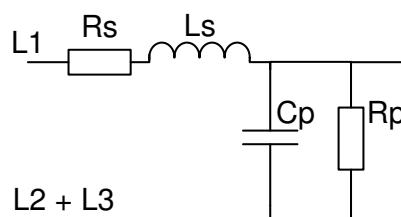


Figure 3.9 the standard transmission line model of a cable [70-72]

This model has been expanded, as illustrated in Figure 3.10 (a) [60] in order to increase the accuracy of the results by including dielectric effects and later to include skin and proximity effects as shown in Figure 3.10 (b) [63].

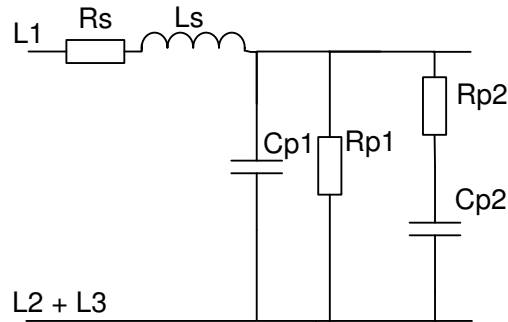


Figure 3.10 (a)

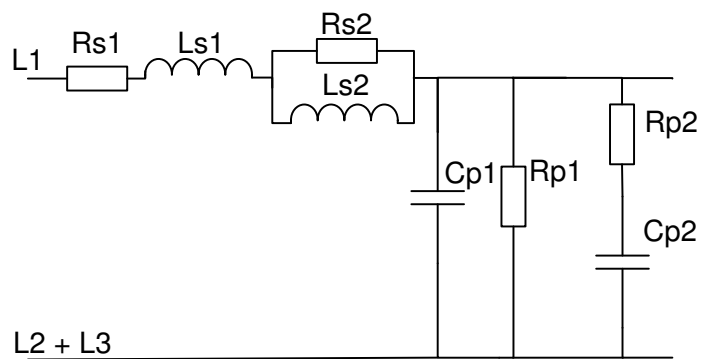


Figure 3.10 (b)

Figure 3.10 expanded high frequency models of the power cable per-unit length. (a) includes the effects of dielectric losses [60], while (b) includes skin and proximity effects [63]

The model proposed in Figure 3.10 (b) will be used since it is the most advanced model and has been used to investigate the effects of cable length [63].

3.4.2 Finding the Model Parameters

A thorough methodology for finding parameter values for the model is detailed in [63]. The method for deriving the model parameters is similar to the method used for deriving the motor model parameters. A short circuit and open circuit impedance response is captured and then asymptotes of the response are used to calculate electrical parameters. The frequency responses were again captured using a HP 4194 impedance analyser. Figure 3.11 (a) shows the short circuit frequency response while Figure 3.11 (b) shows open circuit frequency response of the cable.

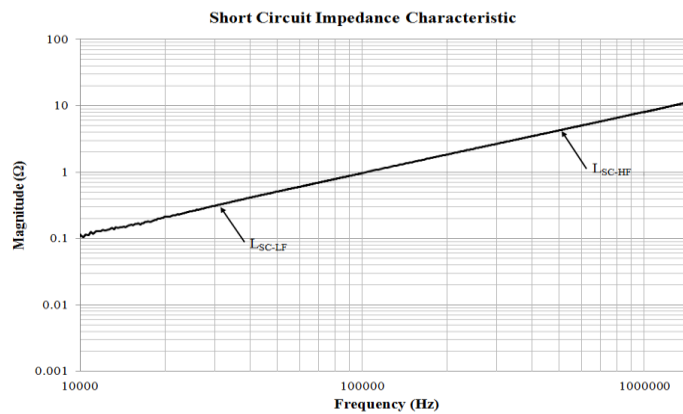


Figure 3.11 (a)

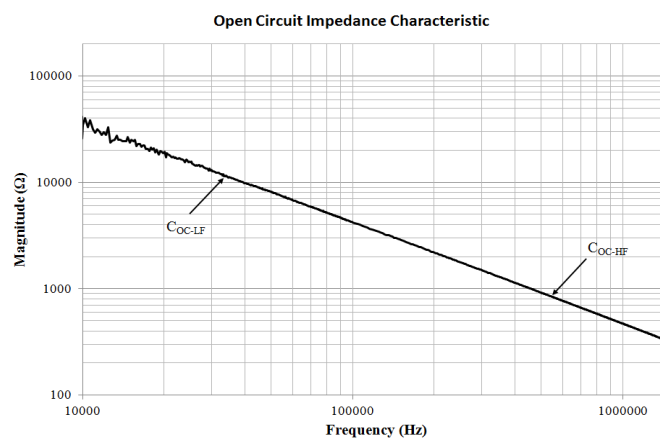


Figure 3.11 (b)

Figure 3.11 Short (a) and open (b) circuit frequency responses of a 1m length of 5 core shielded cable

Once again a number of values were found from asymptotes taken at the points marked in Figure 3.11 (a) and (b). Equations (Eqn 3.13) to (Eqn 3.21) are then used to find the values of the respective impedances in the model [63]. The results are given in Table 3.2.

$$L_{s1} = L_{SC-HF} \quad (\text{Eqn 3.13})$$

$$L_{s2} = L_{SC-LF} - L_{s1} \quad (\text{Eqn 3.14})$$

$$R_{s1} = |Z_{SC-LF}| \cos(\theta_{SC-LF}) \quad (\text{Eqn 3.15})$$

$$R_{s2} = |Z_{SC-HF}| \cos(\theta_{SC-HF}) - R_{s1} \quad (\text{Eqn 3.16})$$

$$C_{p1} = C_{OC-HF} \quad (\text{Eqn 3.17})$$

$$C_{p2} = C_{OC-LF} - C_{p1} \quad (\text{Eqn 3.18})$$

$$R_{p1} = |Z_{OC-LF}| [\cos(\theta_{SC-LF})]^{-1} \quad (\text{Eqn 3.19})$$

$$R_{p1/p2} = |Z_{OC-HF}| [\cos(\theta_{SC-HF})]^{-1} \quad (\text{Eqn 3.20})$$

$$R_{p2} = \left[(R_{p1/p2})^{-1} - (R_{p1})^{-1} \right]^{-1} \quad (\text{Eqn 3.21})$$

Parameter	Value
L_{s1}	249.75 nH
L_{s2}	52.94 nH
R_{s1}	16.34 m Ω
R_{s2}	145.61 m Ω
C_{p1}	461.03 pF
C_{p2}	85.237 pF
R_{p1}	79.77 k Ω
R_{p2}	88.458 k Ω

Table 3.2 calculated component values for the high frequency cable model

The model illustrated in Figure 3.10 (b) was implemented in Matlab Simulink using the component values listed in Table 3.2. Open circuit and short circuit impedance responses could then be captured from the simulation model and compared with the experimental results as demonstrated in Figure 3.12 (a) and (b).

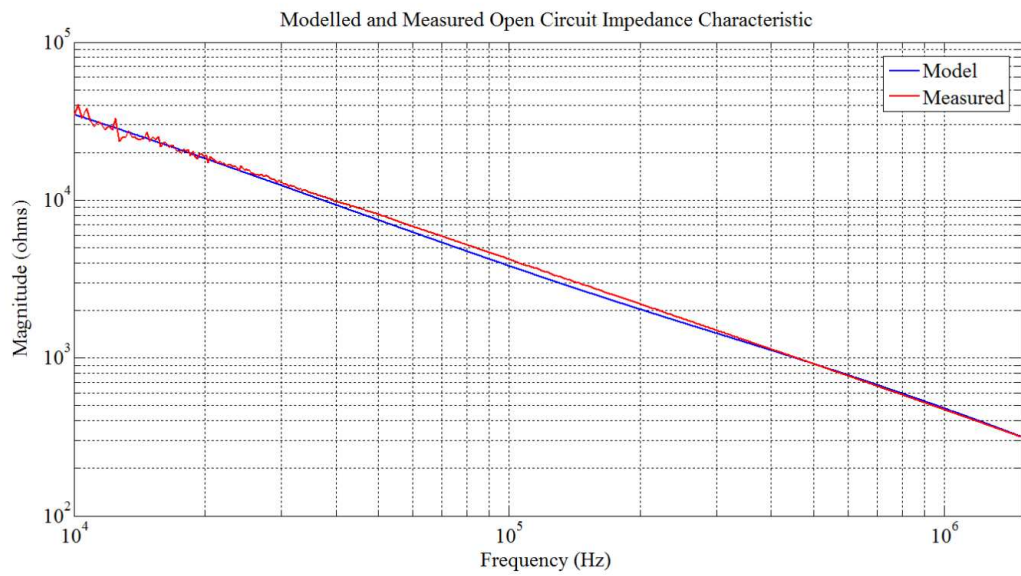


Figure 3.12 (a)

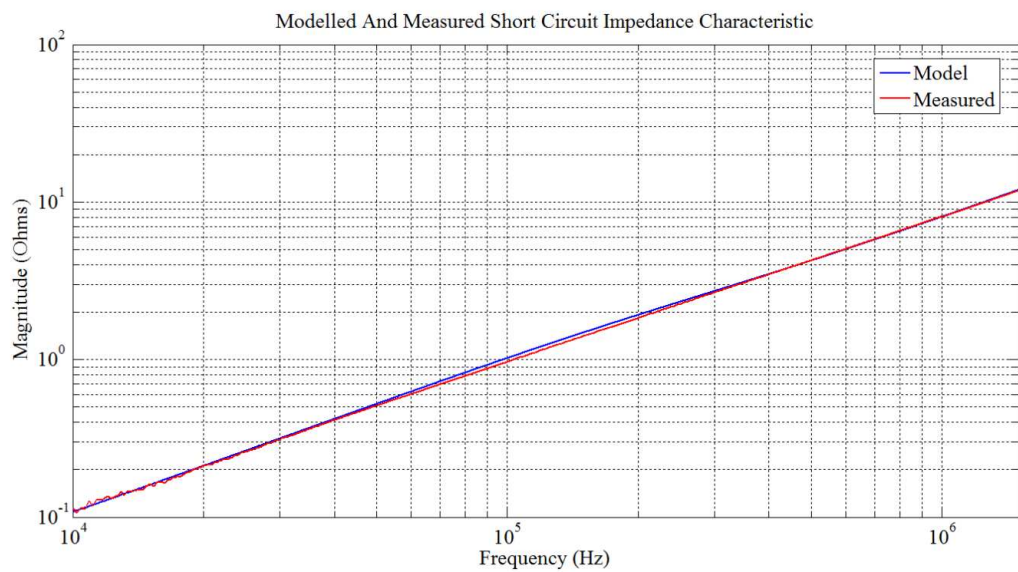


Figure 3.12 (b)

Figure 3.12 A comparison of the measured and simulated open circuit (a) and short circuit (b) impedance responses

3.5 Time Domain Simulation Results

With the cable and motor modelled in the high frequency range, the model was driven by a simulated three phase output from an inverter assuming ideal switching behaviour of the semiconductor devices. Figure 3.13 shows a typical current transient following switching. Also shown is an experimental transient captured at the same current level from the 4 kW ASEA machine and modelled cable being driven by a commercial inverter. Some minor adjustments were made to the model parameters through trial and error to improve the correlation between experimental and simulated impedance responses. Following these adjustments the simulated transient was found to be a reasonable approximation to the experimental results. There is a small difference in the decay rate with the experimental model having a higher decay rate. There is also a small discrepancy at approximately $1.5\mu\text{s}$ where the experimental result appears to be influenced by a lower frequency component. This is not seen in the simulated result.

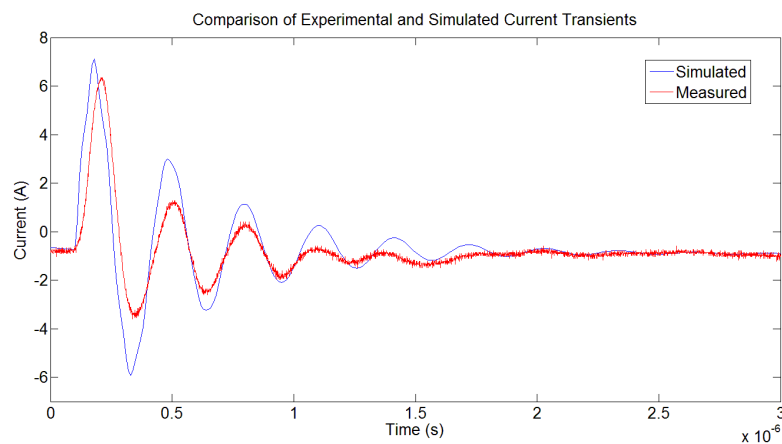


Figure 3.13 Simulated and experimental current transients are compared for their high frequency content

Fourier transforms were performed on the simulated and experimental current transient results shown in Figure 3.13 to examine the frequency

content of the transients. Figures 3.14 (a) and (b) contain the results of the FFT's. The frequency content was very similar for both cases with large DC components and a large dominant high frequency component at approximately 3.3MHz. One small difference lies at around 17 MHz where the experimental transient has a small component while the simulated result does not. This could be because the simulation model was only characterised up to 15 MHz as above these frequencies there is minimal current penetration into the motor windings [55]. The larger DC/low frequency component should not give cause for concern as the low frequency behaviour is not accurately modelled in this case. As described previously; with the present configuration low frequency behaviour is modelled separately.

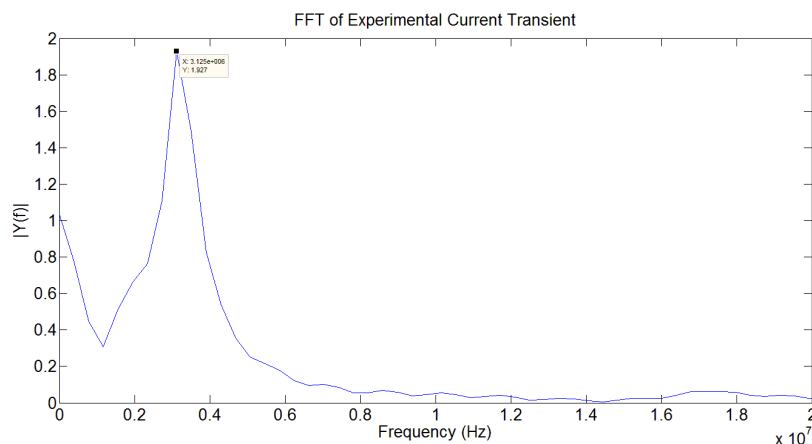


Figure 3.14 (a) Experimental

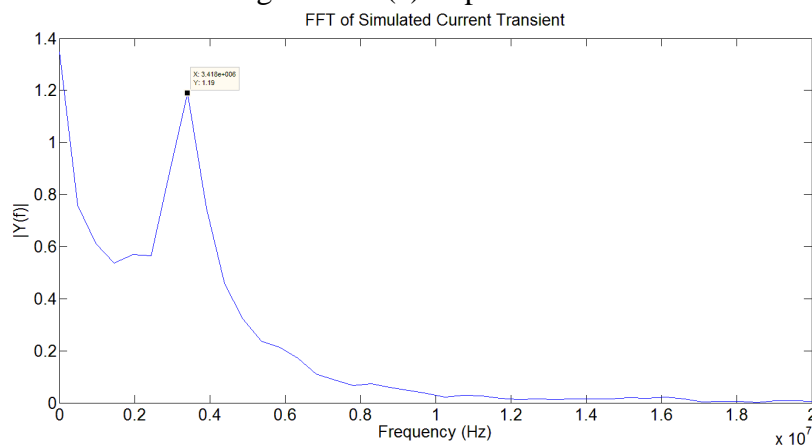


Figure 3.14 (b) Simulated

Figure 3.14 FFTs of the transients shown in Figure 3.13. (a) is FFT of the experimental transient while (b) is FFT of the simulated transient

3.6 Effects of Supply Cable Length

While collecting experimental results it was observed that the length of supply cable used had a large effect on the resulting frequency content of current transient waveform following inverter switching. The longer the supply cable, the lower the dominant frequency present in the current transient. The transients shown in Figure 3.15 illustrate this. It should be noted that these results were not recorded from the motor and cabling modelled previously in the high frequency range. The ‘short’ cable length was 24m while the long cable length was 125m.

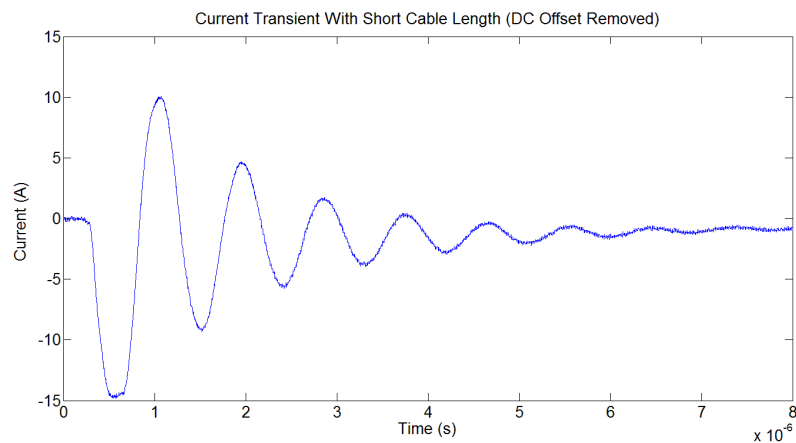


Figure 3.15 (a) Time domain, short cable length

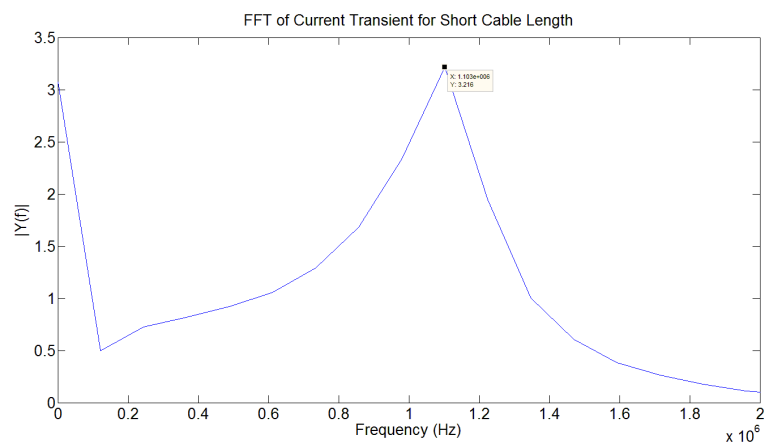


Figure 3.15 (b) Frequency domain, short cable length

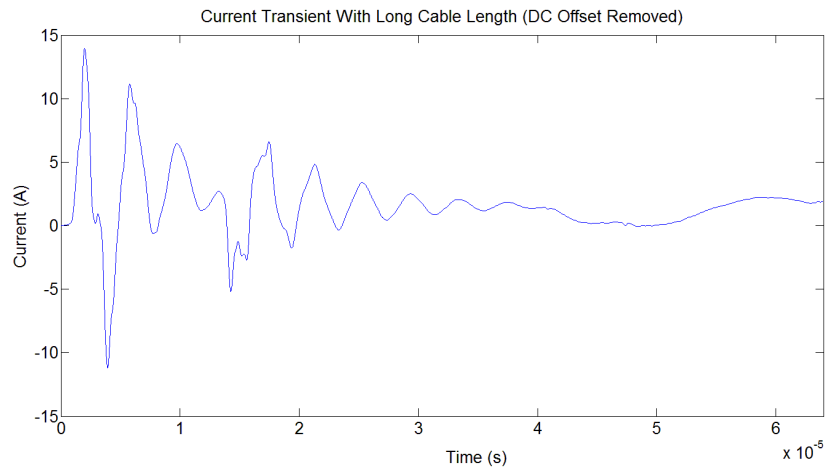


Figure 3.15 (c) Time domain, long cable length

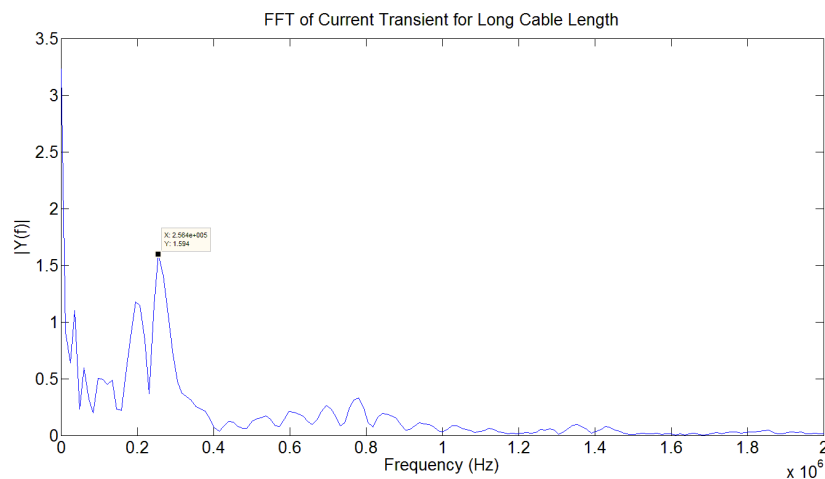


Figure 3.15 (d) Frequency domain, long cable length

Figure 3.15 shows the difference in current transients between short (a) (24m in this case) and long (b) (125m) cable lengths. The transient for the short cable length is dominated by a 1 MHz component, see (c), while the transient corresponding to the long cable length is dominated by a component at approximately 250 kHz, see (d). It is clear that the transient for the short cable length, (a), decays much quicker than the case for a long cable length, (c)

It was impractical and too costly to begin a full experimental investigation into this effect however its behaviour must be understood in order to ensure that any solution arrived at in the course of this research was not limited to applications utilising only short supply cables. From the perspective of a sensorless control application using the established approach of allowing oscillations to decay before attempting to measure the derivative, the presence of a dominant lower frequency component in the current transient means that the oscillations will take longer to decay leading to an increase in the minimum pulse width. The relationship between cable length and dominant frequency is reported in literature [54, 63, 73] and the model used in this research was proven to be able to simulate the effects of increasing cable length on the dominant frequency. This work was able to re-produce the behaviour documented in [63] and the results are shown in Figure 3.16.

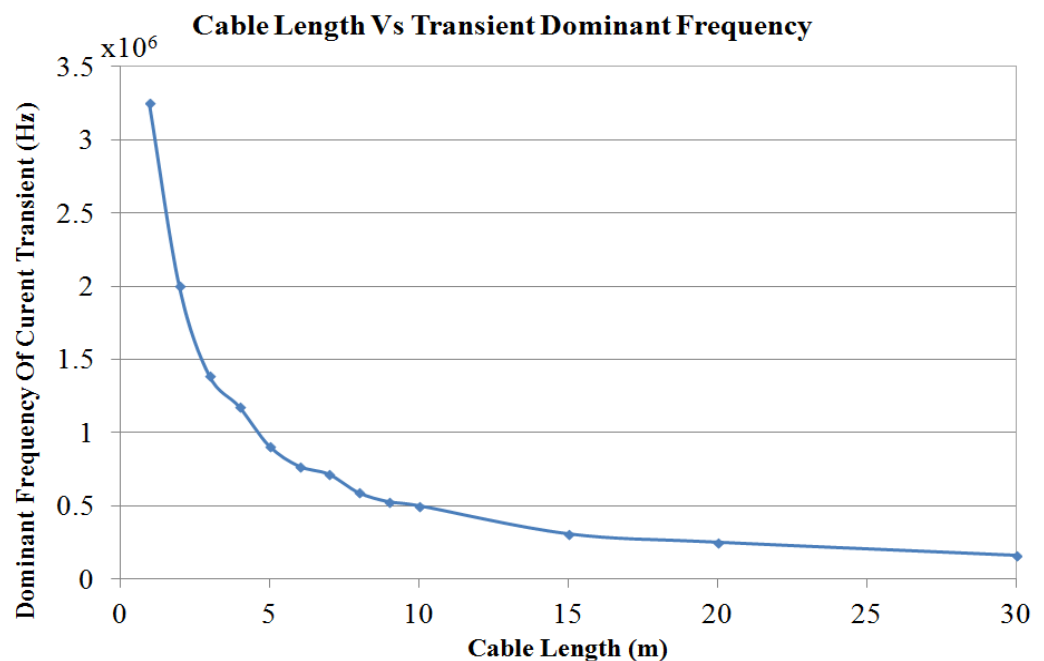


Figure 3.16 shows the effect on the dominant frequency component of increasing the supply cable length (results obtained through simulation and show a similar behaviour to that observed in [63])

Figure 3.16 illustrates the inversely proportional relationship between cable length and dominant frequency allowing a prediction to be made on the dominant frequency component for a given cable length (where the machine being used and the cable (per unit metre) have been characterised in the high frequency range). In terms of the work that is described in Chapters 4 and 5, a decrease in the dominant high frequency component has both positive and negative side effects. The techniques proposed in Chapters 4 and 5 require that the high frequency transient is sampled to a reasonable resolution, which for higher dominant frequency components requires a very high sample rate ADC adding cost and complexity to the hardware design and implementation. A lower dominant frequency relaxes the ADC sample rate requirements to the point where for long cable runs (e.g. > 20m) an ADC sample rate of a few MHz (which is a reasonably common conversion rate in industry) is sufficient.

The major negative factor though is that the lower frequency transients take longer to decay and therefore require an even longer minimum pulse width threshold to be applied in order to allow the transients to sufficiently decay. Later in Chapters 4 and 5, methods which only require a fraction of the high frequency transient are introduced. But even these methods would require a significant minimum pulse width to be imposed when capturing the initial transient of a low frequency oscillation. The enlarged minimum pulse width increases current distortion, torque ripple and audible noise. While the methods proposed later offer an improvement over established methods they still result in large distortion compared to the ideal case where pulse widths remain unmodified.

3.7 High Frequency Behaviour Due to the Drive

Many of the studies documented in literature do not include detailed models of the parasitic impedances of the switching devices themselves in simulation models. The IGBTs used in many of today's commonly found inverters have internal interconnections which will have some associated inductance and resistance. Parasitic capacitances exist between the collector and gate and also between the gate and the emitter. Also when the devices are mounted on a grounded heat sink a capacitance between the device terminals and ground is created forming a path through which common mode currents can flow. Finally the anti-parallel diode also has an equivalent high frequency model. A small number of authors have investigated these parasitic components [64, 74]. The diagram in Figure 3.17 shows the locations of some of the main parasitic elements including the gate capacitances, diode parasitic components, interconnection inductances and capacitance between the device and the grounded heat-sink on which the device is mounted [74].

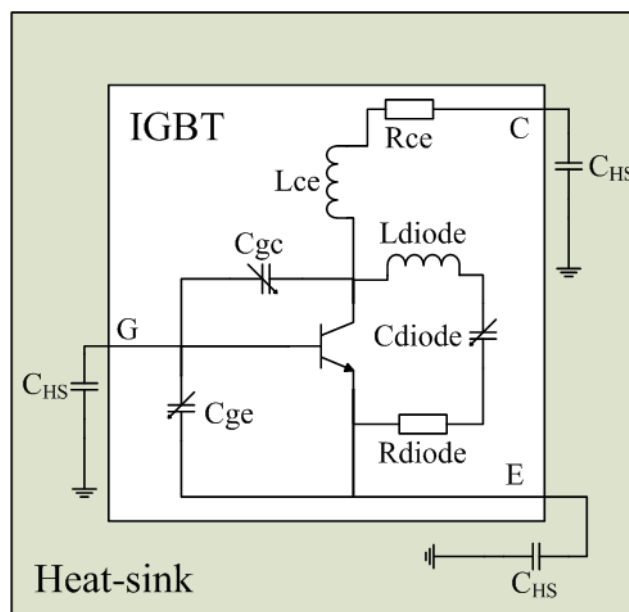


Figure 3.17 Parasitic components present in an IGBT module [74]

In this research the IGBT model used was kept as simple as possible for two reasons. The first is that the parasitic components of the internal module are not easy to characterise and find model parameters for. The second is that the results obtained from the simulations were found to be satisfactory compared to the experimental waveforms. One particularly important aspect relating to the IGBT behaviour is the use of a realistic dv/dt during switching. This could be easily set within the simulation environment by means of a rate limiter [55]. However, the dv/dt that should be applied does not have the same value under all conditions as will be discussed in the next section.

3.8 Influences of Inverter Non-linearities

The high frequency models produced for the ASEA 4kW induction machine and 1m cable were able to reproduce the dominant high frequency oscillatory effects seen in the time domain of the experimental current waveform taken from the machine. However under certain operating conditions there were some differences observed between the response of the model and the real response measured from the machine.

As the current transients are of interest, the key difference in the context of the implementation of the Fundamental PWM sensorless technique was that at low current magnitudes some of the PWM voltage waveforms showed a much slower switching transition. This is only observed at low current magnitudes when the device commutation is from transistor to diode in an inverter leg and results in the transition time for the output voltage of the inverter leg extending from a few hundred nanoseconds up to the dead-time value (usually one or two μs). The effect is caused by the parasitic capacitance present in the switching device, motor and cabling [75-82]. The illustrations in Table 3.3 explain the steps involved in switching a phase leg and how the device parasitic capacitance influences the process.

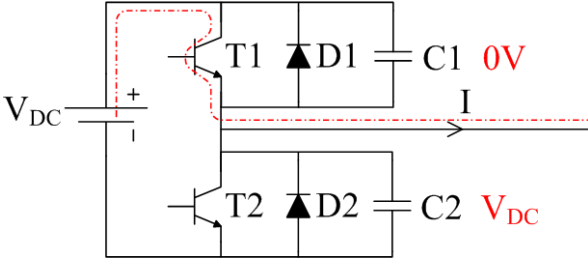
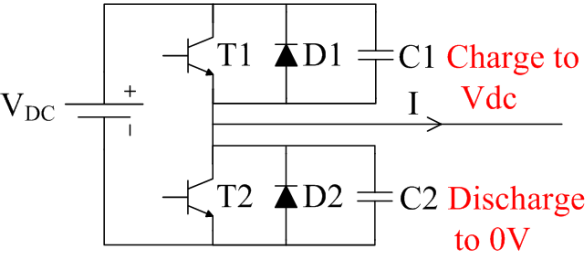
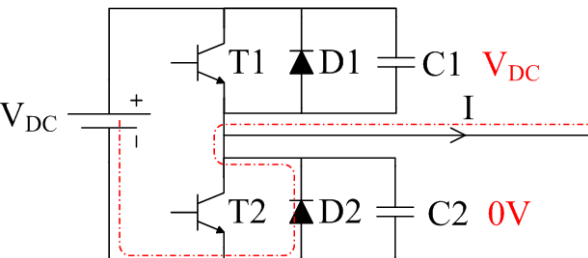
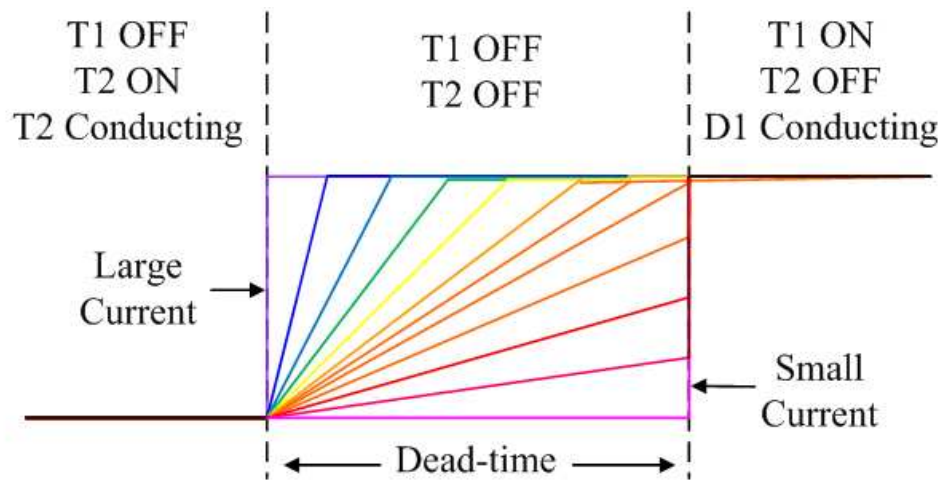
<p style="text-align: center;"><u>State 1 – T1 conducting</u></p> 	<p>The output is $+V_{DC}$. C1 is shorted while C2 is fully charged to $+V_{DC}$</p>
<p style="text-align: center;"><u>State 2 - T1 and T2 off for dead time period</u></p> 	<p>At the beginning of the dead time T1 and T2 are switched off for the period of the dead time. At this point D2 should begin conducting to maintain a current path, but D2 is reverse biased by the voltages of C1 and C2. Before D2 can conduct it must be forward biased which requires C2 to be discharged and C1 charged to V_{DC}. The time taken for this to occur is a function of the motor current</p>
<p style="text-align: center;"><u>State 3 – D2 conducting</u></p> 	<p>D2 is forward biased and begins conducting; the output is now $-V_{DC}$. C2 is now shorted and C1 is fully charged to V_{DC}</p>

Table 3.3 the stages involved in switching an inverter leg and how the parasitic capacitances of the devices effect switching

Commutations from diode to transistor are not affected by this issue since when a dead time period is entered and the active devices are switched off, if there is a non zero current the diodes continue to conduct providing a current path until the end of the dead time period at which point the necessary active device is switched on providing a current path and instant charging/discharging of the capacitances. However when commutation is from transistor to diode and the current magnitude is low the effects illustrated in Table 3.3 are observed.

At high current levels the capacitances are charged/discharged at a high rate and the effect becomes negligible, but at low current levels the rate of charging or discharging of the capacitances $C1$ and $C2$ is reduced significantly (according to $I = C \frac{dv}{dt}$). Hence as the current magnitude approaches 0A the dv/dt of the phase voltage seen at the inverter leg decreases. There reaches a point where the dv/dt of the phase voltage decreases such that the transition time for the phase voltage to reach its intended value extends beyond the period of the dead time. At the end of the dead time period the corresponding active device is switched on which provides rapid charging/discharging of the capacitances and the phase voltage is brought sharply to the correct voltage.

At extremely low current magnitudes the current is insufficient to cause any substantial charging or discharging of the capacitances. In this case hardly any change in the phase voltage is seen until the corresponding active device is switched on (causing the phase voltage to change) [76, 78, 80, 81]. This is illustrated in Figure 3.18 where illustrative switching times are plotted according to the phase current magnitude.



Key:

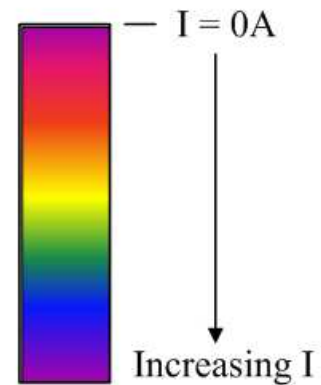
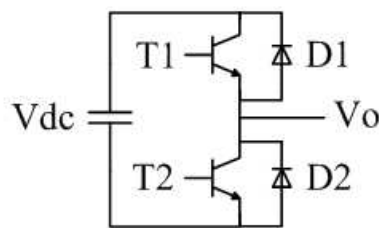


Figure 3.18 Effect of current level on device switching behaviour

The variation in the dv/dt of the switching edge is important for the implementation of the Fundamental PWM sensorless technique for two reasons. Firstly it has the effect of removing high frequency content from the voltage switching edge (because of the reduction in the dv/dt) which is being used as an excitation pulse for position detection and secondly the dv/dt directly influences the shape of the current oscillations in response to switching. Hence if the dv/dt of the voltage waveform varies, the shape of the current waveform will also vary.

Any variation in the shape of the current transient due to a variation in the applied dv/dt must be taken into account by any signal processing approach and rules out a standard “one fits all” approach. There are three

possible transient phase current waveforms that can be observed in an inverter leg when switching causes a transistor to diode commutation. These are;

- 1) High current magnitudes: the standard HF oscillatory response is observed.
- 2) Low phase current magnitude: the parasitic capacitances are charged or discharged within the dead time resulting in a slow voltage transition. The transient current response is distorted and has very low high frequency oscillatory content.
- 3) Very low phase current magnitudes: the voltage transition time exceeds the dead-time. In this case there is current distortion introduced during the dead time period (while charging/discharging occurs) and also some HF content introduced at the end of the dead-time due to the dv/dt of the corresponding switching device.

The problem is made worse by the distributed capacitances in the cabling and motor which also require charging or discharging when the inverter switching state is changed (Once again according to $I = C \frac{dv}{dt}$, the dv/dt is decreased for a given current when the capacitance is increased) [54, 75, 78]. These additional capacitances are illustrated in Figure 3.19.

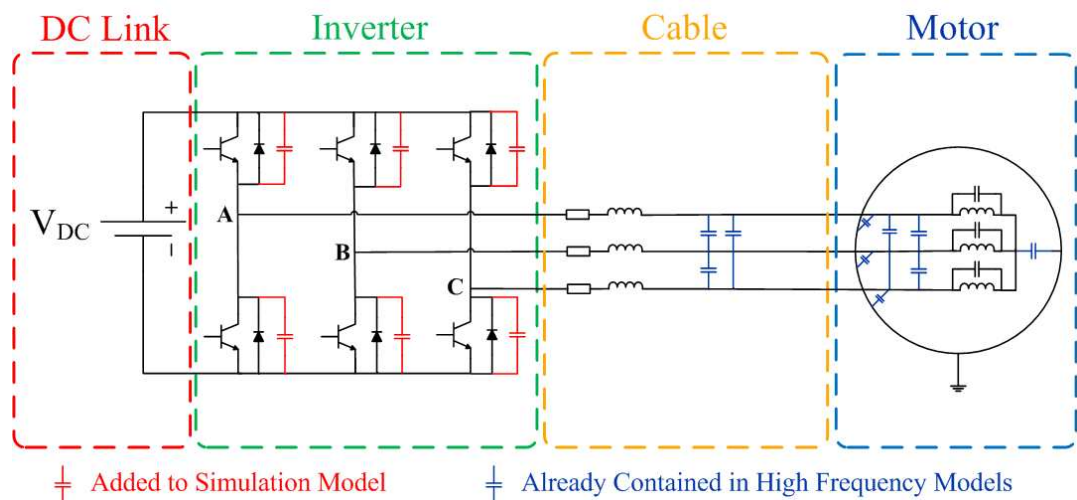


Figure 3.19 Additional Capacitances to be considered in the drive [54, 75, 78]

In order to incorporate these effects into the model, additional capacitances were added in parallel with the active switching devices which previously had been IGBTs with ideal switching performance. The values chosen for the capacitances were arbitrary, the value used in the simulation results presented below was 1nF with a 2 μ s dead-time. The results shown in Figure 3.20 (a) and (b) clearly show the distortion added at low currents when the current polarity is in the direction to cause transistor to diode commutation. At higher currents the dv/dt closely matched the ideal switching case as expected.

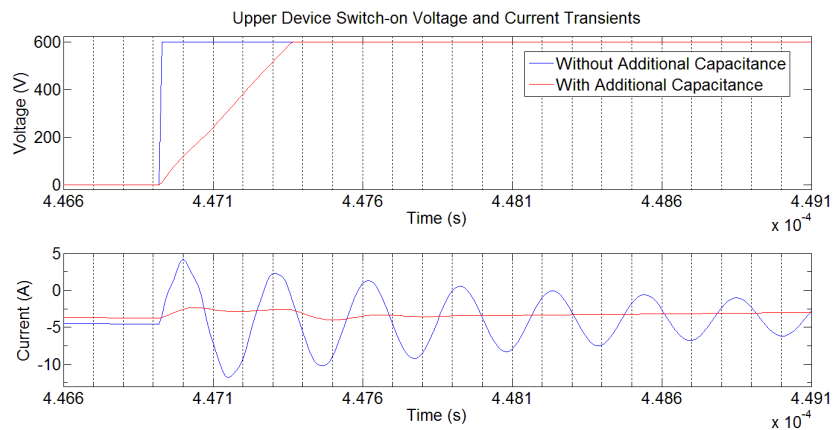


Figure 3.20 (a)

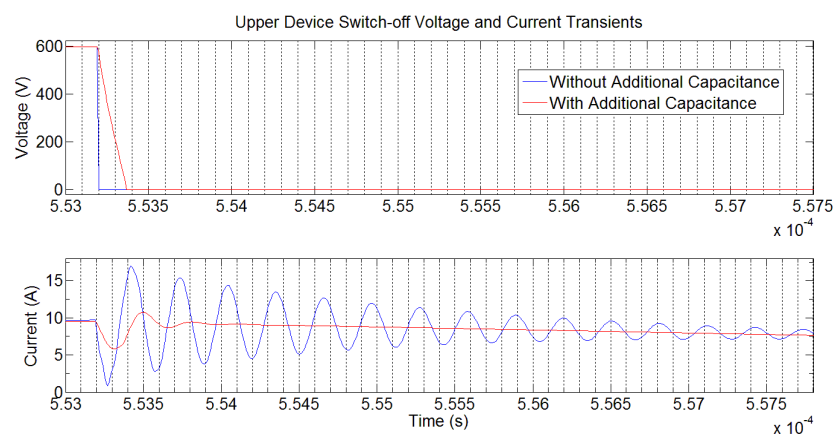


Figure 3.20 (b)

Figure 3.20 the effects on voltage and current transients of additional parasitic capacitances added in parallel with active switching devices to capture non-linear switching behaviour

The simulation results reflect the behaviour seen in the experimental results with switching events involving low phase currents experiencing a reduced dv/dt and therefore an increased switching time. The switching time is proportional to the current magnitude, the smaller the current magnitude, the longer the switching time and the smaller the dv/dt . This is illustrated to some extent in Figure 3.20 where the current magnitude in (a) is smaller and results in a larger switching time compared to (b). The ensuing current transients are also affected in a similar way to those witnessed experimentally, with the smaller dv/dt causing a larger distortion of the current (during switching) and the smaller dv/dt greatly reducing ringing in the current waveform. Only transistor to diode commutation is affected. For very small currents the voltage does not completely reach its target during the dead time and the switching on of the transistor causes a large dv/dt at the end of the dead-time period as seen in the experimental results.

3.9 Conclusions

A model has been identified and implemented that is able to accurately reproduce the high frequency common mode and differential mode responses of an AC motor and cabling. It has also been demonstrated that the models are able to accurately predict the time domain behaviour. This has resulted in an understanding of the main parasitic impedances that are responsible for the high frequency oscillations seen in the current response of the machine. The method for finding model parameters has been described and is relatively simple but requires specialist equipment in the form of an impedance analyser or RLC meter.

At low currents when the commutation in an inverter leg is from transistor to diode the parasitic capacitance of the switching devices becomes significant. This capacitance results in a significant variation in the dv/dt seen

at the output of the inverter. This variation (in dv/dt) is a function of the phase current amplitude and has a large effect on the transient currents following switching, with distortion being introduced.

Despite the understanding gained of the high frequency sources and their behaviour, a solution to prevent the high frequency oscillations has not been realised as the sources that give rise to the high frequency behaviour are intrinsic in the construction of the drive and so cannot be removed. With this in mind the next chapter will explore what can be achieved in terms of reducing the high frequency oscillations and also by attempting to extract the current derivative from current transients affected by high frequency oscillations.

Chapter 4

Current Derivative Estimation in the Presence of HF Oscillations

4.1 Introduction

The current derivative values required for the implementation of sensorless control using the Fundamental PWM technique have traditionally been measured using one of two approaches; direct measurement through a dedicated sensor or indirect measurement by measuring the change in phase current over a set time window (referred to in this work as the two current sample method). When inspecting a transient phase current response following an output phase of the inverter switching, it is evident the gradient of interest is present but obscured (and sometimes distorted) by HF (high frequency) oscillations also present in the response. Hence, the first logical step would be to try and completely remove the high frequency oscillations from the current response leaving only the underlying gradient of interest.

It was established in Chapter 3 that it is the parasitic impedances responding to the high frequency content of a large dv/dt applied to the network during inverter switching that is responsible for the ringing seen in the current response of the machine. The parasitic network cannot be eradicated as it arises from the close proximity of numerous conductors separated by various dielectric materials in the drive. This is a consequence of the necessity to construct the drive in a certain way in order for it to function.

The parasitic impedances cannot be removed, nor can the dv/dt applied to the machine easily be reduced (unless a multilevel converter is used. This reduces the change in voltage applied therefore reducing the dv/dt but adds considerable cost and complexity) since this voltage is required to operate the machine.

Numerous researchers have made attempts to reduce or eliminate these oscillations for a variety of applications. The next section examines some of these methods and explains why they are not suitable in this application.

4.2 Removing or Reducing the High Frequency Content in the Transient Current Response

4.2.1 Use of EMI Filters

Many different EMI filters have been proposed for the removal of high frequency content in the machine response [60, 83-85]. The main basis of the EMI filter is to provide a matched impedance path for the high frequency content of the waveform allowing it to be shunted to ground and therefore removed from the response. Without the EMI filter the point where the motor is connected is seen as an open circuit at frequencies in the MHz range [55] and so the high frequency signals are reflected back down the transmission line. An issue that is difficult to address in general is matching the impedance of the filter to the frequency content that must be removed. This is not difficult on an individual drive basis but when the cable length is modified or the motor is changed the parasitic impedance network is also modified and this changes the frequency of the oscillations the EMI filter must remove [22]. Another

problem with this solution though is that if the PWM edge can be imagined as an ideal step then in the frequency domain it is described by a Fourier series of infinite frequency components. Removing the higher frequency components through filtering makes the voltage waveform appear more sinusoidal and is equivalent to extending the switching device turn on time (reducing dv/dt by increasing dt).

Hence this solution cannot be used in this work as the inclusion of an EMI filter will remove the high frequency content of the voltage pulse applied to the machine through PWM. This high frequency content gives rise to the large current derivatives seen in the response of the machine, needed to track saliencies. EMI filters are also costly since inductors placed in series must be capable of carrying large currents without saturating [55]. The use of passive energy storage components also means that EMI filters are physically large. They will also inevitably increase power losses in the drive during switching.

4.2.2 Variation of the IGBT Gate Impedance

Another method which can reduce the current oscillations involves varying the IGBT gate resistance [23, 43, 44]. Increasing the gate resistance reduces the current supplied to the gate of the IGBT and hence increases the time taken to charge the gate capacitances. This leads to an increase in the time taken to turn on the IGBT thus reducing the dv/dt . This has the disadvantage of increasing switching losses and adds distortion to the current waveform. However the oscillations are reduced in amplitude and duration and this method does provide a level of control for the designer since it is possible to only modify the gate resistance when a derivative measurement is required (in all other instances the transient is unaffected). This is achieved by adding a switch and resistance in parallel with the original gate resistor. The modified gate resistance value can easily be chosen to increase the switching time by the desired amount.

This approach while successfully reducing the high frequency content of the current waveform also removes high frequency components from the voltage waveform and therefore reduces the di/dt . Also while the approach provides a controllable solution that can be applied only when necessary and has been demonstrated successfully in conjunction with the Fundamental PWM technique [23], it also requires additional hardware and control (to switch in the additional parallel gate resistance thereby reducing the overall effective gate resistance).

A variation of this technique has been presented previously. In [86] an additional capacitance was added between the gate and collector of an IGBT. This small capacitance increased the Miller capacitance therefore increasing the turn on time. The technique was used to reduce overvoltage at the motor terminals.

4.2.3 Injection of Low Magnitude Test Pulses

The concept of using low magnitude pulses specifically added to allow the transient current response to be measured and thus track saliency was investigated in [22, 87-89]. During normal SVPWM operation additional test pulses were injected during the PWM null vector and the transient current response to these test pulses was used for estimating the rotor position. The injected pulses could be compensated immediately after their original application to minimise current distortion. This approach is similar to the INFORM method described in Chapter 2. However in this case the additional test pulses had much lower amplitude than the pulses that drive the motor. The implementation of this method involved adding H-bridges in series with the output phases of a standard two level inverter that could be used to generate the test pulses. The DC links supplying the H-bridges had a small voltage amplitude (150V) [22]. The DC link voltage has a large influence on the transient current response according to Eqn 2.5. Reducing the amplitude of the

DC link voltage reduces the amplitude of the transient current response of the motor. As a result the current ripple is reduced when applying test and compensation vectors. This allows a significant reduction in the THD to be achieved. Figure 4.1 illustrates this concept [22].

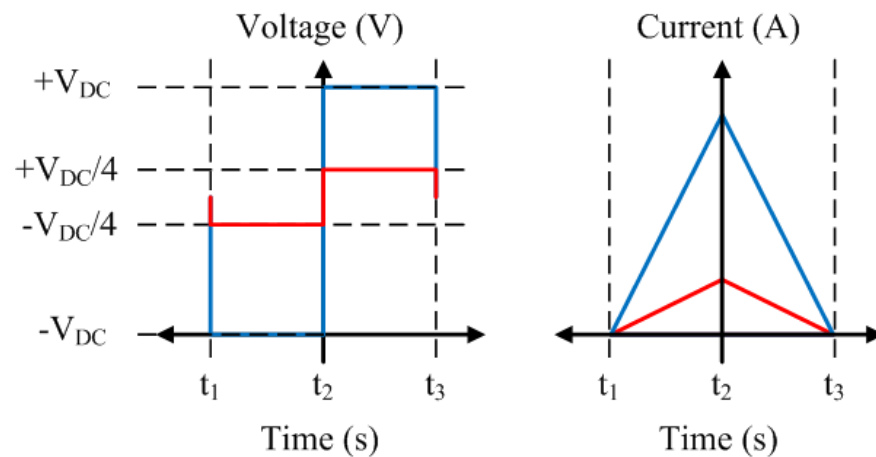


Figure 4.1 An illustration of how reduced amplitude test pulses result in smaller transient current responses and hence a smaller current ripple is introduced [22]

The reduced amplitude of the test vectors resulted in a smaller dv/dt being applied to the machine (when applying test pulses) and therefore the amplitude of the high frequency oscillations seen in the current response was reduced. It was claimed that this allowed current derivative sampling to occur sooner and hence a reduction in the minimum pulse width could be achieved. The amplitude of the test pulses would have little affect the frequency, phase and decay rate of the high frequency oscillations and so the same amount of time would be required for the oscillations to decay completely to zero. However because of the reduced amplitude of the oscillations it may be valid to say that they have a small enough amplitude to have an insignificant effect on the current derivative at an earlier stage therefore current derivative sampling can occur at an earlier stage.

Because the minimum pulse width threshold was applied specifically to the test vectors, a minimum pulse width for the normal PWM vectors was not required and the normal PWM edges themselves were unchanged.

This idea was developed further in [22, 90] where the same converter topology was used to produce a full asymmetric 7-level multi-level converter. The reduction in voltage magnitude between the discrete voltage levels at the output of the converter resulted in smaller transient current responses and the amplitude of the high frequency oscillations seen in the current response was reduced significantly thus allowing a reduction in the THD compared to equivalent two level designs.

These solutions though add a significant amount of hardware, control complexity, cost and create additional losses. The method also still made use of dedicated current derivative sensors.

4.3 Use of Mathematical Techniques

4.3.1 Introduction

It was established in Chapter 3 that it is not possible to remove the parasitic impedances that cause the high frequency oscillations in the phase current response. In 4.2 it was seen that it is undesirable to remove the high frequency content of the voltage waveforms (which would in turn reduce the amplitude and duration of the high frequency oscillations in the current response) because of the effect that would have on the ability to track saliency as well as the need for additional hardware. Following these observations a non intrusive solution which utilises signal processing appears favourable. At first glance this seems a relatively simple problem. The underlying gradient that is of interest can clearly be seen when the transient is viewed in full and the response appears to be dominated by a high frequency exponentially

decaying sinusoidal component. Due to the high frequency of the oscillations and the small time window that they would need to be sampled over, a very high speed data acquisition system would be required. Once the response has been captured signal processing could subsequently be applied to find the derivative. However, the response also includes a number of low frequency components which decay at different rates. Also there is a variation in the shape of the response depending on the inverter operating conditions.

4.3.2 Work by Other Researchers in the Field

There is a limited amount of literature documenting work similar to that proposed in this thesis where the current derivative is estimated through sampling at a high rate (oversampling) and then by subsequently applying signal processing techniques to extract the required information. In [1, 91, 92] the current derivative was established by oversampling the output from a Rogowski coil, following a change in the inverter switching state. Signal processing was then applied to the captured response to find the derivative. In order to reduce the minimum pulse width the current was sampled at 40MSPS to capture the transient response from a Rogowski coil and the derivative was then estimated using three different approaches applied to the captured current derivative data – mean value over a set time window, mean slope and also using a delta sigma modulator and sinc(x) filter. Use of current sensors was also explored in this work (from which the derivative could be found by measuring the change in current over a set time) but these sensors were found to require a large time window in order to allow a measurable change in the underlying gradient to occur.

In [93] the current derivative was estimated by oversampling the current and subsequently applying a recursive least squares fitting algorithm to the result in order to obtain the derivative. Minimum pulse widths of 1 μ s were reportedly achieved. However this approach was never implemented in a real-

time situation. The processing time for such a technique would be high and this is exacerbated in a sensorless application by the need to estimate several current derivatives within a few PWM periods in order to obtain one position estimate. The current waveforms used in the study were captured using a high bandwidth (10 MHz) Lecroy CP150 current probe which could not be used in a commercial drive due to the cost of such sensors. Hence low bandwidth sensors would have to be used instead in a commercial drive. The limited bandwidth of such sensors introduces further complexities into the response.

In [94, 95] standard current sensors were used to measure the current derivative for the implementation of an injection based saliency tracking sensorless technique. Oversampling of the current response was performed and then linear regression was applied to fit a straight line to the “cloud” of measured points to estimate the derivative. The aim of the work was to reduce the effects of random and quantisation noise on the measured current derivative. The method allowed an increase in the accuracy and robustness of the derivative estimation to be achieved. In doing so the HF signal injection amplitude could be reduced by a factor of 7 - 10 (which also reduces the amplitude of the salient component in the current response) but the saliency component could still be accurately identified. Reducing the high frequency injection amplitude significantly reduced the torque ripple and audible noise observed in the machine response. This method however neglected the effects of the high frequency oscillations on the response and instead delayed the sampling of the current waveform until after these oscillations had decayed, hence these were not considered. When the PWM pulse widths reduced beyond the point where a delay and then oversampling could be applied, the method relied instead on a compromise of using the average active vector derivative estimated from the start and endpoints of the current in adjacent null vectors. Whilst this does not imply a minimum pulse width it is less than ideal and it was not clear if, or how, decaying high frequency transients affected the

results. Also no attention was paid to the non-linear switching behaviour of the inverter and the resulting effects this has on the current response.

Whilst the research described above demonstrates the potential for using oversampling and signal processing to establish the derivative accurately and in a reduced time there still remains a number of limitations and factors which require further attention. These include:

- None of the work discussed above considers the non-linear switching behaviour of the inverter and the effect this has on the derivative measurement/estimation.
- Effects of decaying transients on subsequent derivative responses are not considered (i.e. if the inverter switching state is changed before the high frequency transients (due to a previous switching event) have decayed then the high frequency transients due to the previous switching state and the next switching state will be added together).
- In [1, 91, 92] standard current sensors were found to require a large time window in order to allow a detectable change in the underlying gradient to occur meaning that the high frequency oscillations are not the only limiting factor in the use of standard current sensors.
- In [94, 95] the high frequency transient behaviour was ignored and for short vectors the average derivative was estimated from adjacent vectors.
- The limited sensor bandwidth is mentioned in [1, 91, 92] but no suggestion of how this might be overcome is provided.
- For the solutions presented in [1, 91, 92] dedicated Rogowski coils are required.
- In [93] the method proposed was only demonstrated offline and would be difficult to implement in a real-time sensorless application due to timing constraints.

Given the limitations of the research already completed in this field a mathematical curve fitting approach to approximate the high frequency current response to a mathematical description of the response based on prior knowledge of the frequency content of the response was proposed. Attempts to implement this proposed method however were unsuccessful. The attempts made and their reasons for failure will now be described.

4.4 Estimation of the Current Derivative Using Curve Fitting Methods

4.4.1 Introduction

This proposed work is differentiated from the work of previous researchers by the method proposed for obtaining the current derivative and the way in which the current measurements are obtained. The initial proposal in this research was to estimate the current gradient by fitting a mathematical approximation to the experimental waveform using a least squares curve fitting approach. From the fitted waveform the current derivative could be extracted directly. The use of a standard closed loop current sensor is preferable from an industrial perspective owing to its low cost and also its widespread acceptance and use already within commercial drives. However these sensors have a limited bandwidth in which the response can be expected to be linear – this is usually up to a few hundred kHz. As the current data of interest contains frequencies in the order of MHz the measured response will be subject to attenuation and phase shifts. This problem complicates matters; however the underlying gradient information that is of interest will only experience limited effects due to the sensor bandwidth. As long as the amplitude and phase response of the sensor are repeatable in the high

frequency range, its effects on the expected response can be accounted for. The current waveform could be filtered to remove the attenuated and phase shifted components but this would add delay to the low frequency response and would not sufficiently remove all of the higher frequency components.

In order to test the viability of the proposed current gradient estimation technique the method was implemented in Matlab. Scripts were written to evaluate the gradients offline using motor current waveform data measured using a Lecroy CP150 high bandwidth (10 MHz) current probe and oscilloscope.

4.4.2 Curve Fitting to a First Order Linear Approximation

Initial attempts were made to fit experimental current transients to a first order ($y=mx+c$) equation using a linear least squares fit. However over a short time window containing only transient behaviour this produced poor results. The two main reasons for this were complex behaviour of the current immediately after switching where the measured wave does not match the actual gradient. This is because the limited bandwidth of the sensing equipment results in some of the harmonics which form the straight line of interest being attenuated causing non-ideal behaviour around the peaks and troughs. Figure 4.2 illustrates this by showing a triangle wave with a 1MHz exponentially decaying sinusoidal frequency component added at the peaks and troughs. An ideal and filtered version of this wave is also shown. Note the delay and shape of the filtered wave after each peak and trough. A further difficulty lies in the identification of the DC offset. This must be accounted for when performing a fit by identifying the offset and either including or removing the result from the fitting process. Automatically identifying the exact start point of the transient behaviour and therefore the DC offset proved very difficult but also very important as the selection of the DC offset was

found to have a large influence on the accuracy of the result. This was a problem that affected all of the mathematical curve fitting methods tested.

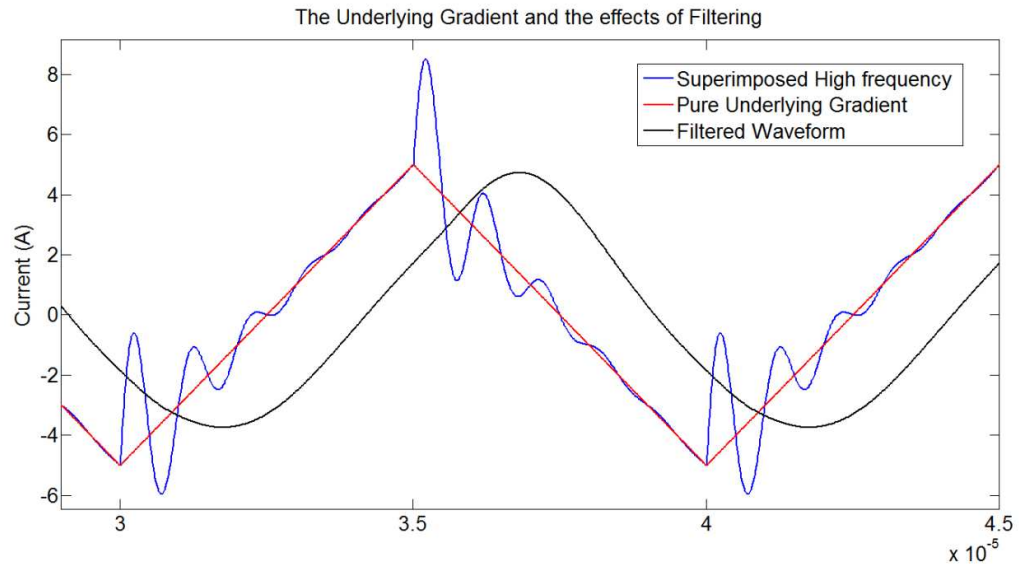


Figure 4.2 An illustration of the effects of filtering the sampled current waveform. The ideal (red) waveform is shown, as is a realistic representation (blue) where a 1 MHz exponentially decaying sin wave is superimposed. This wave is filtered and shown (black), the filter cut off frequency is 250 kHz. The frequency of the ideal triangle wave is 100 kHz. Notice the delay due to the phase shift and the rounding of the wave around the peaks due to the removal of the triplen harmonics which form the triangle wave

The lower frequency content present in the experimentally measured current waveform over a short window caused the least squares fit to deviate away from the actual gradient as it attempted to minimise the error between the fitted and actual waveforms. This is because these low frequency terms are not accounted for in the mathematical fit and also because of the decaying nature of the wave, its appearance about the underlying gradient is asymmetrical. Figure 4.3 illustrates this by showing an experimentally measured transient current waveform along with the underlying gradient. Also shown are the results of passing the original transient waveform through a low

pass filter. In order to highlight the non-symmetrical contribution (with respect to the underlying gradient) made by the lower frequency components.

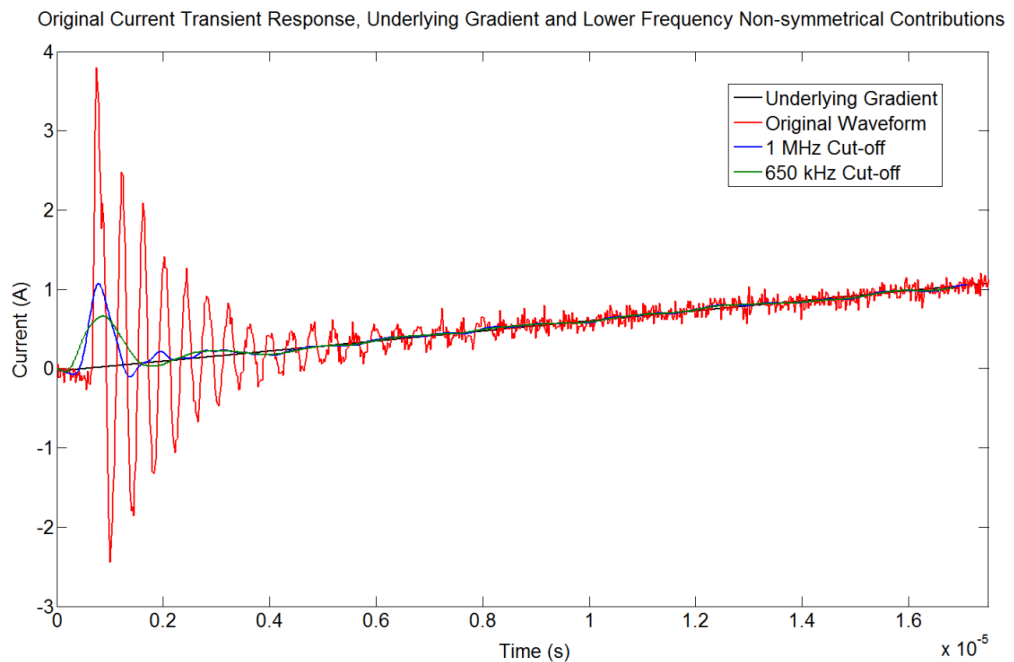


Figure 4.3 Experimentally measured transient current waveform (red) and corresponding underlying gradient (black). Also included are low pass filtered versions of the transient current waveform (blue and green) to show the non-symmetrical contributions made by the lower frequency components

4.4.3 Curve Fitting to a Single Exponentially Decaying Sinusoid Approximation

Given the unacceptable performance of the straight line fitting approach, the performance of a non-linear least squares fit according to Eqn 4.1 was tested.

$$f(x) = a \cdot \sin(2\pi ft + \theta) \cdot e^{-ft} + cx + d \quad (\text{Eqn 4.1})$$

In order to simplify the synchronisation of the transient and fitted waveform responses the first peak of the measured transient response was taken as the start point and the sinusoidal component of the fitted waveform was modified to include a 90° phase shift (θ in Eqn 4.1). Figure 4.4 shows a typical result obtained when using this method.

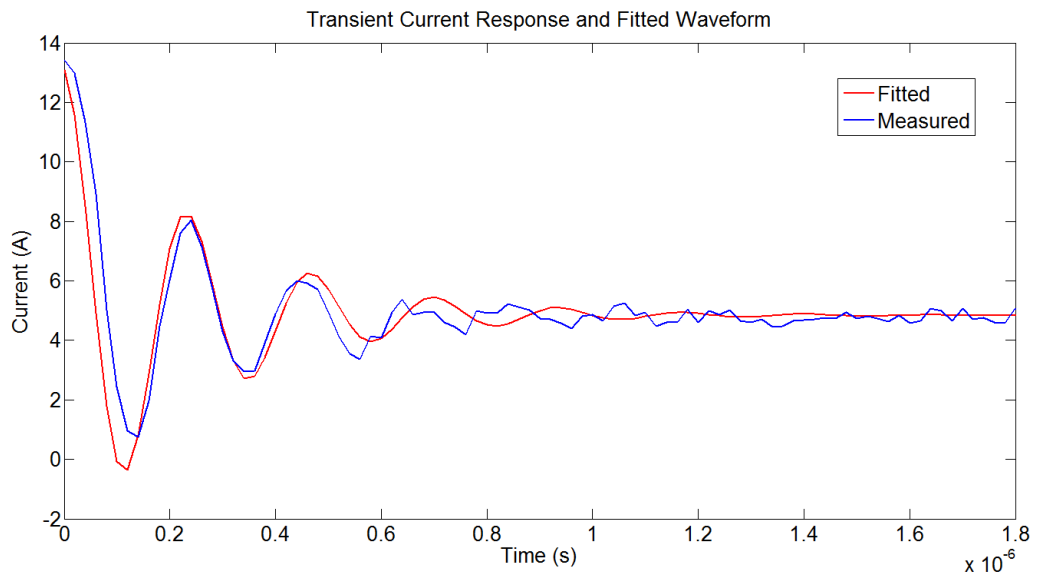


Figure 4.4 Experimental waveform and approximation based on (Eqn 4.1)

The result in Figure 4.4 shows what appears to be a reasonable approximation of the measured waveform. However the estimate obtained for the gradient was inaccurate. Closer inspection of the result in Figure 4.4 reveals the reasons for the inaccurate result. Firstly the large overshoot on the first negative peak is due to a mathematical error caused by the fact that the amplitude profile of the current response cannot be described by a single exponential component, other unaccounted for frequency components contribute significantly to this initial overshoot (see Figure 4.3). It is thought that to remove this error distortion introduced by the sensing apparatus must be accounted for and also other frequency components (with high decay rates meaning these components only appear in the initial response) must be included. Also the absence of lower frequency contributions results in errors in

the fitted waveform which can be seen clearly between approximately $0.6\mu\text{s}$ and $1\mu\text{s}$ in Figure 4.4 where the response appears to become in anti-phase with the fitted waveform. There are also further amplitude errors at around $0.6\mu\text{s}$. When the response is supplied to a least squares fitting algorithm which has knowledge of the dominant frequency component the gradient is modified to match the response and reduce the errors between the fitted and measured waveforms. An inaccurate description of the high frequency elements means that the gradient is actually modified to account for errors added by these high frequency components which are more significant than the errors caused by the differences in the underlying gradient over such a small time window.

Hence the next logical step is to include more frequency components. However this in itself is very complicated particularly in a real time application. Firstly the components must be known which means that the frequency, phase and amplitude information must be known. This is difficult, in the example shown in Figure 4.4 where the dominant component only was considered a prior knowledge of the frequency was assumed. Amplitude information could be obtained by direct measurement while phase information was easily obtained by making the first measured peak the start point (90° shifted sinusoid). However all other frequency components are masked by this dominant term and so direct measurement is not possible. Because the exponentially decaying components are highly correlated it is also very difficult to extract the frequency component properties using a Fourier transform. Attempts were made to filter the response and select the dominant components from a number of windows but the phase shift added by the filter was significant and attenuation of dominant frequencies was insufficient to uncover other hidden components. The large number of frequency contributions meant that identification of one dominant frequency in particular was difficult. An important consideration that must also be remembered is that this approach is likely to require an FFT for every measured response (five per PWM period when implementing the Fundamental PWM sensorless technique) which adds significant computational requirements.

4.4.4 Straight Line Approximation Following Moving Average Filtering

Following the unacceptable performance of the approximation methods described so far a more simplistic approach was attempted which did not rely on accurately describing the high frequency behaviour of the waveform. This approach involved applying a moving average filter to the waveform. The midpoints of each high frequency oscillation were established by taking the average of each two consecutive peaks. The first peak was omitted due to the large initial overshoot followed by a comparatively small undershoot; the average of these two values added a large error to the result. Figure 4.5 shows the current response and resulting waveform obtained using a moving average filter.

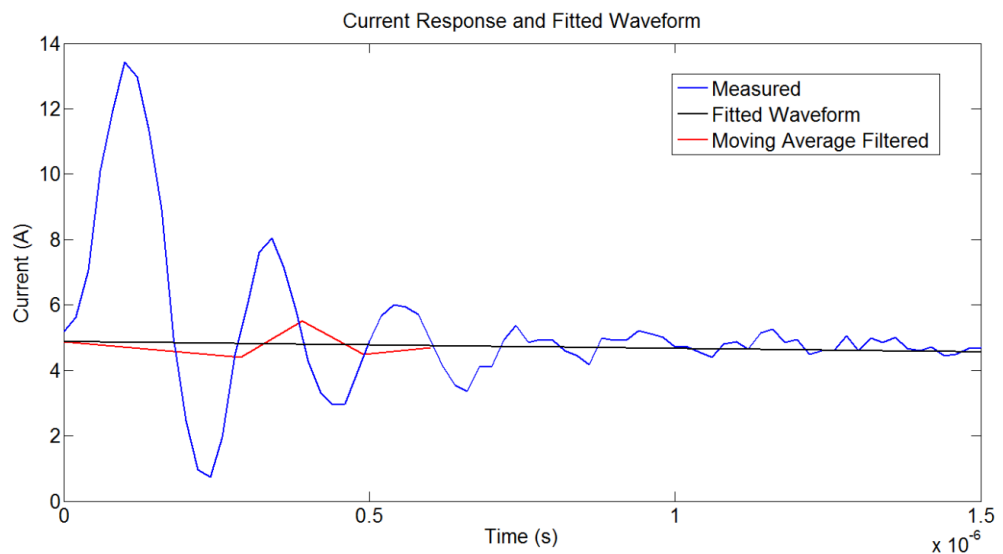


Figure 4.5 Experimental waveform and moving average filtered waveform, a wave fitted to the moving average result is also shown

The new wave consisting of only the average points was processed using a least squares curve fitting approach which tried to fit the points to a straight line. A benefit of this approach is the simplistic fitting required and

the small number of points that require processing. The results were however unsatisfactory. Limitations of this approach include a need to observe a minimum number of current peaks which will enforce a minimum pulse width and also that the method requires that the response is dominated by a single frequency (which is not always the case, as this depends on the parasitic impedance network which determines the high frequency response). If the response contains other significant frequency components and the response does not appear as a single decaying frequency component as in Figure 4.5 then the average values will no longer represent the underlying gradient. This would be the case at low current values when the reduction in dv/dt of the switching device distorts the current.

Figure 4.6 shows the results obtained when using another moving average filter which estimates its points using a step time given by the dominant frequency's period divided by two.

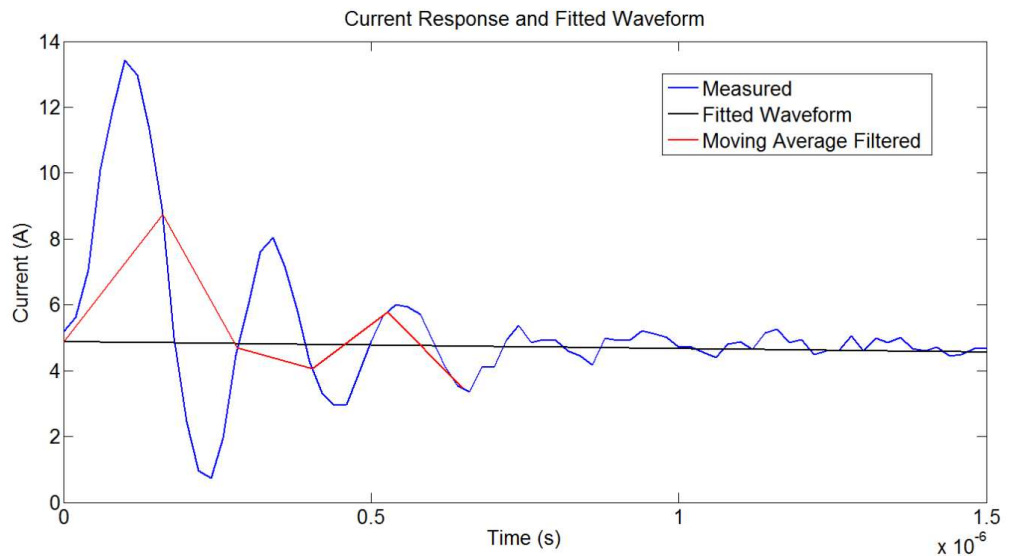


Figure 4.6 Experimental waveform and resulting period moving average filtered waveform, a wave fitted to the moving average result is also shown which provides the gradient estimation

This method also suffers from other high frequency contributions; the result is that there is not one single frequency whose period can be used to

accurately identify the zero crossings (neglecting the gradient and the DC component). This method also suffers from the same limitations as the previous approach which uses the peaks in that a minimum number of peaks must be captured and if there are other significant frequency components present then the result of a moving average filter will not represent the underlying gradient.

4.4.5 Straight Line Approximation Following Dominant Sinusoid Component Cancellation and Low Pass Filtering of Waveform

Because of the difficulties discussed in identifying the other high frequency contributions of the response a different approach was evaluated, the principle of which was to generate an ideal exponentially decaying sinusoid of the dominant frequency observed in the response and then subtract this from the measured current response waveform. The DC offset could also be removed by direct measurement and subtraction. Following this the response only contained the underlying gradient and unaccounted for frequencies. The unaccounted for frequency response consisted mainly of a 1MHz component and a 5MHz component. A digital first-order low pass filter was then applied to the wave in an attempt to remove the remaining high frequency components leaving only the gradient of interest. The difficulty of this approach lay in how to select a cut-off frequency for the filter which would successfully reject the undesirable higher frequency content but would also not degrade the remaining gradient information. If the chosen cut-off frequency was too high then the high frequency components were not sufficiently attenuated and affected the result. While selecting the cut-off frequency to be too low removed too much information from the underlying gradient again affecting the result. Figure 4.7 illustrates the key stages of the process showing the original measured waveform, the waveform with the

dominant high frequency term cancelled leaving the unaccounted for components (or error terms) and the gradient and finally the filtered term. The fitted waveform is also shown but looks identical to the filtered waveform at this scale.

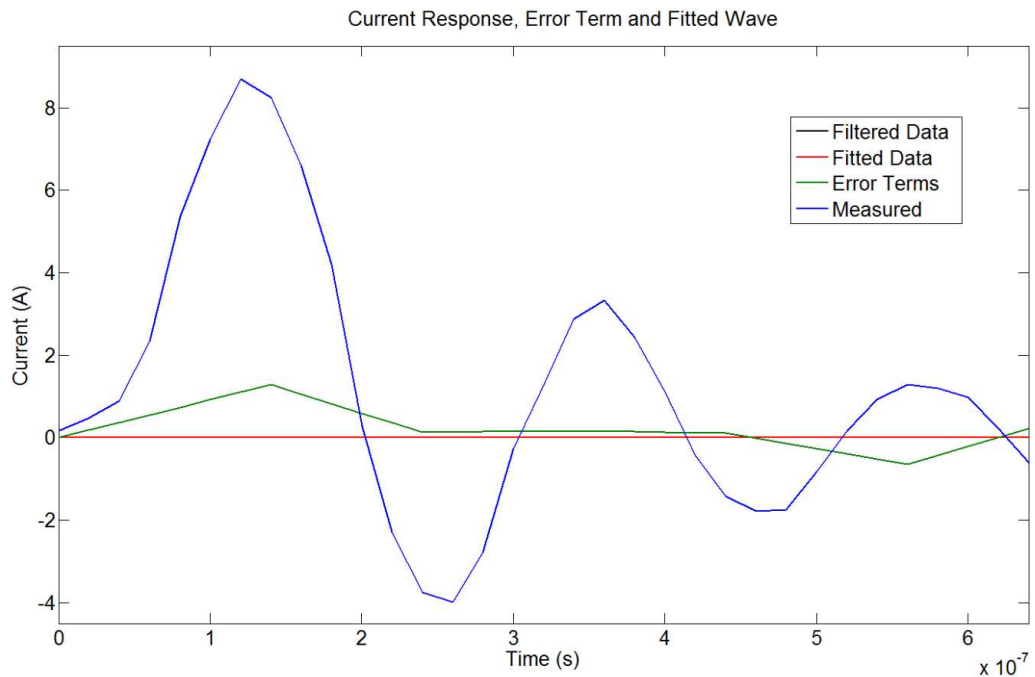


Figure 4.7 The experimental current waveform is shown along with a waveform with dominant exponentially decaying sinusoid component removed; a wave fitted to this result is also shown which provides the gradient estimation. N.B. filtered and fitted waveforms are identical

Many other options were considered in an effort to improve the results obtained using the mathematical curve fitting approach. However due to the time critical nature of the application any methods which required heavy additional computation were discarded. Such approaches included techniques which used Fourier analysis of the sampled waveform (where a very high sample frequency was required to get reasonable resolution in the results) and operating parallel HF models based on the work documented in Chapter 3 which could predict the current waveform frequency content when supplied

with the dv/dt applied to the machine (but required small step intervals due to the high frequency nature of the current waveforms).

In addition, a problem suffered by all of the proposed mathematical techniques is that to offer a significant improvement to the field of sensorless control the proposed solution must be capable of determining the current gradient in a limited time. The mathematical approximation approaches when using a standard current sensor all rely on measuring the change in the underlying amplitude and extracting that information but the small change that is of interest is impractically small in measurement terms over a short time window (of a few μs). From experimental investigation work it is known that current derivatives in the range 10^5 are expected. If a gradient of 10^5 is assumed and a time window of $2\mu s$ is chosen then the change in current amplitude (through a change in the underlying gradient) that needs to be measured is $0.2A$ which is difficult due to noise contributions from external sources, the measurement equipment itself and also the accuracy of the sensors. Hence in order for the method to work satisfactorily the time window may need to be extended in which case little benefit would be offered over simply measuring the current after the high frequency oscillations have passed.

The issue of needing to see a measurable change in the underlying current is combined with the fact that the curve fitting methods investigated all rely on an iterative process to arrive at the derivative result which is inefficient in terms of overall derivative calculation time. This could be critical in a sensorless application where a position estimate is required at least once every few PWM periods.

4.5 Difficulties Associated with Mathematical Curve Fitting Methods

To summarise, for the methods which rely on applying least squares curve fitting to the measured response the following major issues exist

- Approximation of the response to a single dominant frequency component produces unacceptable results as during the least squares fitting the gradient is adjusted to minimise the least squared error. This error is mainly due to other frequencies not included in the curve fitting approximation rather than errors between the estimated and actual gradient.
- To get an accurate result the approximation must include as many frequency contributions as possible which adds computing complexity and also means all frequency components to be included need to be identified prior to implementation.
- If frequency components other than the dominant component are to be included, establishing their amplitude, decay rate and phase information is very difficult. It requires the use of an FFT, adding further complexity to real time implementation.
- The frequency spectrum of the response contains many other significant contributions which are very difficult to identify due to the high correlation between the exponentially decaying components. This is compounded by the fact that when trying to establish the key frequency components, what is a good window for one component for the FFT is a poor window for another component.
- A problem affecting all of these approaches is the high dependence on the accurate determination of the initial offset. If this is incorrect it can have a larger influence on the least squares curve fitting process than

the actual gradient that is of interest, causing an erroneous gradient estimate result. Establishing the initial offset is also very challenging as knowing which point in time to select as the start point and measuring the current accurately at that point is not straightforward.

- The transient current response varies according to the dv/dt applied by the inverter. The mechanisms and variables that influence the applied dv/dt have been identified (allowing a level of predictability about when these responses will occur). However, applying an approximation that describes all possible responses would be difficult due to the number of different possible variations of the waveform. An option would be to delay the defined start of the oscillatory waveform until the initial distortion has passed, however knowing how much delay is required and what the initial offset should be (since the start point is offset by the distortion) would present further challenges.

The work in this chapter has shown that it is not possible to simply apply a curve fitting approach to the transient current response and obtain an accurate result for the current derivative. The complex mathematical description of the waveform, the effects of limited sensor bandwidth and non linear inverter switching (which distorts the current waveform) all present significant challenges to curve fitting methods. Hence an alternative solution is required. An ideal solution would be one where it is not necessary to define all contributing frequency components and one which is able to deal with the effects of limited sensor bandwidth and non-linear inverter switching. The next chapter introduces a solution that meets these requirements by using artificial neural networks to estimate the derivative from a transient current response.

Chapter 5

Derivative Estimation Using Artificial Neural Networks

5.1 Introduction

The limitations associated with using a mathematical approach to estimate the current derivatives prompted investigation into an alternative solution. Artificial neural networks (ANNs) are employed as pattern recognition tools to associate measured transient current responses with steady state derivative values based on prior knowledge obtained during the offline training of the neural network (performed in a pre-commissioning phase).

An attractive feature of artificial neural networks is their ability to work on problems affected by non-linear behaviour. Neural networks can be trained to deal with factors which present major problems for the mathematical approaches detailed in Chapter 4 including low dv/dt transients and the limited bandwidth of the sensing circuitry, both of which distort the measured current response. This removes the need for special handling procedures for low dv/dt cases providing the neural network is adequately trained to deal with such scenarios. They are particularly well suited to this application as no knowledge of the specific mathematical details of the transient response are required (which are difficult to measure as indicated previously and the description of the response mathematically is complex).

Another advantage is the reduced dependence on accurately determining the start of the transient. It has been seen that this has a large effect on the accuracy of the results obtained from least squares fitting techniques. In the case of neural networks, what is more important is the similarity between the training data used and real data encountered by the network. Triggering the sampling of the current waveform to start from the same point with respect the PWM edges (when collecting data for training or when operating in real-time) ensures that this is the case.

A further benefit is that using this approach it is not necessary to physically measure the derivative. This is especially advantageous when standard current sensors are to be used as in a normal implementation the use of standard current sensors dictates that a longer minimum pulse width is maintained to allow a measurable change in the current gradient to occur [1]. As the approach used here is concerned only with the transient response and associating this to a steady state derivative, standard current sensors can be used for very short sampling windows (a few μs). These sensors could be shared to also measure the current for control purposes and hence no additional sensors are required compared to the standard industrial inverter.

Neural networks can also offer the possibility of adaptive learning which could be useful in this case since the high frequency impedance network can change as the winding insulation breaks down which in turn effects the current response [96].

In this chapter neural networks are introduced and their implementation in this work is discussed. Simulation results are presented which demonstrate the ability of neural networks to estimate the current derivative from a transient current response affected by high frequency oscillations. All simulation work was performed using Matlab, initially using the Matlab neural network tool. This provides an easy to use graphical user interface (GUI) which simplifies the implementation. Once the work had reached an advanced stage the networks were implemented using Matlab

commands directly (instead of through the GUI) which provided more control over the network configuration and allowed automation in the processing of data and network training process.

5.2 Artificial Neural Networks and Their General Operation

The design used in this work was based on a feed-forward neural network which features no form of feedback during operation. The neural network consists of several layers; the initial layer (the input layer) is formed by a collection of nodes which accept vector elements as the input. In this application the vector applied to the input contains the points of the sampled current transient. The next layer is known as the hidden layer and contains neurons, the number of which is defined by the network's designer. Each neuron has weighted connections to all input nodes and also receives a bias input. Each neuron sums the weighted and bias at the inputs and then passes the result through a transfer function to obtain a final result. In this work a $\text{tansig}()$ transfer function, given by Eqn 5.1, was used.

$$y = \text{tansig}(x) = \frac{2}{1 + e^{-2x}} - 1 \quad (\text{Eqn 5.1})$$

It is possible to have multiple hidden layers, each with a number of neurons and transfer function selected by the designer. In this work one hidden layer consisting of ten neurons was found to be sufficient. The neuron outputs are then supplied to a final layer called the output layer. The output layer also consists of neurons which are connected to each of the hidden layer's neurons via weighted connections and also have a bias input. Once again the inputs are summed and passed through a transfer function. The number of neurons in the

output layer is set to provide the number of elements required to form the output vector, 1 in this case. Figure 5.1 illustrates the structure of a feed-forward ANN.

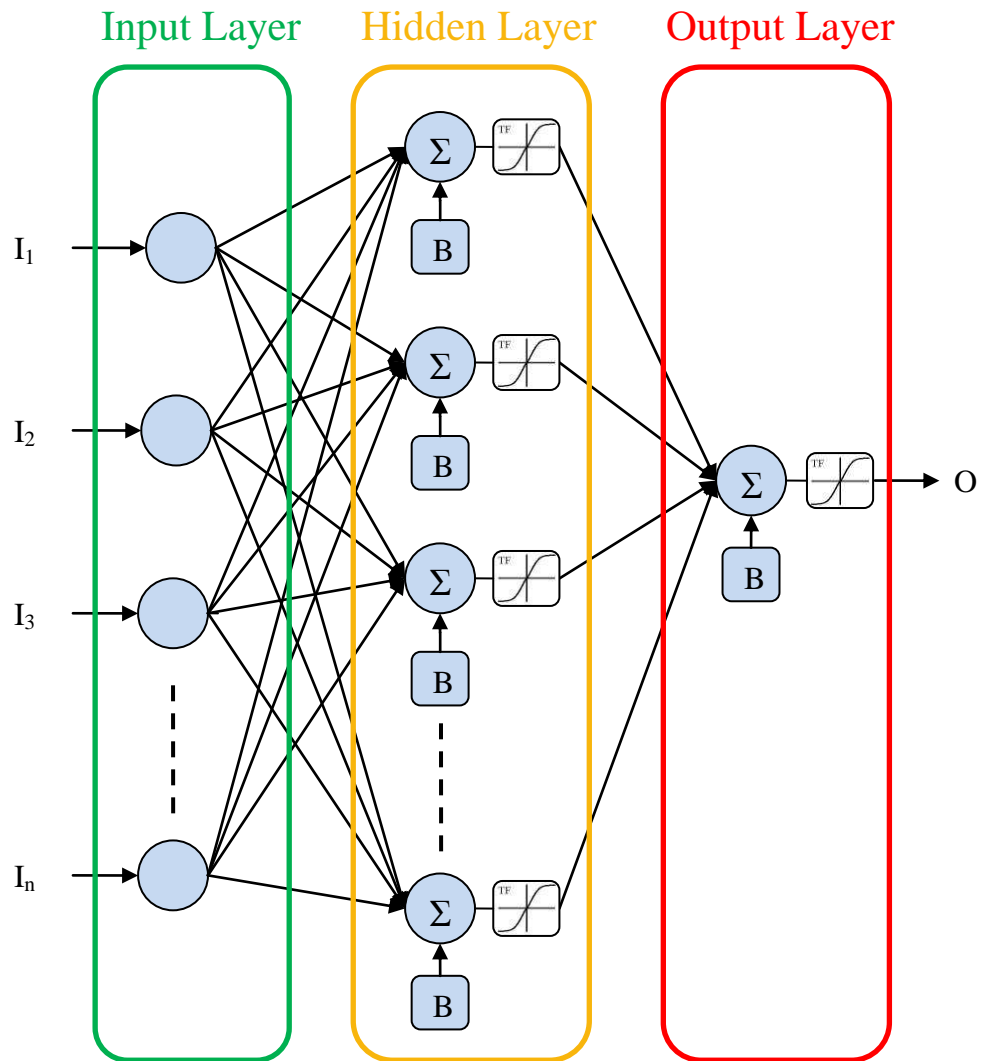


Figure 5.1 The structure of a feed-forward neural network. The interconnections between the inputs and hidden layer neurons and also between the hidden layer neurons and output layer neuron are weighted (I=input, B= bias and O=output)

5.3 Use of Neural Networks in Sensorless Control Applications

The use of neural networks for sensorless control applications has so far been mostly focused on the mathematical modelling approaches where parameter variation can have a large effect on the accuracy of the system. Artificial neural networks have been employed in many applications to track stator and/or rotor resistance variation [8, 97]. They can also be used in place of the conventional adaptive model [98, 99]. In [100] a neural network stator current observer was used as the adaptive model. The estimated stator current is compared with the measured stator current to obtain an error which is minimised by altering the speed estimate. The new method removes the drift and parameter variation associated errors but suffers from instability under regeneration mode [100]. In [101] an ANN was used as a flux observer, replacing the voltage model as the MRAS reference model and removing the integration operation.

Artificial neural networks have also previously been employed in saliency tracking sensorless control methods [102-104]. However the reason for applying neural networks in the case of [102-104] was to try and identify through pre commissioning the variations in the various saliencies due to load and flux. At low speeds a problem arises with saliency components overlapping in the frequency domain making them inseparable by filtering methods. Instead the neural network with prior knowledge of the saliencies and their conditionally dependant behaviour gained during the pre-commissioning could cancel the influences and interactions of the undesirable frequencies without the need for filtering or compensation by lookup values. This work did not consider the way in which the current derivative measurements might be obtained and was not concerned with reducing minimum PWM vector time limitations.

5.4 Estimation of Current Derivatives Using Neural Networks

5.4.1 Training a Neural Network for Derivative Estimation

Given that the neural network must be trained prior to use, this approach would necessitate pre-commissioning when used in any motor drive application. To achieve this, the drive could be operated in open loop mode to apply (extended) PWM vectors to the machine and view the current response over a large time period such that the measured current data contains a significant amount of steady state behaviour. The current transients are captured and the steady state portion of the response is supplied to a mathematical least squares algorithm. A first order equation is fitted to the response and from the results the gradients are established. For every transient captured there is an associated steady state derivative value that could be used to train the neural network. This training process is outlined in Figure 5.2.

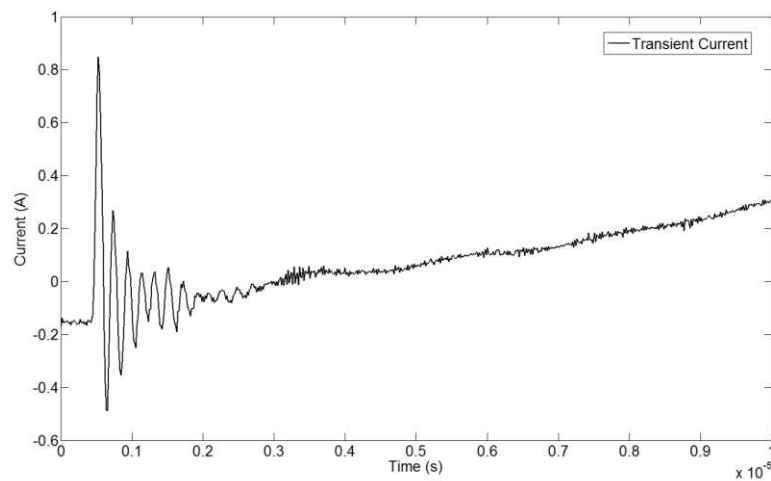


Figure 5.2 (a) Capture the current transient including some ‘steady state’ data after the high frequency oscillations have decayed

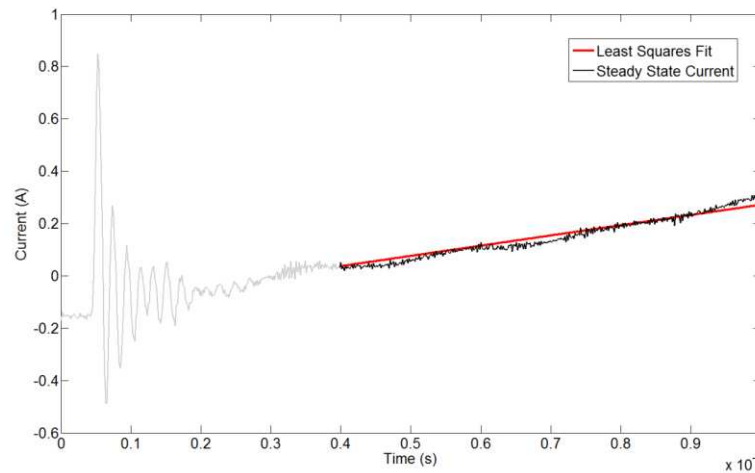


Figure 5.2 (b) Neglect portion of the waveform which contains high frequency transient and apply a least squares curve fit to the steady state section according to $y=mx+c$. The value obtained for m can be used as the target data for this particular transient while the initial part of the current transient (e.g, the first $2\mu\text{s}$) is used as the training data.

Figure 5.2 The proposed method for obtaining training data for the neural network

The network was trained in Matlab using the feed-forward back-propagation algorithm. In this algorithm a set of input and target data is provided. The input data is split into three groups, training, validation and testing. Training data is supplied to the network which generates an output for the given input. This result is then compared with the desired output provided by the target data and an error value is determined. The algorithm then works backwards through the network adjusting the weights of the interconnections between the neurons in each layer to minimise the error. Performance of the neural network is evaluated by performing a mean square error comparison with the output of the neural network and the target data, training continues until the error falls within acceptable levels. In order to avoid a phenomenon known as over-fitting, validation data is also supplied to the neural network to obtain an error estimate. This result is not used to adjust the network

interconnection weights but by monitoring the error when using the validation data this does provide an indication of when the network is over-fitting the training data as a change in inter connection weights shows no improvement in the error function for validation data but does however show an improvement for the training data. The testing data is used as a means of validating the final resulting neural network performance on independent data.

5.4.2 Data Normalisation

All sampled data must first be normalised before it is supplied to the neural network to ensure that the neural network receives data within a set range. Normalising the network inputs allows reduced training times. In this work the `tansig()` transfer function was used as the neuron transfer function in both the hidden layer and the output layer. In this case when the input to the transfer function is greater than approximately 1.5 the neuron output becomes saturated. This can cause small gradients which leads to a slow training process [105], normalisation avoids this. The target data is also normalised during the training process such that the network will give an output in the range ± 1 . Once trained, following a successful execution of the neural network the output data must be de-normalised (which just involves a simple multiplication) to ensure that the output is correctly scaled. The image in Figure 5.3 illustrates the normalisation and de-normalisation process. In this work the input to the system prior to normalisation is the current in Amps and the output post de-normalisation is the current derivative in A/s.

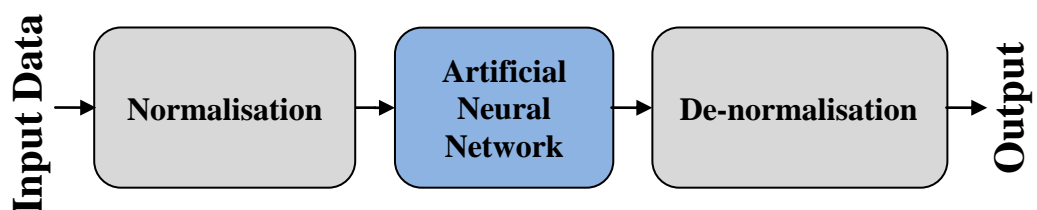


Figure 5.3 Data normalisation required pre and post neural network [105]

5.5 Simulation Results

The approach was tested using current data which was sampled at 62.5 MHz. The platform used to achieve this is described in Chapter 6. A neural network was configured to have 128 inputs (which represents approximately $2\mu\text{s}$ of data when sampled at 16ns intervals (62.5 MSPS)), one hidden layer containing 10 neurons each of which used a `tansig()` transfer function and an output layer which consisted of one neuron which also used the `tansig()` function. A number of other feed forward network designs were evaluated by varying the number of hidden layers, the number of neuron(s) contained in hidden layer(s) and the transfer function(s) used in the hidden layer(s). The described ANN was found to give the best overall performance in terms of accuracy when tested on training data and new experimental data, training time and also neuron count (which translates into resource usage when implementing the design). The results presented are representative of the performance level that can reasonably be expected to be achievable using this method since it cannot be expected that identical results can be reproduced using this approach given the tolerance and sensitivities of ANNs.

5.5.1 Phase A, First Active Vector

Following a successful training operation the neural network was supplied with current transient data. For all of the following tests current transients were collected using the permanent magnet motor drive described in Chapter 6. In each case the machine was operated at 30Hz (600RPM) with 83% of the rated load applied since this was a point used to collect ANN training data and so was expected to give good performance. Initially current transients were collected from the first PWM active vector and supplied to the ANN. In the case illustrated below half of the data supplied to the neural

network had been used to train the neural network while the remaining 50% of the data was previously unseen by the neural network. The plots shown in Figure 5.4 (a) and (b) show the ANN derivative estimates along with the least squares fit result applied to the steady state portion of same current transients. A derivative result was obtained once every PWM period and the switching frequency was 5 kHz. Hence with a fundamental frequency of 30Hz, one fundamental period is represented by 167 samples. In case (a) the transient data was seen by the neural net during training while in case (b) the transients had not been encountered by the ANN previously. Note that there is little difference in the accuracy of the ANN's estimates between cases (a) and (b).

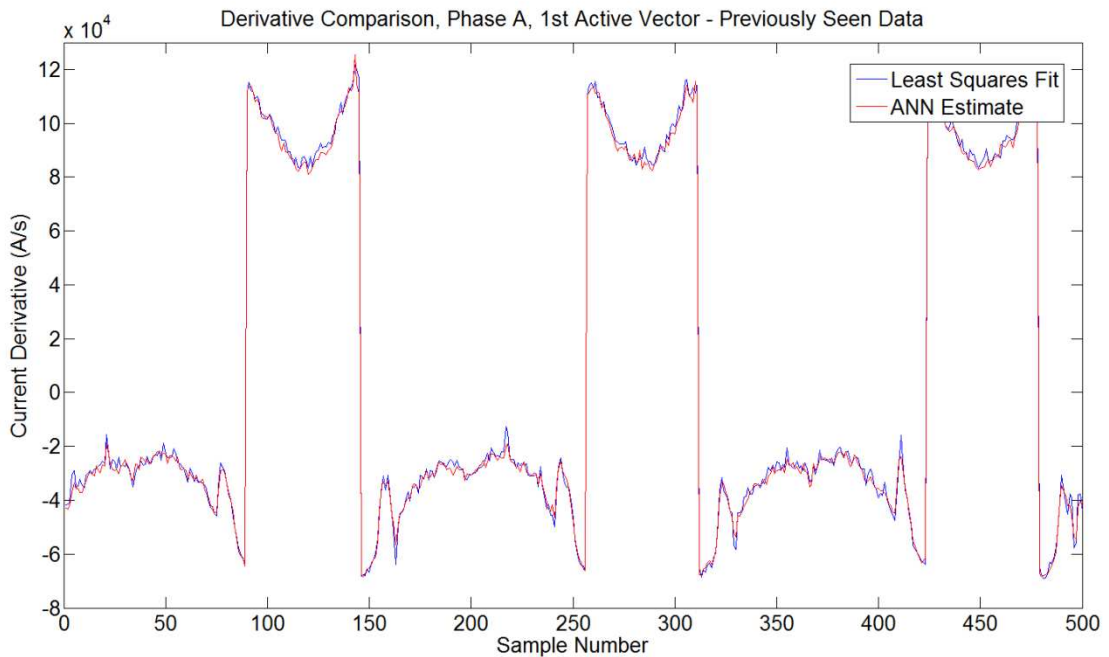


Figure 5.4 (a)

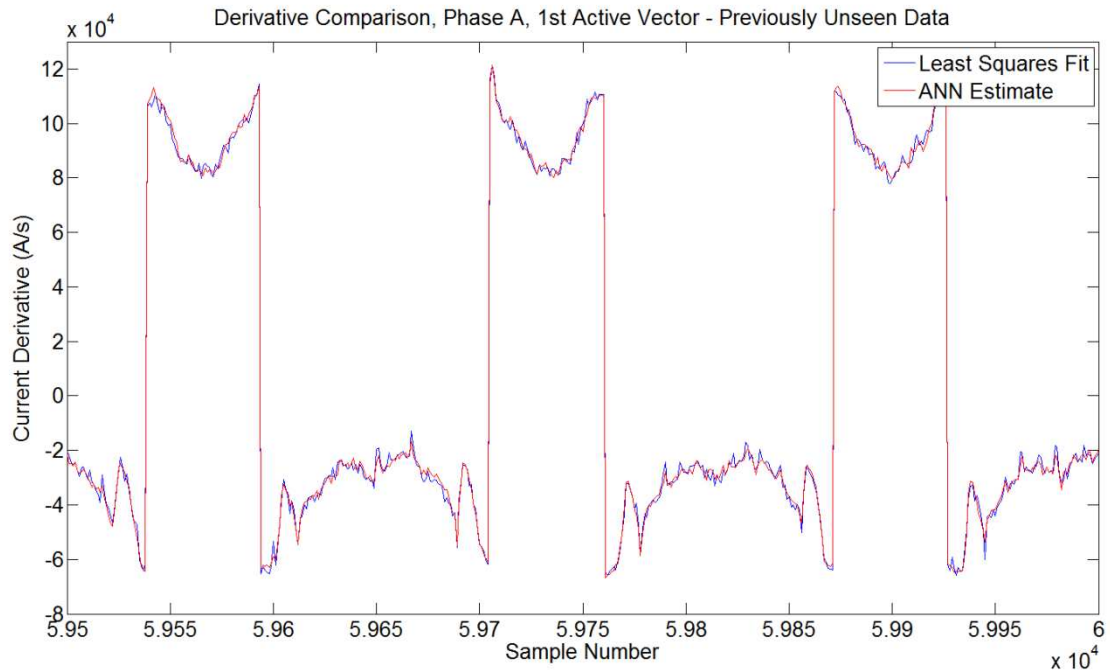


Figure 5.4 (b)

Figure 5.4 The estimated first active vector derivatives from the ANN are shown with the derivatives calculated from a least squares fit for comparison. In (a) the transients supplied to the ANN had been seen during the training process while in (b) the transients supplied to the ANN had not be used previously

In order to quantify the accuracy of the ANN estimated derivative compared to the actual derivative obtained from a least squares fit performed on steady state data, the error between the least squares fit result and the ANN estimate was analysed. Figure 5.5 shows the instantaneous error in each estimate (comparing the ANN estimate the least squares fit result). The RMS error and standard deviation calculated from the instantaneous error are also shown.

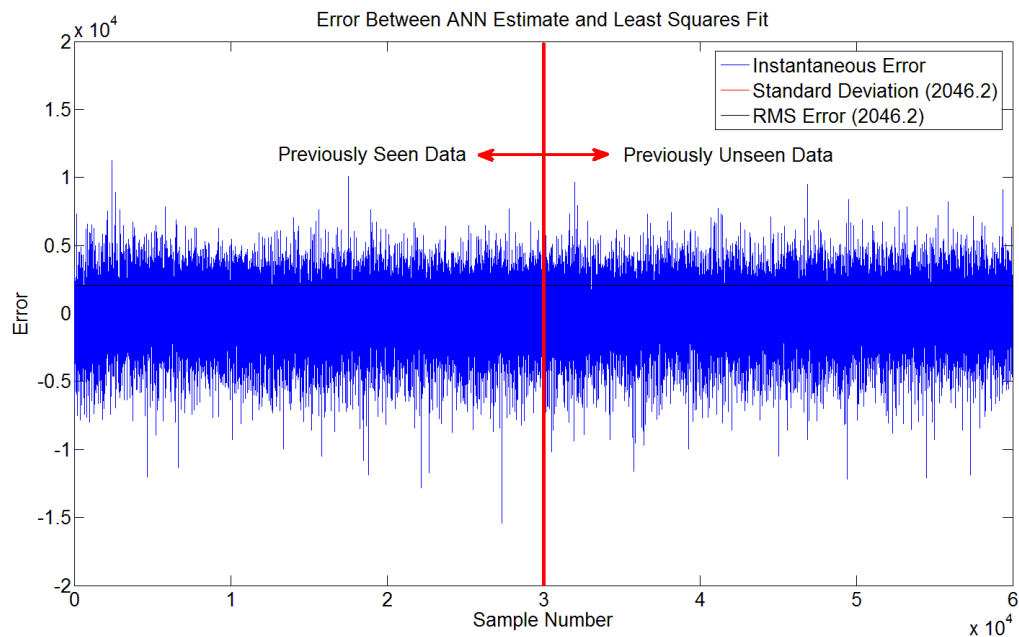


Figure 5.5 The instantaneous error of the ANN estimated first active vector derivatives compared to the least squares fit results

It is clear in Figure 5.5 that there is no notable difference in the performance of the ANN when comparing its performance using previously seen and unseen data. The RMS error for previously seen data was 2046.2 while the RMS error for unseen data only was 2028.0. The ANN showed no notable change in the instantaneous error when estimating negative and positive derivatives. As the negative derivatives had a much larger amplitude this indicates that the ANN is able to estimate the derivative more accurately when the derivative is large. The standard deviation value gives an indication of the error magnitude that can be expected in the ANN estimated results. Figure 5.4 shows that the positive derivatives have an amplitude in the 40000 A/s region. Hence with a standard deviation of 2046 an error of approximately 5% can be expected in the ANN derivative estimates, this value is within the limit of $1 \pm 1.315e^4$ A/s defined in Section 2.6. Inspection of Figure 5.4 reveals that the negative derivatives have amplitude in the -100000 A/s region. Hence an error of 2% can be expected in the result.

5.5.2 Phase A, Second Active Vector

Following the encouraging tests performed using transients collected under the first active vector the same test was repeated using data captured under the second active vector. Once again Figure 5.6 (a) shows the results using transients used during the training of the ANN while the results shown in Figure 5.6 (b) are obtained by supplying the neural network with data it has not previously seen before. The ANN again shows a good ability to estimate the derivatives with reasonable accuracy.

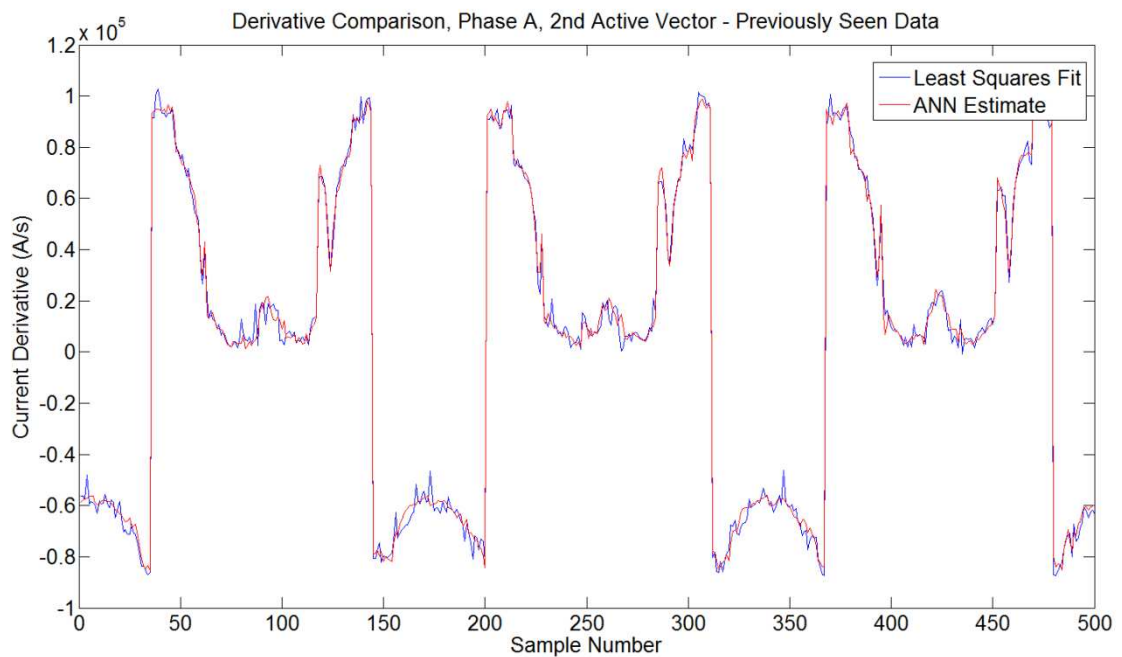


Figure 5.6 (a)

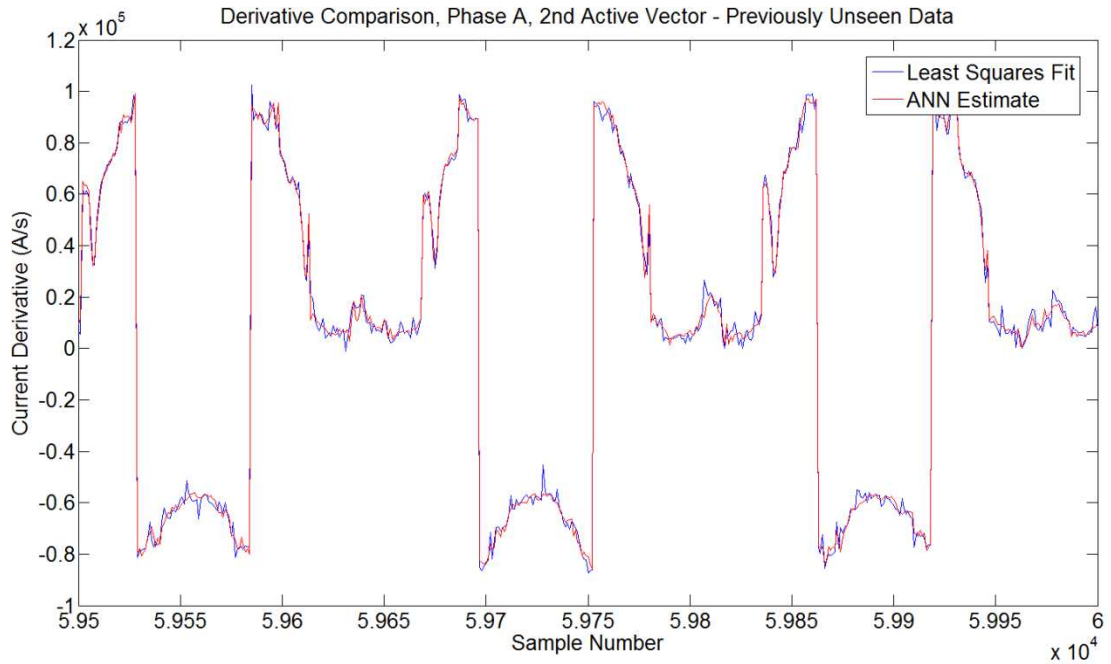


Figure 5.6 (b)

Figure 5.6 The estimated second active vector derivatives from the ANN are shown with the derivatives calculated from a least squares fit for comparison.

In (a) the transients supplied to the ANN had been seen during the training process while in (b) the transients supplied to the ANN had not be used previously

Following the same approach that was applied to the first active vector case, the instantaneous error in the derivative estimates was calculated and analysed. The instantaneous error is shown in Figure 5.7

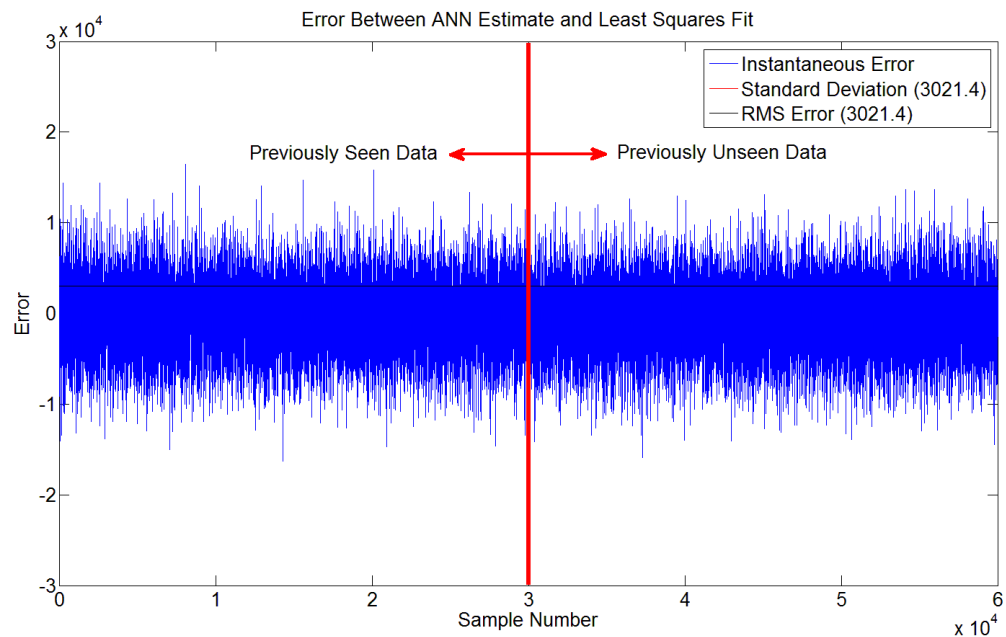


Figure 5.7 The instantaneous error of the ANN estimated second active vector derivatives compared to the least squares fit results

The standard deviation for the second active vector was found to be 3021.4. This result is clearly higher than the result seen in the case of the first active vector derivative estimates but is again within the limit of $1 \pm 1.315e^4$ A/s defined in Section 2.6. Inspection of Figure 5.6 (a) and (b) reveals that the second active vector derivative waveform has a more complicated shape including several discontinuities. If these are not accurately reflected in the estimated derivative then large errors can be introduced, particularly for small derivatives (of which the second active vector derivative has a number) where a small error can have a large effect on the derivative. It could also be that the ANN is simply better trained to the first active vector derivative. This is speculative as apart from the reduced error seen for the first active vector derivative estimates, there is no way to tell whether this is the case. Despite the reduction in performance compared to the first active vector case the second active vector derivative estimates from the ANN still follow the actual derivative closely.

5.5.3 Phase A, Null Vector

It has now been demonstrated that an ANN can be used to estimate the derivative from transient current data under both SVPWM active vectors in a PWM period. In order to be able to implement the Fundamental PWM technique derivatives are also required for the PWM null vectors. Hence the final simulation tests were performed in order to see if this was possible. The tests followed the same procedure as those for the active vectors. Current transients captured under central null vector (V7) were supplied to the ANN to gain a set of derivative estimate results. The results are shown in Figures 5.8 (a) and (b) and once again comprise of results obtained by supplying the ANN with previously seen (a) and unseen (b) transients. The ANN shows a good capability to estimate the derivatives but it is clear that the results are not as accurate as those seen for the active vectors.

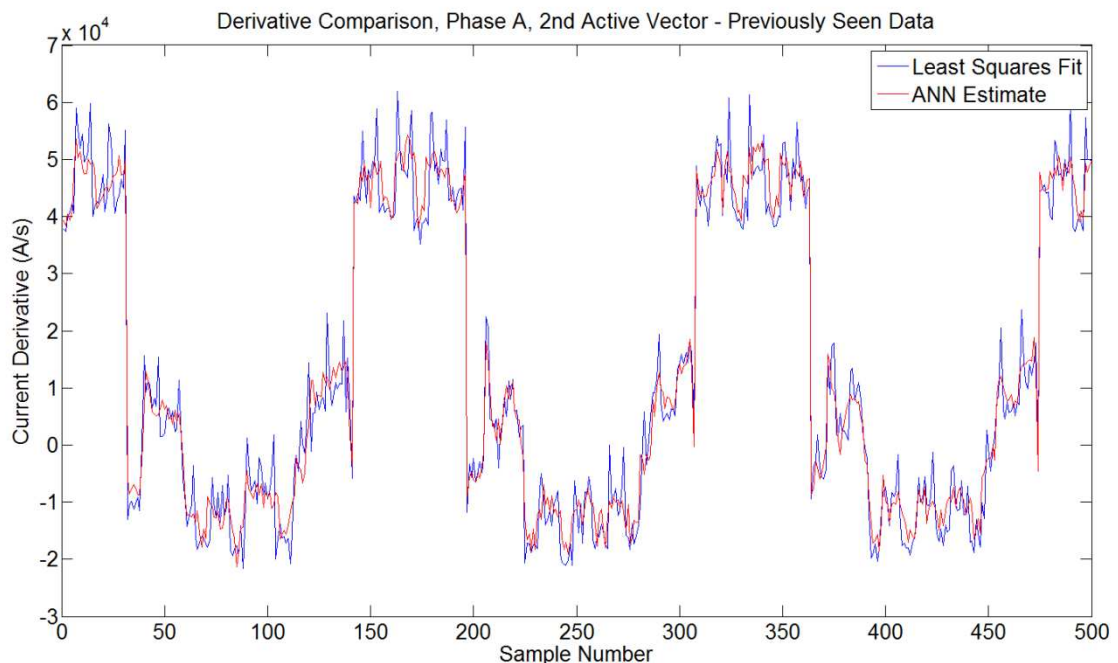


Figure 5.8 (a)

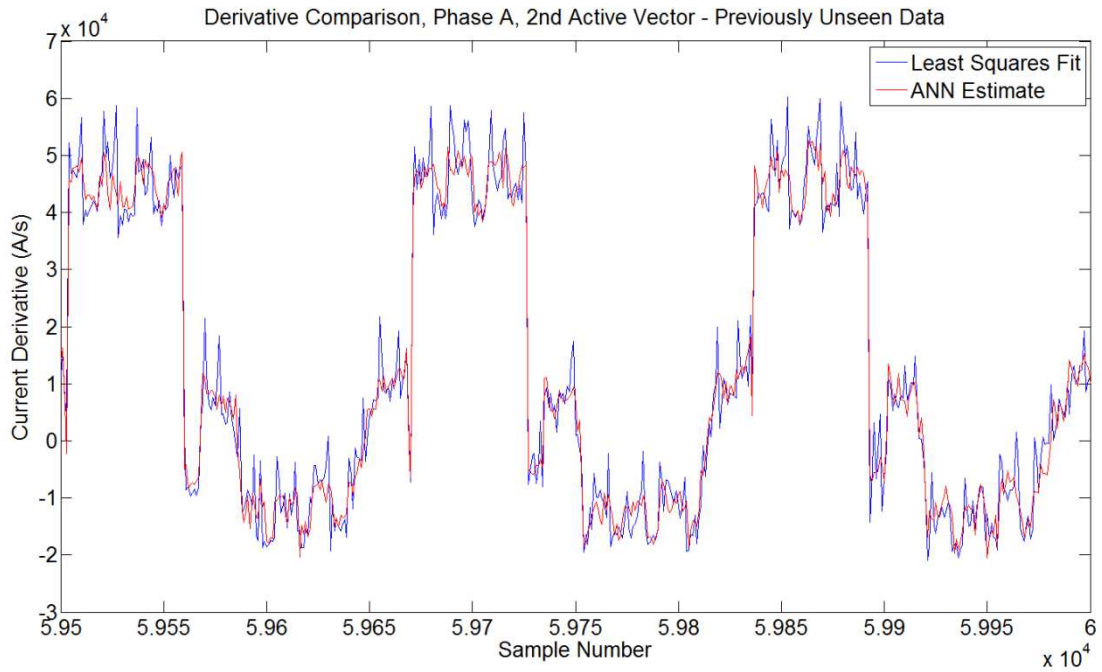


Figure 5.8 (b)

Figure 5.8 The estimated null vector derivatives from the ANN are shown with the derivatives calculated from a least squares fit for comparison. In (a) the transients supplied to the ANN had been seen during the training process while in (b) the transients supplied to the ANN had not be used previously

In order to investigate the accuracy of the estimates the instantaneous errors were again analysed. The instantaneous error is shown in Figure 5.9.

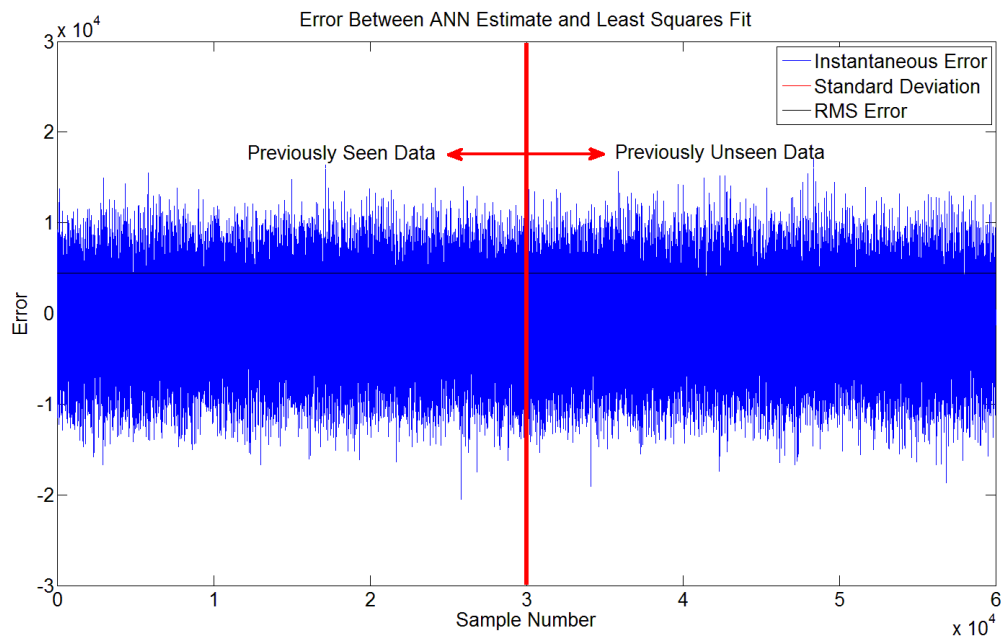


Figure 5.9 The instantaneous error of the ANN estimated null vector derivatives compared to the least squares fit results

Using the instantaneous error results the standard deviation was calculated to be 4476.2. This was the highest standard deviation seen in the results so far and given the small amplitude of the positive derivatives can represent a large error. However the result is less than the limit of $1 \pm 1.315e^4$ A/s defined in Section 2.6. The decrease in the performance of the ANN when estimating the derivatives under null vectors is thought to be due to the fact that the same ANN is also trained to estimate derivatives under active vectors which can have much larger amplitude. The normalisation that must be applied to data supplied to the ANN is based on the amplitude of the largest derivatives expected, since even the largest null vector derivatives are small (compared to those of the active vectors) the active vector derivatives dictate the scaling and normalisation applied and as a result the null vectors are located in a small operating region of the ANN which is close to zero. The limited operating range reduces the resolution and separability of the null vector derivatives and the estimation accuracy is consequently affected. If an

ANN was trained to deal with just null vectors the scaling and normalisation applied could be different and could represent the full operating range of the ANN (± 1). The accuracy of the null vector derivative estimates, while not as good as those for active vectors, are still thought to be accurate enough to be used. It should also be considered that when measuring the null vector derivatives using other techniques the derivatives encountered are so small that measurement noise could introduce large errors using these techniques also.

5.5.4 Phases B and C

Similar tests were performed for data collected from phases B and C and the results obtained reflected a similar level of accuracy to those presented above for Phase A giving confidence in the potential of the proposed technique.

5.6 Conclusions

The results presented demonstrate that a neural network can be used to give an acceptable estimation of the current derivative when supplied with a short section of a phase current transient contaminated with high frequency oscillations. The window length employed was $2\mu\text{s}$, the minimum pulse width that would normally be used on the drive from which the transients were captured would be greater than $5\mu\text{s}$ meaning that at least a 60% reduction in the minimum pulse width is achievable using this technique in this case.

Other tests that could be performed at this stage to evaluate validity and performance with regards to the sensorless position estimation were limited by not having a system available that was capable of sampling the

necessary phase currents (required for the implementation of the Fundamental PWM technique) at a high sample rate. It would have been possible to simulate the entire drive setup which would allow a sensorless position estimation algorithm to be tested. However, simulation tests such as these are only of limited use in this case since the current transient is so sensitive to the real parasitic impedance network and inverter non-linearity affects which are difficult and time consuming to accurately simulate. This means that simulated transients were not sufficiently reflective of the real behaviour to test the techniques true ability to estimate derivatives for position estimation.

Instead it was decided to test the technique on the real machine with the first objective being to sample a single PWM vector of one phase at a high sampling frequency, use an ANN to estimate the derivative and compare the result with that from a dedicated derivative sensor and/or a result from the two current sample method. Upon a successful outcome the test could be expanded to include other PWM vectors of the same phase. Once it could be established that an accurate derivative estimate could be found (by comparing the estimate with a measured derivative) in a real time experimental situation, it naturally follows that this estimate could be used in place of the value measured from the dedicated di/dt sensor which had been successfully used by others in the past for sensorless position estimation [22, 23, 26].

Chapter 6

Hardware and Practical Implementation

6.1 Introduction

Following successful off-line simulation studies using an ANN to estimate the current derivative, it was decided to evaluate the technique in a real environment. A permanent magnet motor drive which had been constructed by an earlier PhD student [34] was available for use. The rig comprised of an inverter together with DSP/FPGA controller and an industrial surface mounted permanent magnet machine (connected to a DC motor and commercial DC drive for loading). Speed (and rotor position) could be measured using a shaft mounted 4096 pulse incremental encoder and this was interfaced to the DSP (Digital Signal Processing) system. This chapter describes the existing rig and the components added by the author (a separate Altera FPGA system) to implement the current derivative estimation. The full system is shown in Figure 6.1

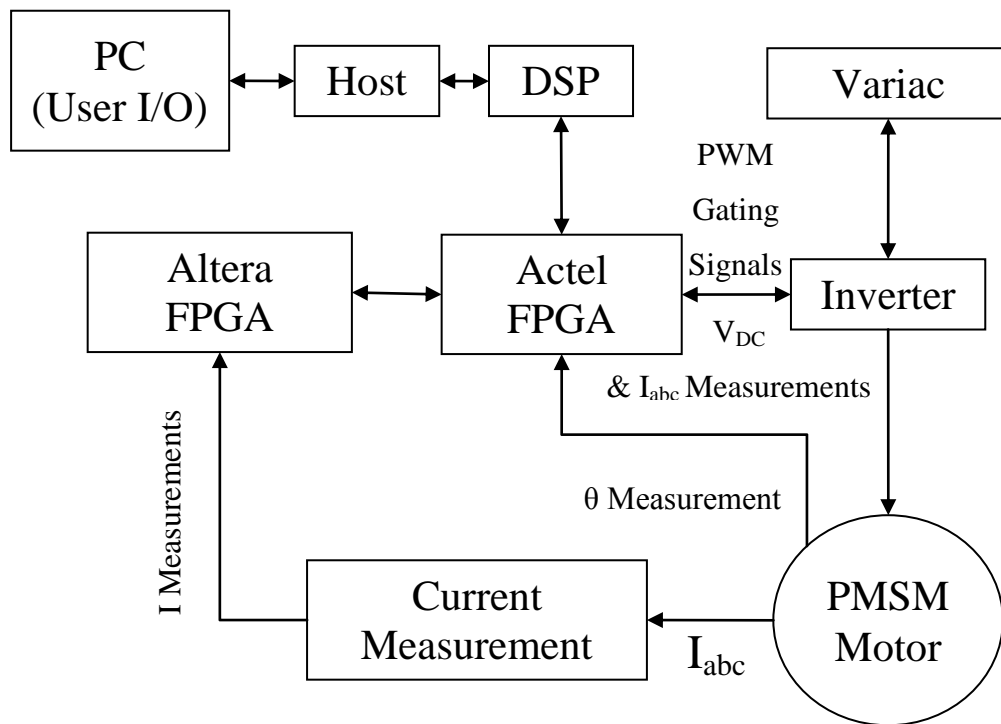


Figure 6.1 A diagram illustrating the layout of the overall system

6.2 Permanent Magnet Motor

The motor used for the majority of the experimental work was a Control Techniques Unimotor, a three phase, six pole, surface mounted permanent magnet AC machine rated at 3.82 kW. The full load current rating of the machine is 7.625A. While the machine is rated at 3000 RPM, in this research it was always operated at 50Hz (1000 RPM) or less. Table 6.1 summarizes the other key parameters of the machine taken from the datasheet [106].

Model Identification Number	142UMC300CACAA
Poles	6
Rated Speed	3000 RPM
Rated Power	3.82 kW
Rated Torque	12.2 Nm
Inertia	$20.5 \times 10^{-3} \text{ kg.m}^2$
K_t	1.6Nm/A
K_e	98.0 V _{rms} /kRPM
R_s	4.7m Ω
L_s	4.15mH

Table 6.1 Permanent magnet motor parameters [106]

6.3 Power Electronics

The Inverter used to supply the permanent magnet machine was a custom built, three phase, two level design rated at 15kW [23] and supplied from a 415V 3 phase supply. This type of drive was chosen because it is very common in industry and its operation causes large dv/dt to be applied to the machine when switching. This in turn produces a strong transient current response for testing of the proposed technique.

The inverter was designed at the University of Nottingham [107] and featured six output phases, although only three were used in this work. The incoming voltage from the supply was rectified via a three phase diode bridge rectifier and supplied to a DC link constructed using four 400V 2mF capacitors. These were arranged as a pair of two series capacitors in parallel

giving a total DC link capacitance of 2mF and a voltage rating of 800V. A three phase inverter then supplied the motor.

The switches used in the inverter were Fuji IGBTs rated to withstand 1200V and carry 100A. Each module contains both upper and lower IGBTs of an inverter leg. Housed on the inverter board were LEM sensors used for measuring DC link voltage (LEM LV 25-P) and the three phase currents (LEM LAH 100-P) with measurements from the sensors being used for both control and protection purposes.

The inverter board also contained the gate drive circuitry which took fibre optic gate drive signals from the Actel FPGA and converted these back into electrical signals with the required amplitude ($\pm 18V$) to switch the IGBTs.

6.4 DSP and FPGA Control Platform

The control platform for the inverter was developed by the PEMC group at the University of Nottingham and consisted of a Texas Instruments TMS320CX6713 DSP with an Actel ProASIC FPGA mapped to the external memory of the DSP and located on a separate PCB. The DSP is responsible for all of the control implementation and software based safety provisions. It is set up to have an interrupt triggered by the FPGA which is configured to occur at the PWM switching frequency. The interrupt routine includes the acquisition of measurements from ADCs, over-current and over-voltage protection checks, position calculation (using measurements obtained from encoder), control equation implementation and SVPWM gating signal calculations. The DSP stores results in specific memory locations which are accessed by the FPGA through a 32 bit external memory interface (EMIF). Values calculated in the DSP as well as general configuration settings (e.g. PWM switching frequency) can be accessed and used by the FPGA which is responsible for generating the PWM gating signals and controlling the

analogue to digital conversion of measured signals supplied to ADC chips. The FPGA board contains nine 12 bit ADCs capable of conversion rates of 3MSPS. The inputs to the ADCs are also supplied to comparators which are set up to generate hardware trips in the event of an excessive reading from the attached sensor.

6.4.1 Modifications to DSP/FPGA Control Platform

With the control platform being well proven for controlling two level inverters supplying AC machines, only minor modifications were required specifically for this application. Additional signals calculated in the Actel FPGA and required by the proposed technique were added as outputs of the Actel FPGA via a ribbon cable which was connected to the GPIO header of the Altera FPGA used to implement the proposed technique.

6.4.1.1 Modifications to the PWM

Space Vector PWM was used to generate the gating signals but it was necessary to ensure that the PWM vectors always respected a minimum pulse time in the first half of the PWM period for the reasons discussed in Chapter 2. The technique for extending and compensating vectors described in Chapter 2 was implemented within the DSP.

6.4.1.2 Trigger Signal

The high frequency sampling of the current signal required a trigger signal to indicate the start of the transient and therefore the point at which to begin sampling. The easiest way to do this was to produce this from the FPGA which produces the PWM signals since the knowledge of the PWM timings

can be used to produce a trigger signal slightly before or after the PWM gating signal to perfect the timing of the high frequency sampling and subsequent transient capture. This allowed delays in the gate driver circuitry to be accounted for.

6.4.1.3 New Period Signal

This signal served a dual purpose and was used in conjunction with the “Trigger” signal. Four trigger signals were expected within each PWM period. The “New Period” signal provided the first while the “Trigger” signal provided the other three. The New period signal was also used as a reset to protect the system in the event that one of the trigger signals was missed and not all of the necessary data had been captured for a position estimate. Without this provision it may have been possible for the Altera FPGA to keep waiting for four trigger signals and actually use transients from different PWM periods. The timing of the new period and trigger signals with respect to the PWM gating signals is illustrated in Figure 6.2.

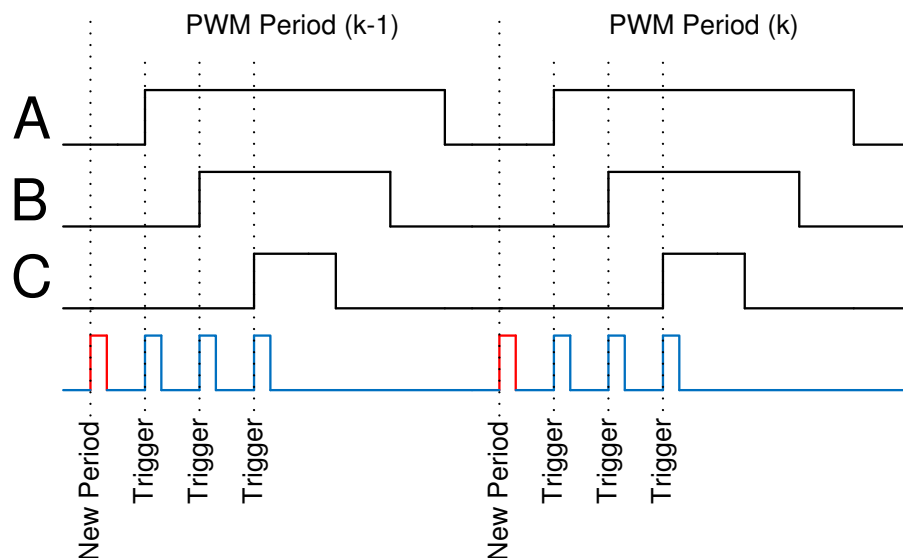


Figure 6.2 an illustration of the positions of the new period and trigger signals with respect to the PWM waveforms

6.4.1.4 Sector

‘Sector’ refers to the segment in which the voltage reference vector lies in the SVPWM plane. This information is already calculated in the DSP as part of the Space vector PWM algorithm. Knowledge of this information was required in the Altera FPGA for the implementation of the Fundamental PWM technique, since it is the sector of operation that governs which phase derivatives are required for position estimation. The Sector always has a value of between one and six and was communicated as a 3 bit signal.

6.4.1.5 Encoder Output

This was used for capturing training data in an attempt to ensure that sampling continued from the same angle in the phase rotation to ensure continuous sampling (in terms of electrical angle) when a break for bulk movement of stored data to external memory was required. This helps to avoid parts of the current waveform being over-represented in the captured data which, if a ANN were to trained using the captured data, could lead to the ANN being over-trained to the more frequently sampled sections of the current waveform. The encoder signals were already present in the DSP/FPGA as pulses from the encoder and were simply directed out of the Actel FPGA.

6.4.1.6 V/F Operation Handshaking Signals

Ideally training data for the ANN would be captured with the machine under open loop V/F operation so that at no point would a mechanical encoder ever be required. This facility was built into the original design to allow the FPGA to request V/F operation of the machine when collecting training data. Following a request, a corresponding acknowledgement of the request (once

V/F operation was enabled) would be sent from the Actel FPGA to the Altera FPGA. This then tells the Altera FPGA that it can begin sampling.

6.5 Implementation of the Proposed Technique in Hardware

6.5.1 Introduction

The proposed technique required that a number of demanding hardware design specifications be met including a very high ADC conversion rate on at least three incoming channels (to measure the phase current transients), large amounts of storage space for bulk recording of training data, I/O for communication with the existing control platform and a DAC operating at a rate fast enough to output the results. The desire to buy an off the shelf platform in order to reduce development time and ensure correct operation (particularly with regard to the high frequency circuitry design) restricted the number of available options. The high sample rate of the ADCs meant that an FPGA based solution for that part of the system was preferable. This directed the selection to either platforms featuring both an FPGA and a DSP or a solely FPGA based solution. Another consideration was the cost of the development boards with a number of the boards being out of budget and FPGA only platforms being generally cheaper than platforms featuring both a DSP and an FPGA.

6.5.2 FPGA Platform

The chosen platform was the Terasic DE3 development board which features an Altera Stratix III FPGA. The DE3 offers large flexibility with the facility to accept expansion boards via 4 HSTC (High-Speed Terasic Connector) connectors and 2 GPIO (General Purpose Input-Output) connectors, allowing customisation of the specification of the development board. The board also features four slide switches, 8 DIP switches and 4 push button switches. These were used to allow the user to configure the setup and mode of operation of the design while 8 RGB LEDs and a 7-segment display were used to indicate the state of operation. Figure 6.3 shows a front view of the DE3 board with key hardware features highlighted [108].

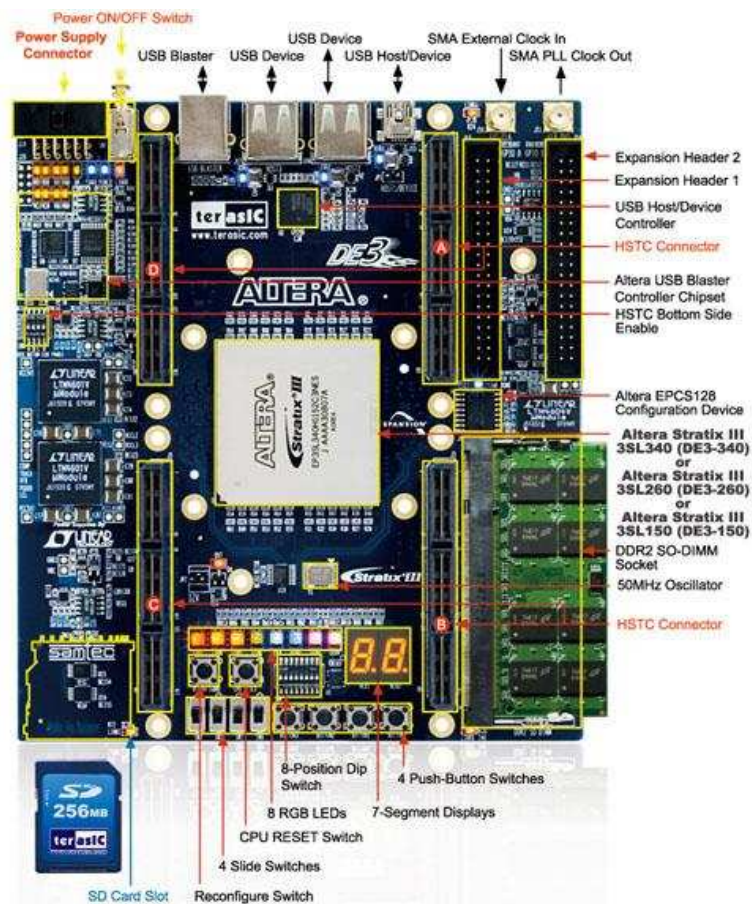


Figure 6.3 Front view of the Terasic DE3 board with key hardware features highlighted. Image courtesy of Terasic [108]

Being a general development board (albeit one fitted with a highly capable FPGA) this was comparatively cheaper to buy when compared with the specialist solutions. The expansion boards that would perform the high speed ADC and DAC were also reasonably priced. Other factors that influenced the decision were:

- Confidence that the entire design could be realised on an FPGA
- Previous experience coding VHDL
- Design confined to a single device.
- Development board offered numerous methods of data storage (DDR RAM, SD card, on-board memory and USB interface that could be used to transmit to a PC for storage) which would be required for bulk storing training data for the ANN.
- Numerous I/O
- Potential for parallel processing to speed up calculations and general operation.

6.5.3 Signal Measurement and High Speed Data Acquisition

The Altera DE3 FPGA development board required additional expansion boards to provide high speed ADC and DAC capability. The Terasic AD/DA board, shown in Figure 6.4 [109], is ideal for this application as the board provides two 14 bit 65MSPS ADC channels and two 125MSPS DAC channels. The DE3 board could accept multiple expansion boards and so two AD/DA boards were installed to provide the necessary number of high speed ADC inputs and DAC outputs.

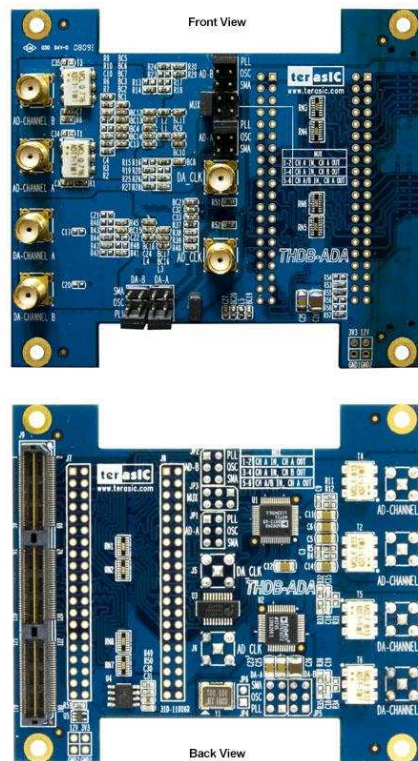


Figure 6.4 Front and Back view of the Terasic AD/DA board. Image courtesy of Terasic [109]

One issue that was identified with the AD/DA boards was that they were fitted with back to back transformers (the back to back configuration is a technique used in RF design to minimise the mismatch in parasitic capacitance of the transformer windings [110]) at the inputs to provide superior high frequency performance and common mode rejection through single-ended to differential signal conversion [111]. However they also acted as a filter on the incoming signal. In the case of the ADT1-1WT transformers used on the boards there was a 0.4MHz cut-off frequency [112] which would remove the low frequency current gradients that were of interest from the sampled current waveform.

With the issue identified the simplest solution appeared to be to remove the transformers which would allow the ADC to operate with a single ended input. However this could lead to poor performance as there is a loss in

common mode rejection performance when compared to using a differential input. The datasheet for the ADC instead recommended the use of a high speed op-amp based ADC driver. The op-amp based ADC driver uses an AD8138 differential op-amp and is illustrated in Figure 6.5 [111].

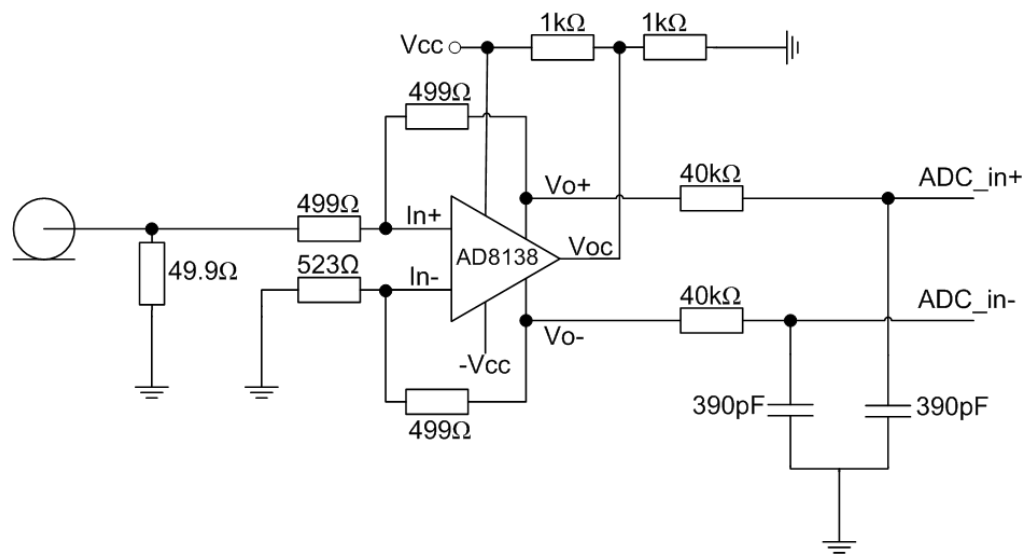


Figure 6.5 The AD8138 produces a differential output from a single ended input centred on the mid-point of the supply voltage (V_{oc})

The op-amp based solution would still be capable of operation in the low MHz range due to the use of high speed op-amps and would also offer good common mode rejection performance. The proposed use of an op-amp ADC driver meant that an interfacing PCB would be required. Similarly it was desired to output DC to low MHz signals on the DAC channels. These channels were also fitted with ADT1-1WT transformers and thus suffered from the same problem of filtering out key data. These transformers were also replaced with op-amps to give differential to single ended conversion at the outputs. The additional PCB was designed “in house” at the University of Nottingham to operate at low MHz frequencies. The board is shown in Figure 6.6. Care was taken with the layout, the impedance of tracks and the components used so as not to affect the incoming high frequency signals. The

supply voltage came from a linear voltage regulator and featured parallel 100nf and 10 μ f decoupling capacitors at all points of connection with ICs.



Front view

Rear view

Figure 6.6 ADC Interface board designed “in house” at the University of Nottingham. The board uses high speed op-amps to provide single-ended to differential conversion at the input and vice-versa at the output

6.5.4 Current Measurement

The sampled current data came from a custom designed current sensing board shown in Figure 6.7. This contained three current sensors whose outputs were scaled to give a 1V output at 10A (approximately 1.3 times the rated RMS current of the permanent magnet machine) to satisfy the input requirements of the ADC’s (± 1 V max). As with the ADC interfacing boards the supply voltages came from linear voltage regulators. Decoupling capacitors were deployed close to the Vcc pins of all devices on the board.

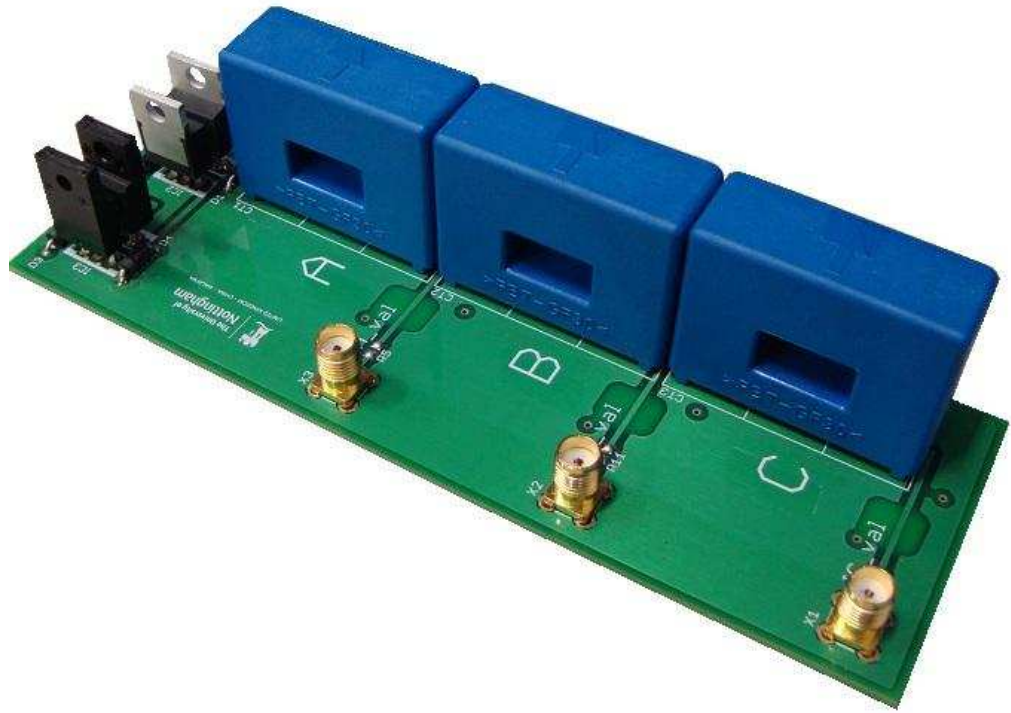


Figure 6.7 Current Sensing Board designed to measure and scale the three phase motor currents

The current sensing board and ADC interface board were designed to be able to transmit the current measurements either as a current (with a burden resistor on the receiving end) or as a voltage with the burden resistor at the transmission end. For voltage transmission, provisions were made to allow matched impedances to be used, preventing reflections in the transmission line.

6.5.5 Justification of the Use of Low Bandwidth Current Sensors

Despite the high frequency content of the current transients, normal low bandwidth industrial current sensors were used to capture the responses. The current sensors used were standard off the shelf LEM LA 25-P closed

loop Hall Effect current sensors. This family of transducers have a standardised footprint meaning that the board could be used to measure currents of up to 100A by selecting the appropriate transducer. The sensors themselves have a maximum rated bandwidth of 200 kHz [113]. Figure 6.8 illustrates the working principle of the LEM closed loop hall effect current sensor which helps to give an understanding of where the bandwidth limits arise.

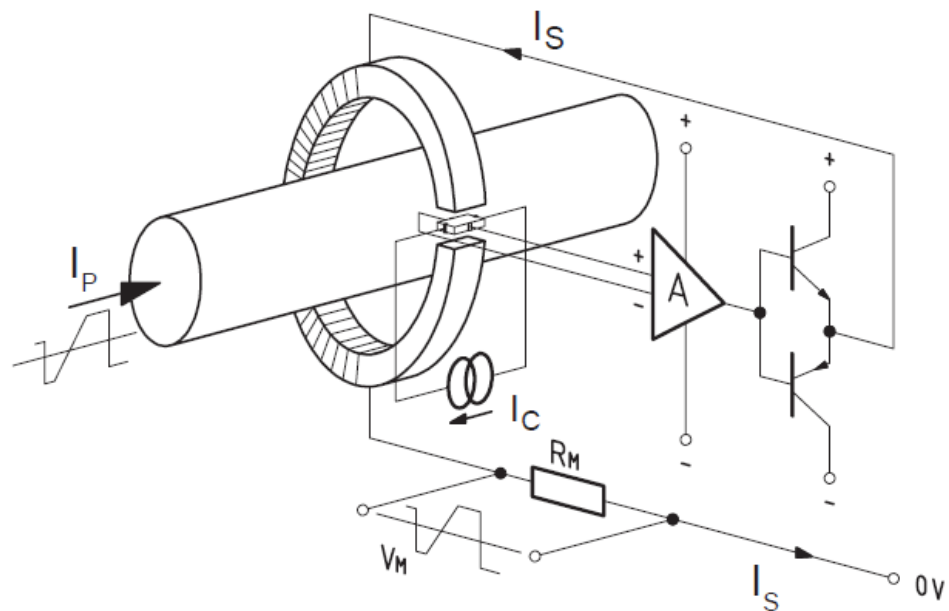


Figure 6.8 Working principle of the LEM closed loop hall effect current sensor. Image courtesy of LEM [114]

The bandwidth limitation arises from two sources; one is due to the internal circuitry of the sensor. At low frequencies the Hall generator principle is used. An amplifier, A in Figure 6.8, amplifies the measured signal due to the primary current, I_p in Figure 6.8 – the current that is being measured. This amplified signal is then used to drive a push pull driver that provides a current through a secondary coil, I_s in Figure 6.8. The secondary coil current is measured at the output of the sensor using a burden resistor. The secondary coil has a large number of turns such that the small secondary current cancels

the field generated by the primary current that is being measured by the sensor [114]. The amplification circuitry sets a relatively low frequency limit and is responsible for measuring DC and low frequency AC currents. This however is not the bandwidth limit of the sensor as at higher frequencies the secondary coil acts as a current transformer [114]. The coil has a high frequency cut-off associated due to the coils leakage inductance and stray capacitance [115] which determines the upper frequency limitation of the sensor. Combining two different current measurement techniques in this way allows a wide bandwidth sensor to be produced with DC capability. The resulting bode plot for the sensor is illustrated in Figure 6.9 [114].

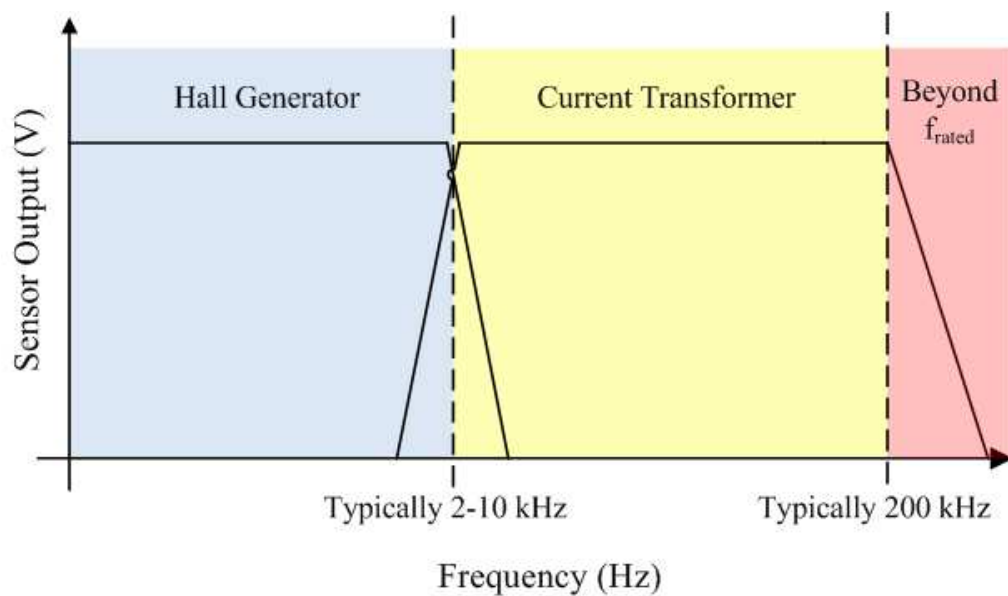


Figure 6.9 LEM current sensor bode plot. Image adapted from [114]

Measurement beyond the upper frequency cut-off is possible but measurements will no longer be made in the flat-gain region (and hence the measured values will not be accurate). Also, operation at high frequency is undesirable as core heating occurs due to eddy current and hysteresis losses [114]. In this research the high frequency signals to be measured are very short in duration meaning that the losses incurred and the subsequent heating are acceptable.

Measurement outside of the flat gain region is also acceptable in this research since it is the shape of the response that is of interest and although not accurate in terms of amplitude or frequency, the current measurements at high frequency are repeatable. This allows a low cost current sensor found in normal commercial drives to be used in a specialist application for both current measurement (for classical dq control) and also derivative estimation. This is beneficial compared to traditional sensorless techniques which require separate special di/dt sensors.

Comparing the measured response from the low cost current sensors (LEM LA 25-P) to one measured using a Lecroy CP150 (10MHz bandwidth) in Figure 6.10, it is clear from the response that the LEM sensor is able to capture a reasonable response in the high frequency range. There is a small difference in the amplitude of the measured currents in Figure 6.10 due to the scaling applied to the LEM sensor measurement.

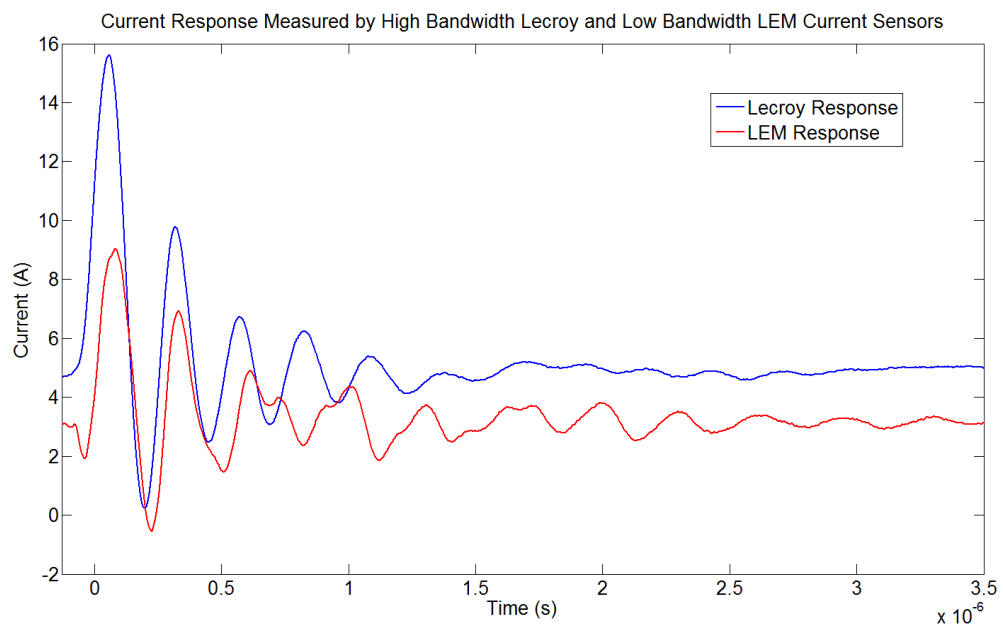


Figure 6.10 (a) Time domain, both sensors

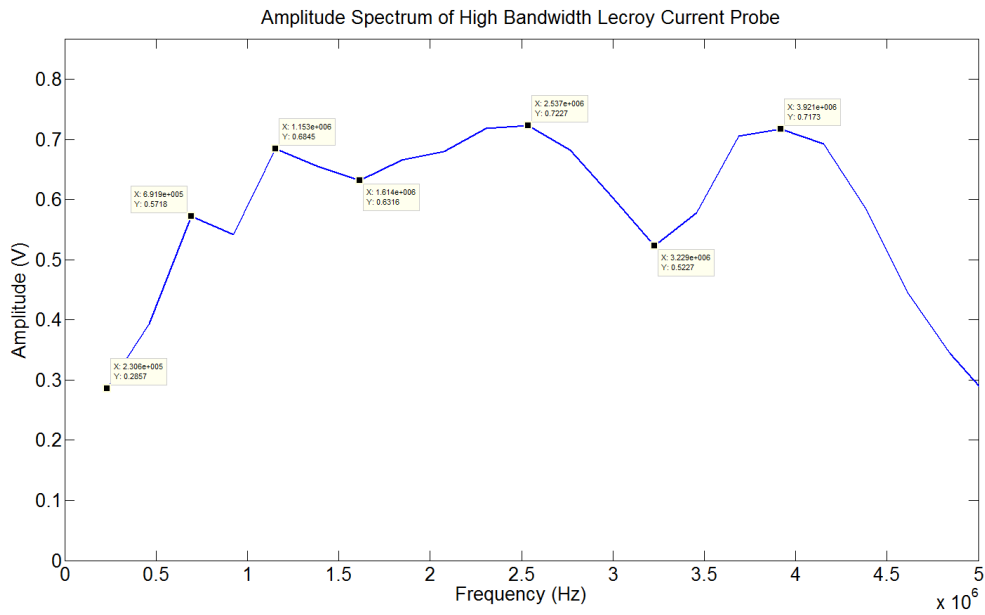


Figure 6.10 (b) High bandwidth Lecroy probe

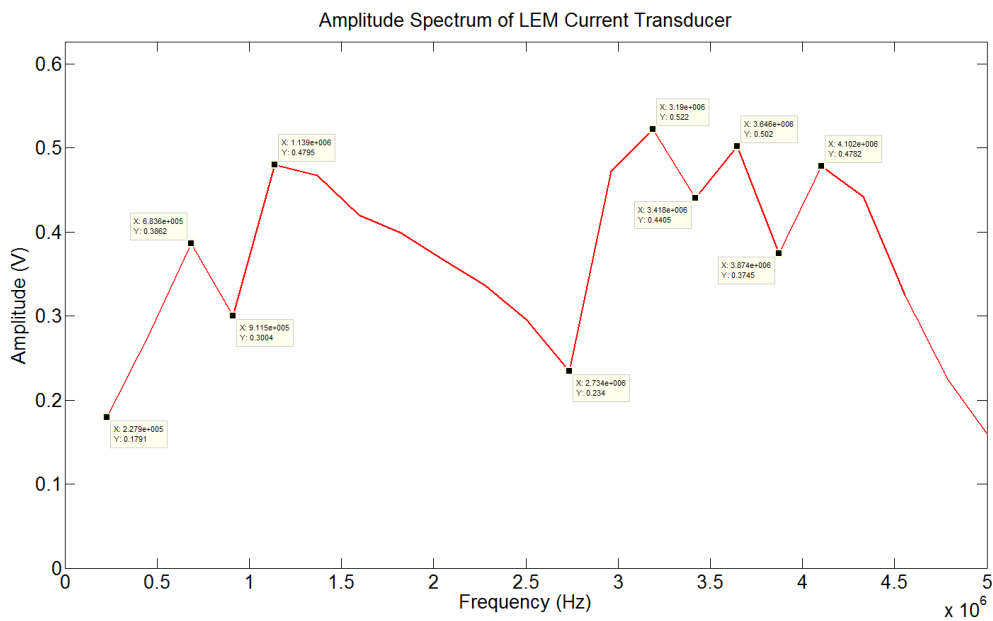


Figure 6.10 (c) Low bandwidth LEM sensor

Figure 6.10 Lecroy Vs LEM current sensors. (a) shows the time domain response captured by the sensors while (b) and (c) show the frequency domain responses of the Lecroy and LEM sensors respectively

6.6 FPGA Design

6.6.1 Introduction

The design of the proposed system was realised using behavioural VHDL and was implemented so that the top level design (named DE3) contained a state-machine that controlled overall operation. Various components were declared in the top level design, each with a specific function in the overall design. Figure 6.11 attempts to illustrate the general structure of the top level design. After a reset the top level state machine would stay in an “Idle” state and wait for a stimulus either from a user input or from a trigger signal. On receiving a trigger signal the top level design would start the ADC controller to begin sampling the current. All components in the top level design had “busy” flag outputs. Whenever a component was initiated by the top level state machine its busy flag would be set to 0 while it performed its function, this temporarily disabled the top level state machine. On completing its task the component would set its busy flag high again and the top level design would be allowed to continue. Following the ADC controller was the ANN controller which arranged the sampled data for the ANN's after which the ANN's were run. After a successful ANN run the di/dt estimates were stored in a block of memory which was configured such that a snapshot of its contents could be taken during real time operation and subsequently processed offline.

Another state machine in the top level running in parallel with the main state machine took the outputs of the design and scaled them appropriately to allow di/dt estimates to be viewed in real time and compared to those measured from a Rogowski coil. The functionality of the main components in the design will now be described in more detail.

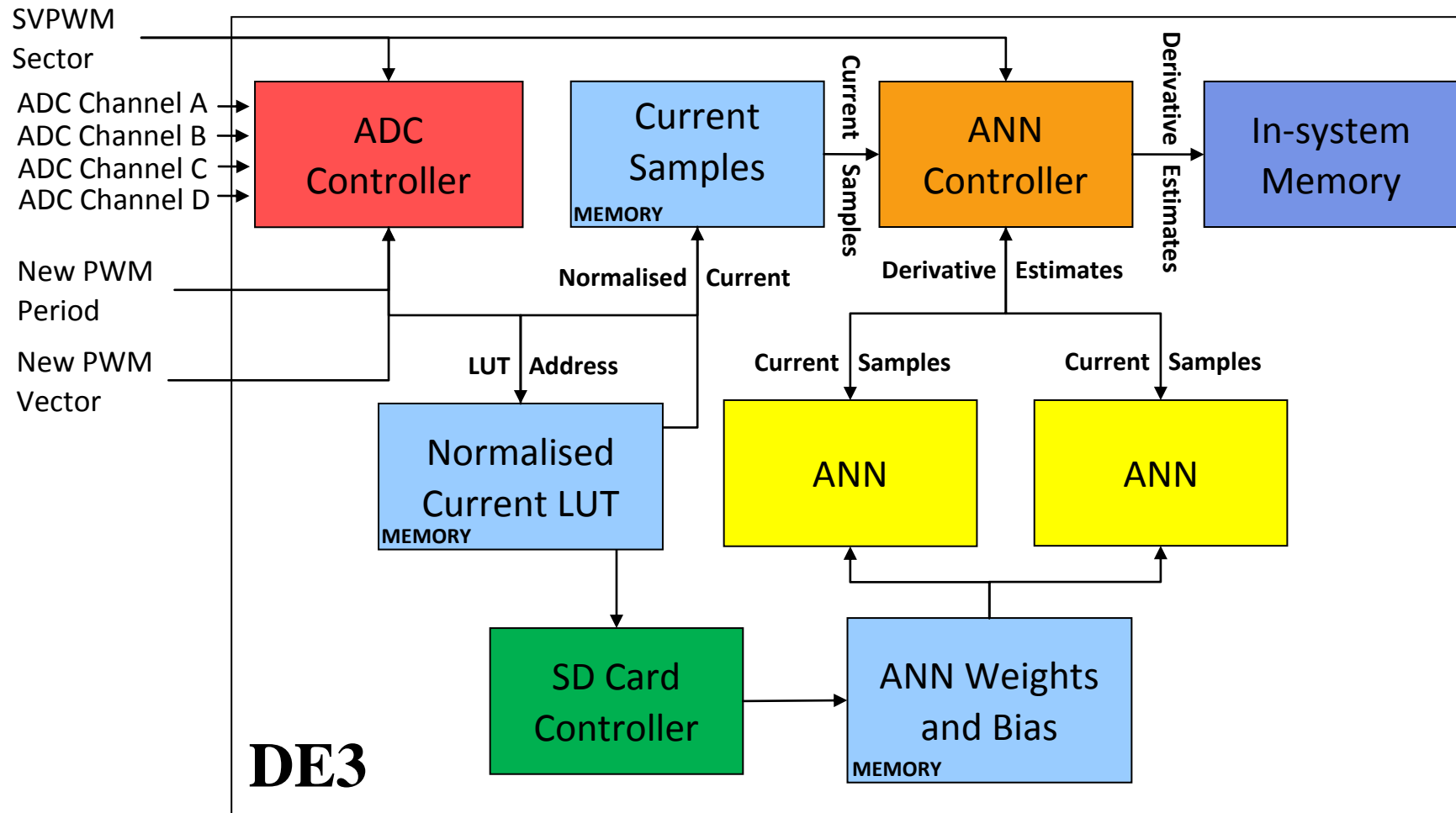


Figure 6.11 An illustrative diagram showing how the main components are connected within the FPGA design

6.6.2 Linear Feedback Shift Register (LFSR)

The purpose of the LFSR is to generate a “random” set of data that can be used as the weight and bias values of the ANN during initialisation.

Initialising the ANN weights and biases with random values has been found to lead to reduced training times and increased accuracy [116].

When the training of the ANN is performed in Matlab the LFSR becomes redundant since the ANN configuration data is read from an SD card and the initial contents do not matter. It was however useful during simulation and testing to have different values stored in the ANN configuration memory as this made it easy to establish if the correct ANN was being used (Without the LFSR the ANN configuration memory would all be initialised to 0's).

6.6.3 ADC Sampling Controller

A controller was required to manage the data acquisition and storage of the data from the ADC expansion boards. Once a trigger or new period signal (aligned with the PWM edges in the first half of the PWM period) had been detected the 7 clock cycle latency of the ADCs had to be observed and then the incoming data could be stored in memory. The ADC's were designed for 65MSPS operation. With the FPGA base clock running at 50MHz it was necessary to use a PLL generated clock to clock the ADC's. The closest achievable clock frequency was 62.5MHz which resulted in samples being taken at 16ns intervals. This meant that 64 samples represented 1.024 μ s while 128 samples represented 2.048 μ s. The use of numbers divisible by 8 for sample window lengths simplified the SD card read/write processes when collecting training data as the SD card stores data in 512B blocks. Sample windows that are multiples of 8 make it easier to collect an integer number of samples that can be stored as an integer number of blocks on the SD card.

Following conversion, the incoming 14 bit signals from the ADCs to the FPGA were in the range 0-16383. The desired amplitude of the measured analogue signal was to be normalised in the range ± 1 before being supplied to the ANN. In order for the incoming sample data to represent a normalised floating point current value some scaling was required. Instead of applying a time intensive offset subtraction and scaling multiplication to every incoming sample, a block of ROM memory was used as a lookup table. The lookup table used 14 bit addressing with the first address containing a value of -1 and the last address containing a value of +1 and every value in between coming from interpolation. The incoming 14 bit data was then used as an address for the lookup table. The output of the lookup table was stored in the sample memory. For full three phase sensorless mode the phases were sampled according to the SVPWM sector of operation and whether it was the first active vector, second active vector or null vector. Figure 6.12 illustrates the operation of the ADC controller when in “Run” mode.

When in train mode the ADC controller collected transients for every trigger signal seen until 100 transients have been captured. This number of transients comes as close as possible to using all of the sample memory assigned in the FPGA while still representing an integer number of memory blocks (500) on the SD card (where the bulk training data is stored). At this point the ADC sampling was paused, and the phase angle from the encoder at the point where sampling ceased was recorded. The data held in the FPGA’s sample memory is then written to the SD card and following a successful SD card write the ADC controller is allowed to continue sampling. The controller waits until the angle (from the encoder) reaches the same value as the point where it stopped previously before continuing. This ensures that sample data is collected from all parts of the reference voltage vector rotation equally. Figure 6.13 illustrates the operation of the ADC controller when in “Train” mode.

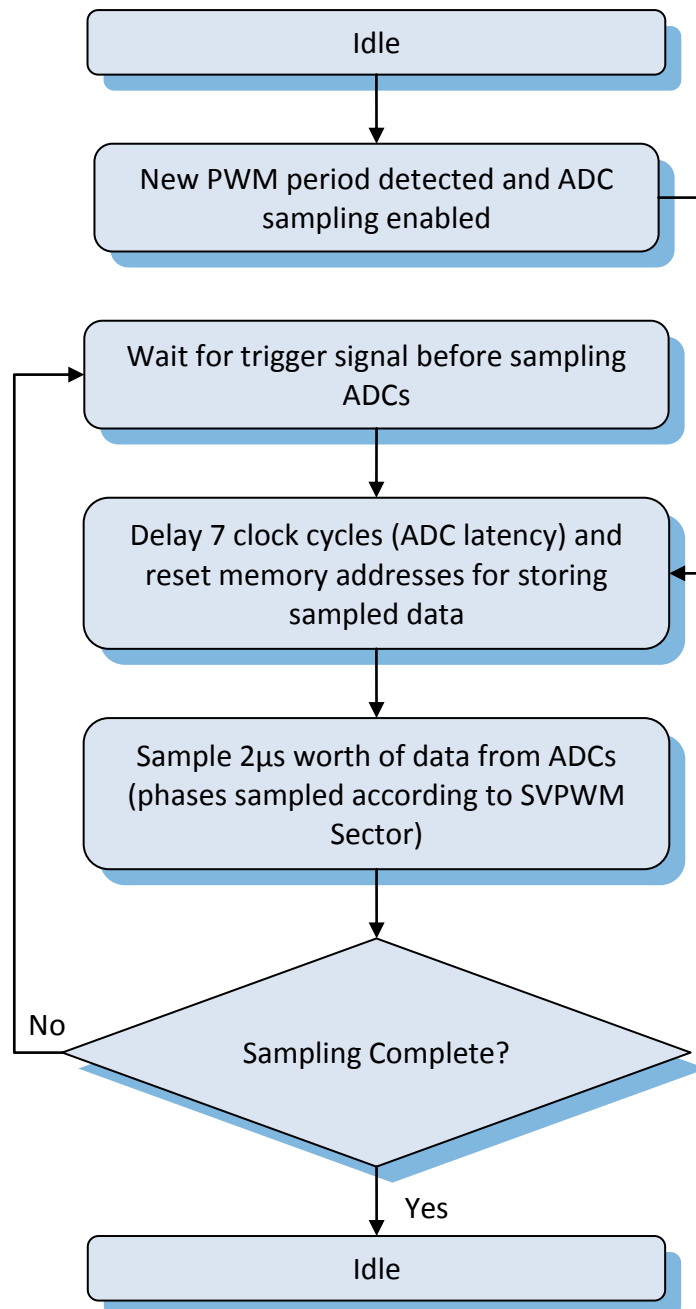


Figure 6.12 ADC Controller operational flow diagram when in “Run” mode

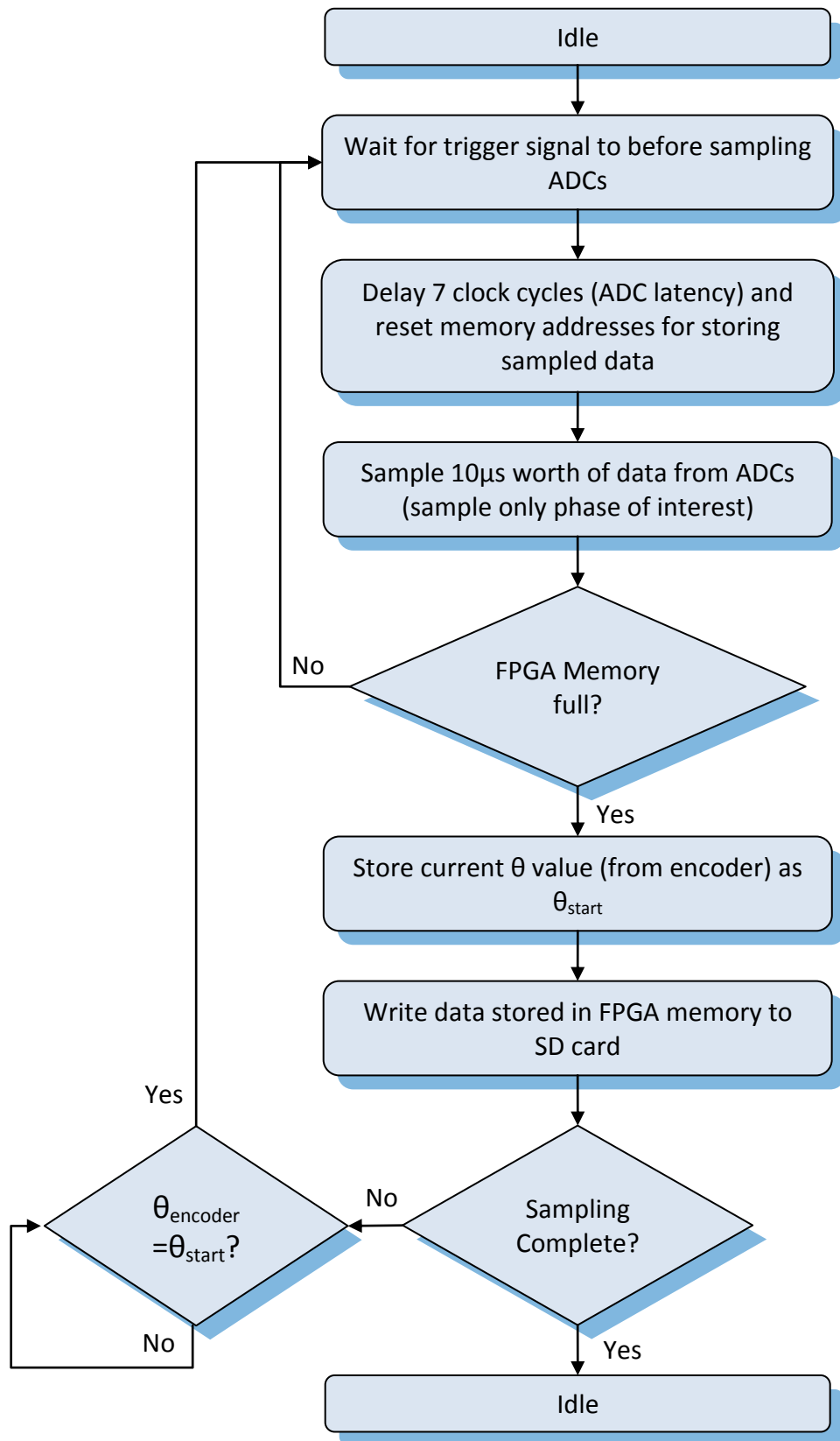


Figure 6.13 ADC Controller operational flow diagram when in "Train" mode

6.6.4 Least Squares Curve Fit Calculator

Early designs featured a least squares fitting component which would, from collected transient current data, produce target derivative estimates that could be used to train the neural network online. This component was later discarded as there were some floating point function requirements that were specific to this component, such as comparing two floating point numbers to find the higher value. Also during testing it was found that the time taken for the Least Squares Curve Fit component to find the training data was much longer compared to storing the raw current transient data and processing it offline in Matlab.

The final overall design was critical on certain FPGA resources (namely “DSP blocks” which were heavily used in the implementation of floating point components). Because of the intensive “DSP block” resource usage of this component and the time taken for it to perform its function coupled with the fact that it was in reality redundant due to the network training being performed much more efficiently in Matlab this component was removed to make way for additional components.

6.6.5 ANN Controller

When operating in “Run” mode the ANN controller followed the ADC sampling. This took the current samples stored in memory and arranged them for processing by the ANNs. Once the data was arranged the networks were allowed to run. Following a successful run of the ANNs the results were stored. Because six current derivatives were required for sensorless operation the three ANNs had to be run twice. So immediately following the first run the next set of transient current data was retrieved from memory and arranged for processing by the networks. This process is illustrated in Figure 6.14.

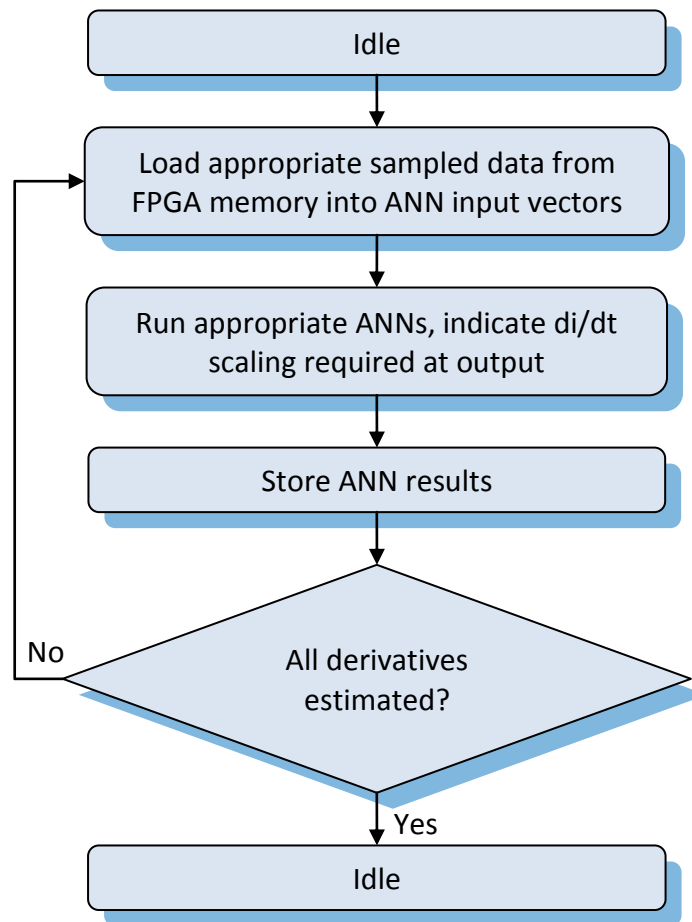


Figure 6.14 ANN controller operational flow diagram

6.6.6 Artificial Neural Network Implementation

The implementation of the ANN on an FPGA was initially based on VHDL code available in the public domain [117]. This code was originally designed to recognise characters which were entered on a seven segment display. There were a number of drivers which led to the decision to make use of this code. The decision had already been made to use an Altera development board for the implementation of the data acquisition and processing system since the complexities of designing hardware with high MHz ADC capability were unfavourable and there was already a suitably high sample rate ADC expansion board available. This combined with a capable

FPGA, in terms of logic resources, provided a good solution. The VHDL code in [117] was designed for use with a lower spec Altera development board and so was already presented in the suitable structure and format. The code included the implementation of an ANN including both normal “run” mode and “train” mode which involved the adjustment of the weights and calculation of the mean squared error during the learning process.

Also ANNs realistically require the use of floating point numbers in order to achieve a reasonable accuracy in the weights, biases and outputs. This had already been taken account of in [117] with the implementation of a floating point arithmetic logic unit (ALU) which made use of Altera’s own Megafunctions to complete floating point arithmetic operations using single precision values. Despite this head start gained by using the code there was still a large amount of work required to adapt the design for this application. The ANN itself required modification to be able to store the weights in the internal memory of the FPGA as opposed to an external SRAM. Also tests conducted in Matlab had found that in this application a `tansig()` transfer function, as shown in Eqn 5.1, was the most suitable, hence this was added. The outputs from the ANN also had to be de-normalised before they could be used as di/dt estimates. The ANN controller required a complete redesign. In the final design the training section and weight and bias section were redundant (since this operation was completed offline in Matlab) and hence removed.

Modifications were also made to reduce the computation time for the ANN. Performing calculations in parallel offered a significant time saving. For example, the hidden layer consisted on 10 neurons. The input to each neuron consisted of the sum of each of the inputs multiplied by the corresponding weights plus a bias value. Having 10 ALUs meant that these calculations could be performed simultaneously for all neurons in the hidden layer, therefore reducing hidden layer calculation time by a factor of 10. Figure 6.15 gives a general overview of the operation of the ANN.

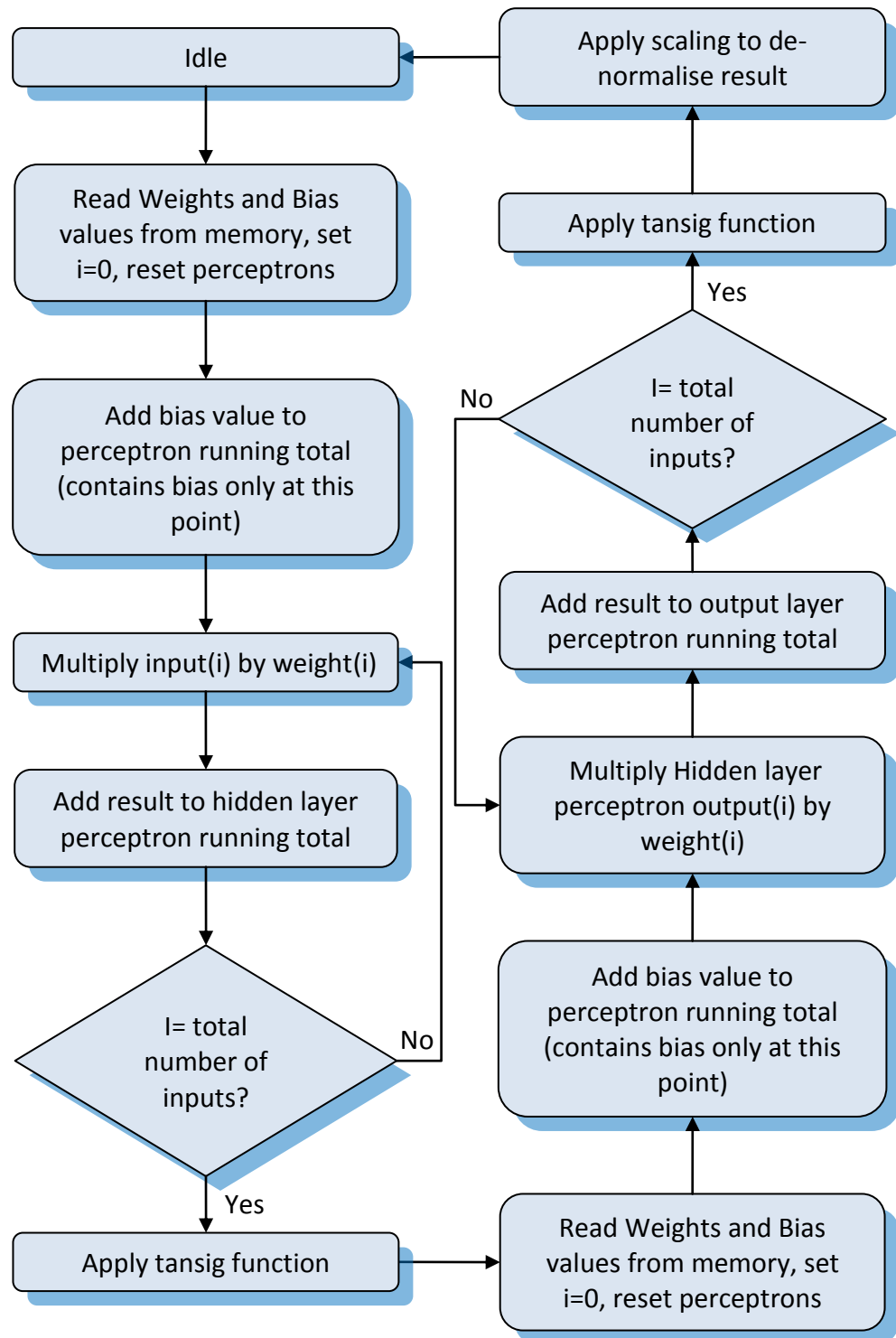


Figure 6.15 Artificial Neural Network operational flow diagram

6.6.7 SD Card Controller

An SD card was used for the bulk storage of transient current data collected for training the ANN. The drivers that led to this decision were comparatively simple implementation, storage space flexibility (various sizes of SD card are available) and the portability offered by SD cards. The SD card could also be used to transfer ANN weight and bias information from a PC (as they were computed in Matlab) although this function was later performed using Altera's "in system memory content editor".

The SD card controller design was initially based on VHDL code available in the public domain [118]. A read process was initiated by a user pressing a button on the user I/O. This initiated the reading of ANN weight and bias values from the SD card which were then stored in a block of memory in the FPGA. Figure 6.17 illustrates the SD card read process.

A "write to SD card" function meant that during the collecting of current transients (for training the ANN), when the on-board FPGA memory was full, the SD card controller could take the memory contents and write them to the SD card. Data lengths were chosen so that sampled current transients could be arranged and stored in integer blocks of memory on the SD card. Each 32 bit single precision value (of a sampled current transient) was broken up into 4 bytes and written to the SD card. This allowed 128 single precision samples to be written to each block of memory on the SD card (512B). 100 sampled transients were written to the SD card in one writing process as this came as close as possible to utilising all of the FPGA's on-board memory with an integer number of transients. An additional feature of the write process took the ANN weight and bias values from FPGA memory and copied them to the SD card. This was added as a validation check. Figure 6.16 provides an overview of the SD card write process.

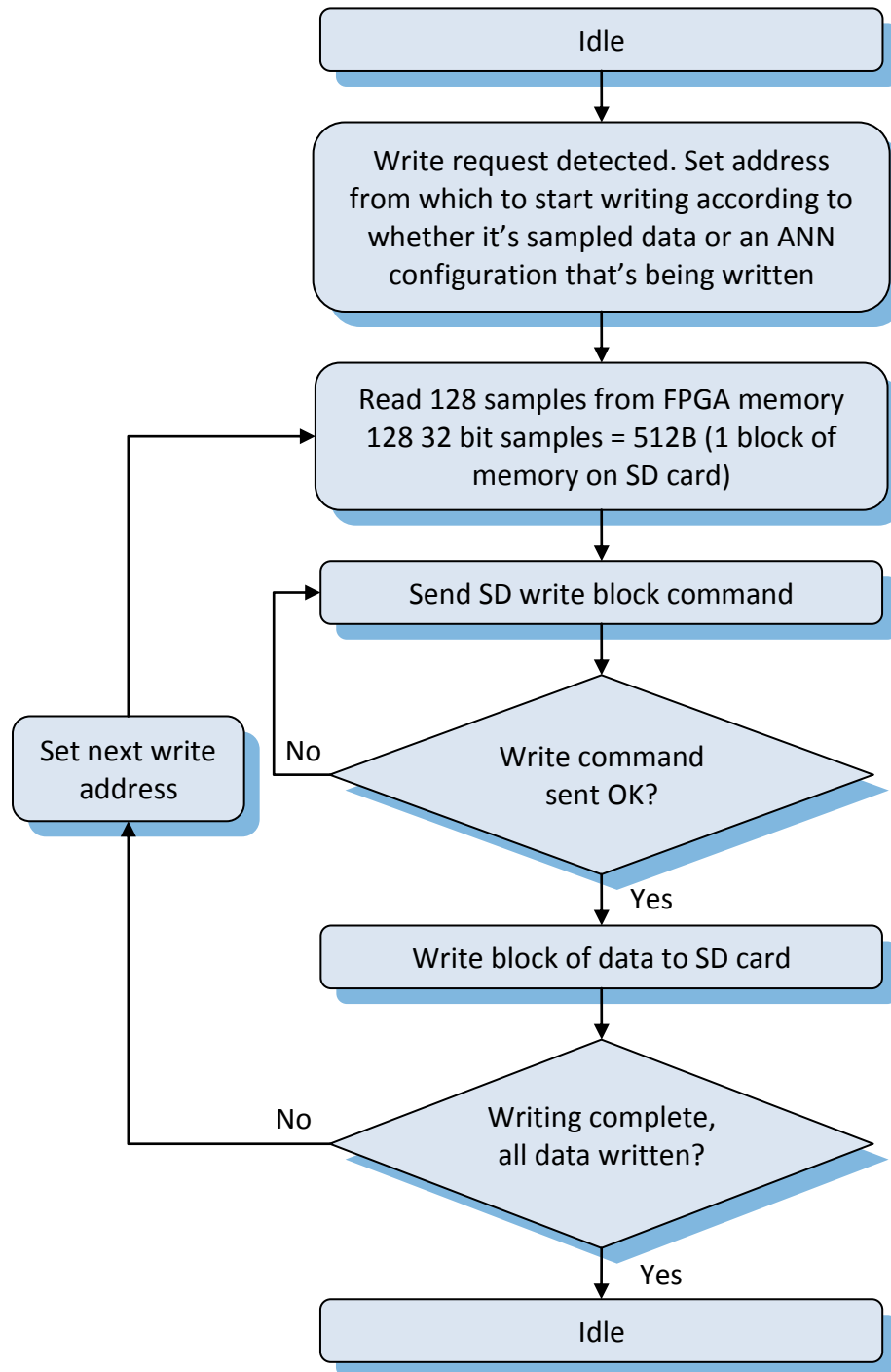


Figure 6.16 SD Card Controller operation flow diagram when writing to the SD card

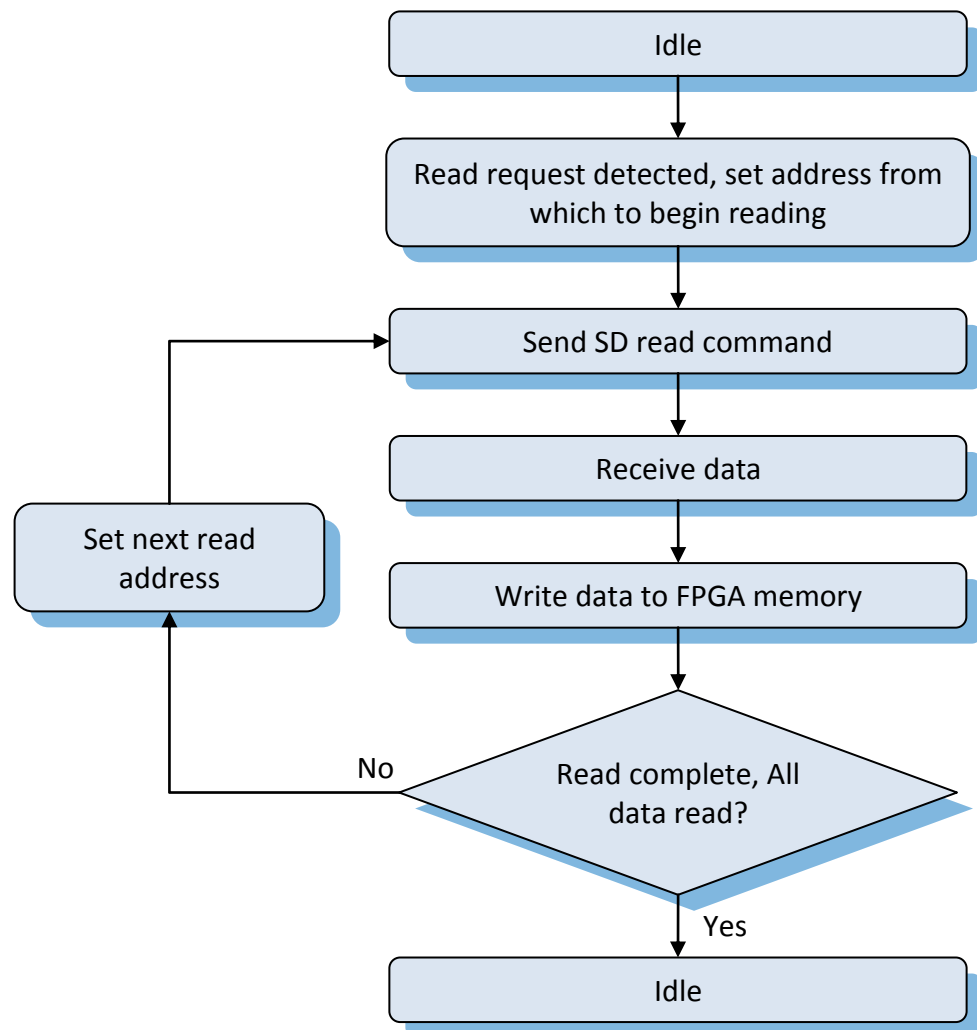


Figure 6.17 SD Card Controller operation flow diagram when reading from the SD card

6.6.8 Position Estimation Based on Derivative Estimates

A basic position estimation component was implemented within the FPGA; this followed the Fundamental PWM implementation procedure detailed in Appendix A. The di/dt estimates were supplied from the ANNs and the position estimator produced a θ estimate. The θ estimate was intended to

give an idea of the raw position estimate yielded by the approach. A simple fixed frequency band pass filter was applied to the $P_{\alpha\beta}$ results to reduce the effects of other saliencies before calculating θ . Figure 6.18 illustrates the operation of the position estimation component.

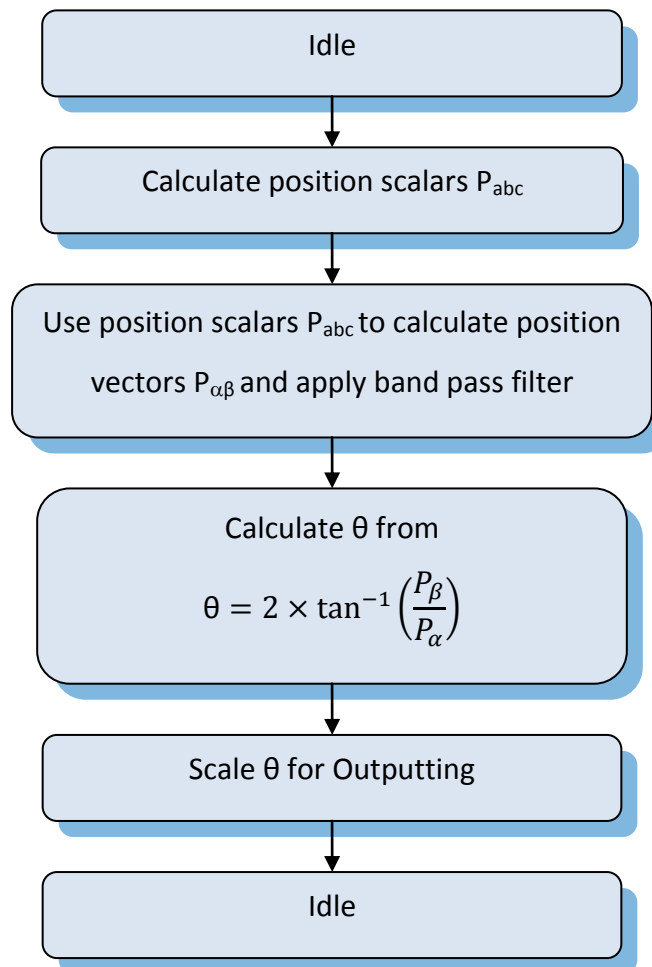


Figure 6.18: Position estimator operational flow diagram

6.6.9 Output State Machine

A state machine was designed to output the derivative results in parallel with the operation of the main state machine. The derivatives were presented as single precision numbers in the range ± 1 . These had to be

converted to 14 bit integer values (0-16383) before they could be output via the DAC for observational purposes. This was achieved by multiplying the single precision values by 50, then adding 50 and multiplying by 163.83. This result was then converted to an integer and presented to the DAC.

6.6.10 Storing Results in the FPGA's On-board Memory for Offline Processing

The design stored the six derivative estimates from the ANNs, six derivative estimates from the two current sample method (if enabled otherwise these memory locations were left blank), the SVPWM sector, Rogowski sensor measurement and Position measurement (from the encoder) in the on-board memory (of the FPGA). This memory was configured to be accessible in real time from a PC through the Altera Quartus development software therefore allowing a snapshot of its contents to be taken. This could then be exported to a file and inspected. A Matlab script was written to extract the file contents allowing the derivative estimates to be post-processed in Matlab which was particularly useful since this provided access to results at all the intermediate stages of the calculations involved in obtaining a position estimate.

6.7 Training of the Neural Network in Matlab

A large number of current transients were captured and stored on the SD card. As explained in (6.6.7), because the SD write process accepts individual bytes the single precision numbers had to be broken down into four

8 bit values. Once all of the training data had been captured the data stored on the SD card could be exported to a PC and used in Matlab to train an ANN. A number of scripts were written to complete this process.

The first script read in four bytes at a time from the SD card, tagged them together and converted the result back to a single precision number. The second script took the transient data (made up of the single precision numbers) and applied a least squares fit to the steady state part of the waveform. This was according to a simple first order equation (as described in Chapter 5) and provided a gradient value for each transient which could be used in to train the ANN. By only using steady state data for the least squares fit any distortion (due to limited sensor bandwidth or non-linear inverter switching) present at the start of the transient had settled and didn't affect the derivative training data.

The next script created a 3 layer feed-forward ANN, specified the number of neurons present in each layer (the configuration described in Chapter 5 was used) and set up the training parameters before initiating the training process.

An additional script (that was used as a validation of the performance of the ANN) ran the trained ANN (supplying it with current transients) and stored the derivative estimate results in an array. These were then presented along with the results of a least squares curve fit applied to the steady state sections of the same transients. The data supplied included all of the captured transients. This included approximately 30000 transients that were not used in the training process to allow the performance of the ANN to be evaluated using data that it had not encountered before. The script also plotted the error between the ANN estimate and least squares result.

A final script extracted the weight and bias values of the ANN in Matlab and arranged them in the order that the ANN on the FPGA was expecting. These values were then stored on an SD card so that they could

easily be transferred into the memory of the Altera FPGA (and subsequently read) without any need to re-arrange the data.

6.8 Conclusions

This chapter has detailed the configuration of the experimental system used to test the real-time performance of the ANN based current derivative estimation technique. The existing permanent magnet motor drive utilised in this work has been described and the modifications required to accommodate the new FPGA platform were explained. The TerasIC DE3 development board and its expansion boards (which provide ADC and DAC capability), that together provide the platform on which the proposed technique was implemented, have been introduced. The use of low bandwidth, low cost industrial current sensors for the capture of high bandwidth signals has been justified. Finally the operation of the components used in the FPGA design to implement the ANN derivative estimation technique has been explained. With the experimental system in place it was possible to test the proposed technique in a real time situation. Chapter 7 will present some of the results from these tests.

Chapter 7

Experimental Results

7.1 Introduction

The design of the experimental system detailed in Chapter 6 allowed the method of using an ANN to estimate current derivatives, as discussed in Chapter 5, to be validated experimentally. This chapter presents experimental results for current derivative estimation by artificial neural networks supplied with $2\mu\text{s}$ of transient data. All of the results presented were captured using the Altera FPGA operating in real time. Initially the performance of the ANN derivative estimator will be examined under long minimum pulse widths ($17\mu\text{s}$) to show that the ANN can be used effectively to estimate the derivative with a small amount of transient data. The effects of speed and load are investigated and the results are compared with those from the two current sample technique (obtained under large pulse widths). Finally the performance of the technique under small minimum pulse widths (where existing methods cannot operate due to the decaying high frequency oscillations) is investigated.

7.2 Single ANN

The first configuration to be tested was the most basic. This configuration consisted of a single ANN which had been trained using current transients captured by the FPGA from one of the motor phases. The derivative estimation performance for the phase that was used to capture the training data (under the same conditions as the training data was captured) was found to be good. However when this ANN configuration was applied to the other two phases the derivative estimation performance was poor under all conditions. Figure 7.1 illustrates this by showing the first active vector derivative estimates for phases A, B and C. The ANN estimates are compared with the results obtained from the two current sample approach. The ANN was trained using data captured from phase A, the machine was operated at 30Hz, 83% load with a minimum pulse width of 17 μ s. This operating point was selected for two reasons: firstly it was a trained operating point of the ANN; secondly, as will be shown later, the technique performs well at higher speed and under high load. Both of these facts combined mean that this operating point is expected to show good performance.

Two factors were thought to be responsible for the inability of a single ANN to work across all phases. The first is the difference in the parasitic impedance network seen at the phase outputs of the drive. This difference could have a large effect on the frequency components contained in the transient response seen by the ANN.

The second factor is due to differences in the data acquisition channels of the FPGA used to sample the current transient. During training only a single channel was used to capture data, but during normal operation separate channels are used for each of the I_{abc} inputs. Any differences in the circuitry of these inputs due to component tolerances or contact quality (which will

influence parasitics) will cause a difference in the measured response which the ANN would be sensitive to.

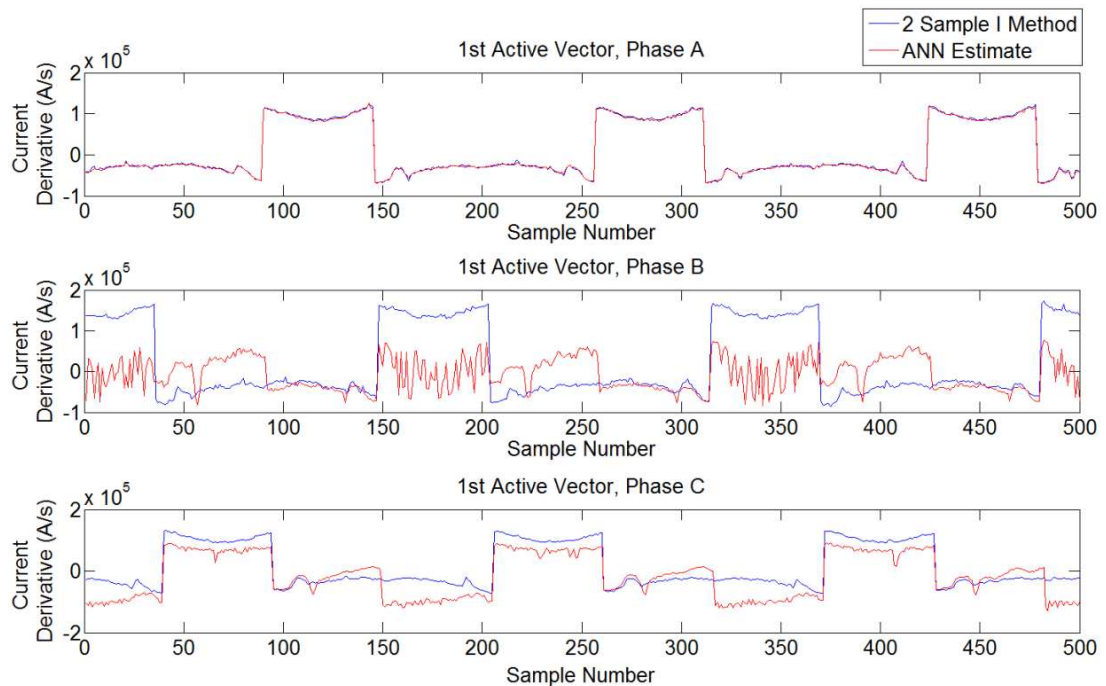


Figure 7.1 ANN estimated first active vector derivatives for each phase when using only one ANN trained with data collected from phase A only. Derivative results obtained from the two current sample method are shown for reference

7.3 Triple ANN

In order to remove the sensitivities described for a single neural network solution a different design was implemented which utilised three different neural networks – each neural network was specific to one phase and data acquisition channel. During training the input channel that would be used under normal operation for a particular phase was used to capture the training data. This meant that any influences of input channel circuitry would be

trained into the ANN and the parasitic network seen during training is exactly the same as the one seen under all normal operating conditions.

When implementing the Fundamental PWM equations (see Table 2.1), despite the reasonable accuracy of the derivative estimates from the ANN, the position vector ($P_{\alpha\beta}$) results were found to have a strong component at f_e and a weak component at $2f_e$ when using derivatives from both the ANN and two current sample methods. Since it is the saturation saliency that is of interest it was expected that the dominant component should be present at $2f_e$. After further investigation it was found that this was due to an assumption which had been made to simplify the implementation. This assumption relied on the shape of the null vectors V_0 and V_7 being the same in a given fundamental period. Assuming these were the same reduced the number of transients that had to be sampled and processed by the ANN from 6 to 5 and reduced the number of ADC sample trigger signals required from 4 to 3. There are some differences between V_0 and V_7 . V_0 is sinusoidal while V_7 has a quasi-square wave profile which means this assumption ($V_0=V_7$) does not hold true and with this not being the case the back-emf was not properly cancelled from the response causing a strong f_e component. With V_0 included in the implementation a strong component was seen at $2f_e$ when operating under the trained condition and the derivative estimate results obtained were similar to those obtained using the two current sample method.

The results for the individual vector derivative estimates were found to be a close match to the actual results obtained from a dedicated Rogowski coil which was used for validation purposes. Figures 7.2 to 7.5 show a representative set of derivative results. The error of the ANN derivative estimates is analysed by comparing it with the derivative results from the two current sample method. Histograms also show the spread of the error amplitude. A Gaussian distribution centred around zero is expected. The two current sample method was chosen as the reference as measurements from the Rogowski coil appeared to be affected by random noise to a greater extent

than the two current sample method. This is likely to be due to the amplification applied to the Rogowski coil measurements which would also amplify noise. The results shown in the Figures 7.2 – 7.5 were obtained with the machine operating at 30Hz under 83% load with a large $17\mu\text{s}$ minimum pulse width, Once again this operating point was chosen as it was one of the operating points used during the training process and the high load, medium speed condition was known to give good performance. The variation in performance away from the trained operating points will be discussed later.

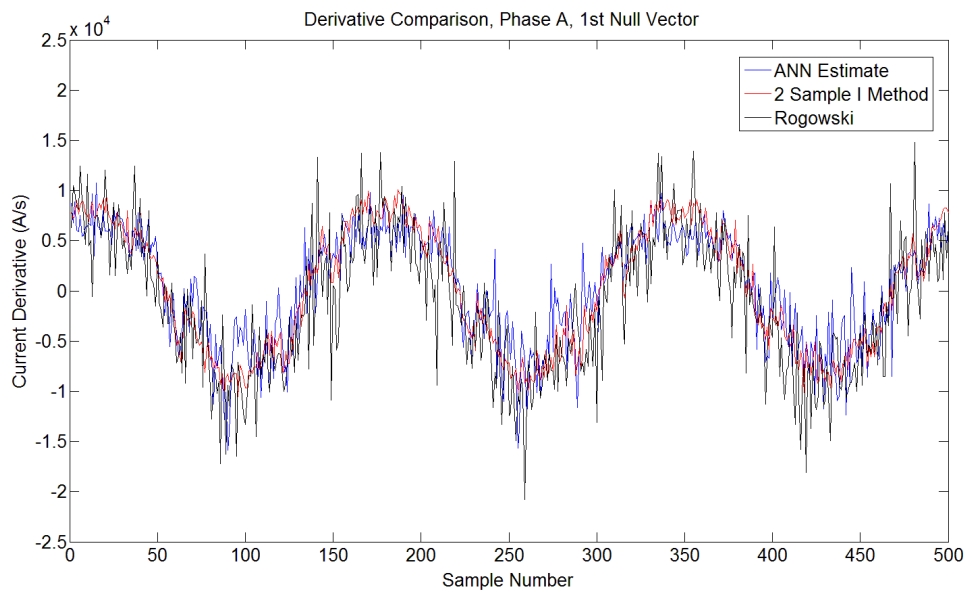


Figure 7.2 (a) First Null Vector

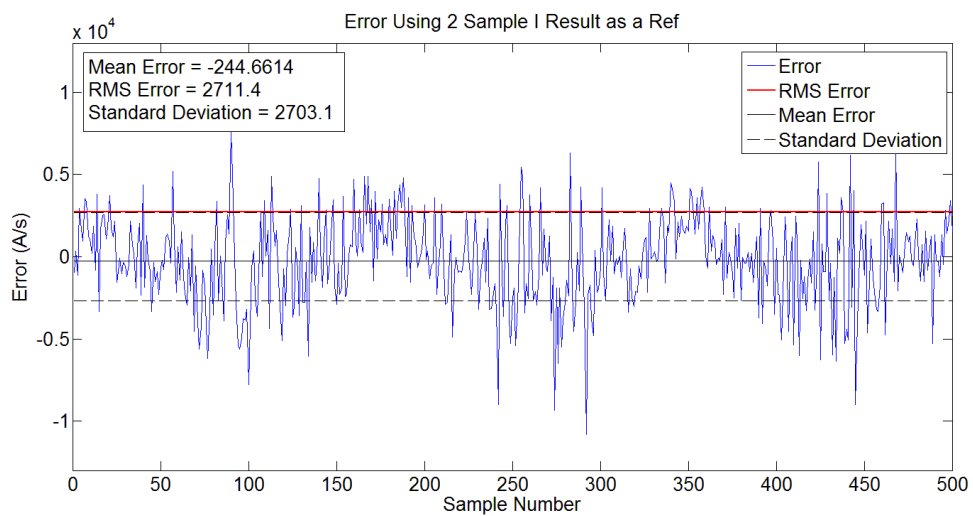


Figure 7.2 (b) Error

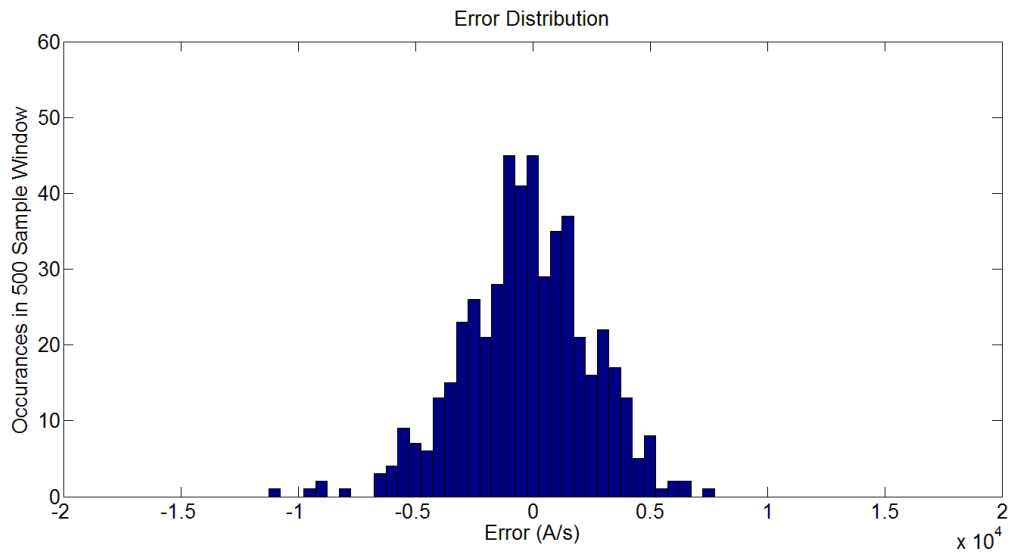


Figure 7.2 (c) Error distribution

Figure 7.2 First null vector estimates of the ANN plotted with measured values from a Rogowski coil and a result obtained from the two current sample method (a). Using the two current sample results as a reference, the error of the ANN estimate is calculated and also shown in (b). The distribution of error amplitude is also shown in (c)

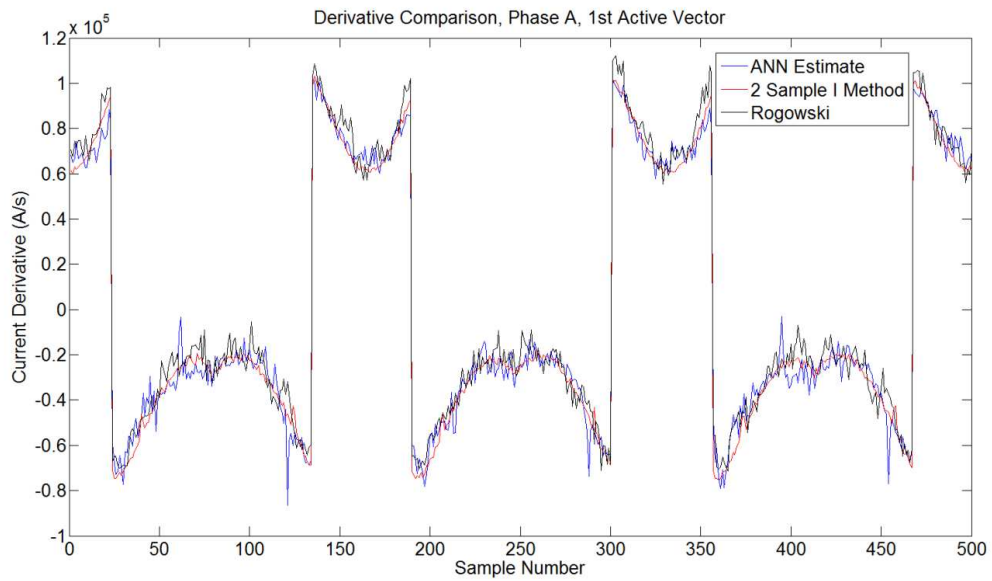


Figure 7.3 (a) First Active Vector

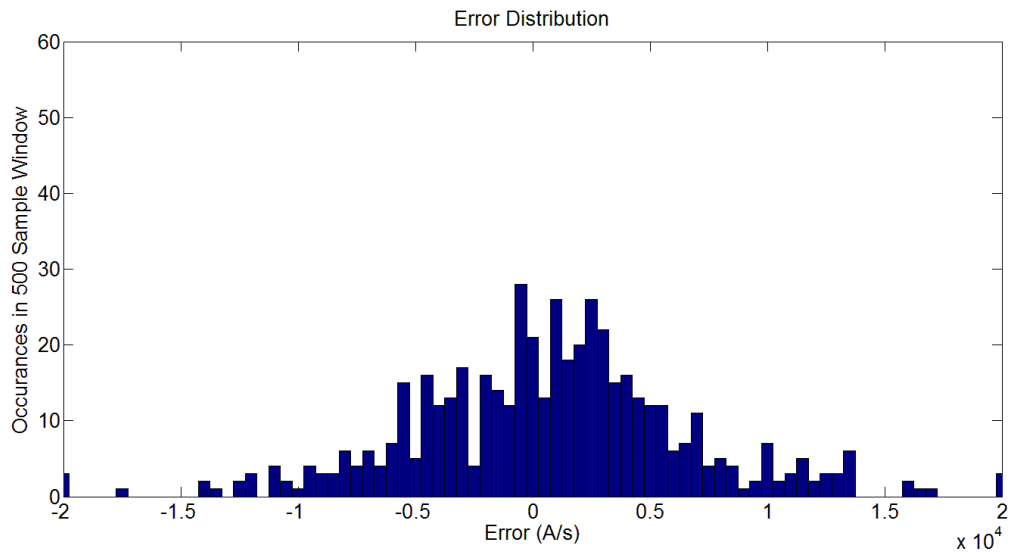
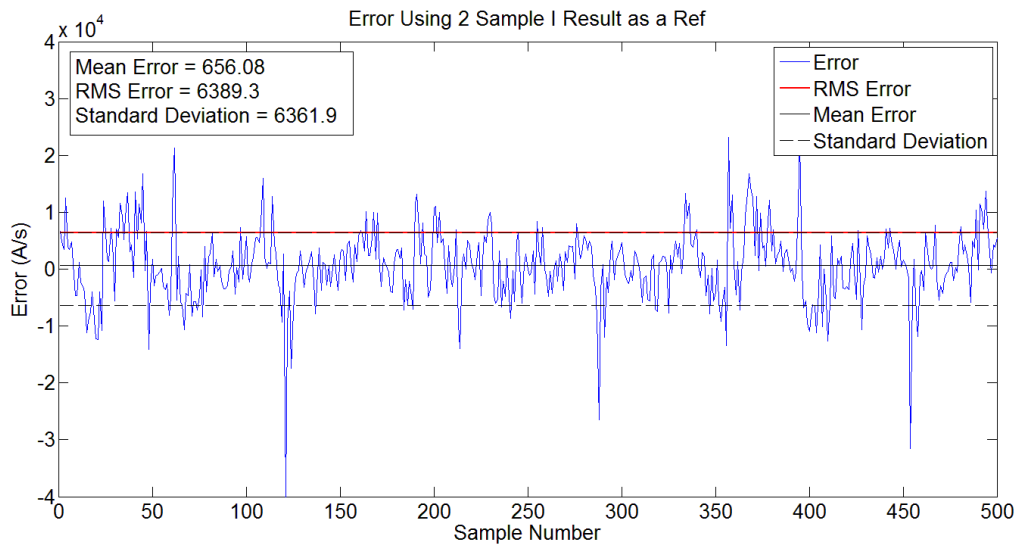


Figure 7.3 First active vector estimates of the ANN plotted with measured values from a Rogowski coil and a result obtained from the two current sample method (a). Using the two current sample results as a reference, the error of the ANN estimate is calculated and also shown in (b). The distribution of error amplitude is also shown in (c)

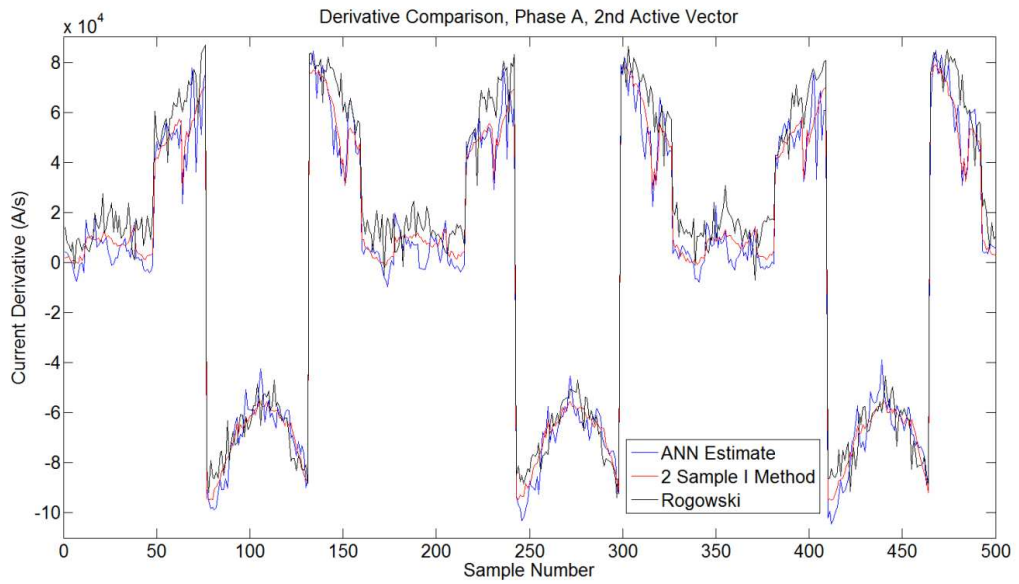


Figure 7.4 (a) Second Active Vector

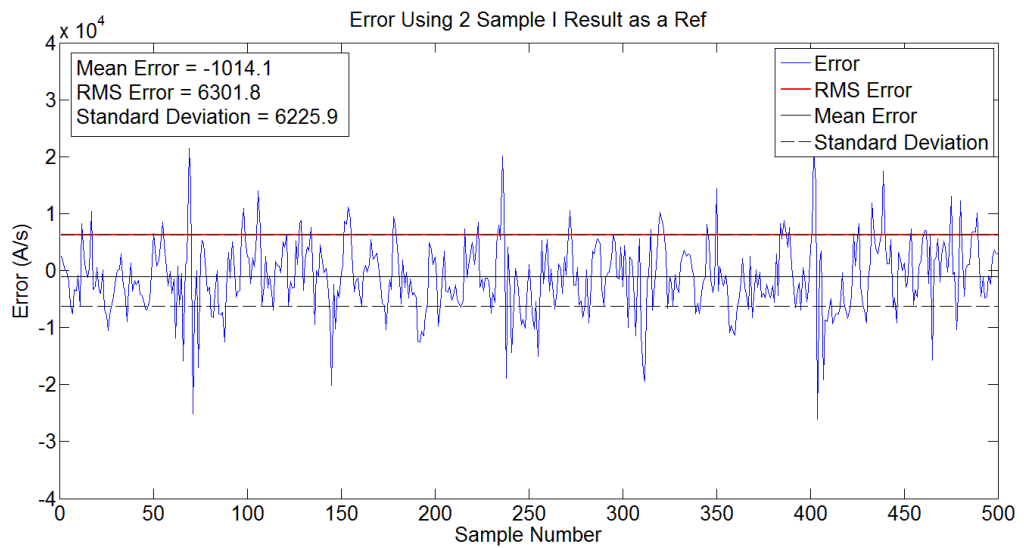


Figure 7.4 (b) Error

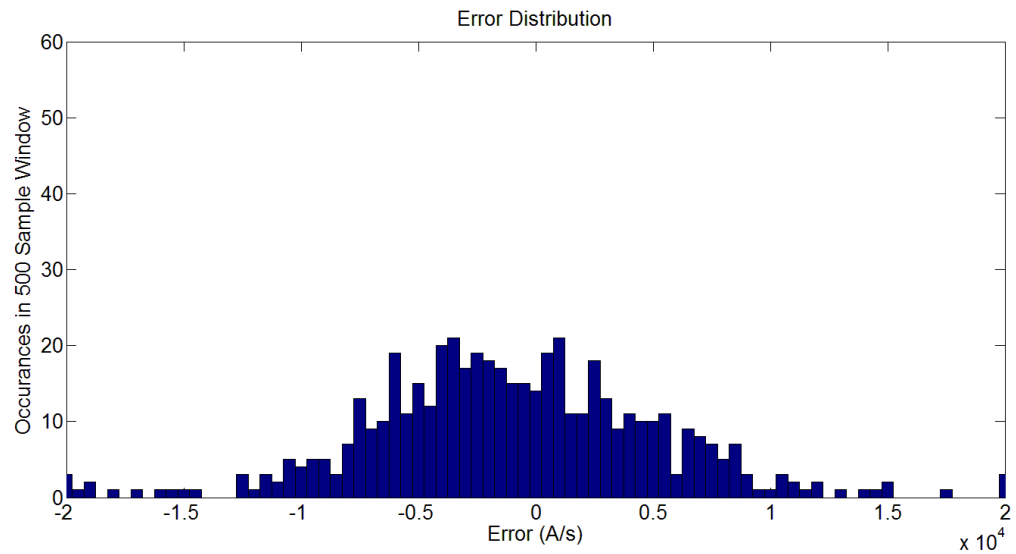


Figure 7.4 (c) Error distribution

Figure 7.4 Second active vector estimates of the ANN plotted with measured values from a Rogowski coil and a result obtained from the two current sample method (a). Using the two current sample results as a reference, the error of the ANN estimate is calculated and also shown in (b). The distribution of error amplitude is also shown in (c)

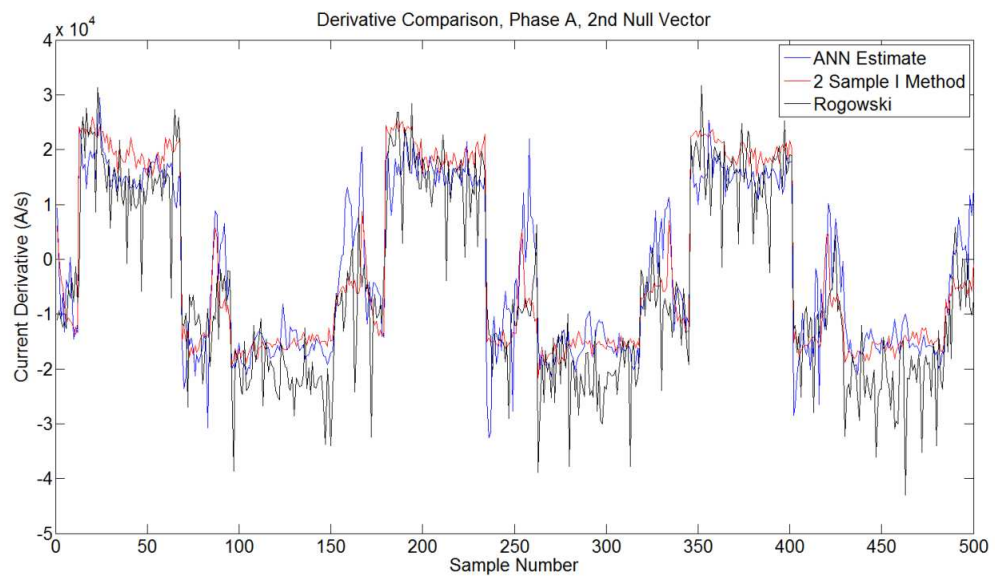


Figure 7.5 (a) Second Null Vector

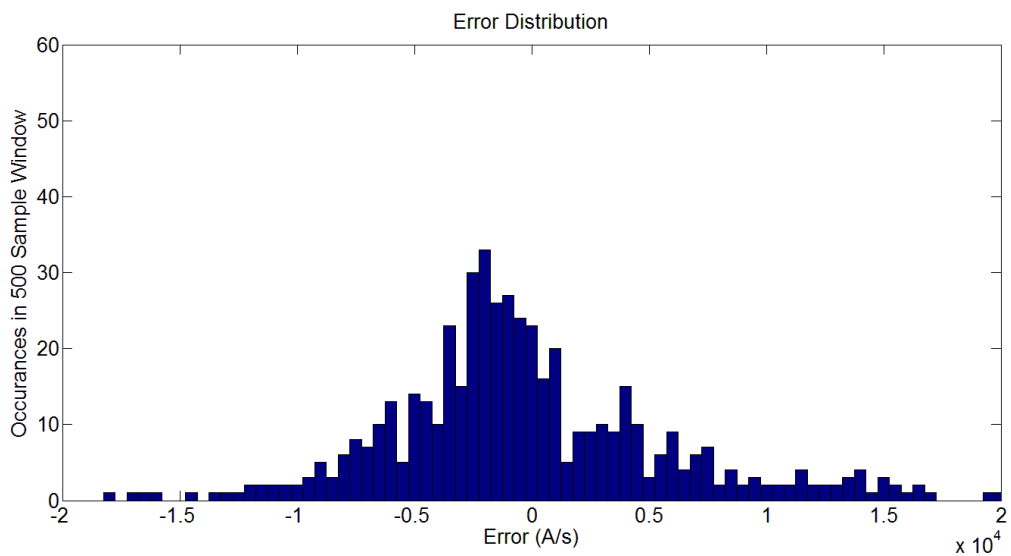
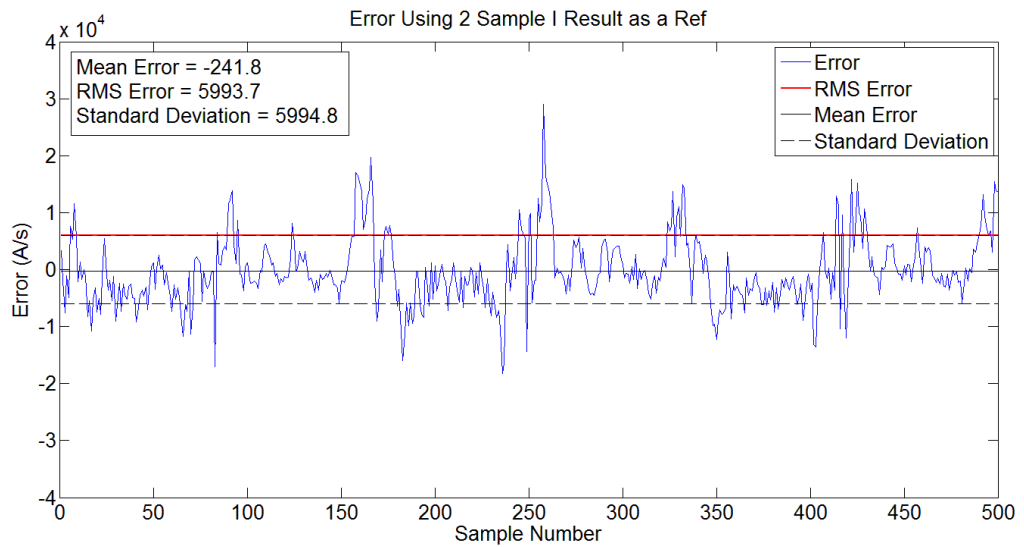


Figure 7.5 Second null vector estimates of the ANN plotted with measured values from a Rogowski coil and a result obtained from the two current sample method (a). Using the two current sample results as a reference, the error of the ANN estimate is calculated and also shown in (b). The distribution of error amplitude is also shown in (c)

The derivative estimates from the ANN shown in Figures 7.2 (a) to 7.5 (a) visually show a good agreement with the results of the Rogowski coil and the two current sample method. Analysis of the error in Figures 7.2 (b) to 7.5 (b) shows that a standard deviation of approximately 6000 A/s was found for the first active and second active vectors. Although this is higher than the simulated results in Chapter 5, this is an acceptable result considering that it is less than the limit of $1 \pm 1.315e^4$ A/s defined in Section 2.6 and the active vectors have a peak amplitude in the region of 100,000 A/s. The result for the second null vector was less accurate. Once again a standard deviation of approximately 6000 A/s was obtained (again less than the limit of $1 \pm 1.315e^4$ A/s defined in Section 2.6) but this vector has a peak amplitude in the region of 40,000 A/s, so the standard deviation as a percentage of the peak expected result is much higher. The results for the first null vector were very good. This could be due to a combination of limited amounts of oscillations in the sampled transients (since there has not been a change in the inverter switching state in the PWM period prior to this point) and the fact that results from this vector would be presented first to the ANN during training so there may be some element of bias towards this vector.

The histograms (Figures 7.2 to 7.5 (c)) show the error distribution for each of the vectors. In each case a Gaussian distribution is seen indicating that there is no bias point where the ANN produces a particularly high non zero error. Also notice that the distribution for the first null vector (Figure 7.2 (c)) is narrow around and centred zero. The distributions for the active vectors (Figures 7.3 and 7.4 (c)) are more broadly spread but similar to each other while the distribution for the second null vector (Figure 7.5 (c)) is wide, in line with observations made previously.

The error between the Rogowski and two current sample method measurements visibly increases in the case of the second active vector (Figure 7.4 (a)) and second null vector (Figure 7.5 (a)) compared to the first null vector (Figure 7.2 (a)) and first active vector cases (Figure 7.3 (a)). This is

thought to be due to decaying transients from the previous vector affecting the measurements even with the large minimum pulse applied ($17\mu\text{s}$).

With the derivatives estimated by the ANN the position vectors could be found. Figures 7.6 (a) shows a typical position vector result for the same conditions as the derivative results above. The results are shown in the frequency domain to allow easy identification of the saliency components contained in the signal. The component of interest in this case lies at 60 Hz ($2f_e$, where $f_e = 30$ Hz). Because of the large minimum pulse width that was applied the two current sample method could also be used to identify the position vector. For validation the position vector obtained from the two current sample method is also shown in Figure 7.6 (b)

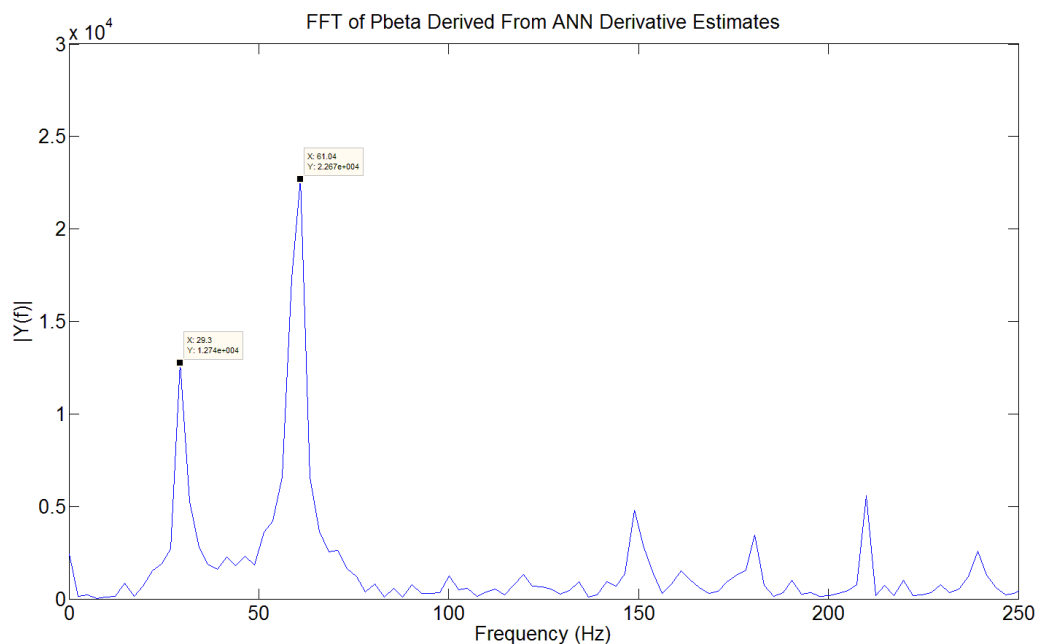


Figure 7.6 (a) ANN

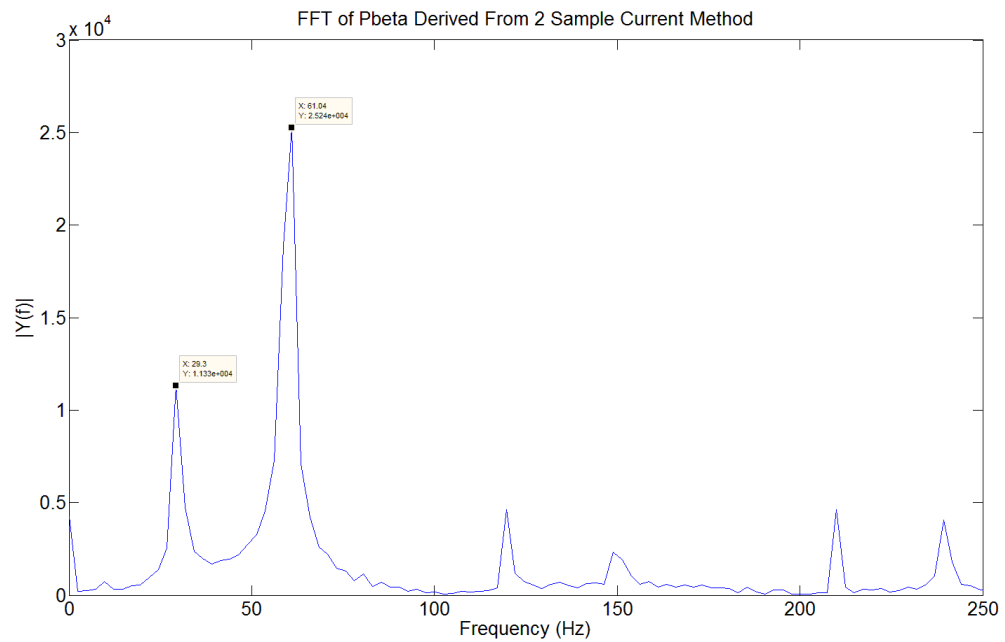


Figure 7.6 (b) Two current sample method

Figure 7.6 the frequency content of the position vectors for both the two current sample method (a) and the ANN method (b) is shown above, these were calculated using the derivatives shown in Figure 7.2 - 7.5 (a)

The results of Figure 7.6 (a) and (b) are similar but the two current sample frequency components have slightly larger amplitudes. It is also clear that there are some differences in the higher order harmonic components found, with the ANN method having a larger high harmonic content.

Note that the ANN method only uses the first $2\mu\text{s}$ of the data captured, whereas the two current sample method in this case uses samples with at least $17\mu\text{s}$ worth of separation: with the large separation it is expected that the performance of the latter technique should be good.

7.4 Operating Point Variation

One of the key demands of any variable speed drive is the ability to operate at various speeds and loads. With the derivative estimation performance proven at the trained operating point, attention turned to the performance of the technique at operating points not previously seen by the neural network during training. Variation of speed was found to make little difference providing the electrical frequency demand applied to the machine was kept above 5Hz, the reasons behind this will be discussed later.

However an increase in loading beyond levels seen during training caused a deterioration of the derivative estimates and a loss of the saturation saliency component at all speeds. This is logical since an increase in loading will lead to an increase in the amplitude of the phase current of the machine into a region the neural network has no learned behaviour to reference. This is illustrated in the Figure 7.7 which shows the relative strength of the 2nd harmonic component (the saturation saliency component that is of interest) of the position vectors with respect to the other harmonics present in the response. This measure was found by dividing the amplitude of the 2nd harmonic component (measured in the frequency domain) by the sum of the remaining harmonics up to the 5th harmonic. The larger the value, the stronger the 2nd harmonic component in relation to the other harmonics present. A value of greater than one represents a good result. Also note that a small value does not necessarily mean that only a small second harmonic component exists. This could mean that very large harmonic components exist which swamp the second harmonic component and would be difficult to remove from the response.

Notice that at the trained points (no load and 44% load) a reasonable result is achieved. However between the training points the performance

diminishes and at higher loads beyond the trained points the performance is very poor.

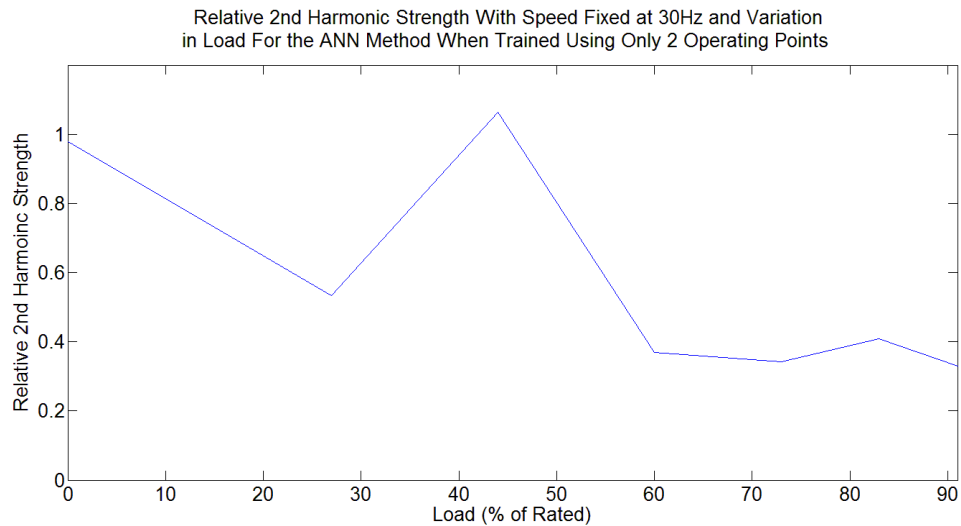


Figure 7.7 Relative second harmonic strength found from ANN estimates. The ANN was trained using data captured at 30Hz, no load and 30Hz, 44% load

The poor performance outside of the trained loading points was improved by increasing the number of operating points used during ANN training. One speed was found to be sufficient (30Hz was chosen) but several loading points must be included in the training data. With training data captured at no load, 44% load and 83% load, the derivative estimates and the ability to track the saturation saliency component were found to vary little with speed and load and were also found to closely match the results obtained from the two current sample approach and Rogowski coil when operated away from the no-load region. This is illustrated by the surface plots in Figures 7.8 (a) and (b) which show the relative harmonic strength of the saturation saliency component at a number of speeds and loads. The results also allow a comparison to be made between the performance of the ANN method and the two current sample method (a minimum pulse width of $17\mu\text{s}$ was applied once again).

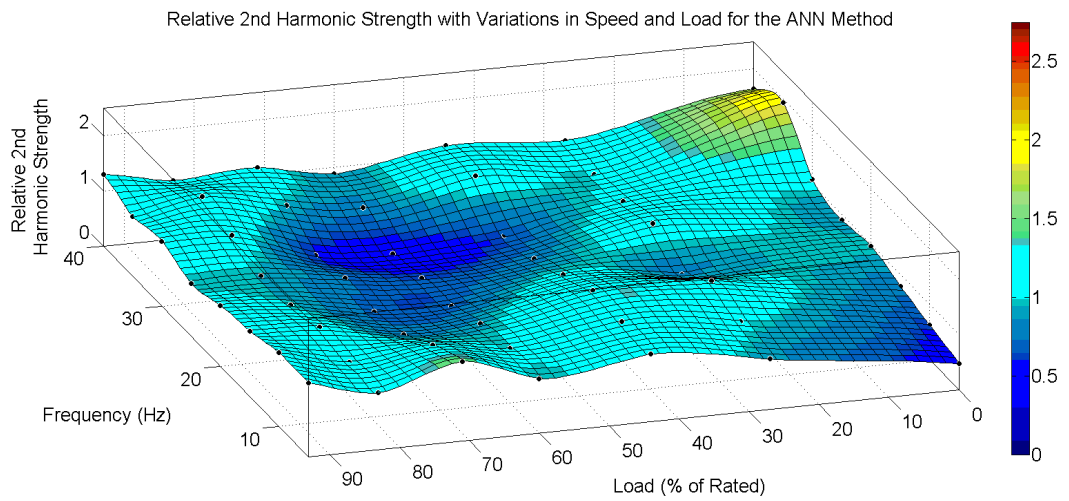


Figure 7.8 (a) ANN

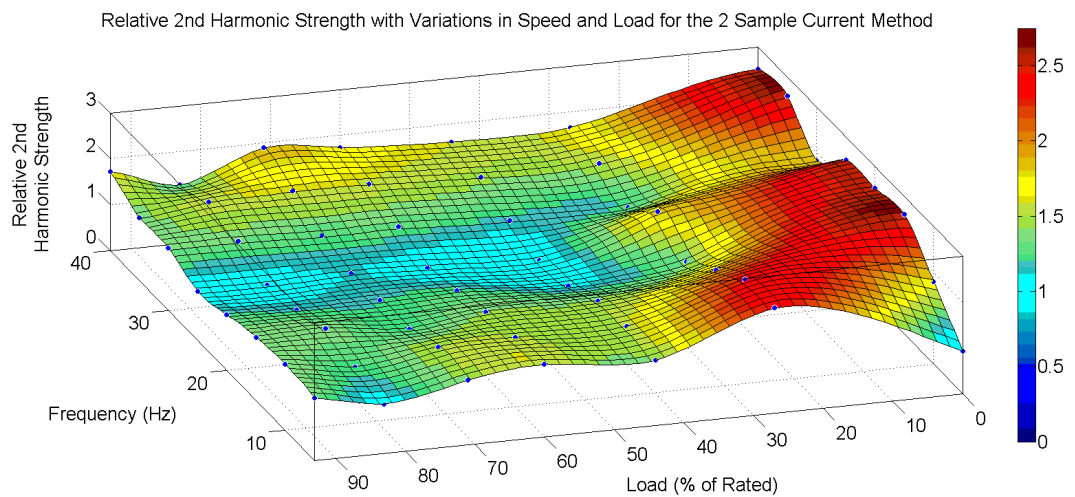


Figure 7.8 (b) Two current sample method

Figure 7.8 Surface plots illustrating the performance of the ANN and two current sample methods at various speeds and loads. For these tests the minimum pulse width was maintained at $17\mu\text{s}$

Figure 7.8 (a) and (b) allow some interesting observations to be made. It is apparent that the ANN method has some stronger higher order harmonics present when $P_{\alpha\beta}$ are viewed in the frequency domain (see Figure 7.6 and

results contained in Appendix B). Although the saturation saliency component identified by the ANN is generally smaller than that obtained from the two current sample method (as will be shown later), the harmonic content is the main reason behind the relative 2nd harmonic strength results being smaller for the ANN method. The increased harmonics of the ANN method are not thought to be problematic and a good position estimate could be extracted from the response.

Note that the performance of the ANN technique at no load is poor at speeds other than the trained no load speed (30 Hz). At the trained no-load speed the performance is good and comparable to the two current sample method.

Also note that there is a region at approximately 25Hz, at medium to high loads where the performance of both techniques is reduced. This is believed to be due to a resonance point in the mechanical system located at this frequency. The resonance is audibly apparent in the behaviour of the machine and leads to a distortion of the motor current which in turn affects both methods similarly.

Away from the no-load region and the 25Hz region the ANN produces some good results. As indicated previously though, some of the results appear to be worse than they actually are due to the size of the harmonics also present. For additional clarity the saturation saliency component alone is plotted against speed and load in Figure 7.9. The estimated ANN value follows a very similar profile to the two current sample method results but generally is slightly smaller in amplitude than the two current sample approach. At low speed under high loads the ANN method produces a stronger component than the two current sample method. At low load the amplitude of the saturation saliency component reduces for both methods.

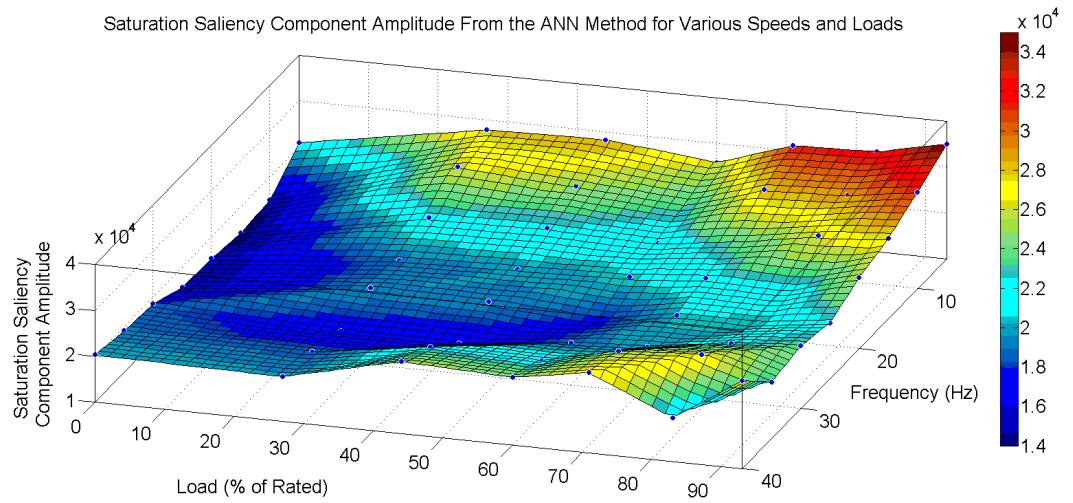


Figure 7.9 (a) ANN

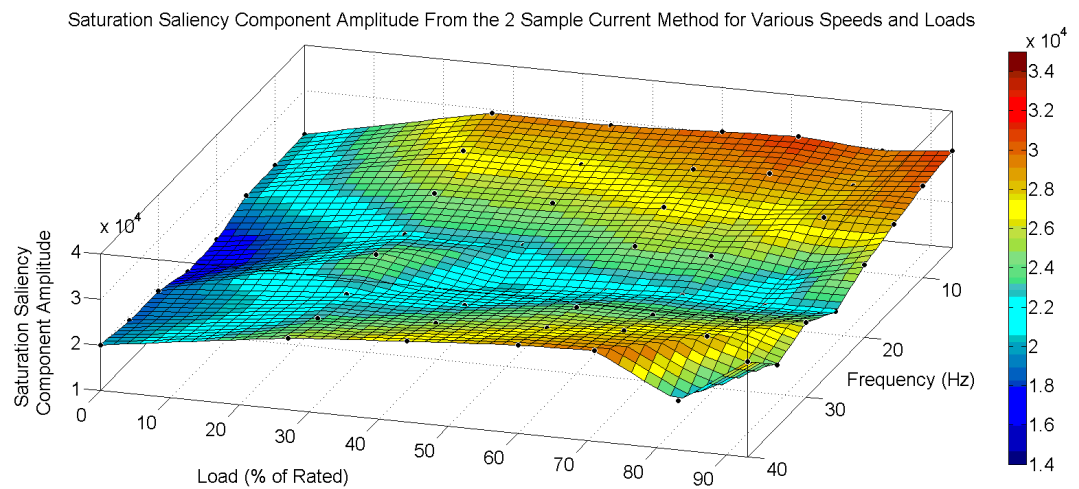


Figure 7.9 (b) Two current sample method

Figure 7.9 Saturation saliency component amplitude found from derivatives obtained from the ANN method, (a), and the two current sample method, (b), at various speeds and loads

7.5 Low Speed Performance Limitations

The major limitation for this technique when operating at low speed is being able to capture reliable training data for low speed operation. The capturing of training data dictates that a long pulse width must be applied in order to allow the sampled waveform to contain both a transient and a steady state portion (that can be used for training). This time depends on the parasitic impedance network of the drive and so will vary between setups. In this research a value of $17\mu\text{s}$ was used. At low speed the large pulse width has a much bigger influence on the behaviour of the machine since this is a condition where naturally small pulse widths would occur. With such a large minimum pulse width threshold all of the active vectors are extended by a considerable amount. This is compounded by the fact that in this application the distortion caused by extending the pulse widths is corrected in the second half of the PWM period, not immediately after the pulse extensions. This distortion of the current waveform causes torque pulsations and variations in shaft speed. Training data captured under these conditions is not representative of normal machine operation at the chosen demand frequency. An encoder was still being used to achieve the closed loop speed control of the machine and as a result the variation in shaft speed was detected and led to the current controller changing the current applied to the machine to try and correct the variations in shaft speed (caused by the torque pulsations) which worsened the problem. It is also clear from Figures 7.9 (a) and (b) that for both the ANN and two current sample approaches at 5 Hz the saturation saliency component increases as speed is reduced. However the relative saturation saliency component strength shown in Figures 7.8 (a) and (b) reduces as the speed is reduced (under no load conditions) which indicates that the results start to encounter large harmonic components in addition to the saturation saliency component.

7.6 Minimum Pulse Width Reduction

Results presented up to this point had been performed with the minimum pulse width fixed at $17\mu\text{s}$ (the same value that was used when collecting training data). The neural networks only use the first $2\mu\text{s}$ of the transient. In theory this means that the pulse widths can be reduced down to $2\mu\text{s}$ which is the main advantage of the ANN approach over existing methods which require an extended pulse width to allow transient oscillations to settle and, in the case of the two current sample method, a measurable change in the current amplitude to occur. In order to illustrate this, a current transient captured using the Altera FPGA is shown in Figure 7.10.

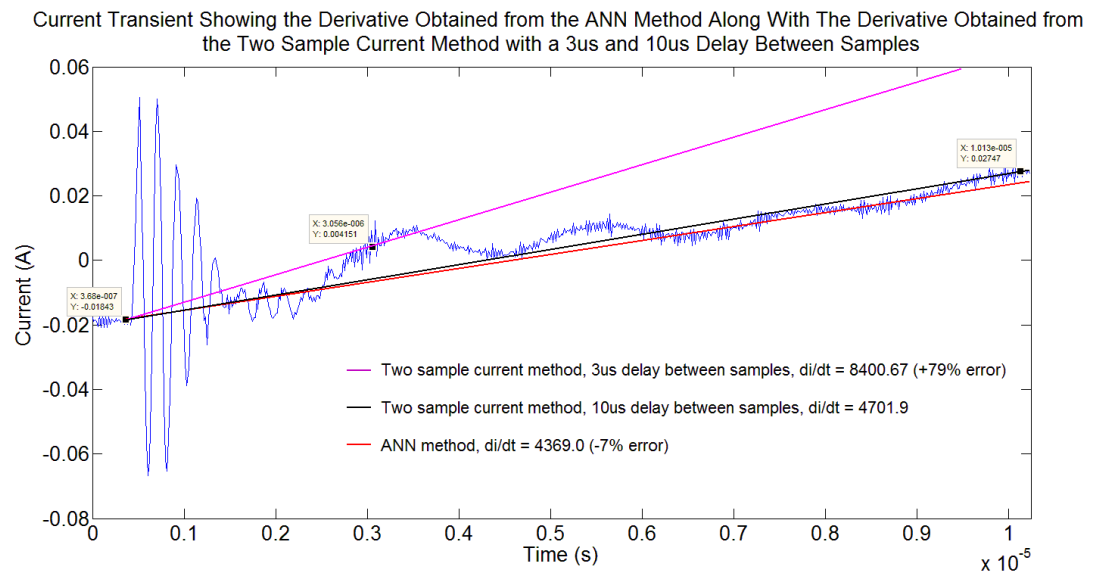


Figure 7.10 Current transient and a corresponding derivative estimate from the ANN (red) and derivative measurements using the two current sample method with a $10\mu\text{s}$ delay between sample points (black), a $3\mu\text{s}$ delay between sample points (pink)

Only $10\mu\text{s}$ of the current transient waveform is captured when collecting data with the Altera setup. In this case the high frequency oscillations have decayed by approximately $2\mu\text{s}$, however a lower frequency

component is clearly still present in the response and will cause significant errors to be introduced when measuring the derivative using the two current sample method (by $17\mu\text{s}$ this lower frequency component will have decayed and its effect will be negligible). The two current sample method was applied to the response in Figure 7.10 with a delay between the two samples of $3\mu\text{s}$ and $10\mu\text{s}$. The ANN was also supplied with the first $2\mu\text{s}$ of the transient to obtain an ANN derivative estimate. The results show that the ANN estimate is a close match (7% error) to the derivative result obtained using the two current sample method with a $10\mu\text{s}$ delay between sample points. However the result when obtained using the two current sample method with a $3\mu\text{s}$ delay between sample points is almost double at approximately 180% of the result obtained with a $10\mu\text{s}$ delay. It is also clear that there would be a significant variation in the result if the second sample point were varied around $3\mu\text{s}$, making the result totally unreliable.

With the performance of the design proven for speed and load variations at $17\mu\text{s}$, the minimum pulse width was reduced to investigate the effects on the performance of the ANN technique. A number of minimum pulse width thresholds were applied and the load was varied from 0% to 95% for each case. The position vectors were calculated and plotted in the frequency domain. This allowed the relative second harmonic strength and second harmonic amplitude to be identified for each case. The results are given in Figure 7.11 (a) and (b) for the case when the speed demand was 30Hz.

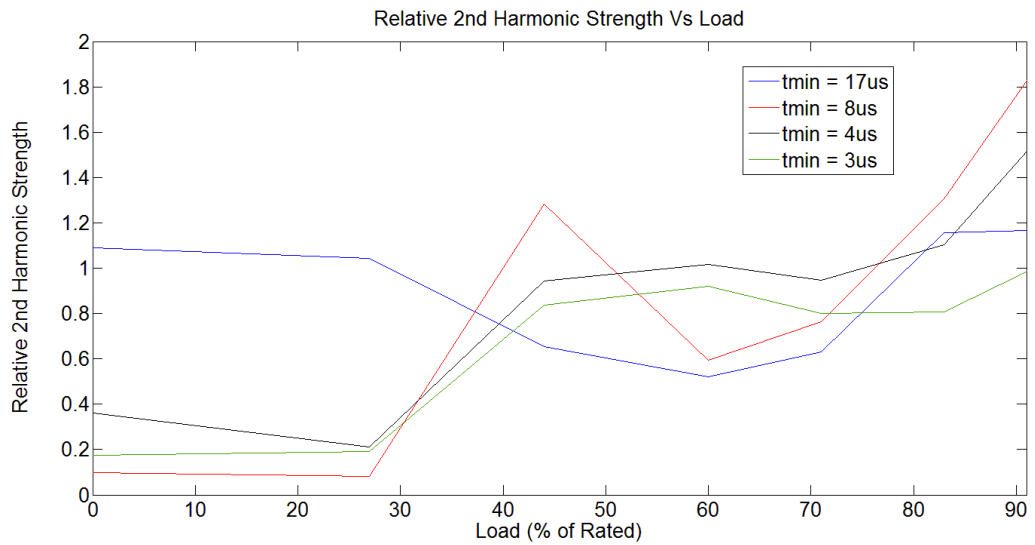


Figure 7.11 (a)

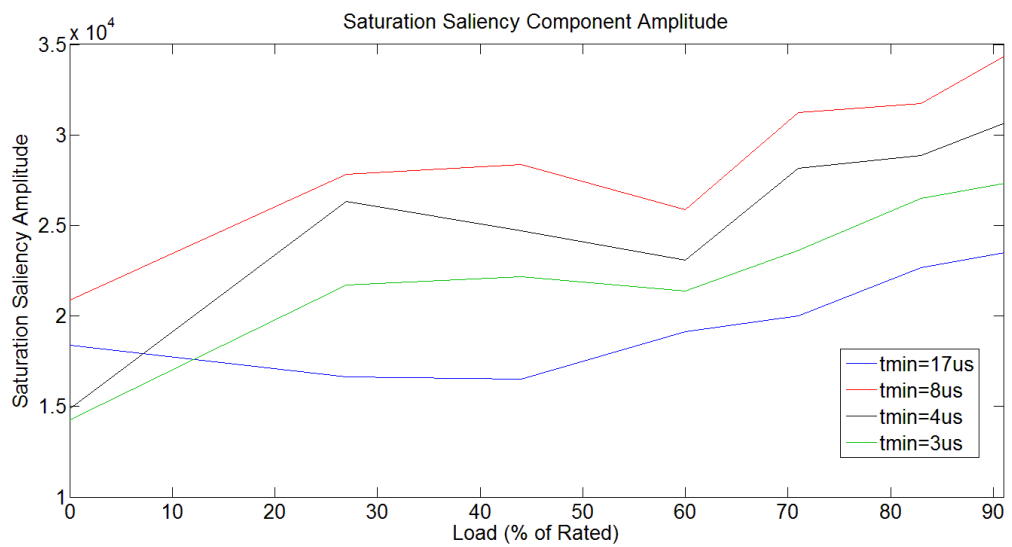


Figure 7.11 (b)

Figure 7.11 shows the relative second harmonic strength (a) and the amplitude of the second harmonic component (b) for ANN derivative estimates found under reduced pulse widths. Notice that under no load the relative second harmonic strength is poor due to the high harmonic content

By performing the same test at a number of speeds it was clear that the ANN again showed a good ability to track the saturation saliency at reduced minimum pulse widths despite changes in speed (as long as the demand frequency was maintained above 5Hz).

There were some differences observed with changes in load. Figure 7.11 (a) reveals that at medium (>30%) loads and high loads the saturation saliency was identified well in all cases. However at low loads the relative second harmonic component strength was very poor (neglecting the trained 17 μ s case) despite only a small drop in the amplitude of the second harmonic component itself (see Figure 7.11 (b)). This is because at low loads the response was dominated by other harmonics with a component at f_e and higher order harmonics of f_e (3rd, 4th, 5th etc) thought to be due to geometric saliencies. The reduction in the amplitude of the saturation saliency component at low loads coincides with an increase in the amplitudes of other harmonic components which dominate the response at low currents.

Figure 7.11 (a) indicates that the ability of the ANN to reject unwanted saliency components at low loads (and therefore low currents) is poor unless the ANN is trained for the conditions, as in the 17 μ s case which shows much better performance at low loads. It is thought that the ability of the neural network to reject unwanted saliency components could be improved at reduced pulse widths (therefore increasing the relative second harmonic component strength at low loads (see Figure 7.11 (a))) if a way of training the neural network with reduced pulse widths could be found. Reducing the pulse widths reduces (or even removes completely) the amount of steady state data available to identify the derivative (with which the ANN is trained). It is thought that if the ANN approach were tested on an induction machine to track say rotor slotting saliency for example that this issue may not be so severe since an induction machine requires a magnetising current, so even at no load there is still a reasonable current being drawn (a few amps).

As the load is increased the second harmonic component amplitude (Figure 7.11 (b)) increases and is larger for larger minimum pulse widths (again neglecting the 17 μ s case). The relative second harmonic strength (Figure 7.11 (a)) also increases with load as the second harmonic component amplitude increases (Figure 7.11 (b)) and the undesirable harmonic content reduces. However there is a dip in the relative second harmonic component amplitude (Figure 7.11 (a)) at approximately 60% load. A dip is also seen in the saturation saliency component amplitude at approximately 60% load but all traces are similarly affected. This is not the case when considering the relative second harmonic component strength (Figure 7.11 (a)) as the 8 μ s case experiences a much larger dip compared to the 3 μ s and 4 μ s cases. This indicates that this dip corresponds not only to a decrease in the saturation saliency component amplitude but also to an increase in undesirable harmonic content with larger minimum pulse widths being more adversely affected by the harmonic content.

The results shown are encouraging. While a reduction in the minimum pulse width to 3 μ s reduces the saturation saliency component amplitude compared to the 4 μ s and 8 μ s cases, the reduction is acceptable and the amplitude is still higher than the 17 μ s case. Also the ability of the ANN to reject harmonics at the dip seen at 60% load was better for smaller pulse widths. Figures 7.12 (a) – (d) compare the derivative estimates from the ANN when a 17 μ s and a 3 μ s minimum pulse width are applied. The machine was operated at 30Hz under 83% load, the same conditions that were used to obtain Figures 7.2-7.5, to allow comparisons to be made. The results visually show only a small deterioration in the quality of the derivative estimates.

The saliency components identified using the derivative estimates are also shown. Notice that for the ANN case when a 3 μ s minimum pulse width is applied (Figure 7.13 (a)) the higher order harmonics have a larger amplitude compared to the 17 μ s case (Figure 7.13 (c)). The results obtained using the two current sample method are also shown for reference in Figure 7.13 (b) and

(d). In the $17\mu\text{s}$ case (Figure 7.13 (d)) the saturation saliency component is identified well as expected. However in the $3\mu\text{s}$ case the two current sample method fails to identify the saturation saliency component to the same level of accuracy and the response also contains large unwanted harmonic components.

Finally the derivative estimates obtained from the ANN method, the two current sample method and a Rogowski coil when a $3\mu\text{s}$ minimum pulse width is applied are shown for comparison in Figure 7.14 (a) - (d).

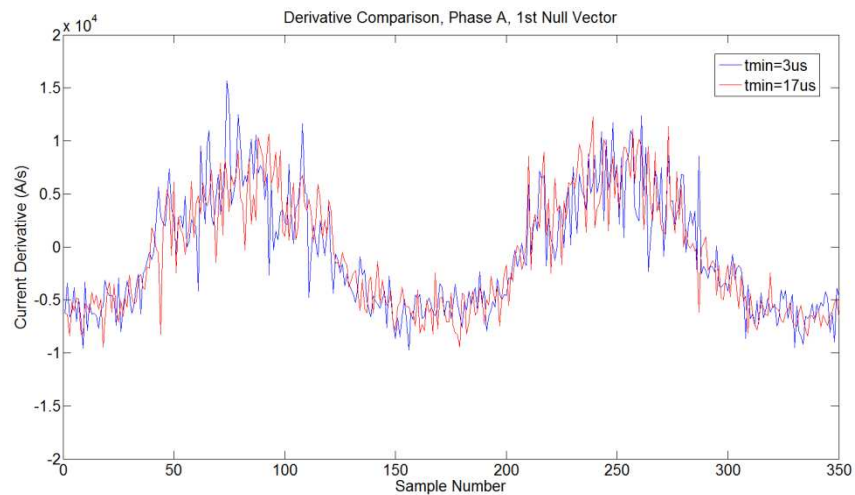


Figure 7.12 (a) First null vector

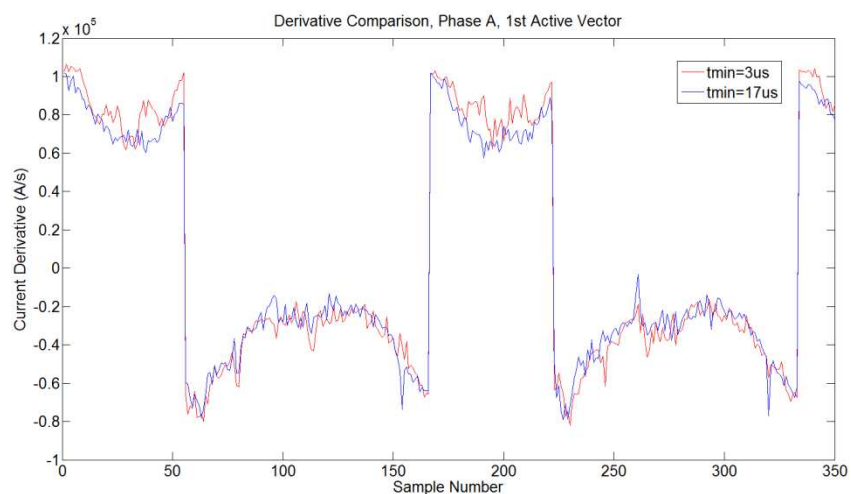


Figure 7.12 (b) First active vector

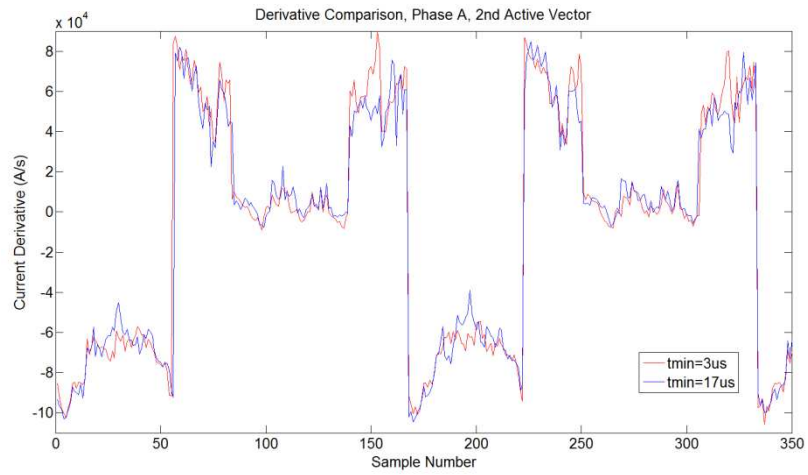


Figure 7.12 (c) Second active vector

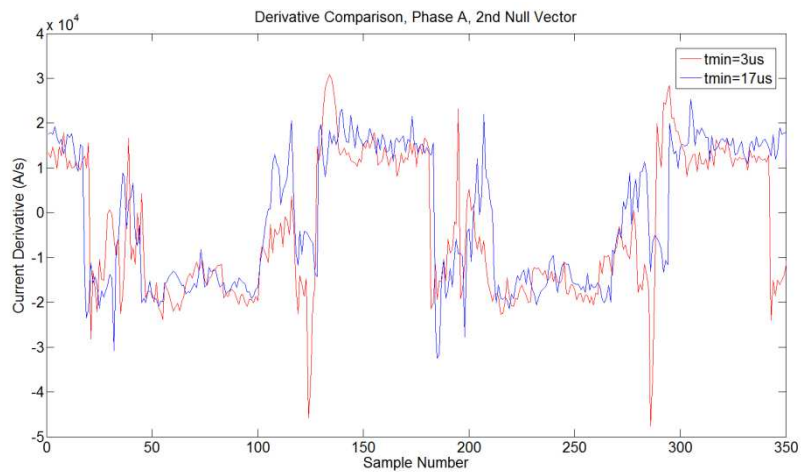


Figure 7.12 (d) Second null vector

Figure 7.12 Comparison of the vector derivative estimates by the ANN when applying $3\mu s$ and $17\mu s$ minimum pulse widths

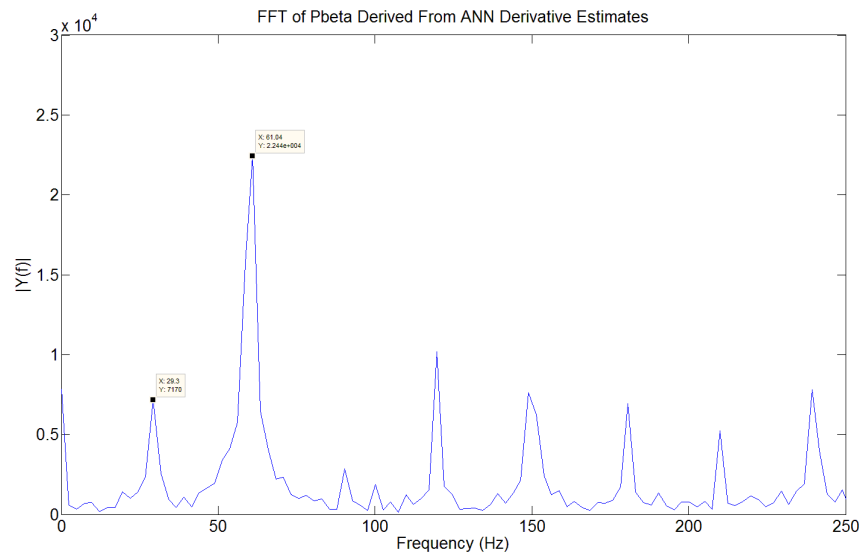


Figure 7.13 (a) 3 μ s ANN

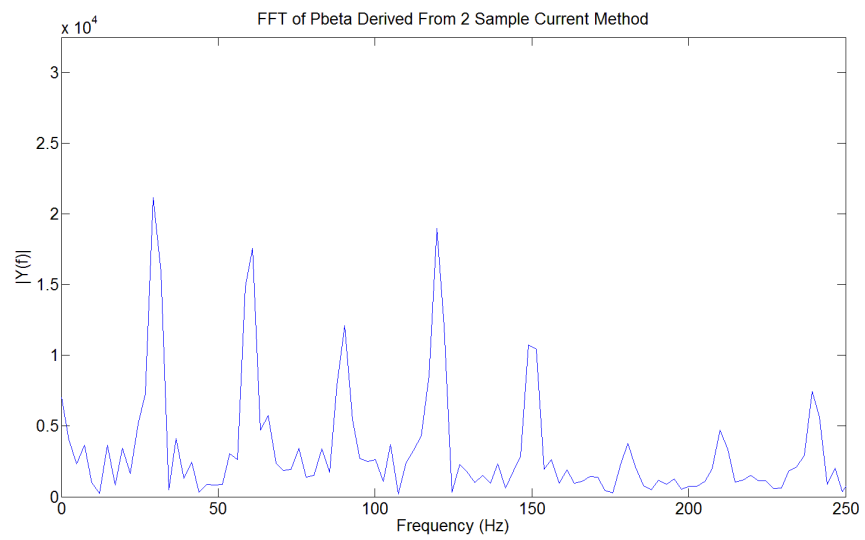


Figure 7.13 (b) 3 μ s Two current sample method

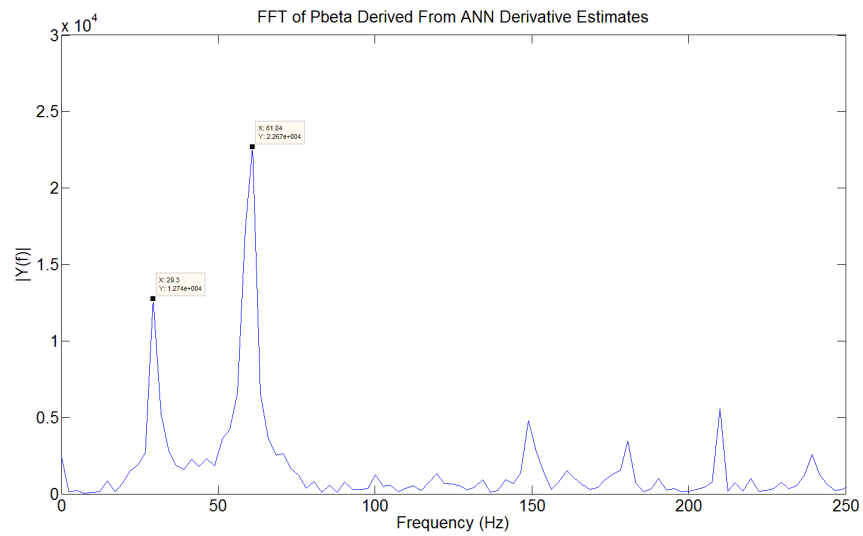


Figure 7.13 (c) 17 μ s ANN

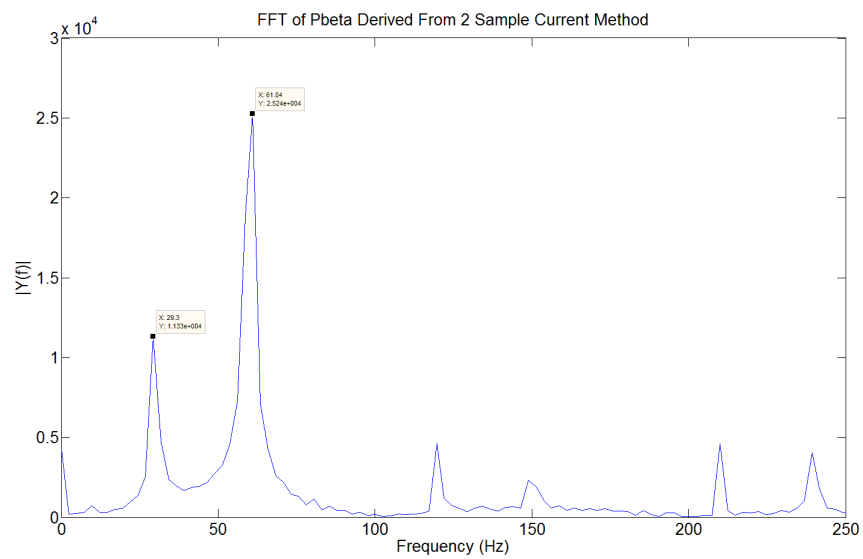


Figure 7.13 (d) 17 μ s Two current sample method

Figure 7.13 Comparison of the harmonic contents of P_β derived from (a) ANN with 3 μ s t_{\min} , (b) two current sample method with 3 μ s t_{\min} , (c) ANN with 17 μ s t_{\min} and (d) two current sample method with 17 μ s t_{\min}

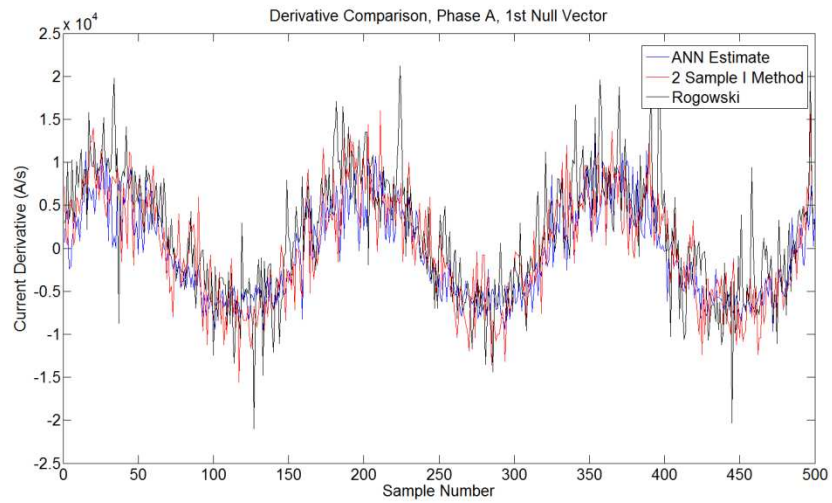


Figure 7.14 (a) First null vector

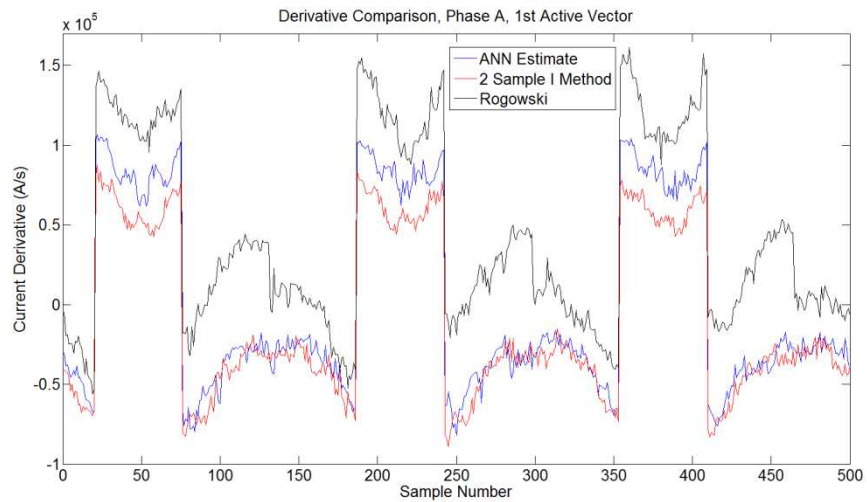


Figure 7.14 (b) First active vector

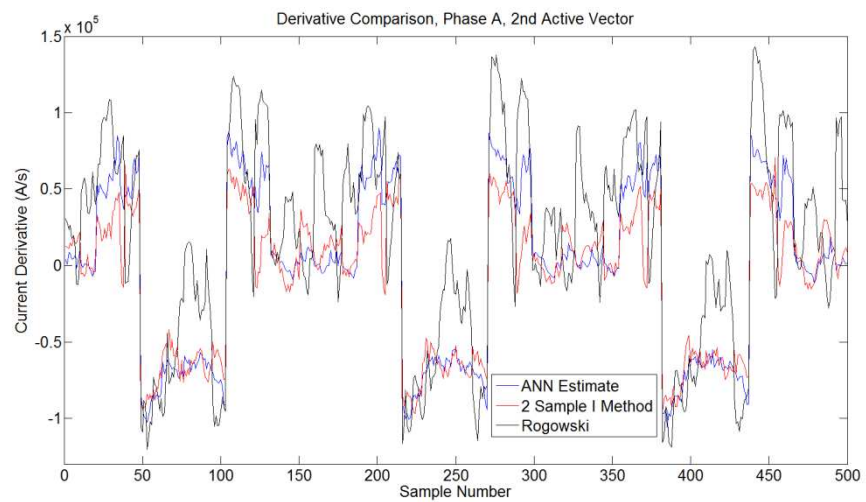


Figure 7.14 (c) Second active vector

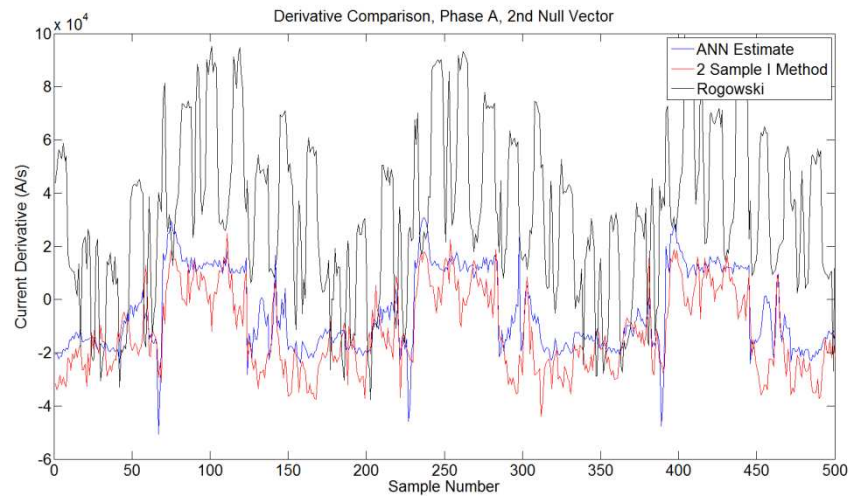


Figure 7.14 (d) Second null vector

Figure 7.14 Comparison of the vector derivative estimates from the ANN, two current sample method and Rogowski coil when a $3\mu\text{s}$ minimum pulse width is applied

Inspection of Figures 7.14 (a) - (d) reveals that it is clear that there is a deterioration in the results obtained from the Rogowski coil. The two current sample method shows better performance although there are still a large number of errors introduced when operating under the $3\mu\text{s}$ minimum pulse width threshold. There was some variation observed in the errors introduced to the Rogowski and two current sample method results as the minimum pulse width was reduced, with the results becoming worse and then improving before becoming worse again as the pulse width was reduced. This is due to the decaying low frequency transient and the sample points coinciding with the peaks, troughs and zero crossings of decaying high frequency component.

A problem that affects all methods including the ANN method is that when operating under a narrow pulse width threshold (that is less than the decay time of the high frequency oscillations) the transients in the current response excited by the inverter switching don't fully decay before the next vector is applied and so there is some residual oscillations seen in the following current transient. For the machine and cable length used in this

research the high frequency transient was dominated by a 4MHz component and decayed rapidly, however a lower frequency component was also seen and it was this component which affected results at short pulse widths. The first null vector and first active vector are less susceptible to the effects of the previous vector since the first null vector is preceded by the last null vector of the previous PWM period which at low to medium speeds has a large pulse width associated. Also, since the null vector from the previous PWM period is maintained at the start of a new PWM period there is no requirement to change the switching state of the inverter. This also means that there is no new current transient initiated which could have a residual effect on the first active vector. For these reasons the transients in Figure 7.14 (a) and (b) appear more accurate than those in Figure 7.14 (c) and (d).

When implementing the Fundamental PWM equations it was possible to calculate the position scalars using either two results from the first active and null vectors and one from the second active and null vectors or vice versa. Since the first active and null vectors are less vulnerable to influences from residual current oscillations, two estimates were used from these vectors and only one from the second active and null vectors. This led to an improvement in the results obtained when operating under narrower pulse widths (all results presented in this chapter were acquired using this approach).

7.7 Conclusions

The results presented have shown that it is possible to use an artificial neural network to estimate current derivatives using a small portion of the transient current waveform. The accuracy of the ANN derivative estimates were found to be good compared to the two current sample approach and this performance allowed a good estimation of the saturation saliency component to be made from the ANN derivative estimates. The actual saturation saliency

components found by the ANN method were generally smaller in amplitude than the values found using the two current sample method and also had a higher harmonic content. In most cases the two current sample method was superior when operating under large minimum pulse widths.

With the ANN proven but not able to match the two current sample method one could wonder what the reason behind using the ANN approach would be. The key factor is the ability of the ANN to produce a good derivative estimate from a standard current sensor as the pulse widths are reduced to levels where the Rogowski coil and two current sample methods cannot be relied upon to give an accurate derivative value. This has been proven with the ANN giving an improved performance compared to the Rogowski coil and two current sample methods when operating with a $3\mu\text{s}$ minimum pulse width with load applied. However when operating under no load or a very small loads, the ability of the ANN method to identify the saturation saliency was poor because of the reduction in the amplitude of the saturation saliency component and an increase in undesirable harmonic content from other saliencies.

An area where an improvement could be made to the ANN technique is no load operation at speeds other than the training speed for large pulse widths (see Figure 7.8 (a)). At the trained frequency, the no-load behaviour was better than at any other speed. As load was applied the performance improved and speed had little influence thereafter. It is thought that if data collected at multiple no-load speeds were incorporated into the ANN training then an improvement in performance could be realised.

Chapter 8

Conclusions, Discussions and Suggestions of Future Work

8.1 Conclusions and Discussions

This thesis has presented a new way to estimate current derivatives in the presence of high frequency noise. The technique can improve the performance of the Fundamental PWM Technique by reducing the minimum pulse width compared to previous implementations allowing a reduction in the current distortion, audible noise, torque ripple and vibration.

A basic understanding of the merits and limitations of the various sensorless techniques has been provided. Mathematical model based approaches cannot operate reliably at low and zero speed and require machine parameters to be accurately defined. Parameter variation with temperature also presents issues. Saliency tracking techniques can operate (theoretically) across the entire speed range and are immune to parameter sensitivity. However they require high frequency signals to be applied either by modifying the fundamental output of the inverter or by modifying the specific switching patterns output by the inverter and making use of the high frequency content of the voltage steps.

The Fundamental PWM technique is an attractive saliency tracking technique since it makes use of the switching waveform applied to the

machine (by the inverter) under normal operation. However measurements of the current derivative are required to track the saturation saliency and estimate the rotor position. The current derivatives following a switching event are affected by high frequency oscillations that prevent immediate measurement of the current derivative. In existing methods a delay is applied prior to derivative measurement which allows the high frequency oscillations to decay. The length of this delay and subsequent time required to measure the derivative led to a minimum PWM pulse width threshold. PWM vectors less than the minimum pulse width are extended. The vector extensions introduce undesirable current distortion, audible noise, torque ripple and vibration. The minimum pulse width threshold represents the single biggest limitation affecting the Fundamental PWM technique and significant improvements in operating performance could be achieved if this limitation could be reduced.

The high frequency oscillations arise from parasitic impedances in the motor, drive and cabling. The impedances have been modelled in this work and the common mode frequency response, differential mode frequency response and the crucial high frequency oscillatory time domain response has been accurately reproduced. The key modelled parameters (of the motor) include the stator winding turn to turn capacitance, the skin effect of the windings, the high frequency iron loss, the stator winding leakage inductance and the stator winding to frame and stator neutral to frame capacitances. With regards to the cable model in addition to the standard transmission line model parameters, skin and proximity effects and dielectric losses must also be modelled in order to accurately reproduce the frequency response.

This is sufficient to reproduce the high frequency behaviour seen experimentally; however the parasitic capacitance of the switching devices must also be included to accurately capture the non-linear switching behaviour seen at low currents when the commutation in an inverter leg is from a transistor to a diode. This has the effect of reducing the dv/dt of the switching

transient. When operating at high currents no effect due to these capacitances is seen.

Several methods have been presented (EMI filters, variation of IGBT gate circuitry and the use of multilevel converters) which offer the possibility of reducing the amplitude of the high frequency oscillations (that appear in the current waveform) and therefore could offer a reduction in the minimum pulse width threshold. However they all affect the fundamental operation of the inverter by reducing the dv/dt of the switching transients which also reduces the high frequency content of the voltage pulses. This in turn reduces the magnitude of the saliency components in the current response which is undesirable in a sensorless application since these must be identified and tracked. Instead the possibility of extracting the current derivative from a transient response affected by the high frequency oscillations was investigated. A limited amount of work has previously been done in this area. However this work was not considered complete for a number of reasons that included a reliance on dedicated derivative sensors, offline implementation only, limited sensor bandwidth and the neglect of non-linear inverter switching effects.

The use of curve fitting approaches to extract the derivative was explored with a number of simple and some more advanced methods being investigated. Taking the transient current response from an experimental rig utilising a short supply cable, it was not possible to accurately extract the derivative by simply fitting a decaying high frequency sinusoid to the experimental waveform (over a short time window) despite the response appearing to be dominated by a single high frequency exponentially decaying component. This is due to the response containing a large number of frequency components, some of which appear as a gradient when viewed over a very short time window (a few μs). Also the limited bandwidth of the current sensor means that the response is distorted which adds further to the estimate error. Even if it were possible to find the derivative using curve fitting methods, transients in the low current region when commutation is from

transistor to diode present further issues. Under these conditions the dv/dt of the switching edge is reduced and the current is distorted during switching. The amplitude of the subsequent high frequency oscillations is reduced. This would introduce large errors into the derivative estimates obtained from a curve fitting approach.

Given these limitations the use of artificial neural networks to estimate the derivative directly when supplied with a current transient was investigated. This is a promising option since the ANN can be trained to take account of limited sensor bandwidth and recognise the non-linear inverter switching effects which occur at low current. The ANN was trained to associate the initial transient responses captured using a standard industrial current sensor with steady state current derivatives during a pre-commissioning phase. Simulated results using current transients captured from an experimental setup showed promising performance with a good ability to estimate current derivatives under PWM active and null vectors when supplied with only $2\mu s$ of the phase current transients.

Given the promising performance of the simulated ANN it was decided that the proposed approach should be evaluated in a real time experimental environment. The major difficulty associated with this was the need to sample the motor phase currents at a very high sample rate. For short cable lengths (1m) the dominant high frequency component was 4 MHz. It was decided that to capture this to a good resolution the sample rate needed to be at least 10 times the dominant frequency component meaning that at least 40 MSPS ADC capability would be required. Many options were explored but the most attractive was found to be an FPGA based solution in the form of the TerasIC DE3 development with high speed data acquisition expansion cards. This provided the necessary specification required, although the input to the data acquisition boards required some modification since it blocked key low frequency information. This was solved with the addition of a custom board featuring a high speed op-amp ADC driver. The ANN was also implemented

in the FPGA meaning that the whole design was confined to the development board. Training of the ANN was still performed in Matlab and the ANN weights and biases were transferred via an SD card.

This allowed the ANN approach to be validated experimentally. Initial attempts used only a single neural network trained using data collected from a single phase. While this provided good performance on the phase used to collect training data, the derivative estimation performance on the other two phases was unacceptable. This was due to the ANN being sensitive to changes in the parasitic impedance networks seen by the phases and differences in the data acquisition circuitry between phases (these circuits were designed to be identical but differed due to component tolerances). Using a dedicated neural network for each phase solved this problem and the performance observed was now similar across all three phases.

The technique was tested using large minimum pulse widths to establish how well the derivative could be tracked and also understand the influences of speed and load without considering narrow pulses. This also allowed a comparison with the results obtained from the two current sample method and Rogowski coil to be made since these approaches can be used when a large pulse width is defined. The results showed that the ANN could estimate the derivative to a reasonable accuracy using only $2\mu\text{s}$ of the current transient and while the performance observed was not as good as that of the two current sample method, the results were comparable.

The relationship between speed, load and derivative estimate accuracy was also investigated. Variations in speed were found to have little effect on the estimation accuracy. However if the load was changed from the values the ANN was trained to then the derivative estimation accuracy became poor. This was solved by collecting training data at several load points to include the effect of load variation into the ANN training. The performance improved

significantly and the load could now be varied and the derivative estimation accuracy remained good even under loads not seen during training.

The ability of the technique to accurately estimate the derivative at no load at speeds other than at the speed used to capture training data was poor. It is thought that if more speeds (with zero load applied) were included in the training of the ANN then this may improve performance.

Low speeds (<5Hz) also presented problems as training data could not be collected at these speeds due to the large minimum pulse width (17 μ s) applied when collecting training data. The large pulse width significantly increased the time that the PWM active vectors were applied for compared to their original demand values. A large current distortion was introduced and the shaft rotation was not smooth. As an encoder was still used for the closed loop control of the machine this variation in shaft speed was detected and fed back to the control loop which tried to compensate the effect. All of this meant that the drive operation was not representative of that which may be experienced by the ANN under normal operation when a low speed demand is applied. Without any training data the ANN did not have experience of operating at these speeds and hence the performance was poor. In order to improve the performance a method of extracting the steady state derivative in a reduced time is required. It is thought that a reduction in the 17 μ s used in this work is achievable. Implementing this and investigating whether or not low speed performance is improved remains outstanding for a future task.

Finally the performance of the technique when operating under narrow pulse widths was evaluated. It was found that narrowing the pulse widths leads to some degradation in the performance of the ANN derivative estimation accuracy but this still represents an improvement compared to the two current sample method and dedicated derivative sensor. It is thought that the reduction in accuracy could be due to the effects of decaying transients of the previous vector. This is not seen in the training data due to the large minimum pulse

width threshold which is set in order to ensure steady state data is observed. Performance under no load when pulse widths are narrowed was poor. This is due to a reduction in the saturation saliency component amplitude and an increase in the amplitude of the harmonic components seen in the derivative response. In order to improve the ANN performance the training of the ANN must be improved, ideally by collecting training data under narrow pulse widths to improve the ANN's ability to reject the undesirable frequency components.

This work has met the objectives set out at the beginning of this thesis. The ANN approach can estimate the current derivative using only $2\mu\text{s}$ of transient data. For the experimental setup used the minimum pulse width that would be applied using traditional methods was over $5\mu\text{s}$. This represents at least a 60% reduction in the minimum pulse width. The reduction in the minimum pulse width results in a reduction in the THD (as documented in 2.4.3) and a noticeable difference in audible noise and vibration emitted from the machine. The method relies on measurements of the phase current only. Although SVPWM and trigger signals (to initiate ADC sampling) were required these were easily supplied by the controlling DSP. The solution is a bolt-on solution and has minimal affect on the operation of the drive with only a comparatively small minimum pulse width threshold being required. The ability of the method to estimate derivatives in real time, in a way that would allow a position estimate to be produced has been demonstrated. However, in order to utilise the full potential of the technique, operation at low speed must be improved as it is at low speed where the reduction in the minimum pulse width threshold gives the most benefits.

8.2 Future Work

Given the amount and nature of the work involved in this research it was impossible to ensure each part of the work was explored and implemented to its full potential. This section aims to give a brief outline of a number of areas where it is thought with further attention could yield performance improvements.

8.2.1 Improved High Frequency Simulation Model

In this work the high frequency modelling of the drive, cabling and motor were only carried out to the extent that an understanding of the major parasitic sources that effect the current transient could be understood and a general transient response could be replicated. The causes of the non-linear inverter switching waveforms were also investigated. If more focus was directed at matching this simulation to the real drive setup then this could offer the possibility to train the neural network on simulated data.

8.2.2 Alternative Neural Networks

Research carried out into the type and configuration of the neural network to be used for estimating current derivatives indicated that a feed-forward neural network would be the best configuration to use. The number of layers, the number of perceptrons in each layer and the perceptron transfer functions used were all chosen initially to be a good compromise between performance and resource usage. The fine tuning of this was then done by trial and error. The aim of this was to find a neural network which had a reasonable

training time and gave good derivative estimation performance on both data used to train the network and new data.

Hence with some expert knowledge in this area it may be possible that there is a neural network configuration which could be used that offers an improvement in performance.

8.2.3 Improved Training Data

The key to the accuracy of the results produced by neural networks is in the quality of the training. Every effort was made to ensure that the ANN was only supplied with only relevant training data. However, it would be possible to further improve the timings of data sampling to further remove redundancy in the training and normal run mode data.

8.2.4 Improvements to the Present Implementation

Two major limitations in this work were the size of the arrays that could be used in Matlab without incurring memory related errors (this limited the amount of training data that could be used) and the amount of time that it took to retrieve training data from the SD card and use this to train the network. This resulted in a limitation of 60000 samples being applied to the training data in order to allow three neural networks to be trained in a day. 90000 samples were achieved without incurring memory errors. However this took approximately 13 hours just to retrieve the data from the SD card before training could even begin. Hence this was not a practical solution.

Major improvements could be made to the training process used which is still currently very time consuming. The main areas which could be improved are the bulk storage of training data. Data is currently stored on an SD card and compared to the time taken to capture data, the time taken to

write the data to the SD card is large. Once on the SD card the data must be exported to Matlab for processing which is also very time consuming. Finally the training process itself can also take a long time to complete. This is partly due to the high threshold standards that the training process must meet. If these could be relaxed without impacting greatly on derivative estimate accuracy then an improvement in training time could be achieved. Until these issues have been solved it is not possible to say whether this approach could be adopted in industry. At present the training time is prohibitive to the use of the technique.

8.2.5 ANN Online Adaptive Learning

During normal operation at higher speeds the Narrow Vector Problem becomes less of a burden as the PWM vectors only require extension around the SVPWM boundaries. When operating away from these boundaries longer vectors are applied to the machine. If these vectors were long enough to allow the high frequency oscillations to settle then a value for the derivative could be obtained using the two current sample method and used to train the ANN online. It is not known practically how well this approach would work. It is thought that the increase in training data would make the ANN more robust. However consideration must also be given to avoid the possibility of over training the ANN to operating points where long vectors exist (as these will be the only training points available).

8.2.6 Hybrid Derivative Estimate Techniques

Experience gained using the experimental setup in this research has shown that null vectors always allow sufficient time to allow a derivative measurement to be made via the two current sample method when operating at low to medium speeds. The possibility of only using the ANN to estimate

active vector derivatives while calculating null vector derivatives using the two current sample method should be explored since this would allow a decrease in computation resources required and half the computation time (since only three derivatives would need to be estimated by the ANN this could be done in one pass instead of two using the system designed as part of this work).

8.2.7 Use the Derivative Estimates to Produce a Position Estimate that can be used for Closed Loop Control

The work so far has demonstrated the ability to use an ANN to estimate the current derivatives required for position estimation using the Fundamental PWM technique. It has also been shown that the derivative estimates can be used to identify the saturation saliency component and thus track the rotor position. In order to progress this work further and make it attractive to industry it would be necessary to use the derivative estimates to produce a position estimate in real time and then use this to implement full sensorless closed loop control of the machine.

8.2.8 Improvements to the Derivative Estimation Performance of the ANN at Low Speed and Under Low Load

The experimental results presented in this thesis showed that under zero loads at the speed used to collect data to train the ANN the ability to estimate derivatives and identify the saturation saliency component was reasonable. However at speeds not included in the training of the ANN the

ability to estimate the saturation saliency was diminished with the amplitude of other saliency components increasing. It was suggested that if the ANN was trained at a number of speeds (with zero load applied) then the performance under no load when the speed is varied may be improved. This is certainly something that should be investigated further.

Additionally the ANN could not be demonstrated at very low and zero speeds because it was not possible to provide the ANN with training data for low and zero speeds. When collecting training data a large minimum pulse width ($17\mu\text{s}$) had to be applied in order to capture a steady state response. This placed a limit on the minimum speed that could be reached since at low speed all of the active vectors applied to the machine were extended which in turn had a large effect on the machine behaviour. When operating the ANN in normal run mode the minimum pulse width could be reduced significantly meaning that it was possible to operate at zero and low speeds but as the ANN had not been provided with any reference behaviour in the low speed region (during training) its derivative estimation performance was poor. If methods to obtain training data at low and zero speed could be developed then, it would be of great interest to evaluate the performance of the proposed techniques at lower speeds since this is where the highest benefit of reducing the minimum vector time is seen.

8.2.9 Use ANN Derivative Estimation Technique to Track Saliency in an Induction Machine

Further to the discussion in 8.2.8 regarding the poor accuracy of the ANN derivative estimates when operating at low loading points not included in the training data, it is thought that an improvement in low load performance could be realised if the technique were applied to an induction machine instead of a permanent magnet machine. When using a permanent magnet machine the

no load current is very small and it is difficult to measure the derivative. The frequency response of the resulting position vector is dominated by other harmonic components thought to be due to geometric saliencies. It is thought that the low load performance of the ANN derivative estimation technique when applied to an induction machine could see an improvement due to the need to maintain a magnetising current in an induction machine, even at no load, therefore guaranteeing a reasonable current magnitude at all operating points.

8.3 Publications

Some of the work presented in this thesis has led to a conference paper being published [119].

Appendix A

In this appendix the position vector equations of the Fundamental PWM technique used in this research are derived. The derivation is based on [26, 40, 41]. The stator circuit diagrams under vectors V_1 , V_2 and V_0 of the SVPWM plane and illustrated in Figure A.1

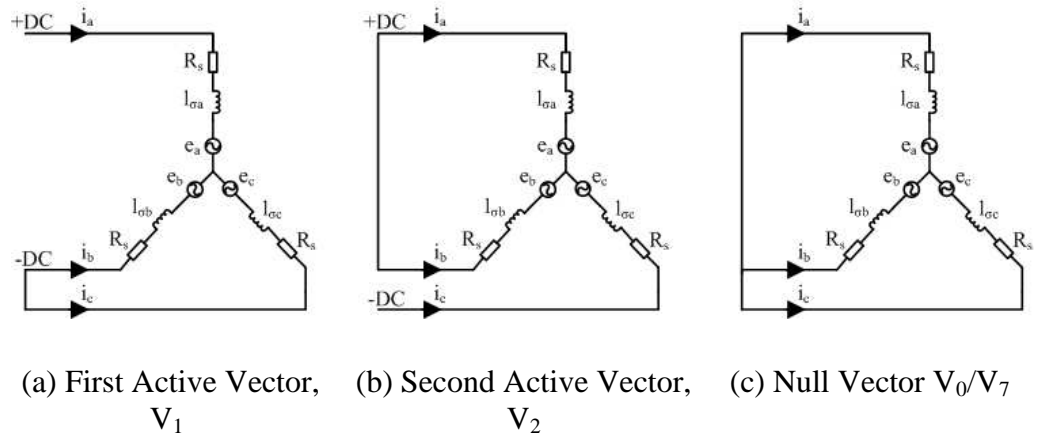


Figure A.1 Stator circuits when vectors V_1 , V_2 and V_0/V_7 of the SVPWM plane are applied to the machine

For the case shown in Figure A.1 (a), V_1 , the following equations can be defined for V_{ab} , V_{bc} and V_{ca} .

$$V_{ab} = V_{DC} = R_s \cdot i_{aV_1} + l_{\sigma a} \cdot \frac{di_{aV_1}}{dt} + e_{aV_1} - R_s \cdot i_{bV_1} + l_{\sigma b} \cdot \frac{di_{bV_1}}{dt} + e_{bV_1} \quad (\text{Eqn A.1})$$

$$V_{bc} = 0 = R_s \cdot i_{bV_1} + l_{\sigma b} \cdot \frac{di_{bV_1}}{dt} + e_{bV_1} - R_s \cdot i_{cV_1} + l_{\sigma c} \cdot \frac{di_{cV_1}}{dt} + e_{cV_1} \quad (\text{Eqn A.2})$$

$$V_{ca} = -V_{DC} = R_s \cdot i_{cV_1} + l_{\sigma c} \cdot \frac{di_{cV_1}}{dt} + e_{cV_1} - R_s \cdot i_{aV_1} + l_{\sigma a} \cdot \frac{di_{aV_1}}{dt} + e_{aV_1} \quad (\text{Eqn A.3})$$

While for the null vector case shown in Figure A.1 (c), the following equations can be defined.

$$V_{ab} = 0 = R_s \cdot i_{aV_0} + l_{\sigma a} \cdot \frac{di_{aV_0}}{dt} + e_{aV_0} - R_s \cdot i_{bV_0} + l_{\sigma b} \cdot \frac{di_{bV_0}}{dt} + e_{bV_0} \quad (\text{Eqn A.4})$$

$$V_{bc} = 0 = R_s \cdot i_{bV_0} + l_{\sigma b} \cdot \frac{di_{bV_0}}{dt} + e_{bV_0} - R_s \cdot i_{cV_0} + l_{\sigma c} \cdot \frac{di_{cV_0}}{dt} + e_{cV_0} \quad (\text{Eqn A.5})$$

$$V_{ca} = 0 = R_s \cdot i_{cV_0} + l_{\sigma c} \cdot \frac{di_{cV_0}}{dt} + e_{cV_0} - R_s \cdot i_{aV_0} + l_{\sigma a} \cdot \frac{di_{aV_0}}{dt} + e_{aV_0} \quad (\text{Eqn A.6})$$

If the separation between the points where samples are taken under the null vector V_0 and the active vector V_1 is small then it may be assumed that $i_{xV_1} \approx i_{xV_0}$ and $E_{xV_1} \approx E_{xV_0}$ (where x is either a, b or c). With this assumption the effects of back EMF and stator resistance voltage drop can be cancelled by subtracting (Eqn A.4), (Eqn A.5) and (Eqn A.6) from (Eqn A.1), (Eqn A.2) and (Eqn A.3) respectively which yields

$$V_{DC} = l_{\sigma a} \cdot \left(\frac{di_{aV_1}}{dt} - \frac{di_{aV_0}}{dt} \right) - l_{\sigma b} \cdot \left(\frac{di_{bV_1}}{dt} - \frac{di_{bV_0}}{dt} \right) \quad (\text{Eqn A.7})$$

$$0 = l_{\sigma b} \cdot \left(\frac{di_{bV_1}}{dt} - \frac{di_{bV_0}}{dt} \right) - l_{\sigma c} \cdot \left(\frac{di_{cV_1}}{dt} - \frac{di_{cV_0}}{dt} \right) \quad (\text{Eqn A.8})$$

$$V_{DC} = l_{\sigma c} \cdot \left(\frac{di_{cV_1}}{dt} - \frac{di_{cV_0}}{dt} \right) - l_{\sigma a} \cdot \left(\frac{di_{aV_1}}{dt} - \frac{di_{aV_0}}{dt} \right) \quad (\text{Eqn A.9})$$

Multiplying (Eqn A.7) by $l_{\sigma c}$, (Eqn A.8) by $l_{\sigma a}$ and (Eqn A.9) by $l_{\sigma b}$, and then subtracting each result from the other results and then substituting

$3L_o \left(1 - \left(\frac{\Delta L}{2L_o} \right)^2 \right)$ for $l_{\sigma a}l_{\sigma b} + l_{\sigma b}l_{\sigma c} + l_{\sigma c}l_{\sigma a}$ yields

$$\frac{V_{DC}(l_{\sigma b} + l_{\sigma c})}{3L_o \left(1 - \left(\frac{\Delta L}{2L_o} \right)^2 \right)} = \left(\frac{di_{aV_1}}{dt} - \frac{di_{aV_0}}{dt} \right) \quad (\text{Eqn A.10})$$

$$\frac{-V_{DC}(l_{\sigma b})}{3L_o \left(1 - \left(\frac{\Delta L}{2L_o}\right)^2\right)} = \left(\frac{di_{cV1}}{dt} - \frac{di_{cV0}}{dt}\right) \quad (\text{Eqn A.11})$$

$$\frac{-V_{DC}(l_{\sigma c})}{3L_o \left(1 - \left(\frac{\Delta L}{2L_o}\right)^2\right)} = \left(\frac{di_{bV1}}{dt} - \frac{di_{bV0}}{dt}\right) \quad (\text{Eqn A.12})$$

Defining a constant c as:

$$c = \frac{3L_o \left(1 - \left(\frac{\Delta L}{2L_o}\right)^2\right)}{V_{DC}} \quad (\text{Eqn A.13})$$

and replacing $l_{\sigma a}$, $l_{\sigma b}$ and $l_{\sigma c}$ with equations (Eqn 2.1) – (Eqn 2.3) allows (Eqn A.10) - (Eqn A.12) to be re-written as:

$$\left(\frac{di_{aV1}}{dt} - \frac{di_{aV0}}{dt}\right) = \frac{1}{c} \left(2 - \frac{\Delta L}{L_o} \cos(n_{an}(\theta_{an}))\right) \quad (\text{Eqn A.14})$$

$$\left(\frac{di_{bV1}}{dt} - \frac{di_{bV0}}{dt}\right) = -\frac{1}{c} \left(1 + \frac{\Delta L}{L_o} \cos\left(n_{an}\left(\theta_{an} - \frac{4\pi}{3}\right)\right)\right) \quad (\text{Eqn A.15})$$

$$\left(\frac{di_{cV1}}{dt} - \frac{di_{cV0}}{dt}\right) = -\frac{1}{c} \left(1 + \frac{\Delta L}{L_o} \cos\left(n_{an}\left(\theta_{an} - \frac{2\pi}{3}\right)\right)\right) \quad (\text{Eqn A.16})$$

The position vector is defined as:

$$\begin{aligned} p &= p_a + \alpha p_b + \alpha^2 p_c \\ &= \frac{\Delta L}{L_o} \cos(n_{an}(\theta_{an})) + \frac{\alpha \Delta L}{L_o} \cos\left(n_{an}\left(\theta_{an} - \frac{2\pi}{3}\right)\right) \\ &\quad + \frac{\alpha^2 \Delta L}{L_o} \cos\left(n_{an}\left(\theta_{an} - \frac{4\pi}{3}\right)\right) \end{aligned} \quad (\text{Eqn A.17})$$

Hence (Eqn A.14) to (Eqn A.16) can be re-arranged to define p_a , p_b and p_c

$$p_a = 2 - c \left(\frac{di_{aV1}}{dt} - \frac{di_{aV0}}{dt} \right) \quad (\text{Eqn A.18})$$

$$p_b = -1 - c \left(\frac{di_{cV1}}{dt} - \frac{di_{cV0}}{dt} \right) \quad (\text{Eqn A.19})$$

$$p_c = -1 - c \left(\frac{di_{bV1}}{dt} - \frac{di_{bV0}}{dt} \right) \quad (\text{Eqn A.20})$$

Different DC offsets and a lack of knowledge of the exact value of the constant c mean that these equations alone cannot be used to establish the rotor position as these terms will not cancel. However the process described above can be repeated for the second active vector leading to the definition of three more position scalar equations:

$$p_a = -1 + c \left(\frac{di_{bV2}}{dt} - \frac{di_{bV7}}{dt} \right) \quad (\text{Eqn A.21})$$

$$p_b = -1 + c \left(\frac{di_{aV2}}{dt} - \frac{di_{aV7}}{dt} \right) \quad (\text{Eqn A.22})$$

$$p_c = 2 + c \left(\frac{di_{cV2}}{dt} - \frac{di_{cV7}}{dt} \right) \quad (\text{Eqn A.23})$$

By selecting position scalars with the same offset from (Eqn A.18) to (Eqn A.23) for P_a , P_b and P_c it is now possible to construct a position vector where the constant, c , and DC offsets will cancel.

The position vector in this case can be found from

$$p = \left(-1 + c \left(\frac{di_{bV2}}{dt} - \frac{di_{bV7}}{dt} \right) \right) + \alpha \left(-1 - c \left(\frac{di_{cV1}}{dt} - \frac{di_{cV0}}{dt} \right) \right) + \alpha^2 \left(-1 - c \left(\frac{di_{bV1}}{dt} - \frac{di_{bV0}}{dt} \right) \right) \quad (\text{Eqn A.24})$$

In terms of $\alpha\beta$:

$$\begin{aligned}
 p_\alpha &= p_a - \frac{1}{2}(p_b + p_c) \\
 &= c \left(\left(\frac{di_{bV2}}{dt} - \frac{di_{bV7}}{dt} \right) + \frac{1}{2} \cdot \left(\frac{di_{cV1}}{dt} - \frac{di_{cV0}}{dt} \right) \right. \\
 &\quad \left. + \frac{1}{2} \cdot \left(\frac{di_{bV1}}{dt} - \frac{di_{bV0}}{dt} \right) \right) \quad (\text{Eqn A.25})
 \end{aligned}$$

$$\begin{aligned}
 p_\beta &= \frac{\sqrt{3}}{2}(p_b - p_c) \\
 &= \frac{\sqrt{3}}{2} c \left(- \left(\frac{di_{cV1}}{dt} - \frac{di_{cV0}}{dt} \right) + \left(\frac{di_{bV1}}{dt} - \frac{di_{bV0}}{dt} \right) \right) \quad (\text{Eqn A.26})
 \end{aligned}$$

Finally the position can be found by taking the inverse tangent of p_β/p_α .

$$\theta_{an} = \frac{1}{n_{an}} \tan^{-1} \left(\frac{p_\beta}{p_\alpha} \right) \quad (\text{Eqn A.27})$$

Where n_{an} is the number of saliency cycles per shaft revolution (=2 when considering the saturation saliency). Similar derivations can be performed for the remaining active and corresponding null vectors of the SVPWM plane to provide a table of position scalar equations. The table of position scalar equations for a star connected machine was given in Table 2.1.

Appendix B

This appendix contains a number of experimental results collected as part of the investigation presented in Chapter 7. Fourier transforms of the β component of the position vector calculated at various speeds and loads using both derivatives found from the ANN method and two current sample method are shown. Following this, the ability of the ANN to estimate the saturation saliency under narrow pulse widths is demonstrated by showing Fourier transforms of the β component of the position vector calculated using derivatives from the ANN method when a narrow pulse width is applied.

Configuration – Three neural networks (one for each phase) trained using data captured at 30Hz with 17 μ s minimum pulse width at 3 loading points; No load, 44% load and 83% load.

When viewing the saliency components in the frequency domain, in each case the electrical demand frequency is given in the figure caption. The saturation saliency component that is of interest lies at twice the electrical frequency.

Variation in Load and Speed

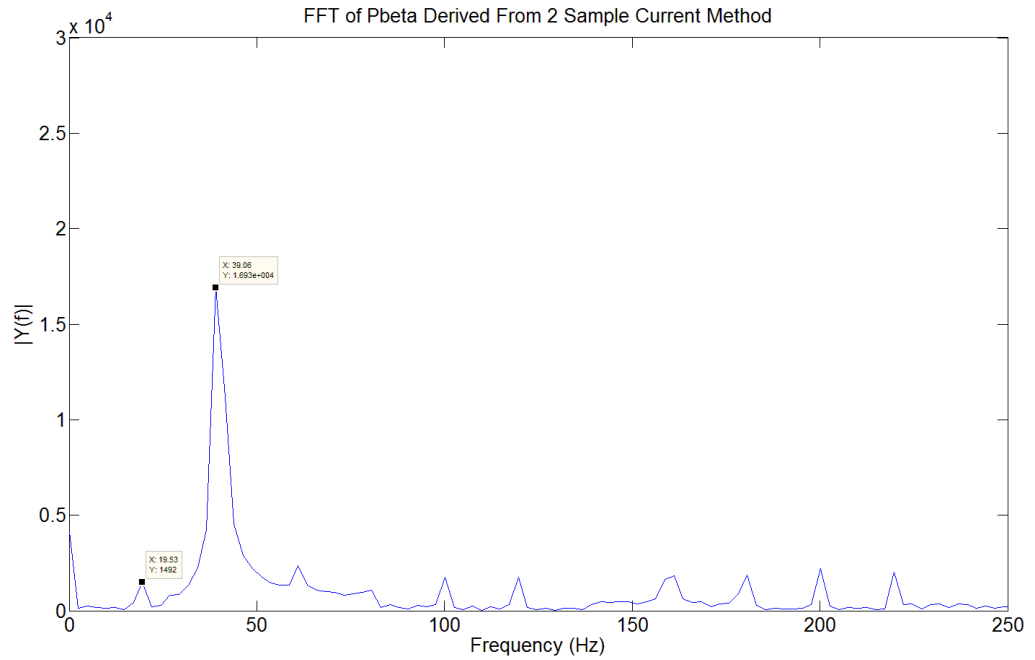


Figure B.1 Two current sample method, 20Hz, no load

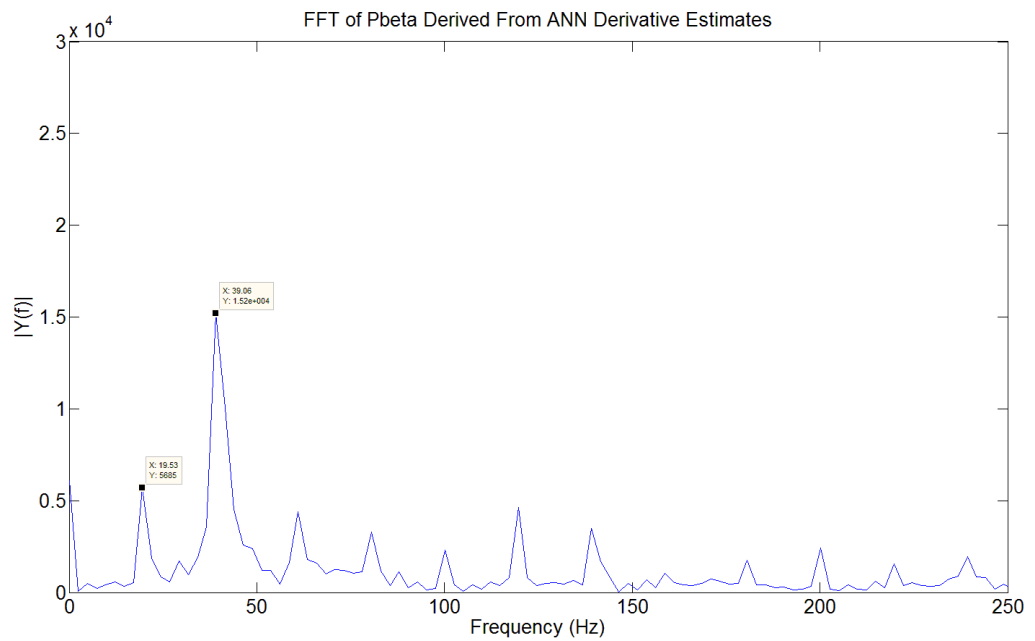


Figure B.2 ANN method, 20Hz, no load

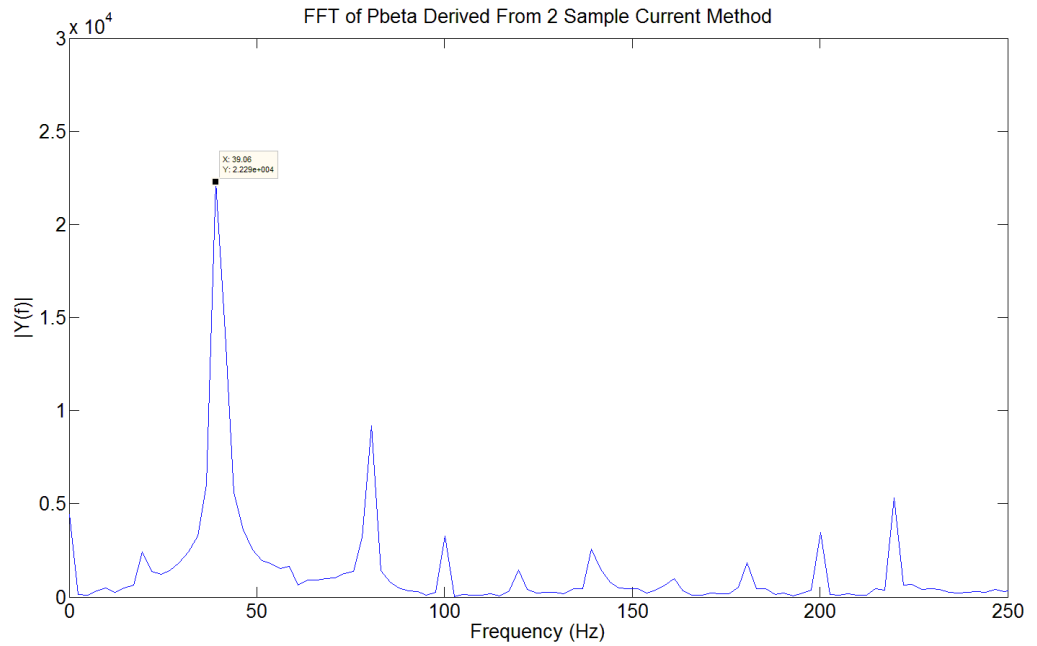


Figure B.3 Two current sample method, 20Hz, 27% Load

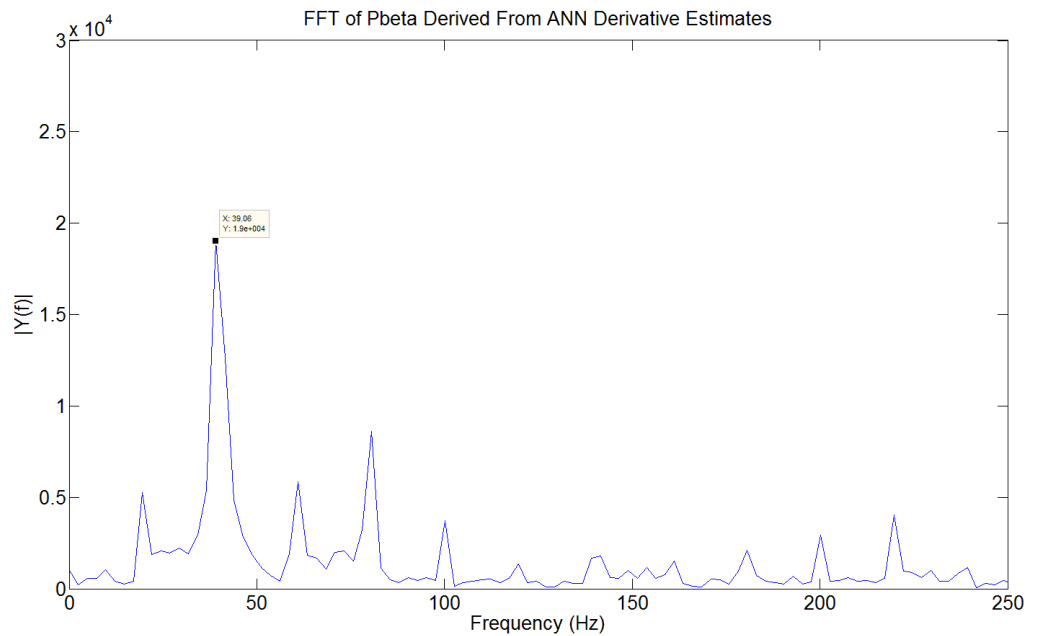


Figure B.4 ANN method, 20Hz, 27% Load

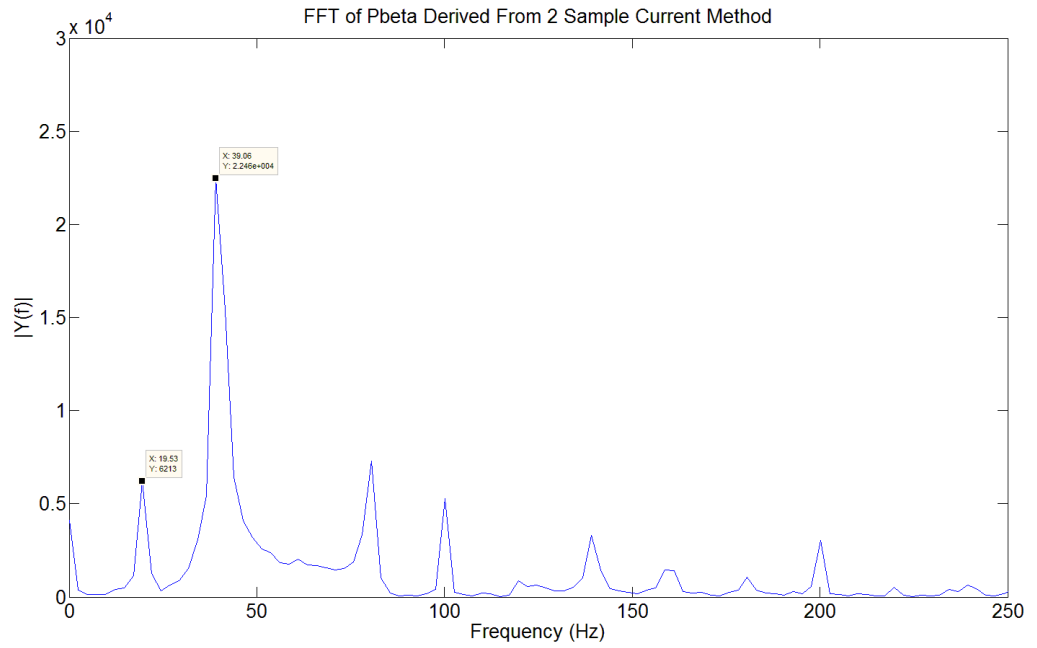


Figure B.5 Two current sample method, 20Hz, 44% Load

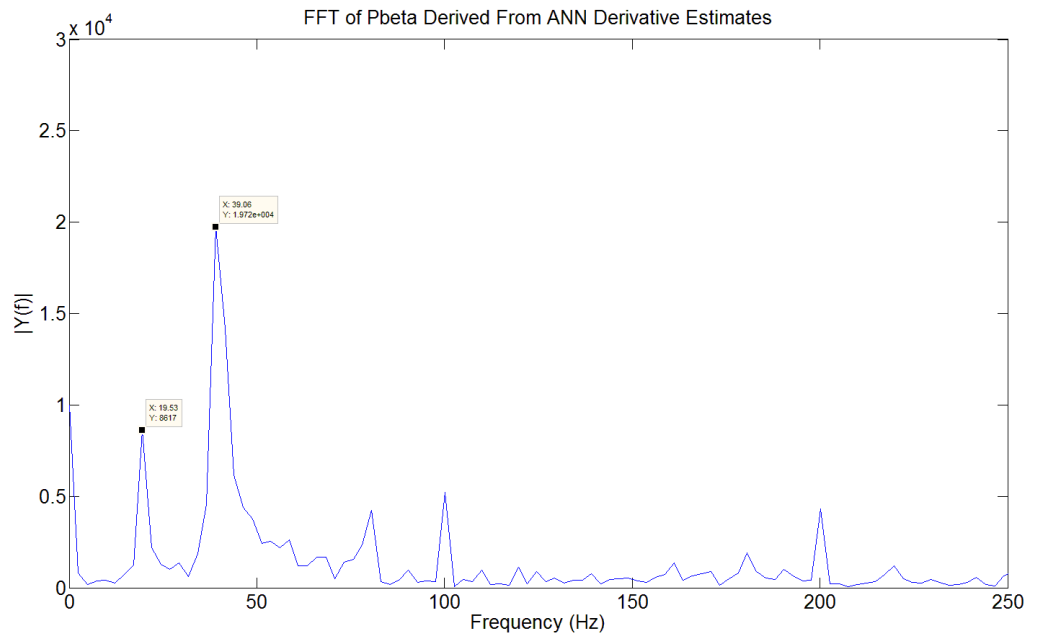


Figure B.6 ANN method, 20Hz, 44% Load

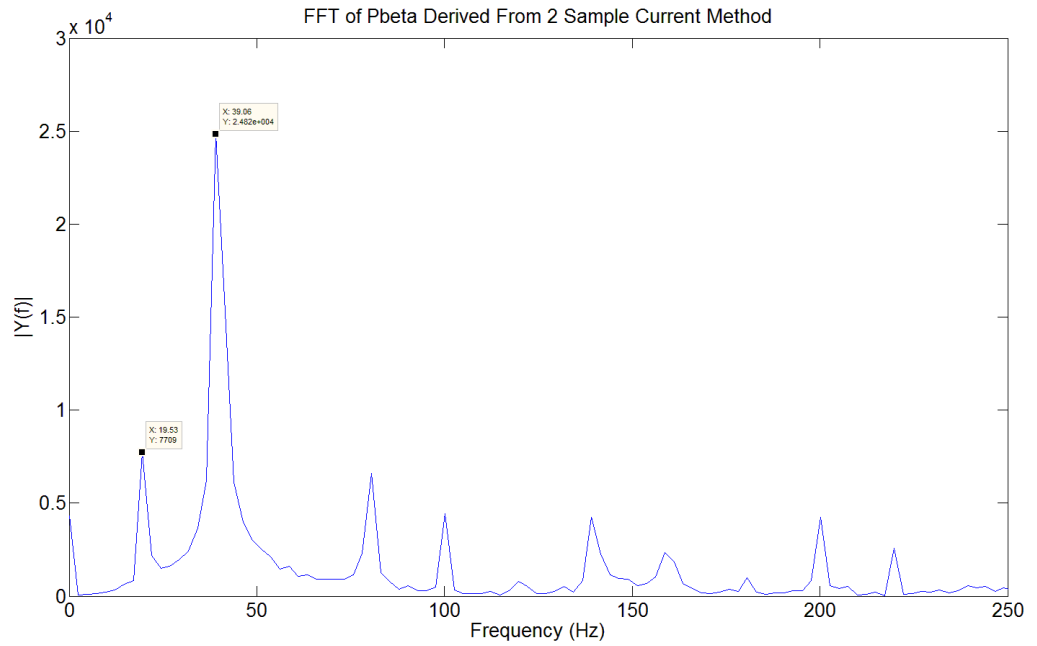


Figure B.7 Two current sample method, 20Hz, 60% Load

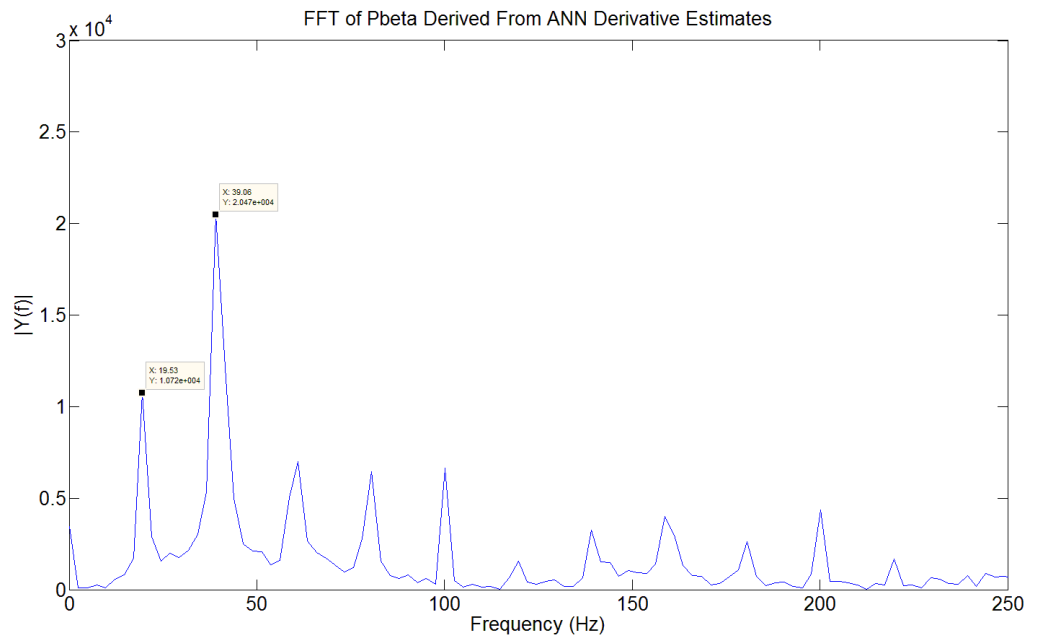


Figure B.8 Two current sample method, 20Hz, 60% Load

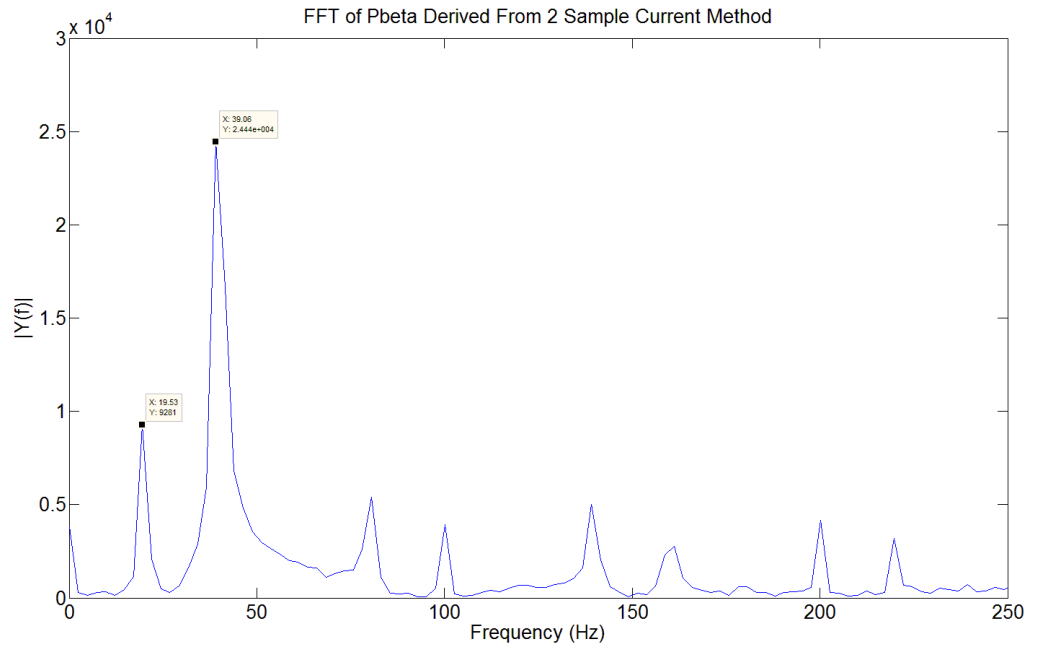


Figure B.9 Two current sample method, 20Hz, 73% Load

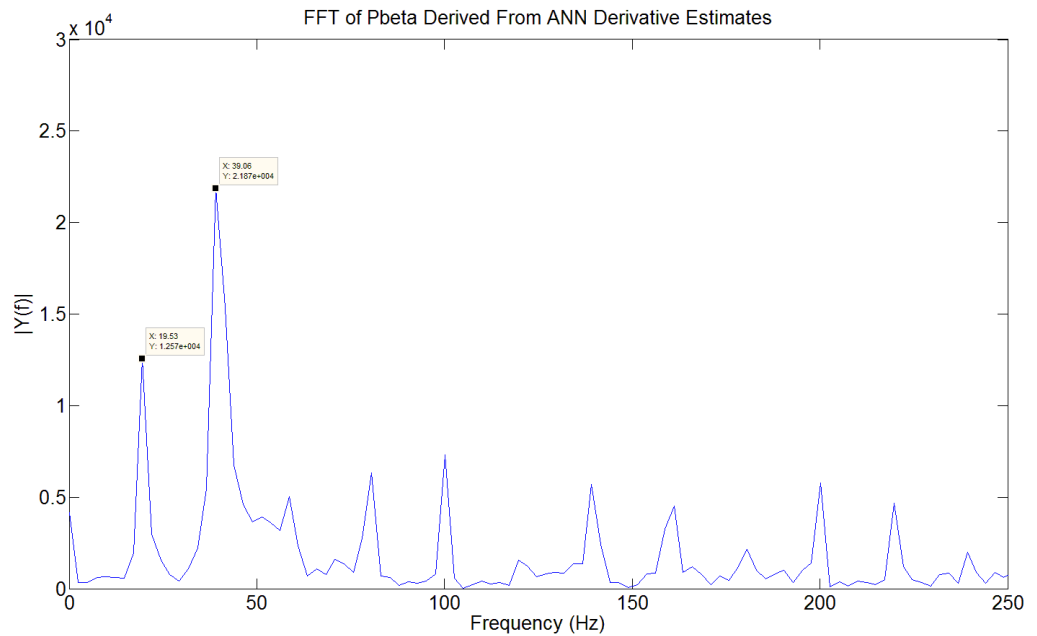


Figure B.10 ANN method, 20Hz, 73% Load

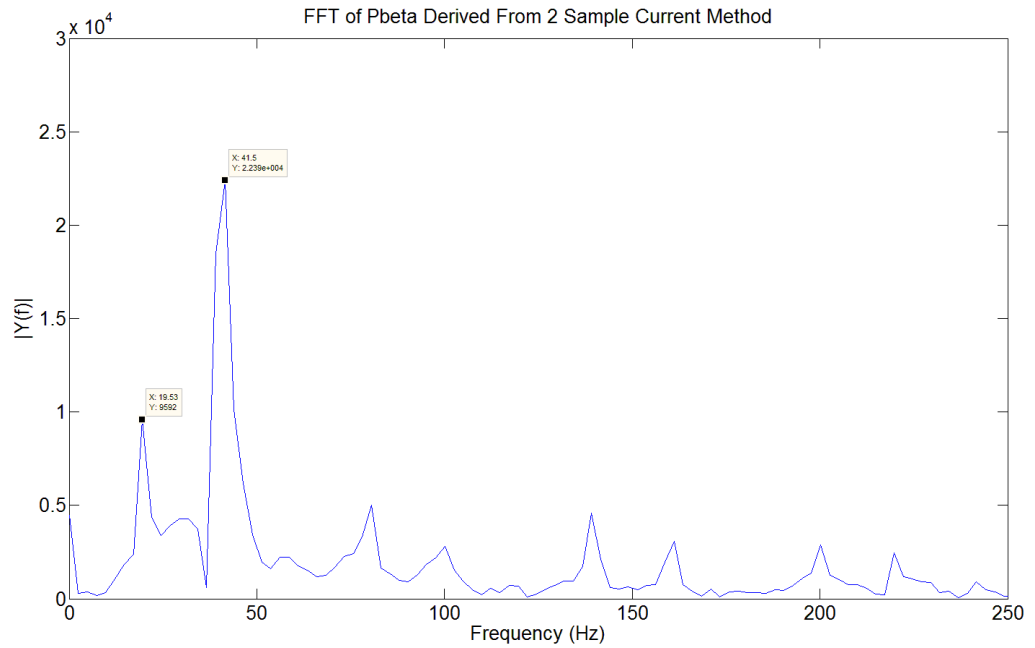


Figure B.11 Two current sample method, 20Hz, 83% Load

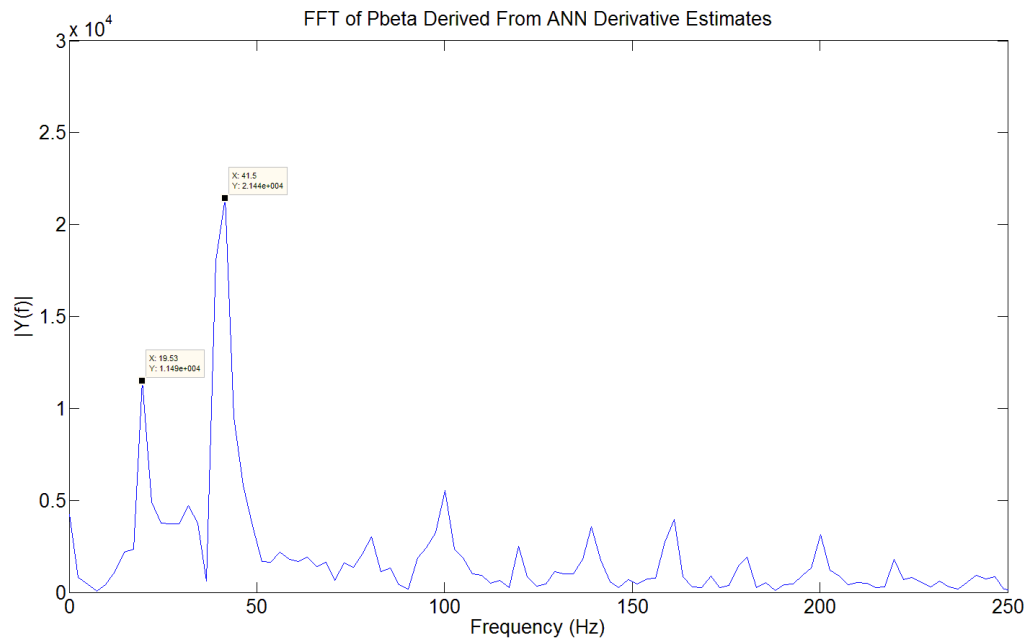


Figure B.12 ANN method, 20Hz, 83% Load

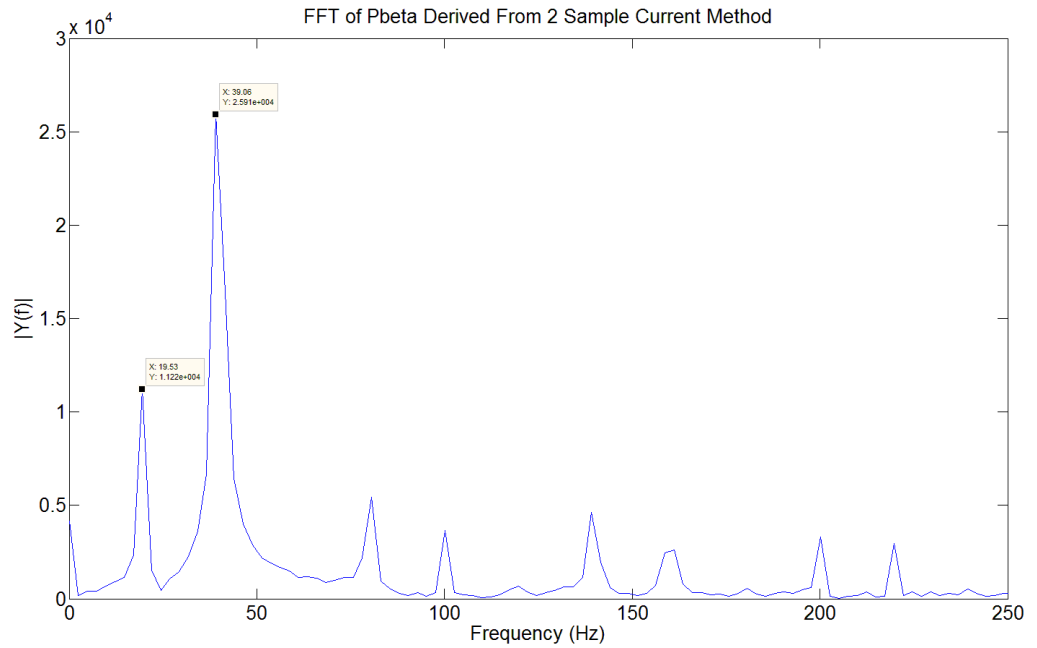


Figure B.13 Two current sample method, 20Hz, 91% Load

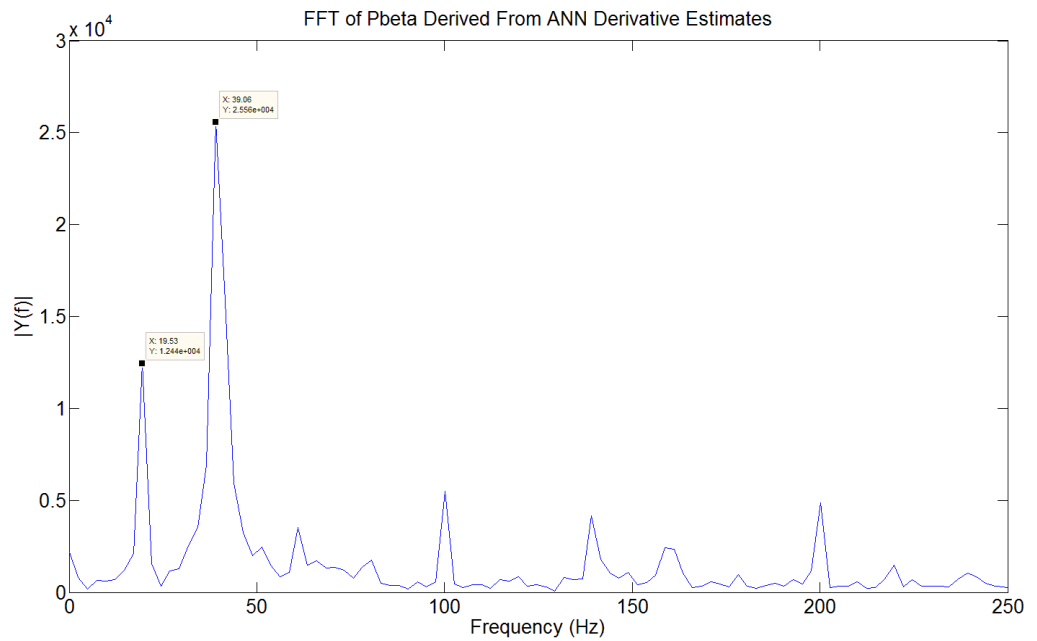


Figure B.14 ANN method, 20Hz, 91% Load

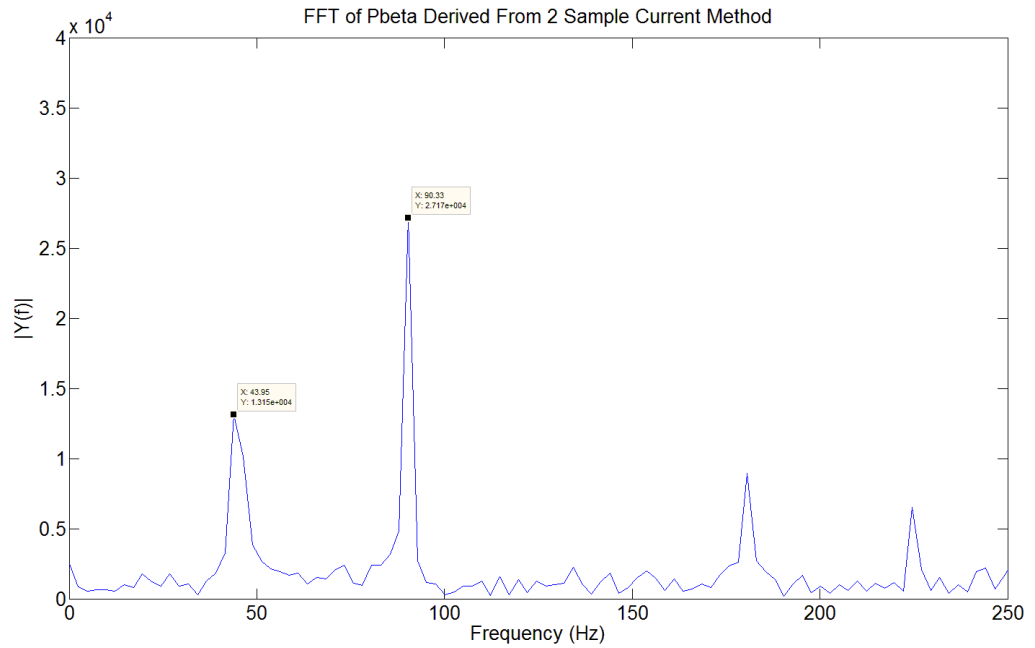


Figure B.15 Two current sample method, 25Hz, No Load

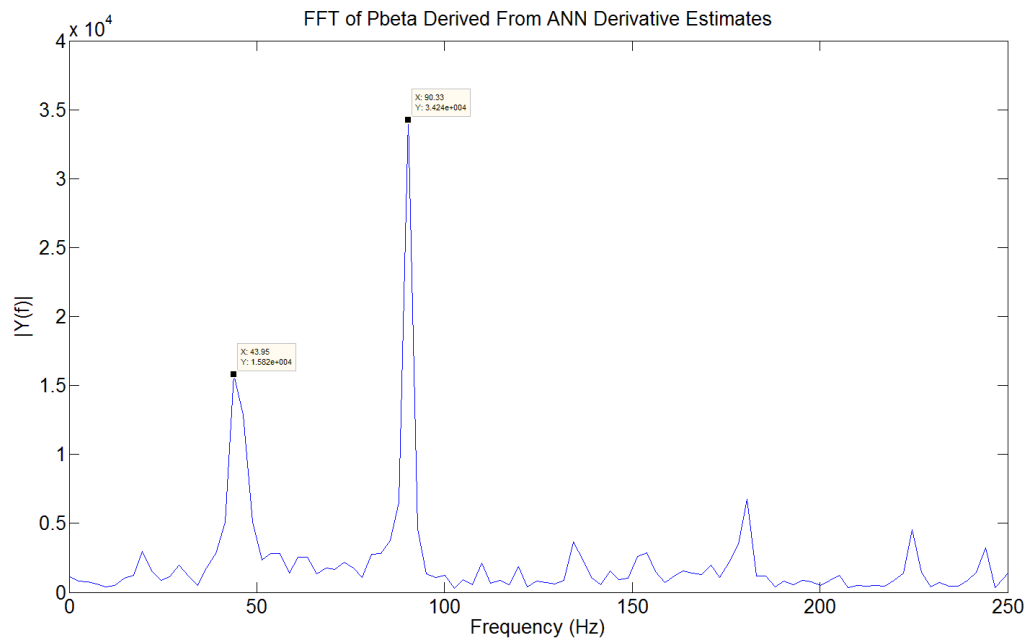


Figure B.16 ANN method, 25Hz, No Load

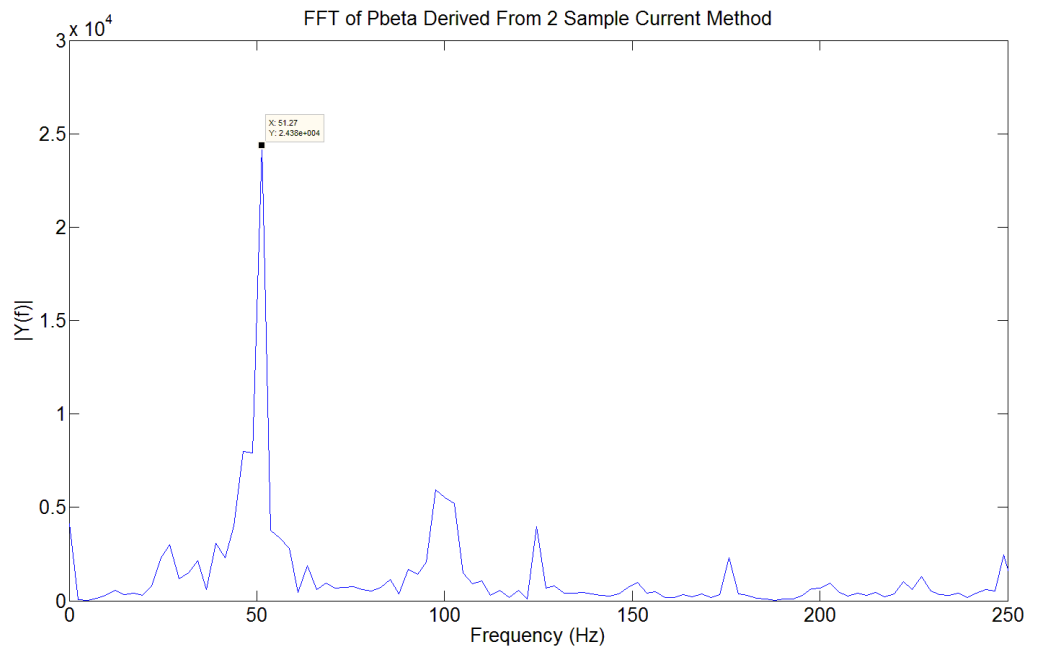


Figure B.17 Two current sample method, 25Hz, 27% Load

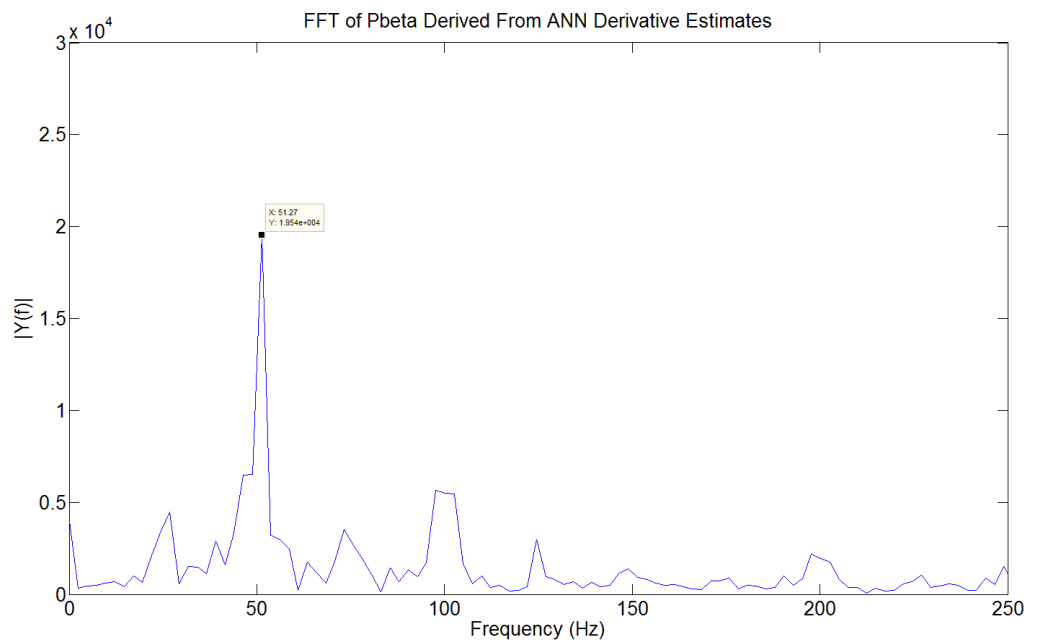


Figure B.18 ANN method, 25Hz, 27% Load

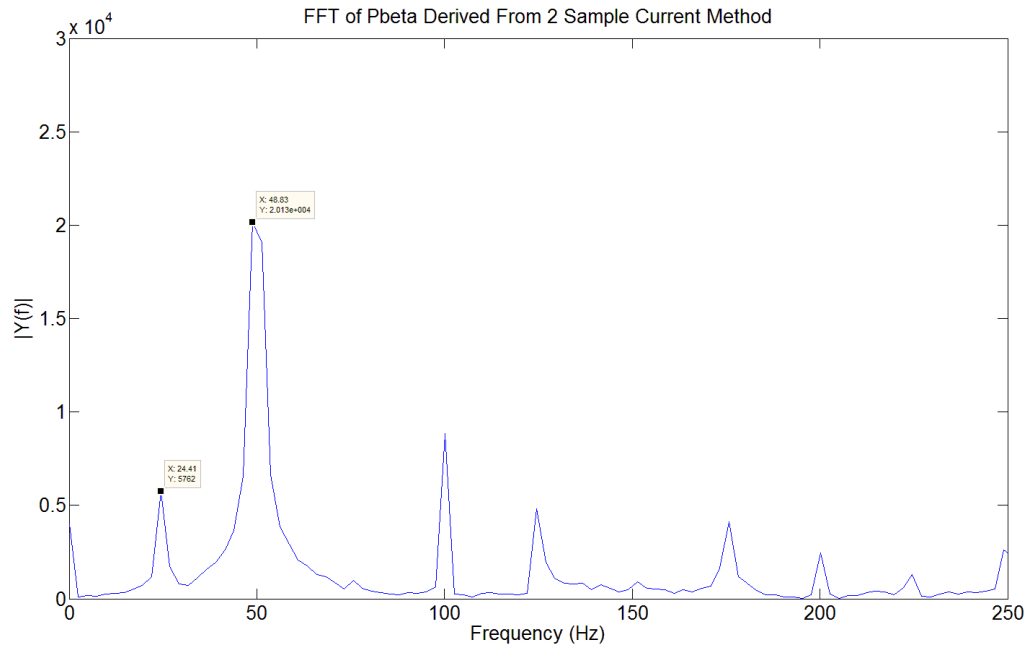


Figure B.19 Two current sample method, 25Hz, 44% Load

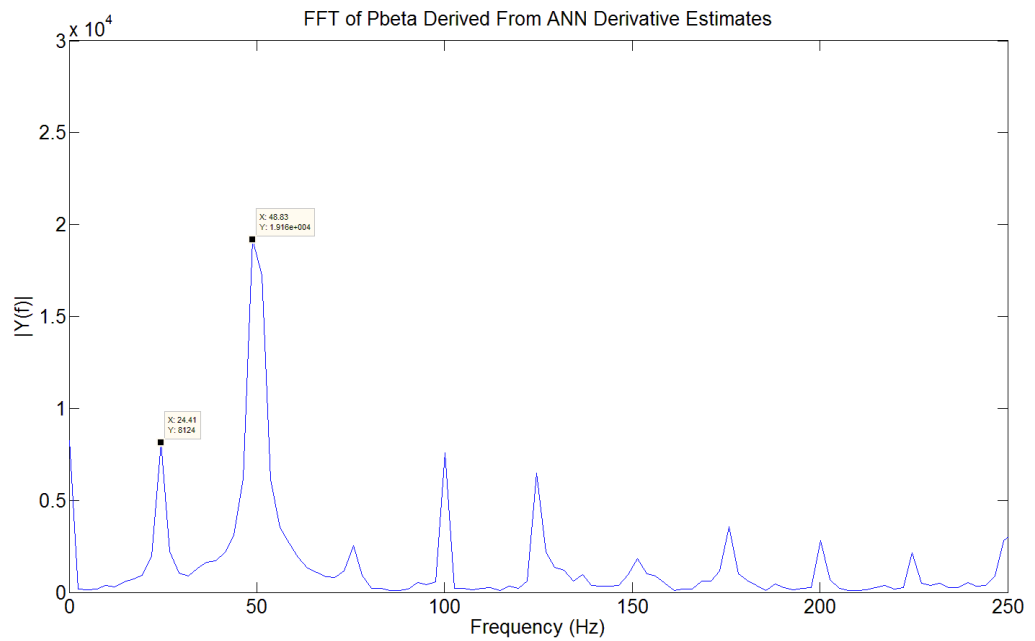


Figure B.20 ANN method, 25Hz, 44% Load

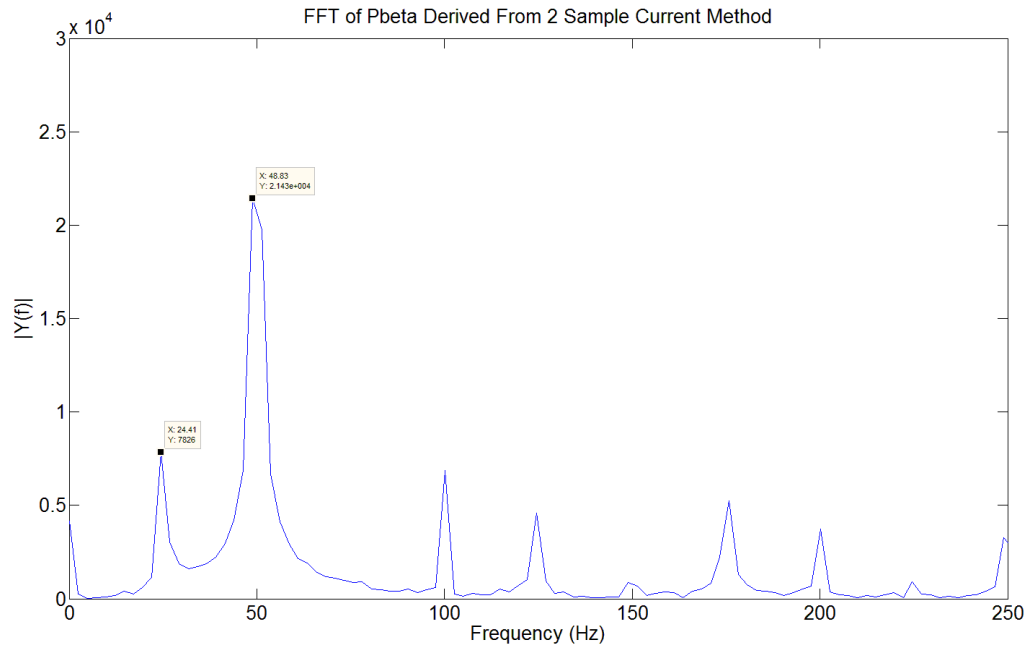


Figure B.21 Two current sample method, 25Hz, 60% Load

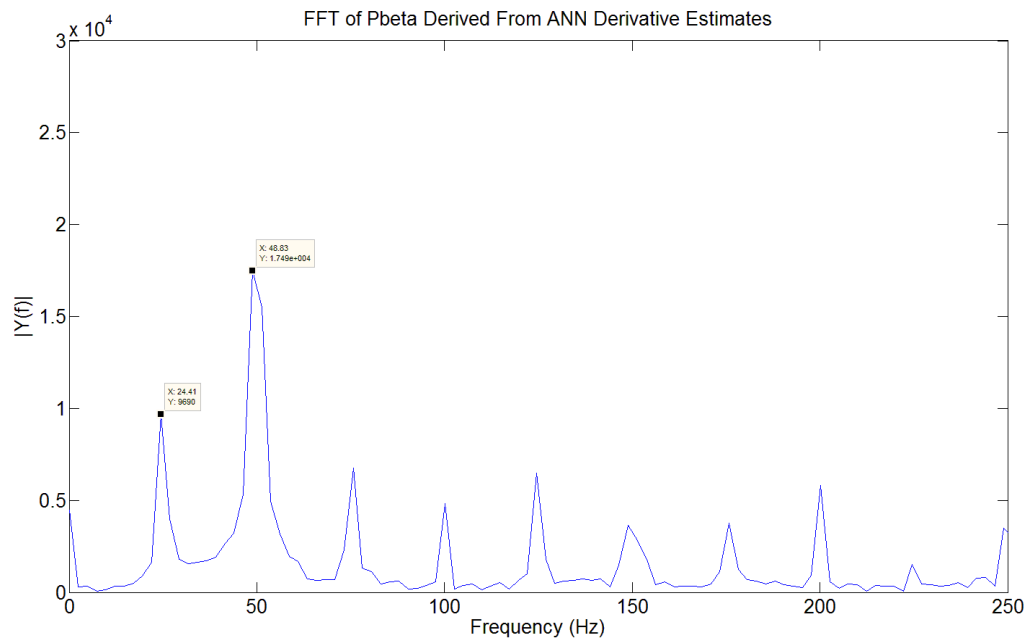


Figure B.22 ANN method, 25Hz, 60% Load

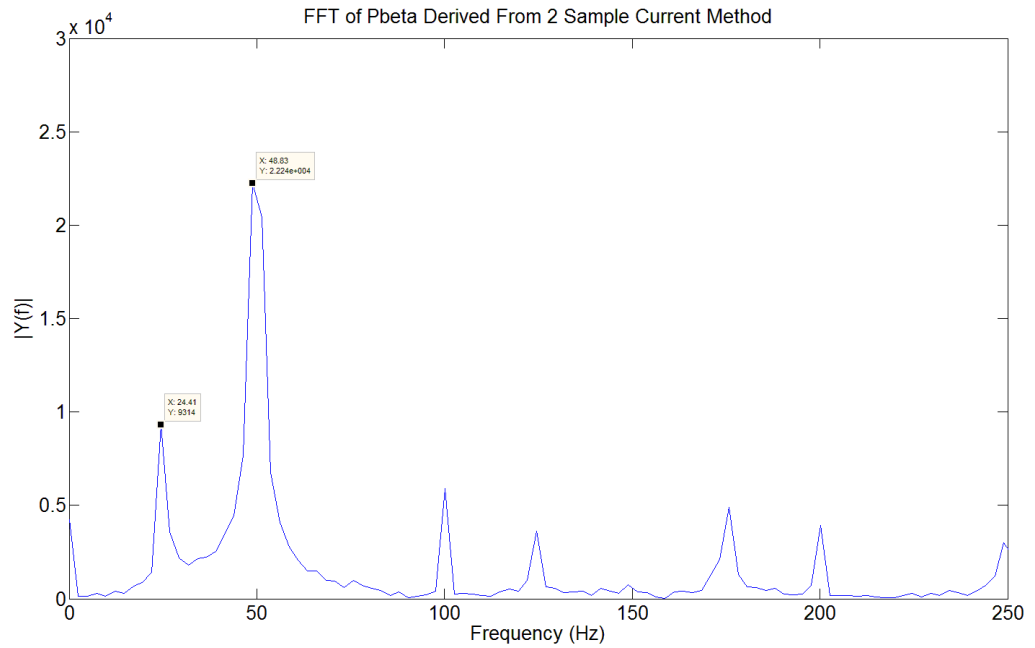


Figure B.23 Two current sample method, 25Hz, 73% Load

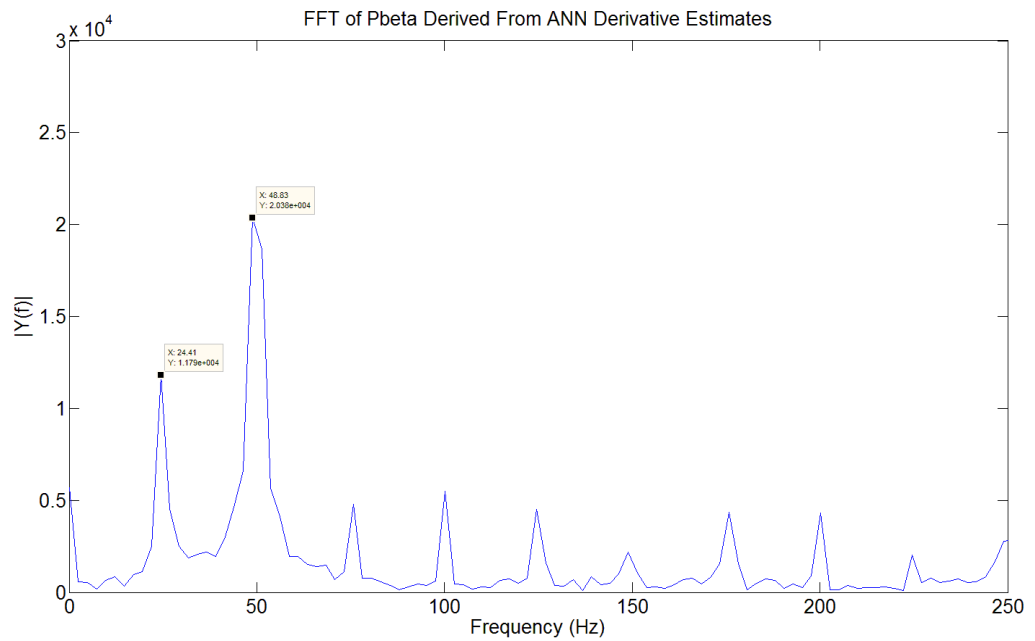


Figure B.24 ANN method, 25Hz, 73% Load

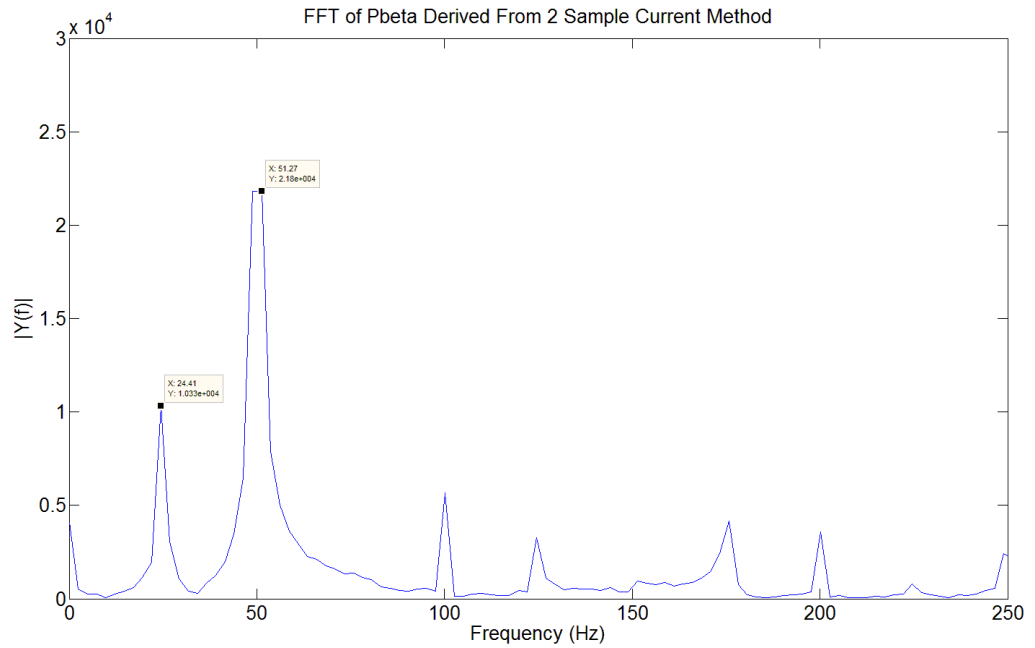


Figure B.25 Two current sample method, 25Hz, 83% Load

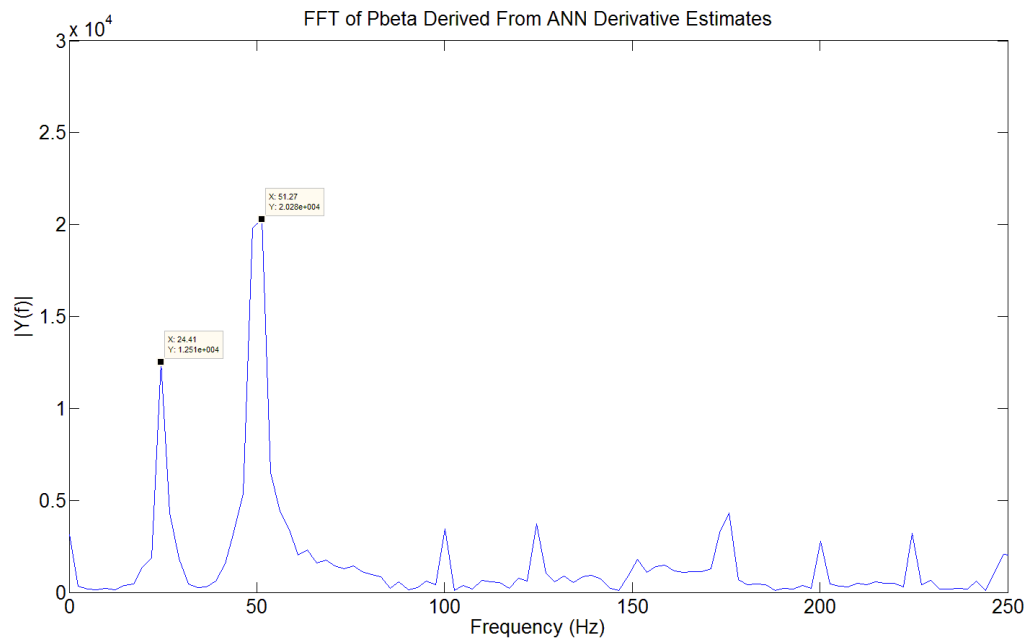


Figure B.26 ANN method, 25Hz, 83% Load

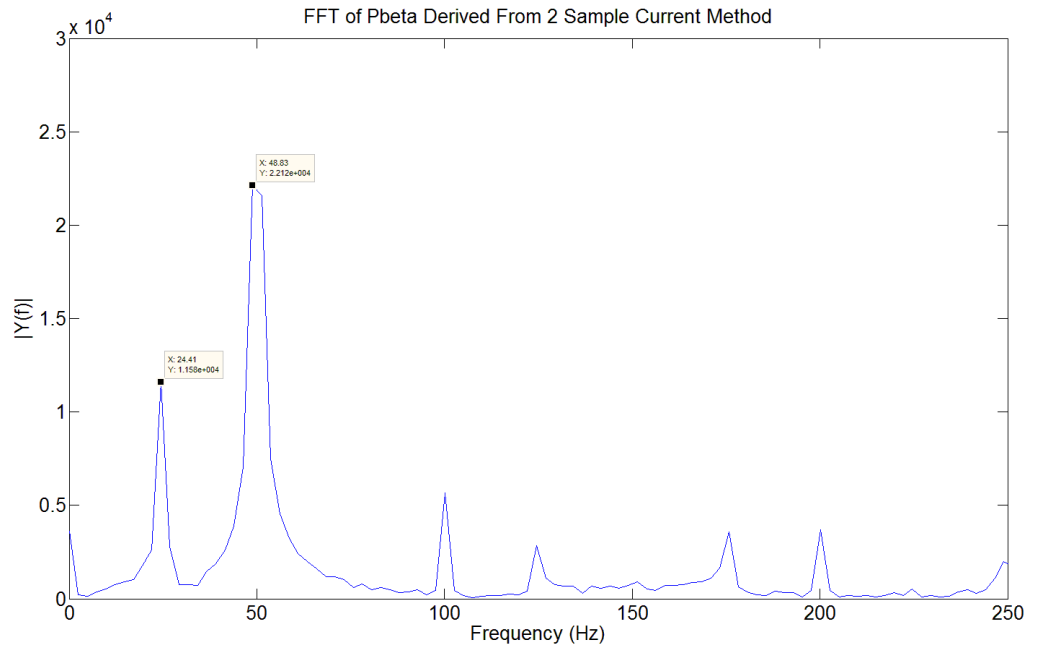


Figure B.27 Two current sample method, 25Hz, 91% Load

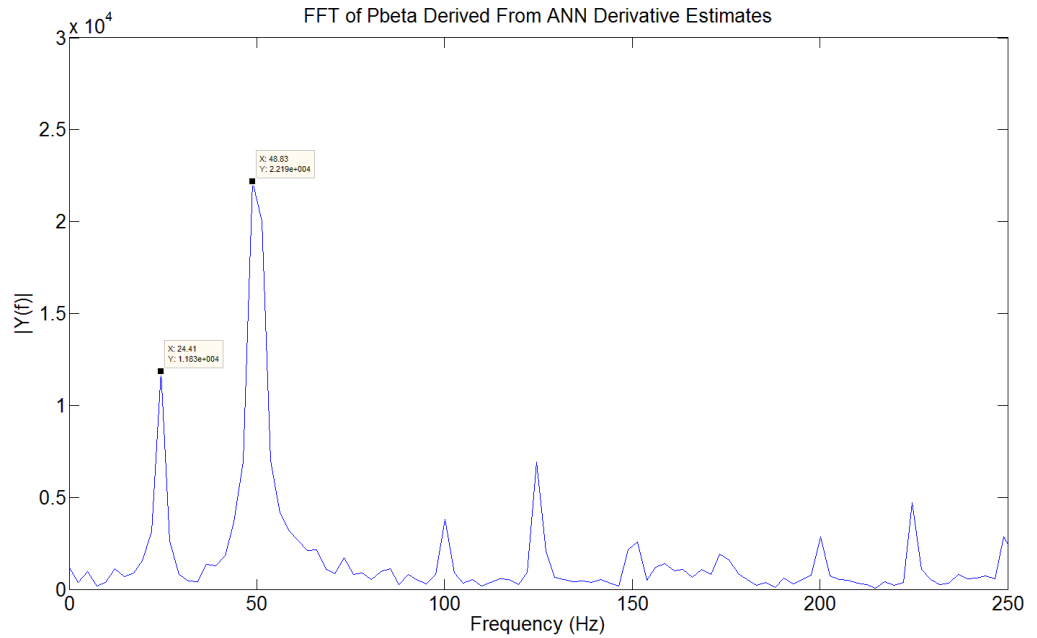


Figure B.28 ANN method, 25Hz, 91% Load

30Hz (Trained Frequency)

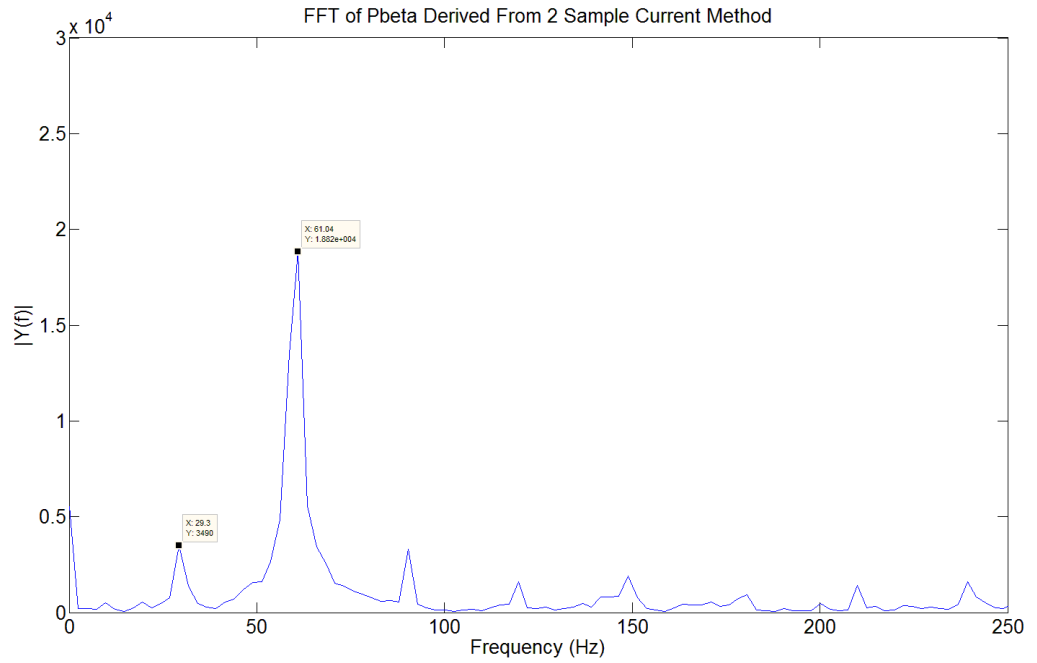


Figure B.29 Two current sample method, 30Hz, No Load

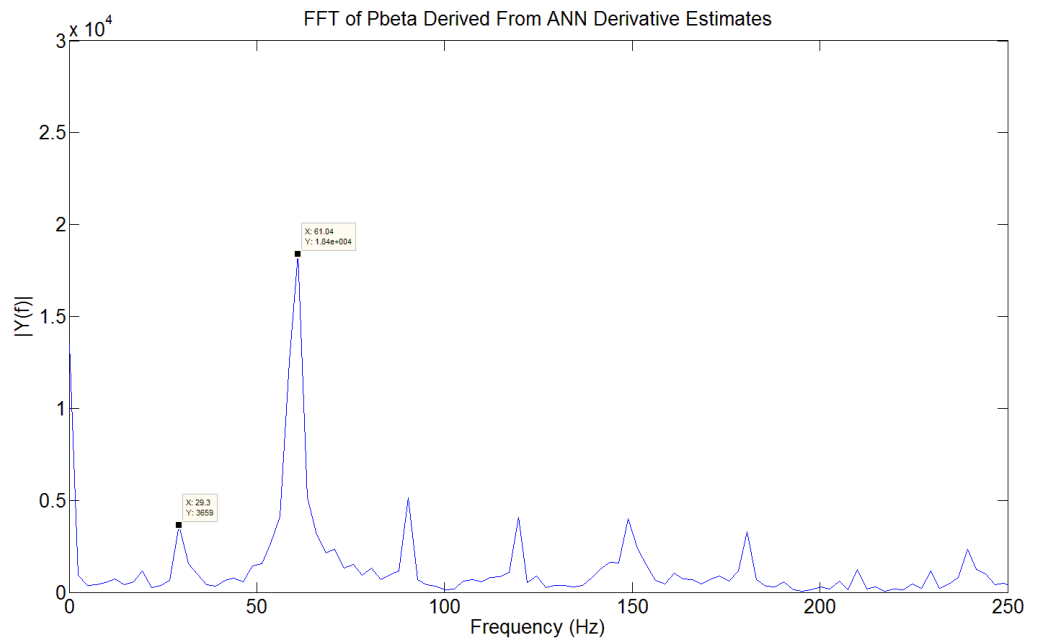


Figure B.30 ANN method, 30Hz, No Load

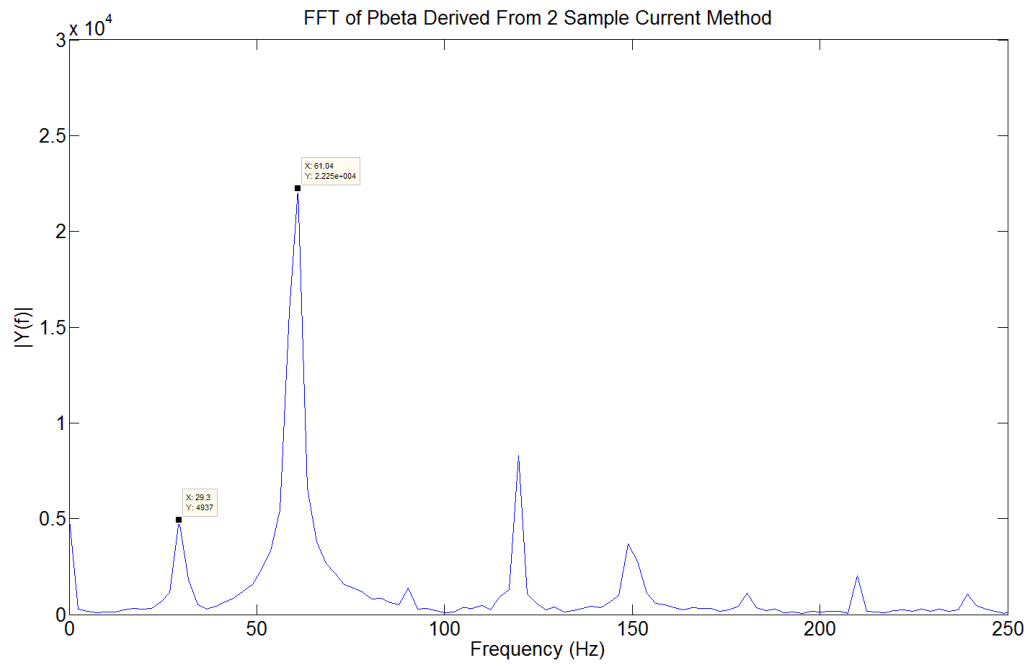


Figure B.31 Two current sample method, 30Hz, 27% Load

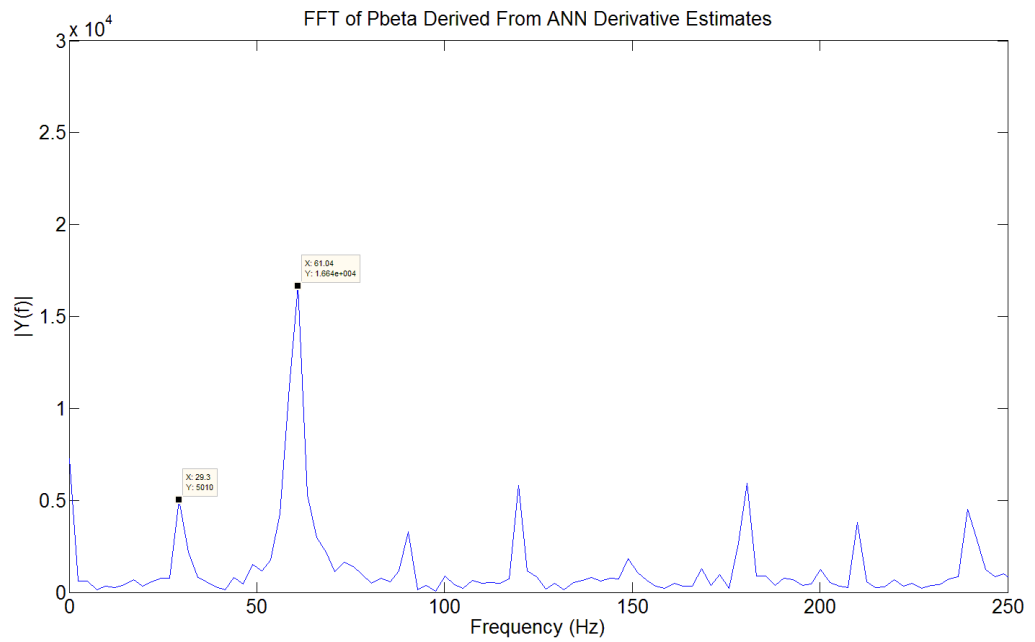


Figure B.32 ANN method, 30Hz, 27% Load

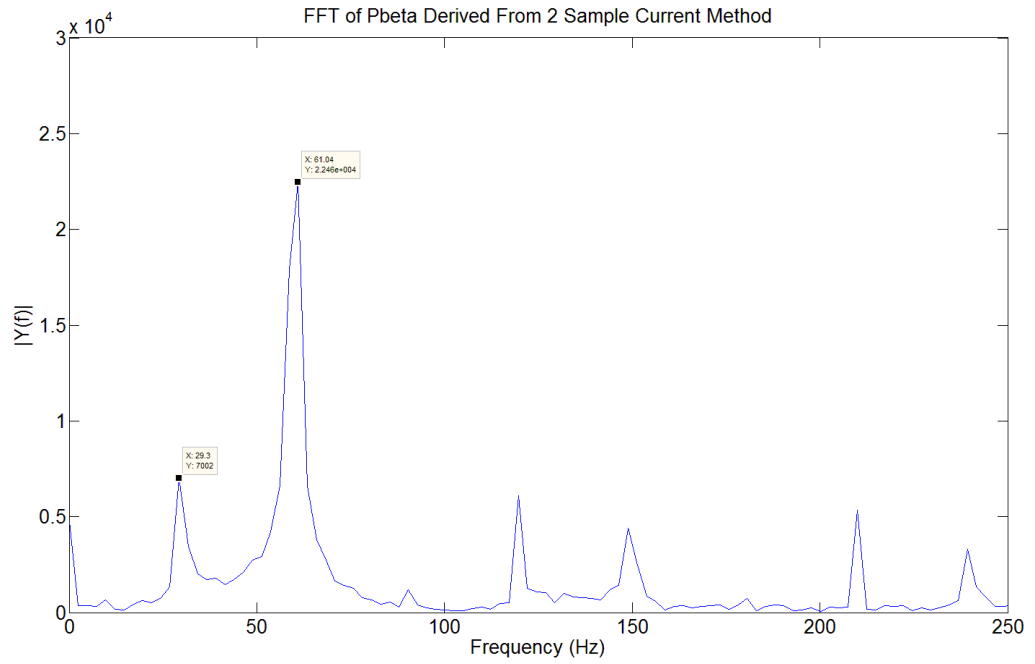


Figure B.33 Two current sample method, 30Hz, 44% Load

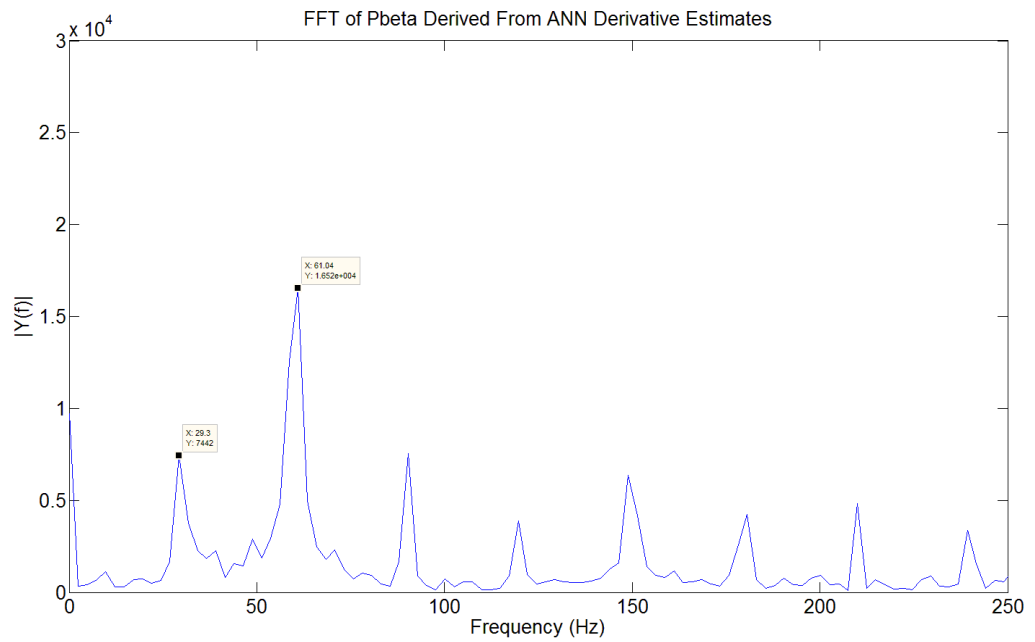


Figure B.34 ANN method, 30Hz, 44% Load

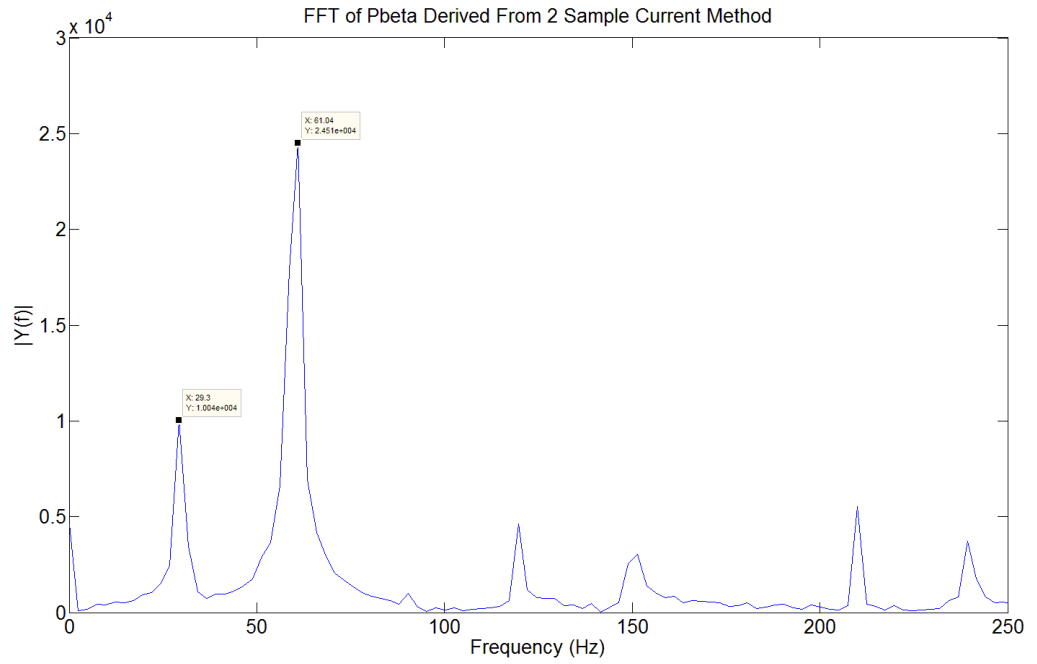


Figure B.35 Two current sample method, 30Hz, 60% Load

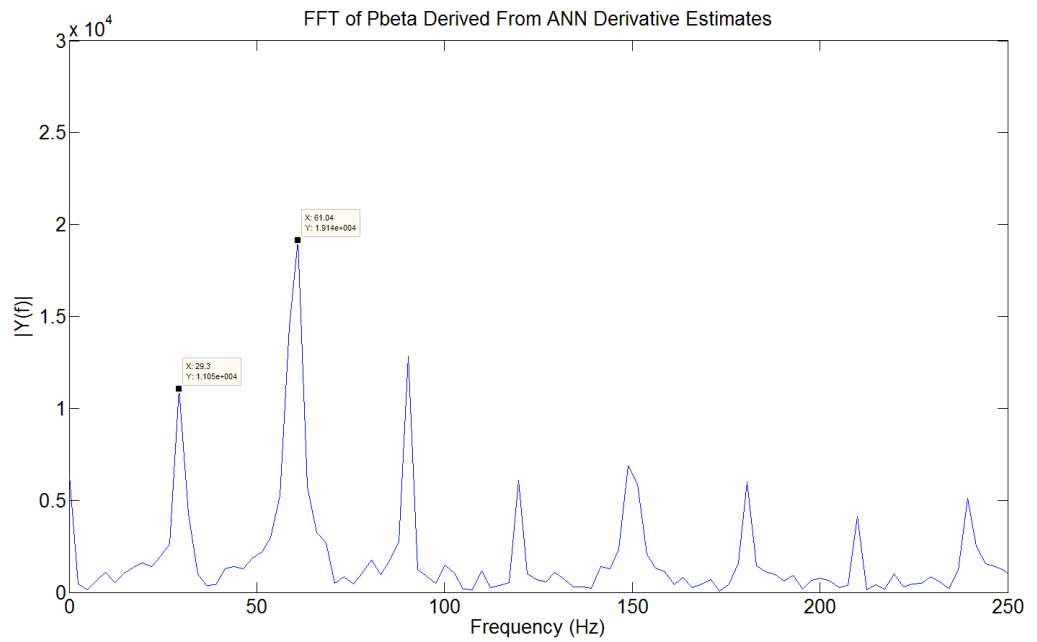


Figure B.36 ANN method, 30Hz, 60% Load

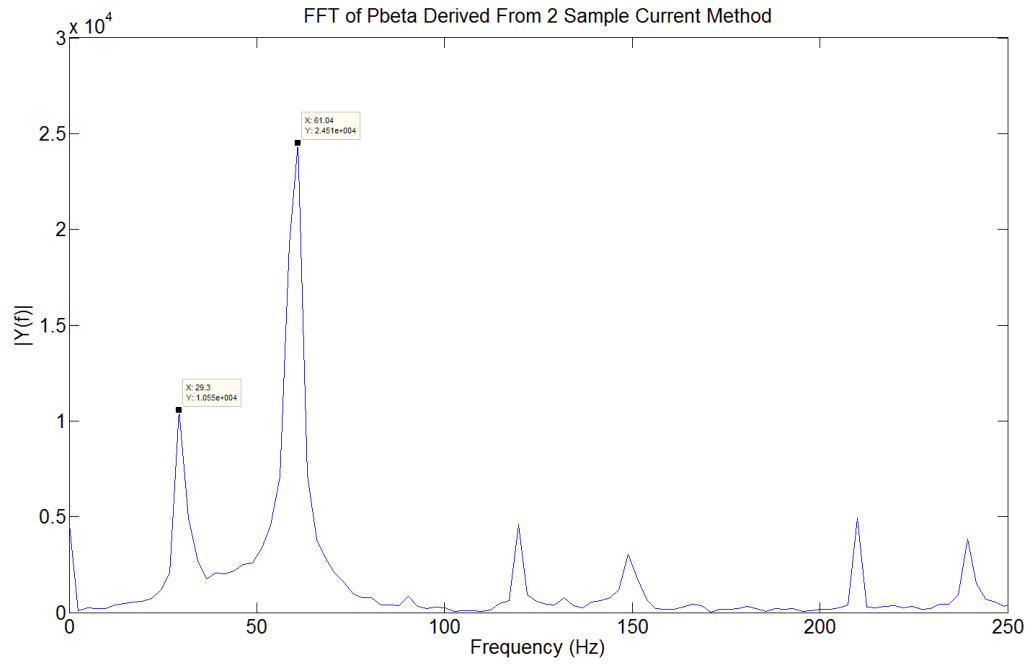


Figure B.37 Two current sample method, 30Hz, 73% Load

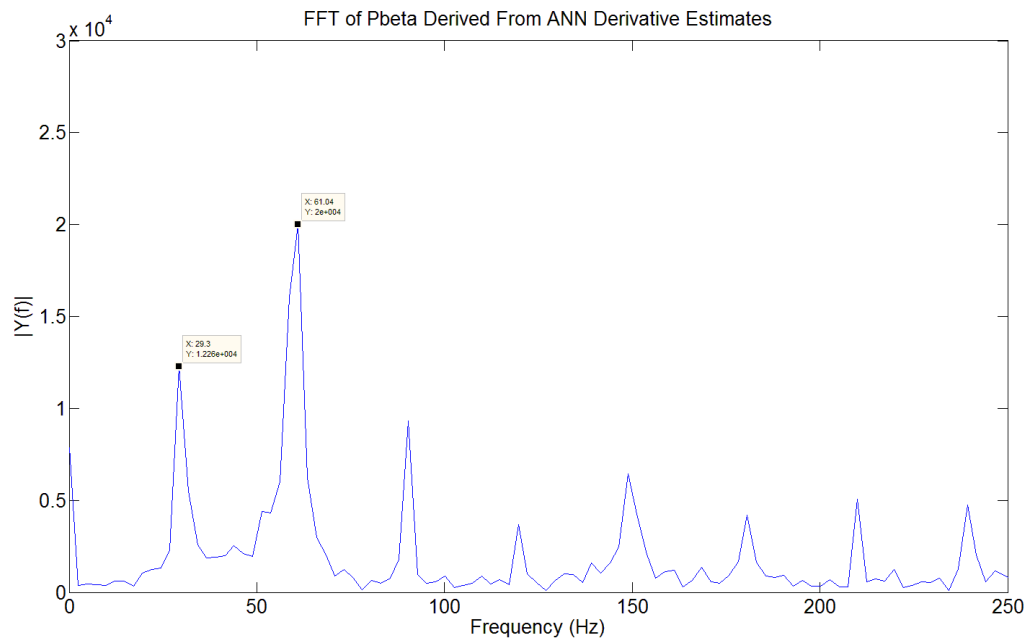


Figure B.38 ANN method, 30Hz, 73% Load

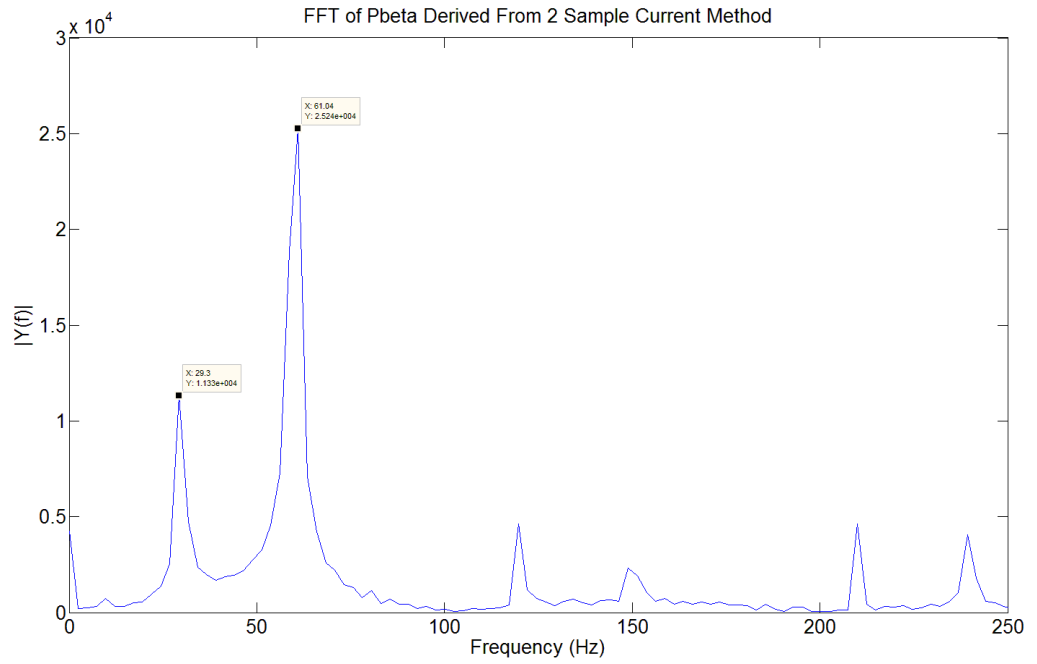


Figure B.39 Two current sample method, 30Hz, 83% Load

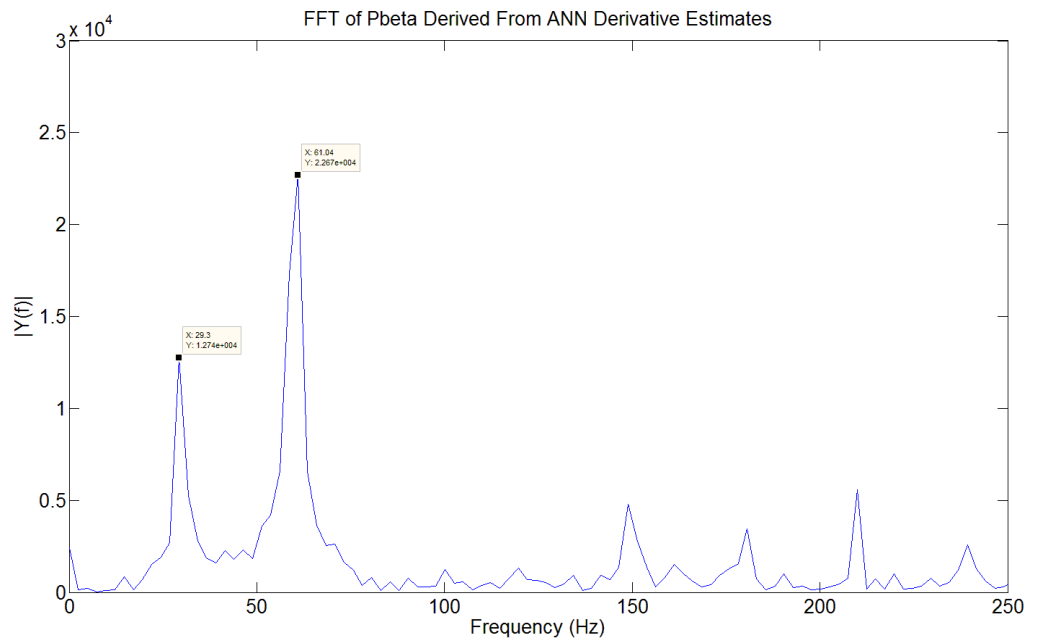


Figure B.40 ANN method, 30Hz, 83% Load

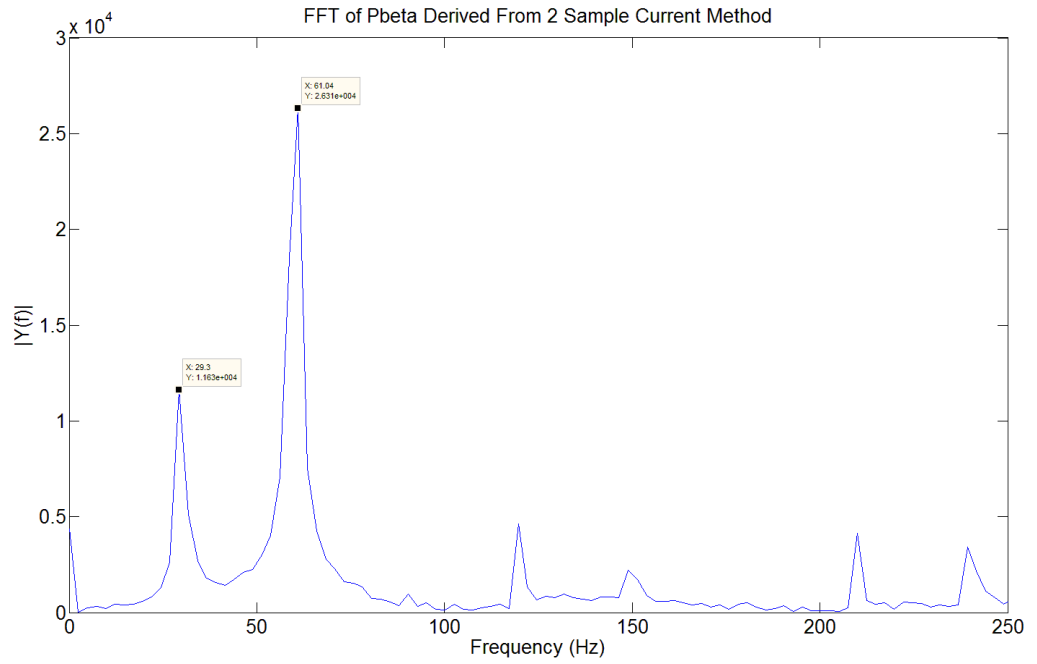


Figure B.41 Two current sample method, 30Hz, 91% Load

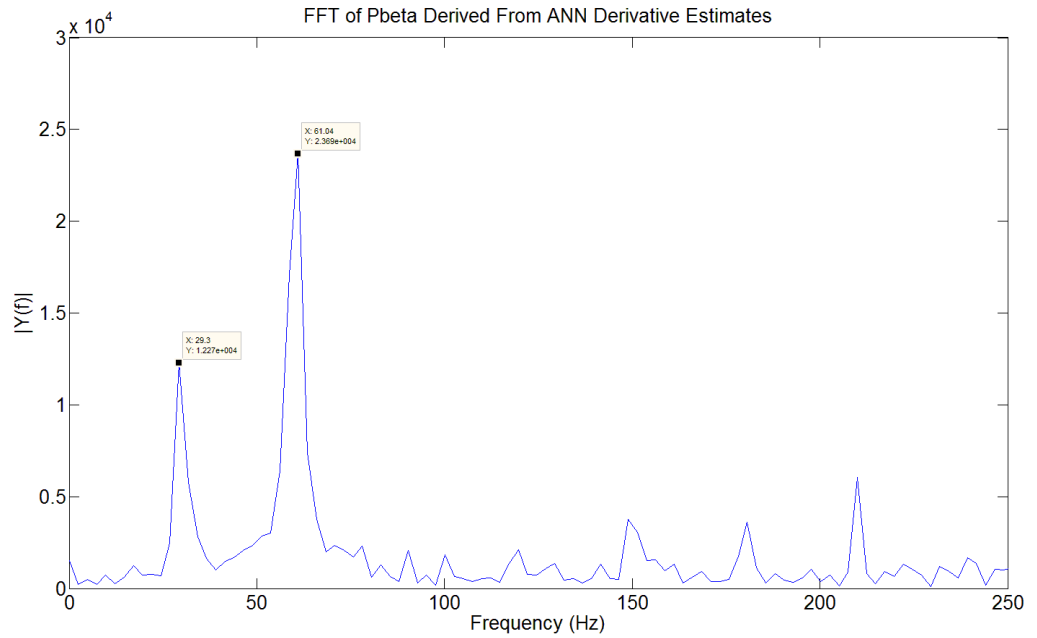


Figure B.42 ANN method, 30Hz, 91% Load

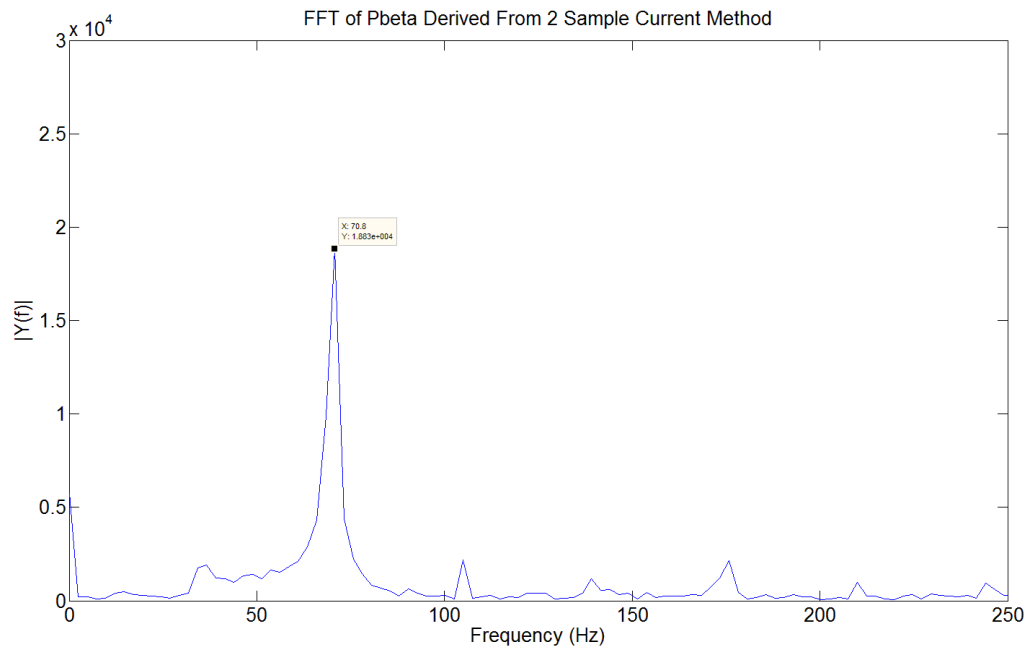


Figure B.43 Two current sample method, 35Hz, No Load

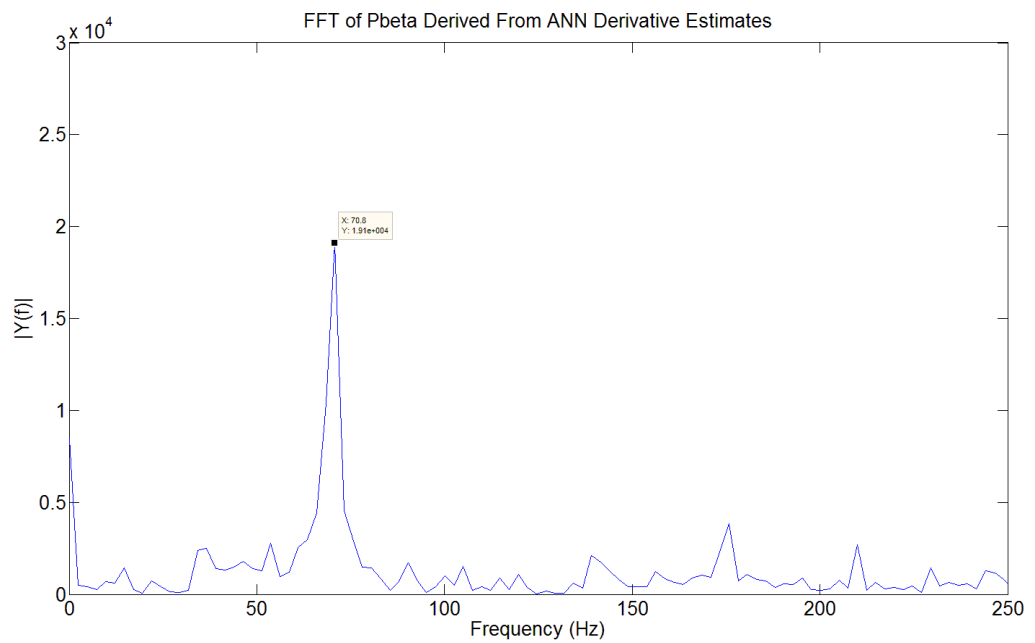


Figure B.44 ANN method, 35Hz, No Load

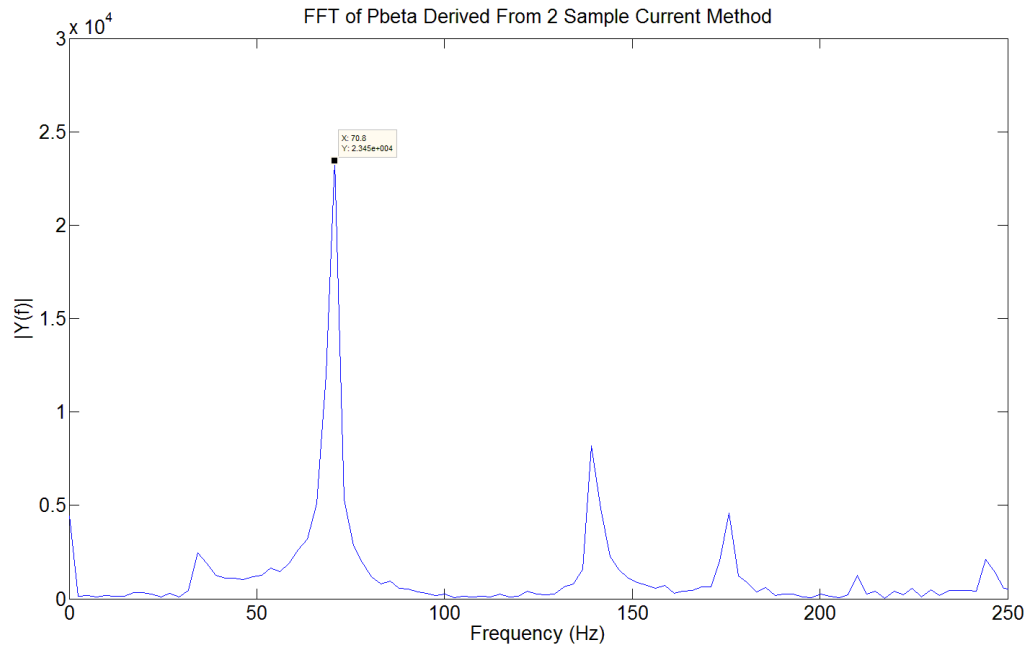


Figure B.45 Two current sample method, 35Hz, 27% Load

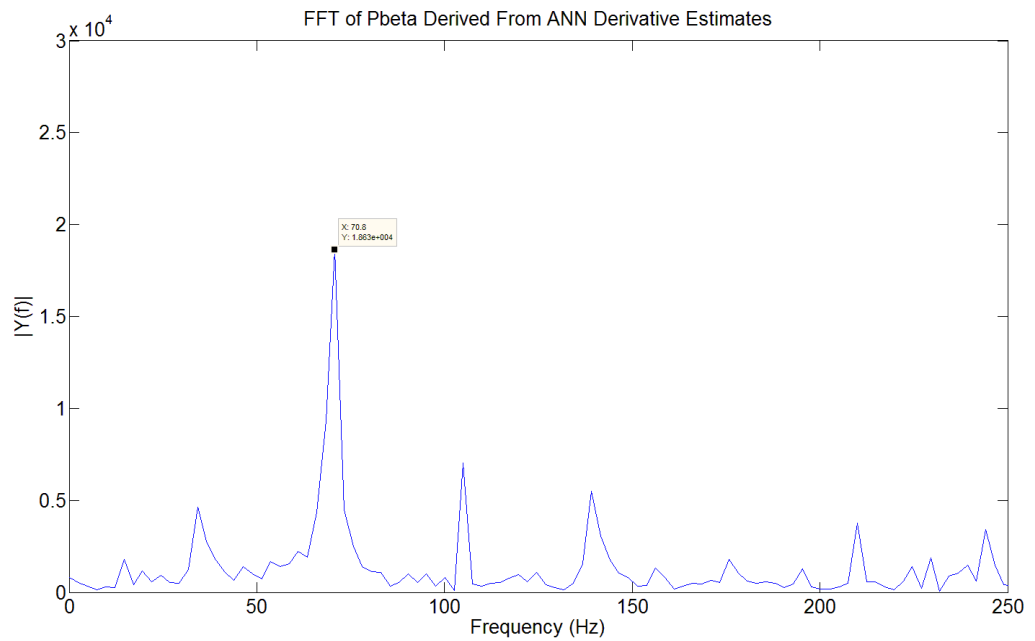


Figure B.46 ANN method, 35Hz, 27% Load

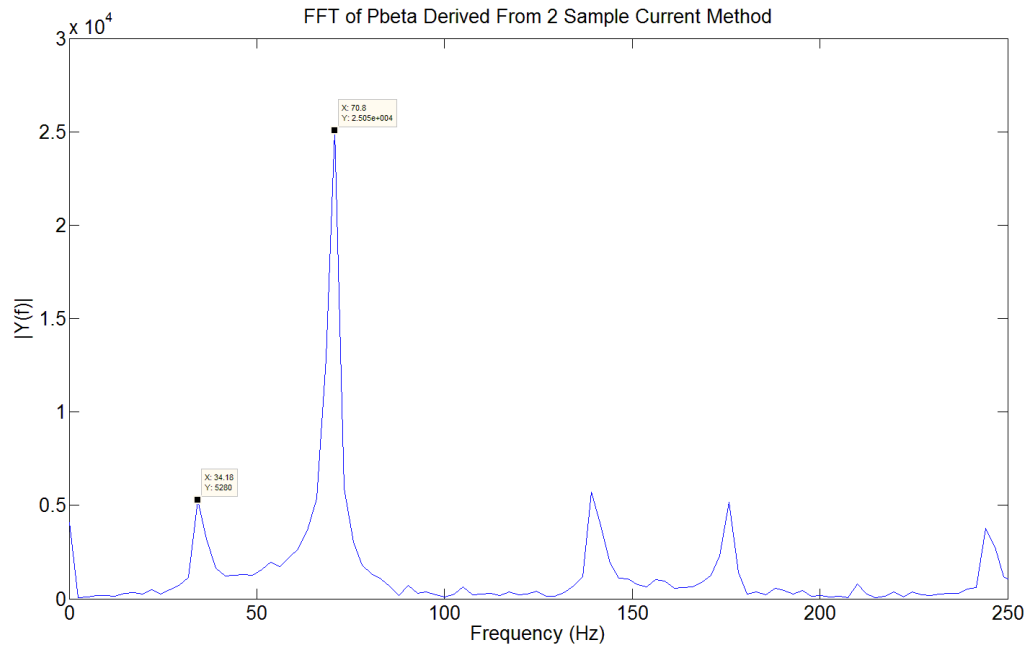


Figure B.47 Two current sample method, 35Hz, 44% Load

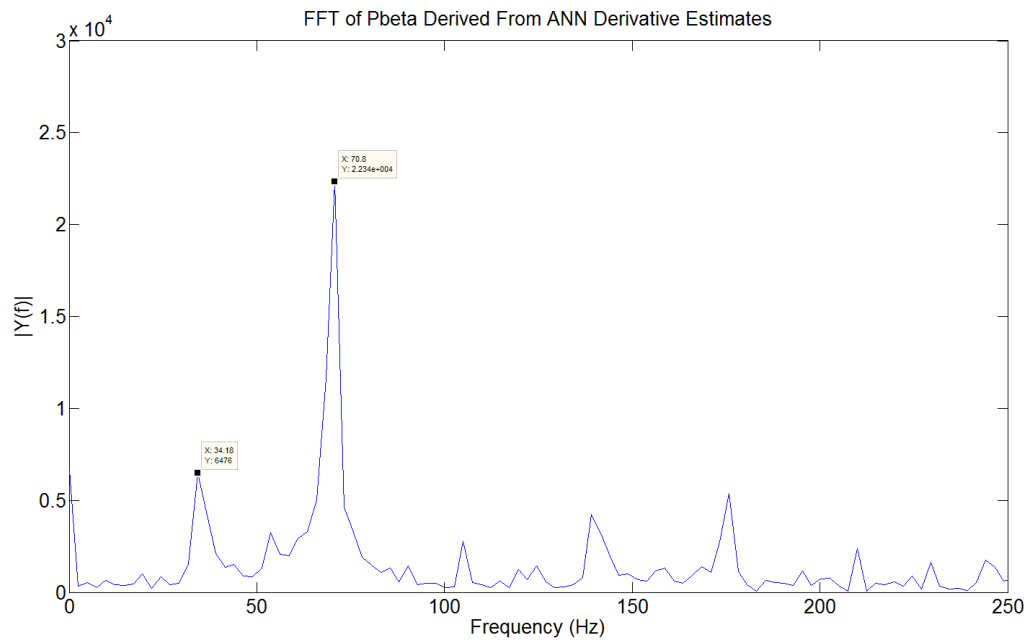


Figure B.48 ANN method, 35Hz, 44% Load

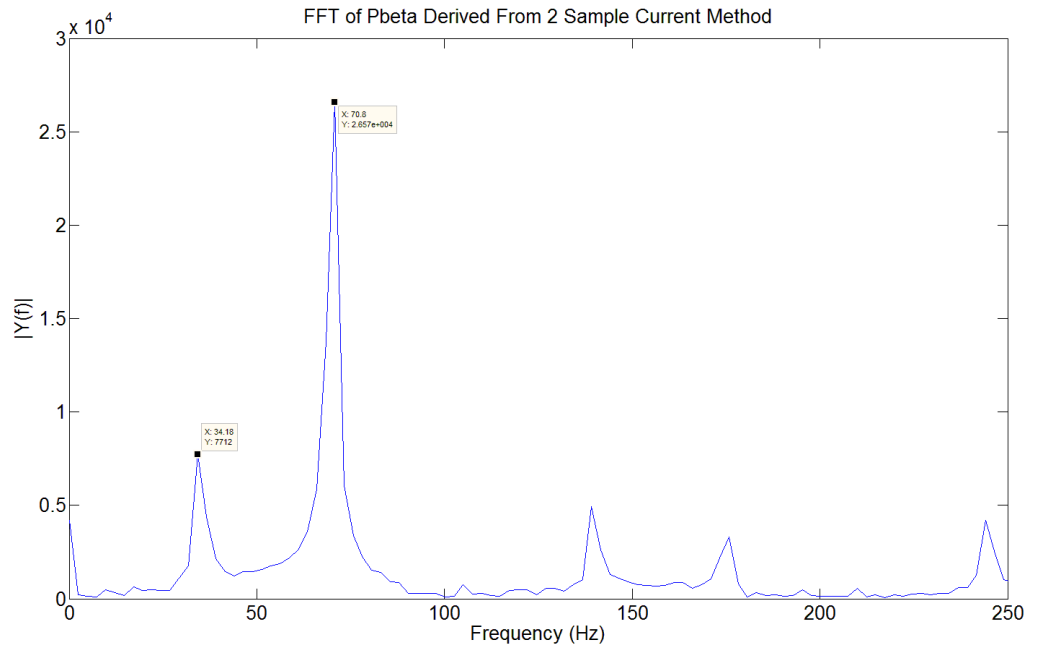


Figure B.49 Two current sample method, 35Hz, 60% Load

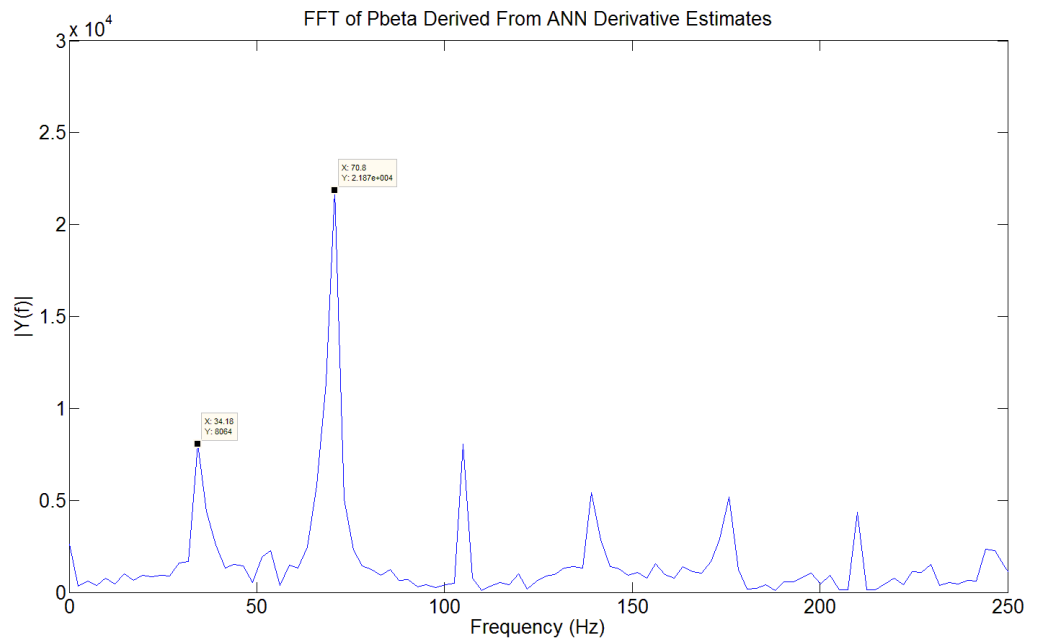


Figure B.50 ANN method, 35Hz, 60% Load

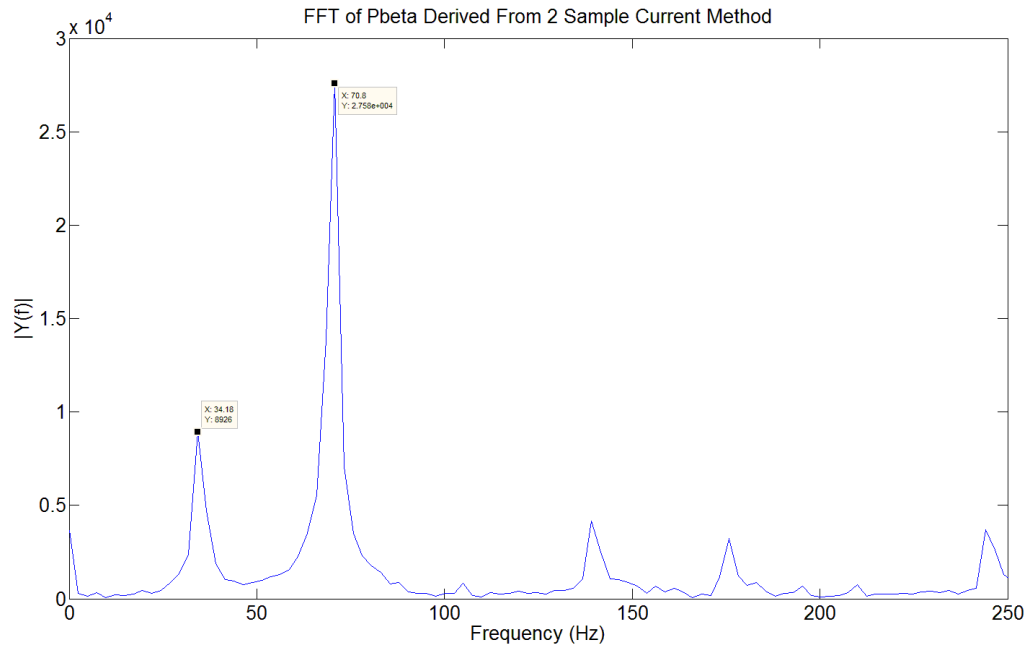


Figure B.51 Two current sample method, 35Hz, 73% Load

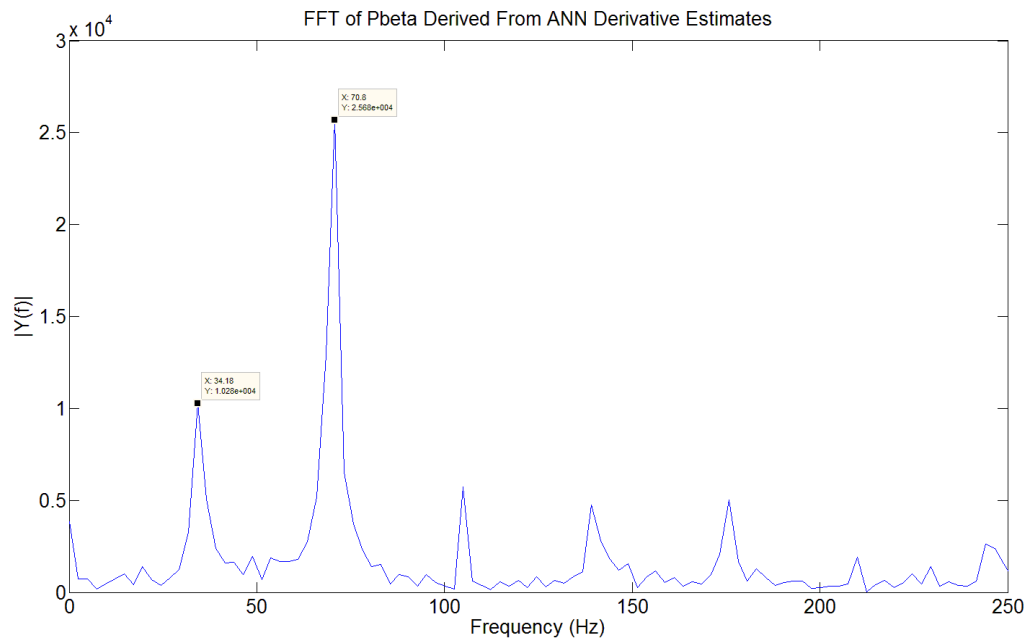


Figure B.52 ANN method, 35Hz, 73% Load

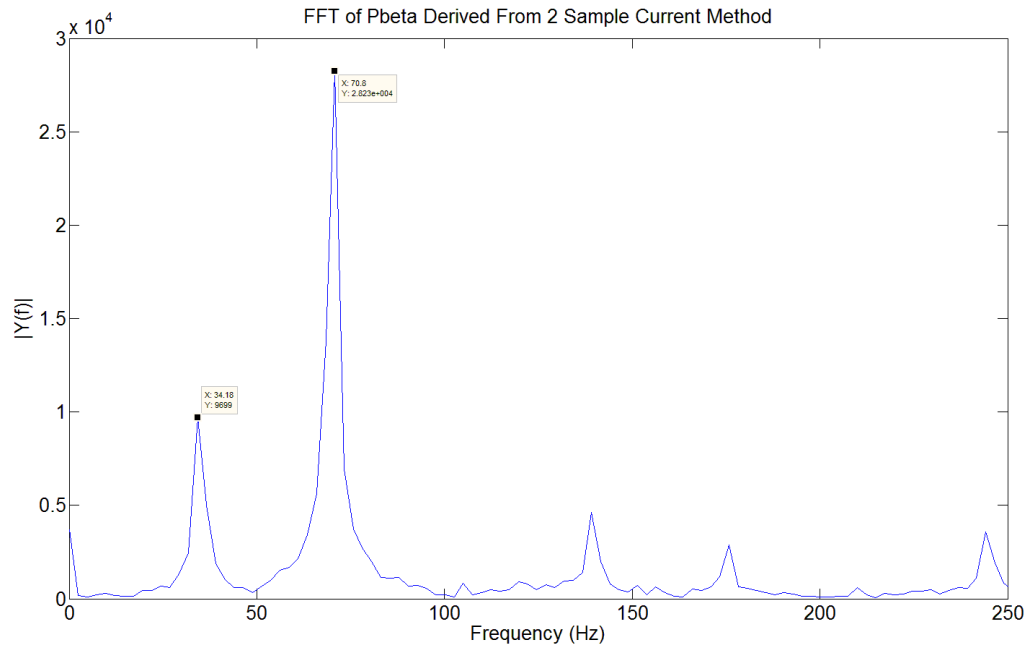


Figure B.53 Two current sample method, 35Hz, 83% Load

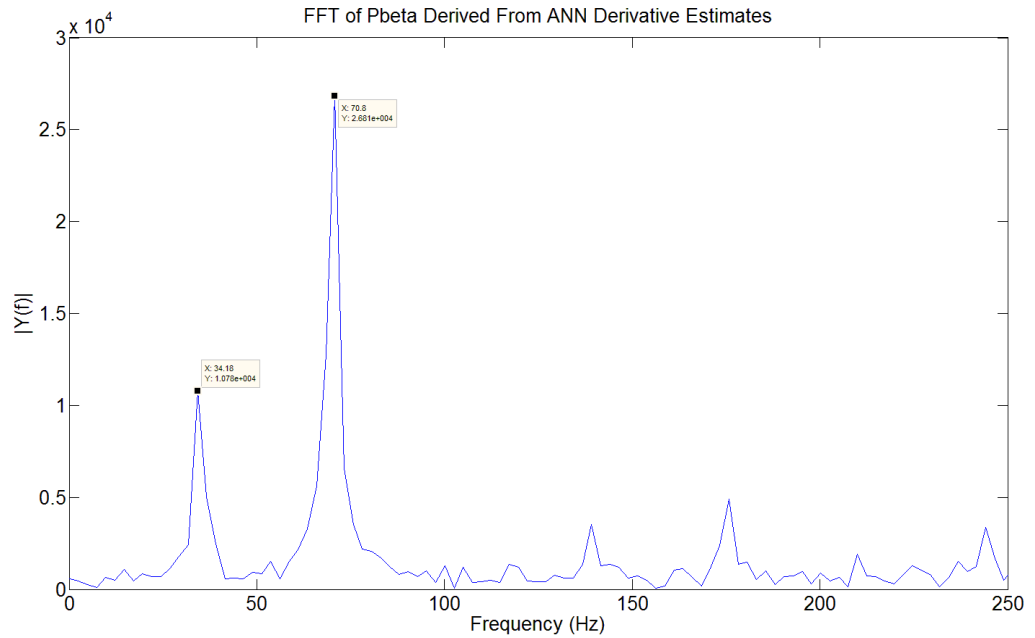


Figure B.54 ANN method, 35Hz, 83% Load

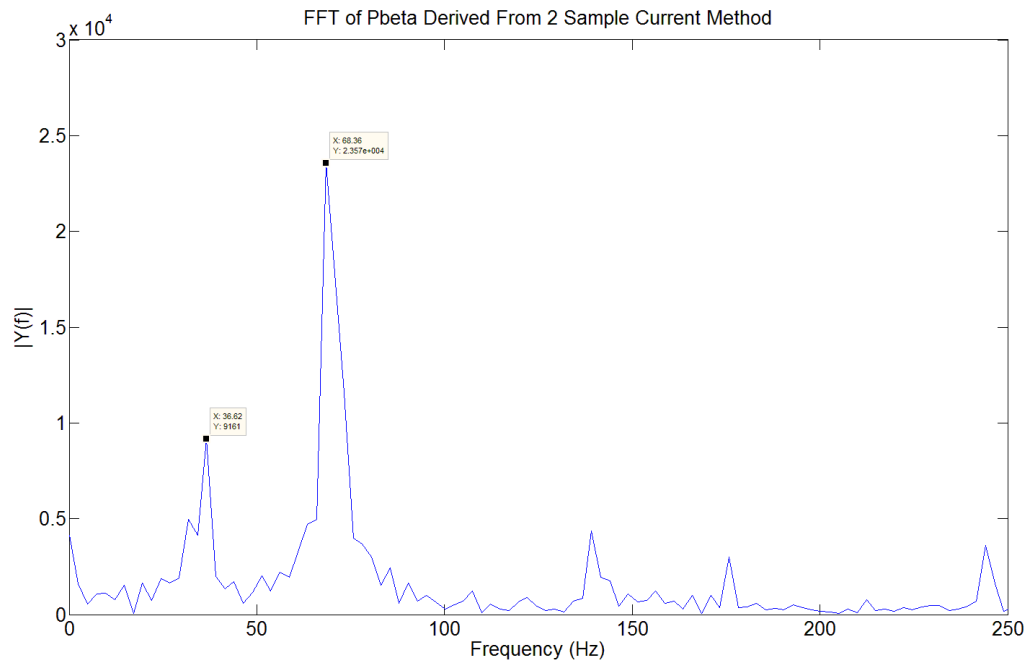


Figure B.55 Two current sample method, 35Hz, 91% Load

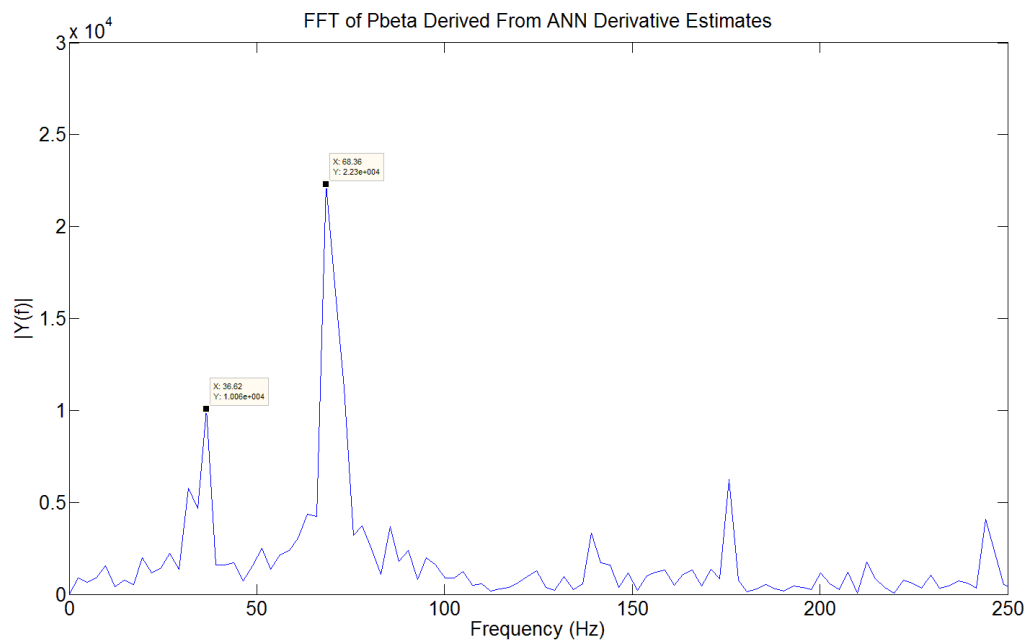


Figure B.56 ANN method, 35Hz, 91% Load

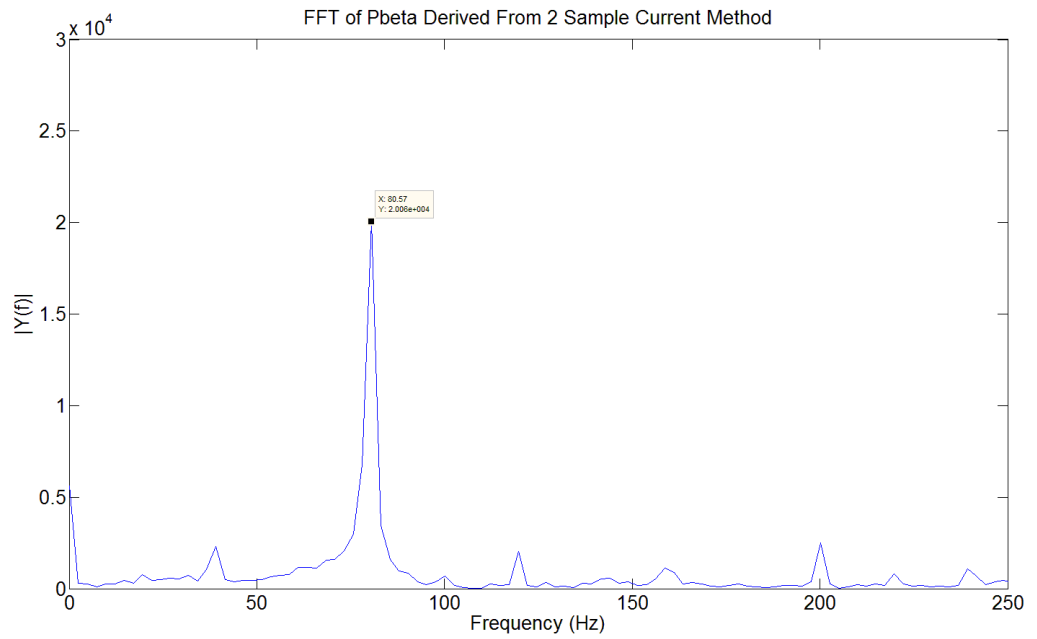


Figure B.57 Two current sample method, 40Hz, No Load

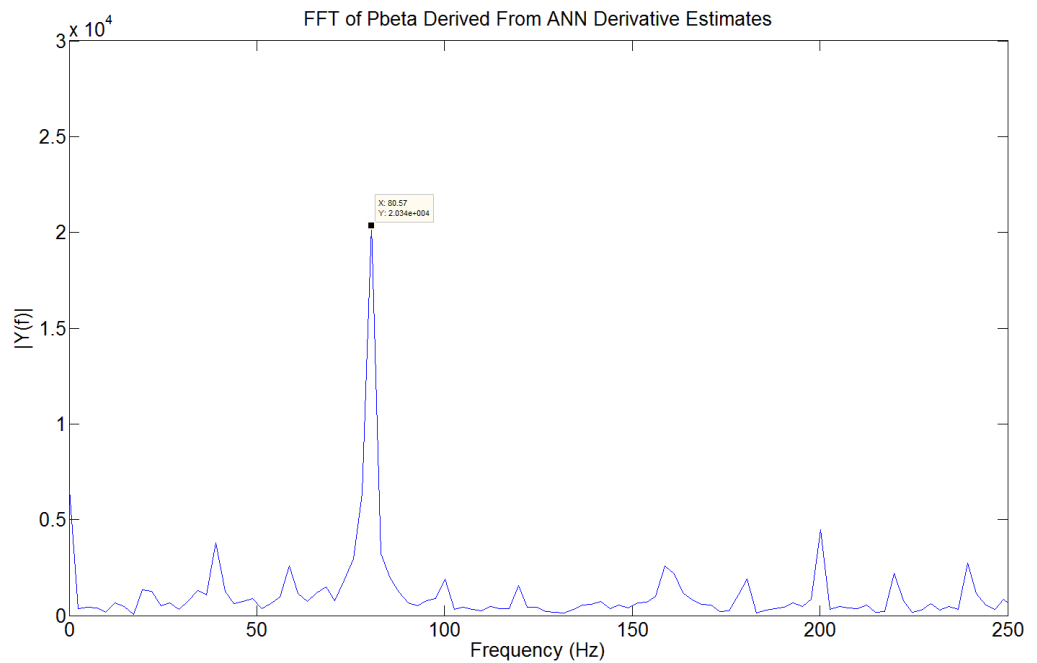


Figure B.58 ANN method, 40Hz, No Load

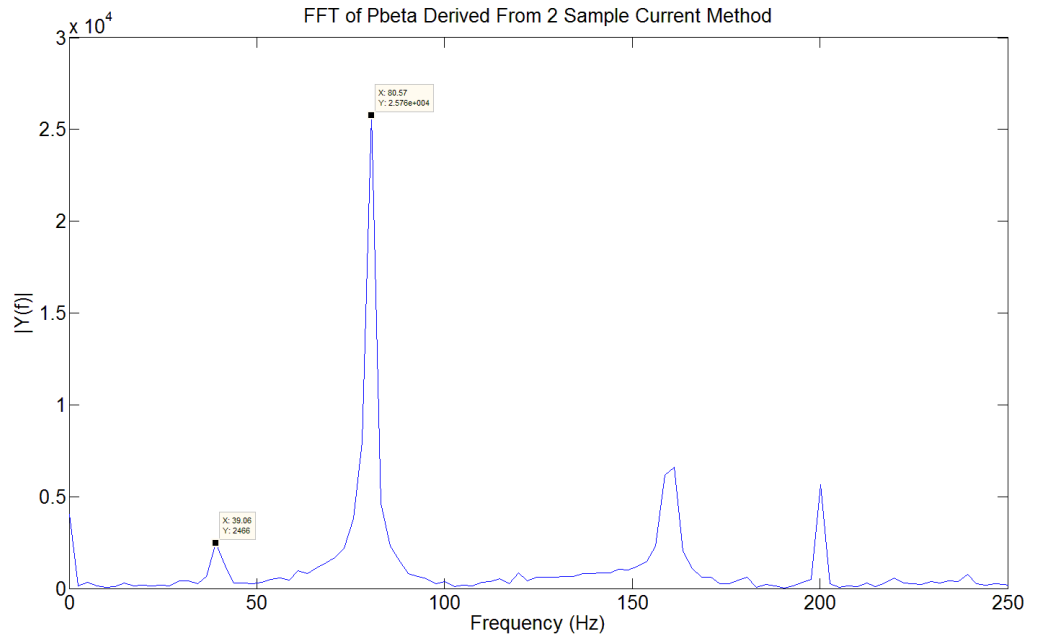


Figure B.59 Two current sample method, 40Hz, 27% Load

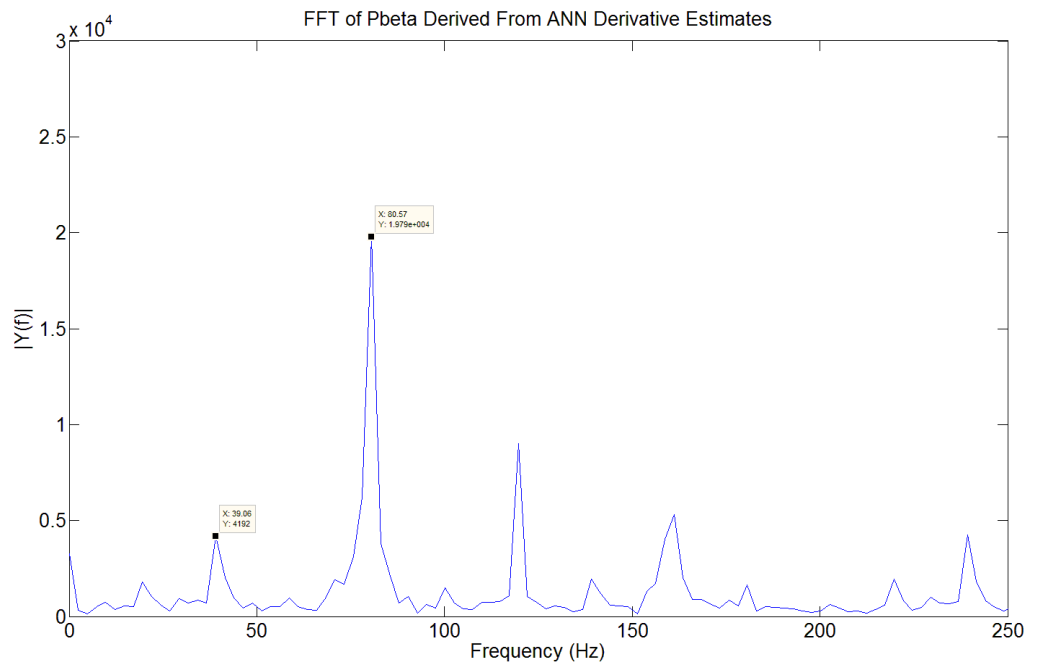


Figure B.60 ANN method, 40Hz, 27% Load

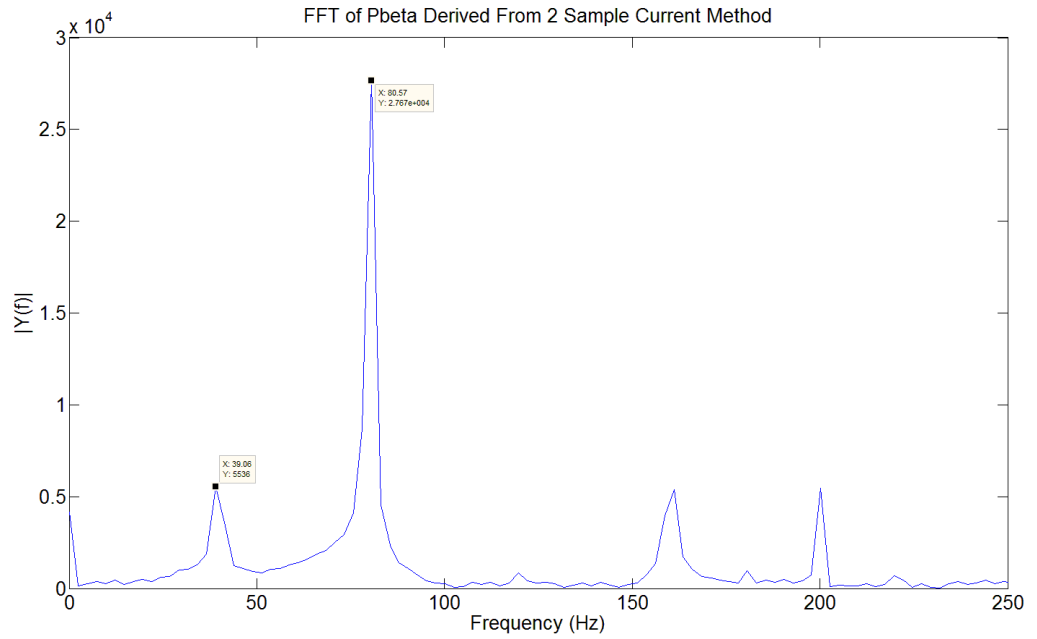


Figure B.61 Two current sample method, 40Hz, 44% Load

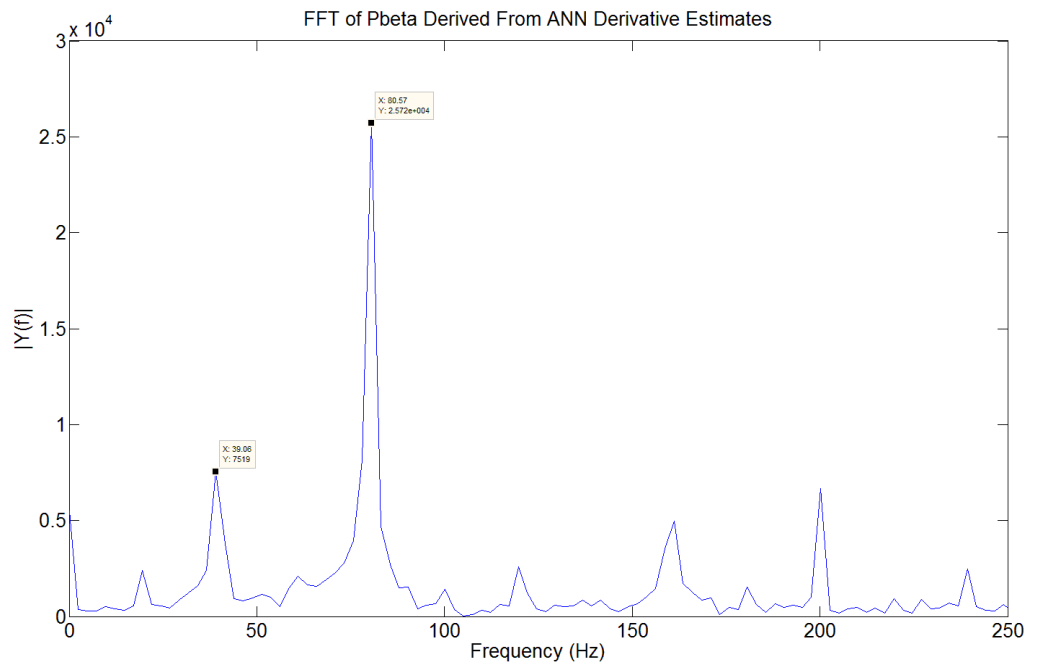


Figure B.62 ANN method, 40Hz, 44% Load

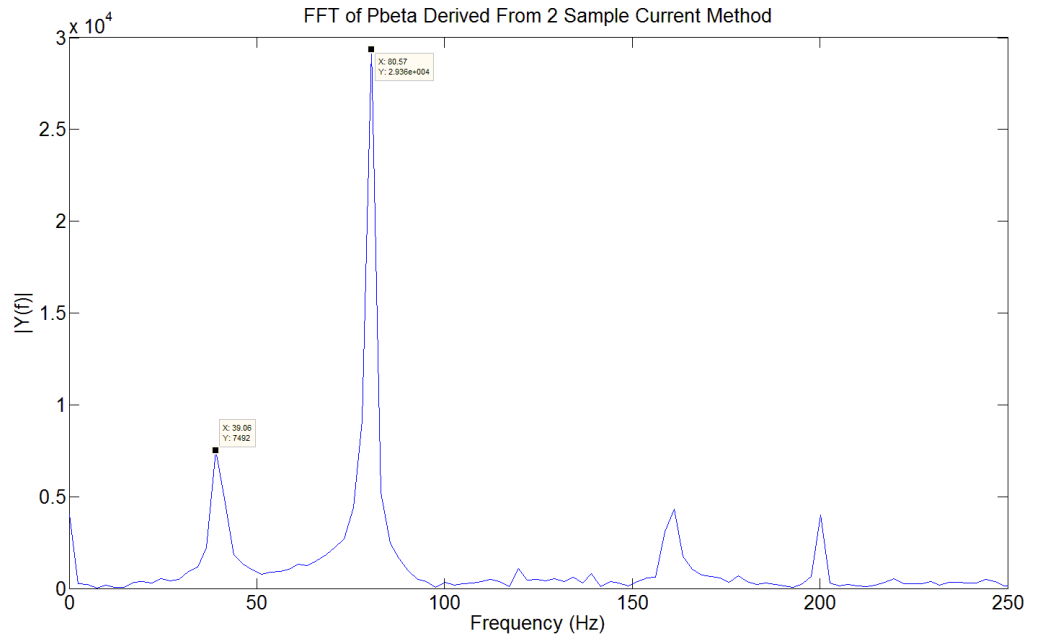


Figure B.63 Two current sample method, 40Hz, 60% Load

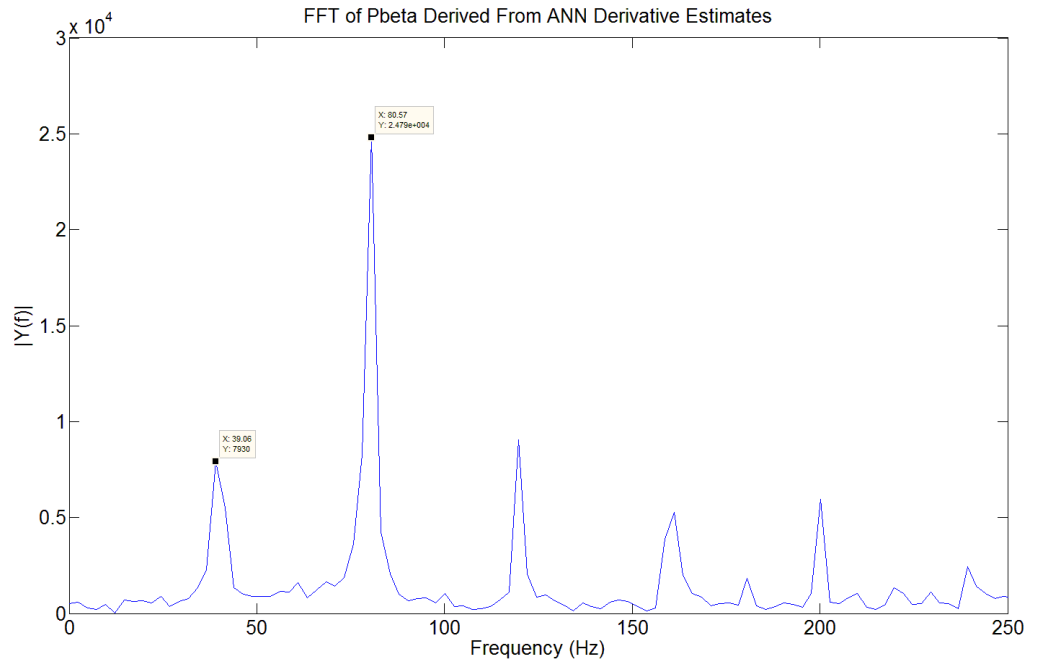


Figure B.64 ANN method, 40Hz, 60% Load

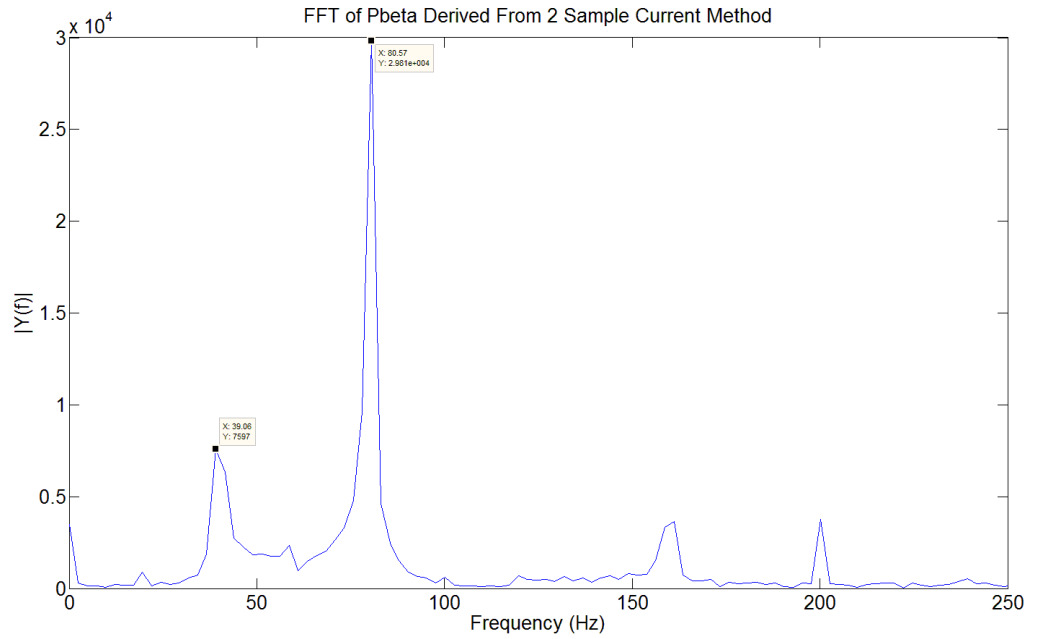


Figure B.65 Two current sample method, 40Hz, 73% Load

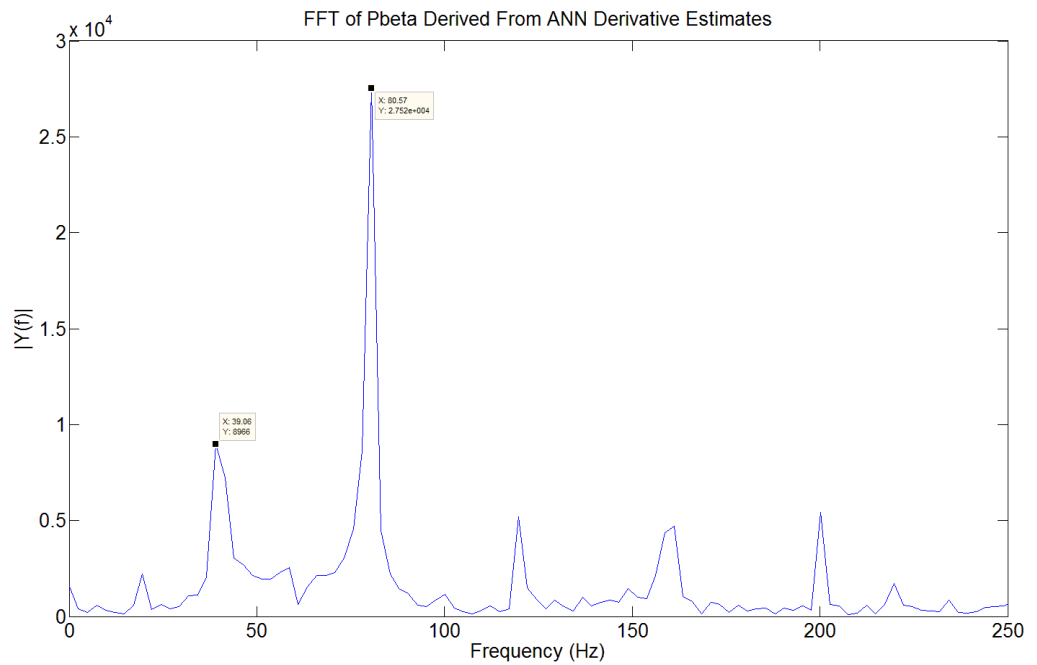


Figure B.66 ANN method, 40Hz, 73% Load

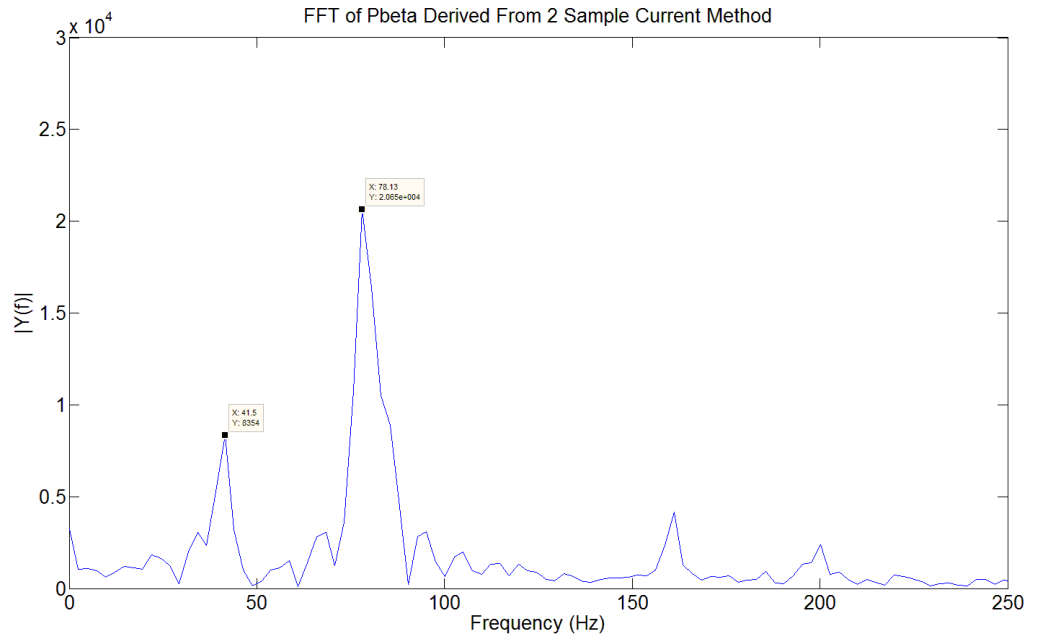


Figure B.67 Two current sample method, 40Hz, 83% Load

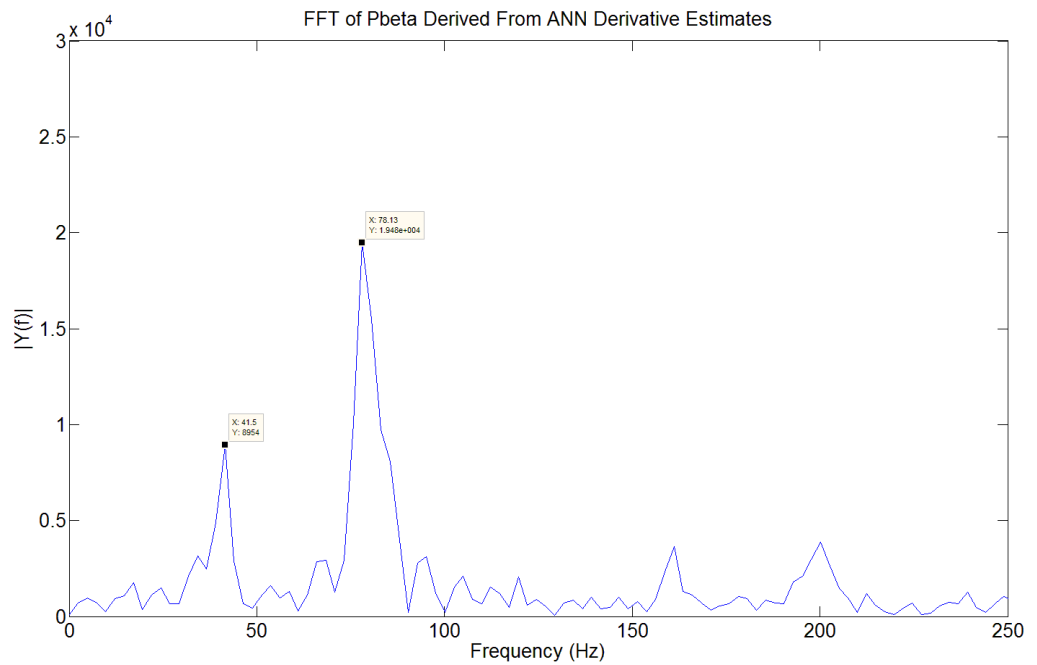


Figure B.68 ANN method, 40Hz, 83% Load

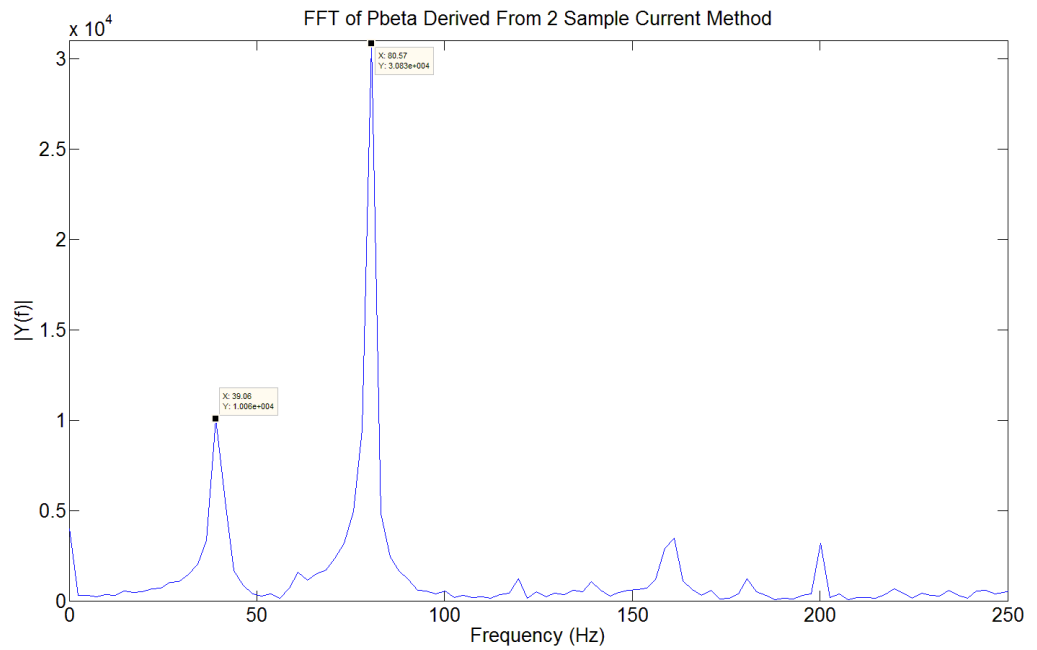


Figure B.69 Two current sample method, 40Hz, 91% Load

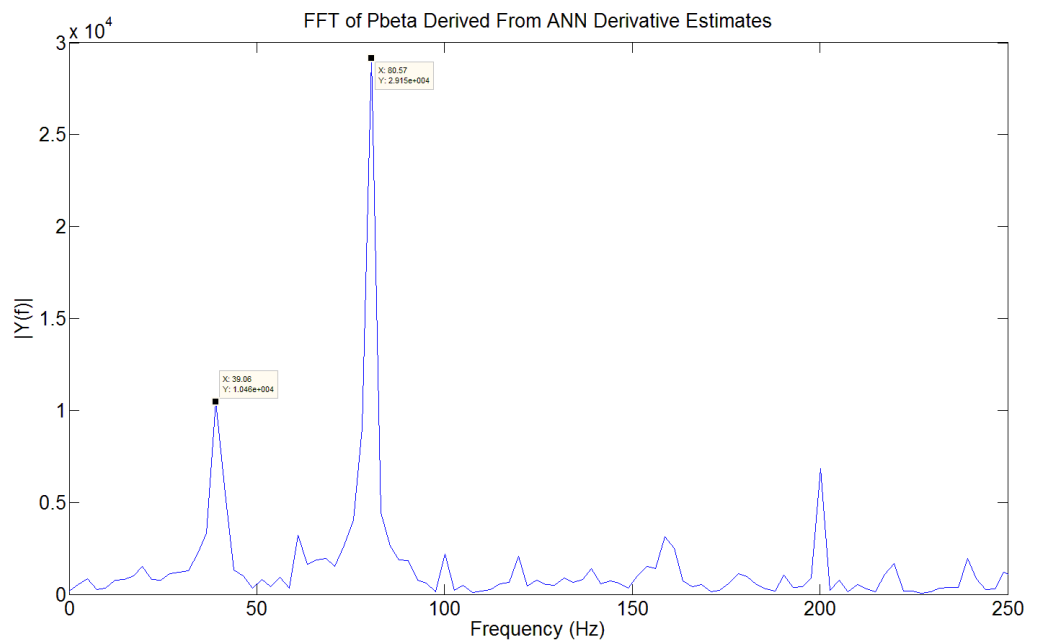


Figure B.70 ANN method, 40Hz, 91% Load

Minimum Pulse Width Variation

The minimum pulse width is reduced to allow the ANN estimates when using short vectors to be assessed, the frequency was maintained at 30Hz ($t_{\min} = \text{minimum pulse width}$).

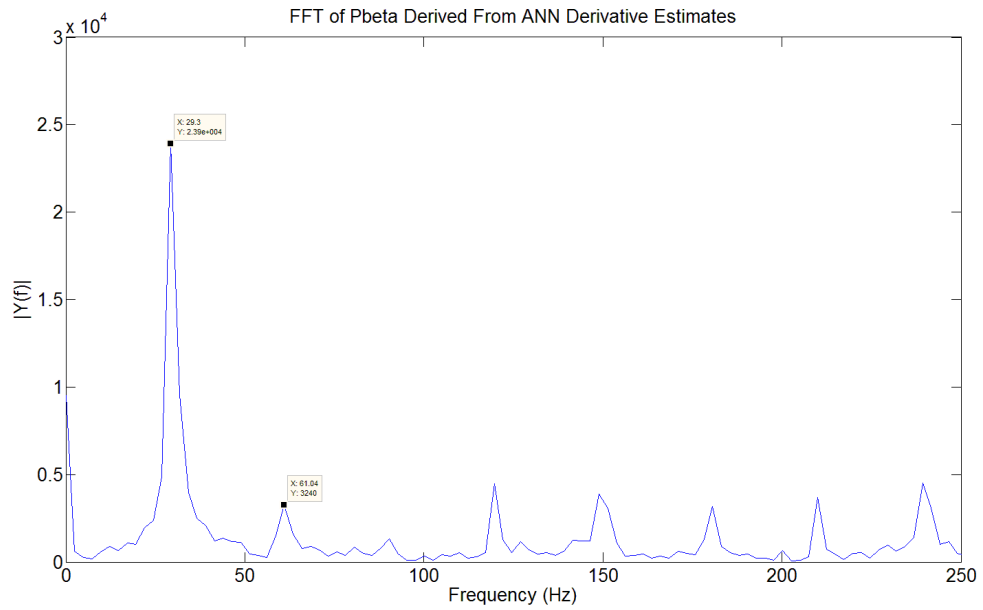


Figure B.71 $t_{\min} = 8\mu\text{s}$, No load

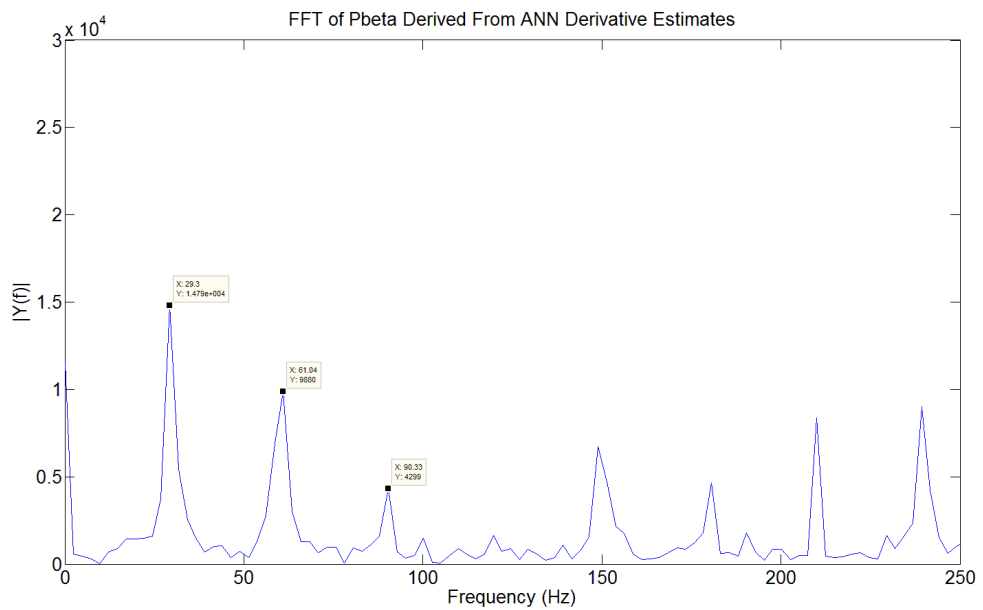


Figure B.72 $t_{\min} = 4\mu\text{s}$, No load

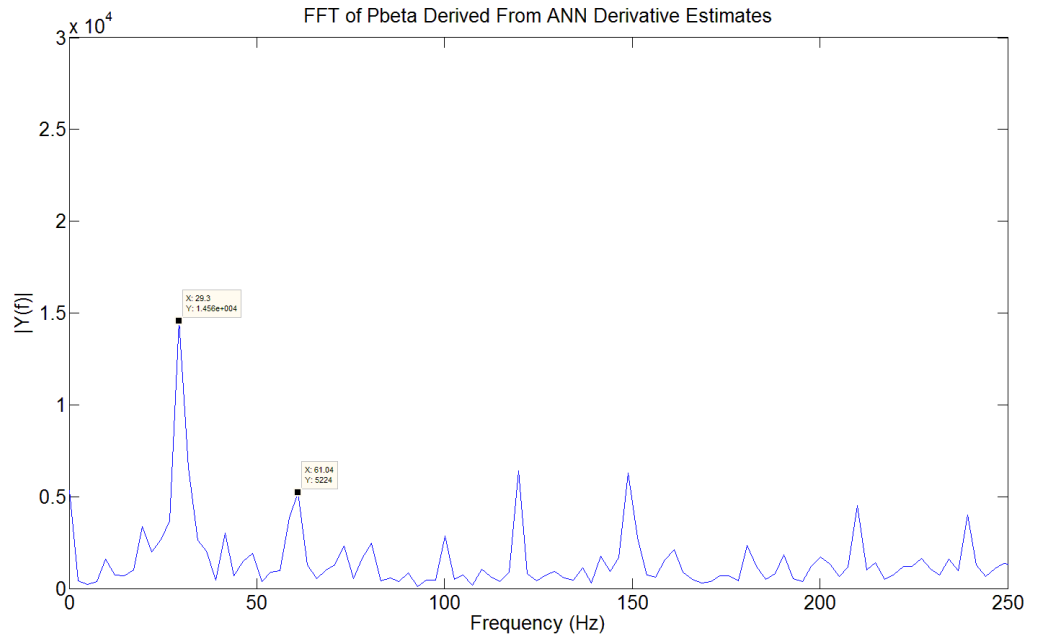


Figure B.73 $t_{\min} = 3\mu\text{s}$, No load

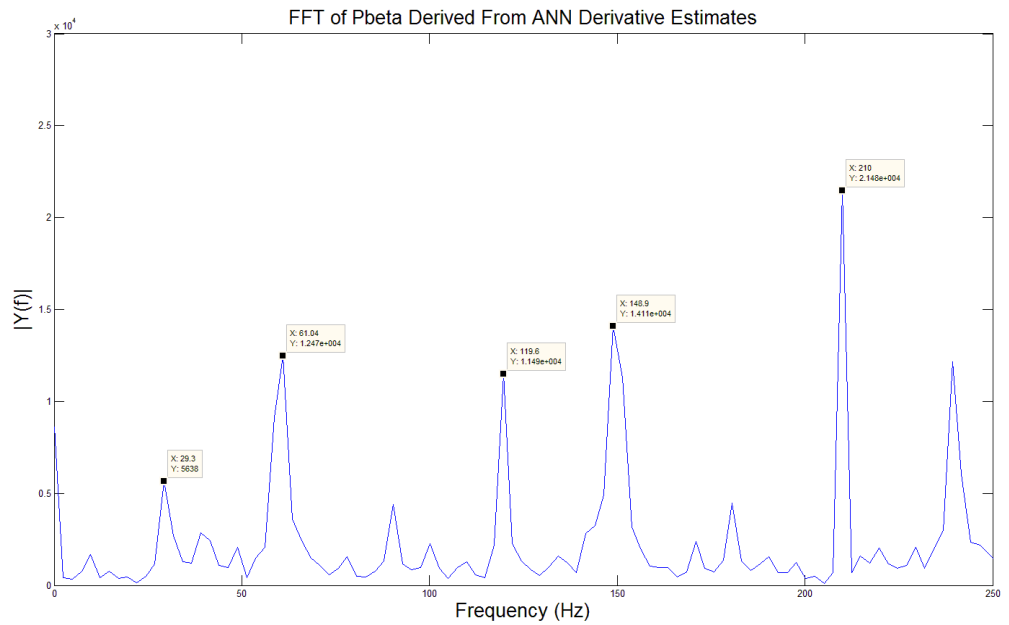
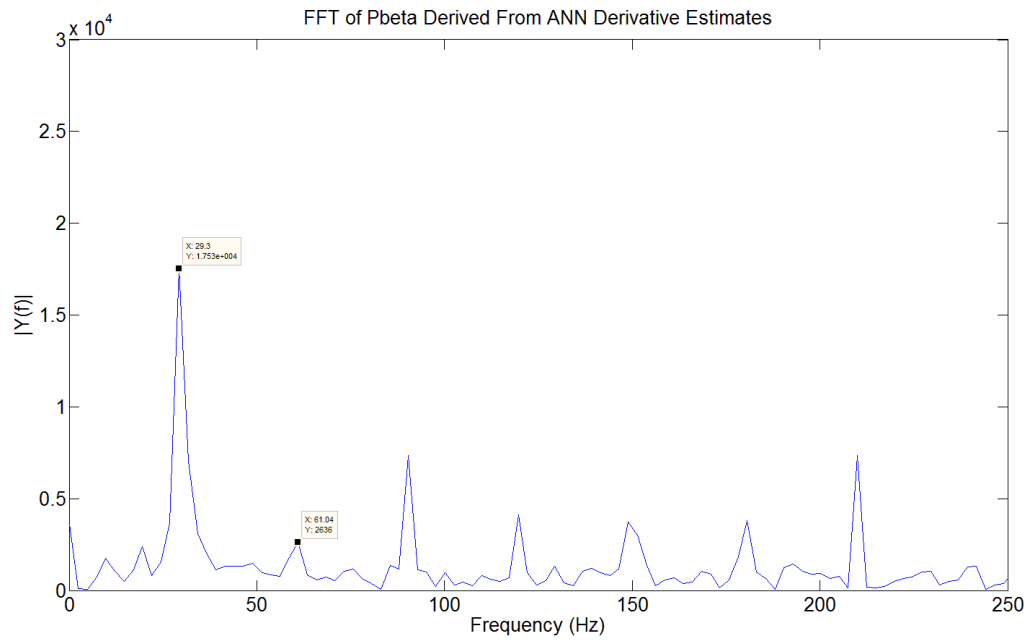
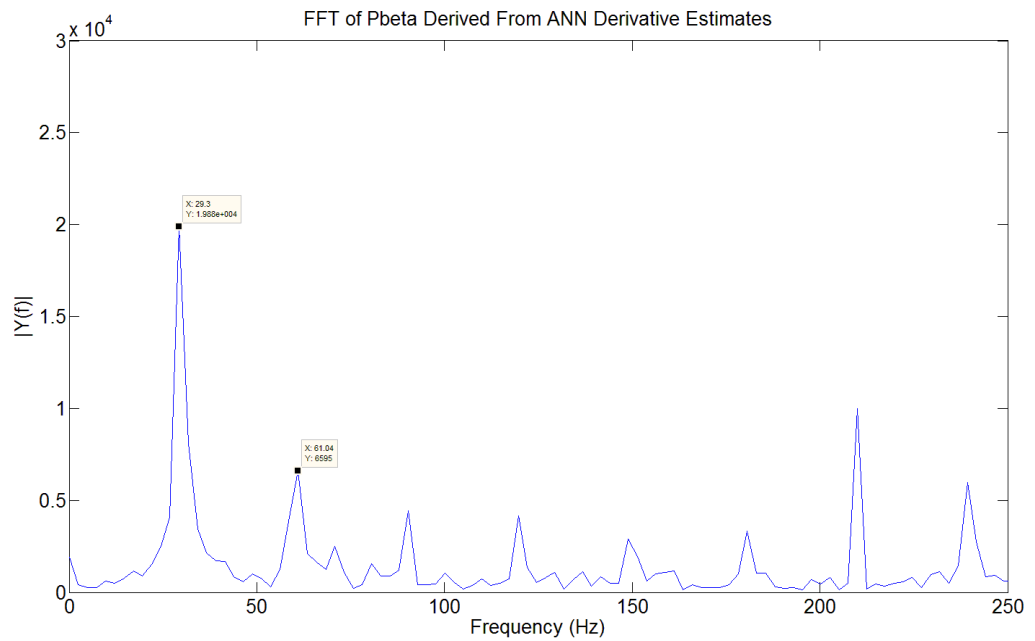


Figure B.74 $t_{\min} = 2.25\mu\text{s}$, No load

Figure B.75 $t_{\min} = 8\mu\text{s}$, 27% loadFigure B.76 $t_{\min} = 4\mu\text{s}$, 27% load

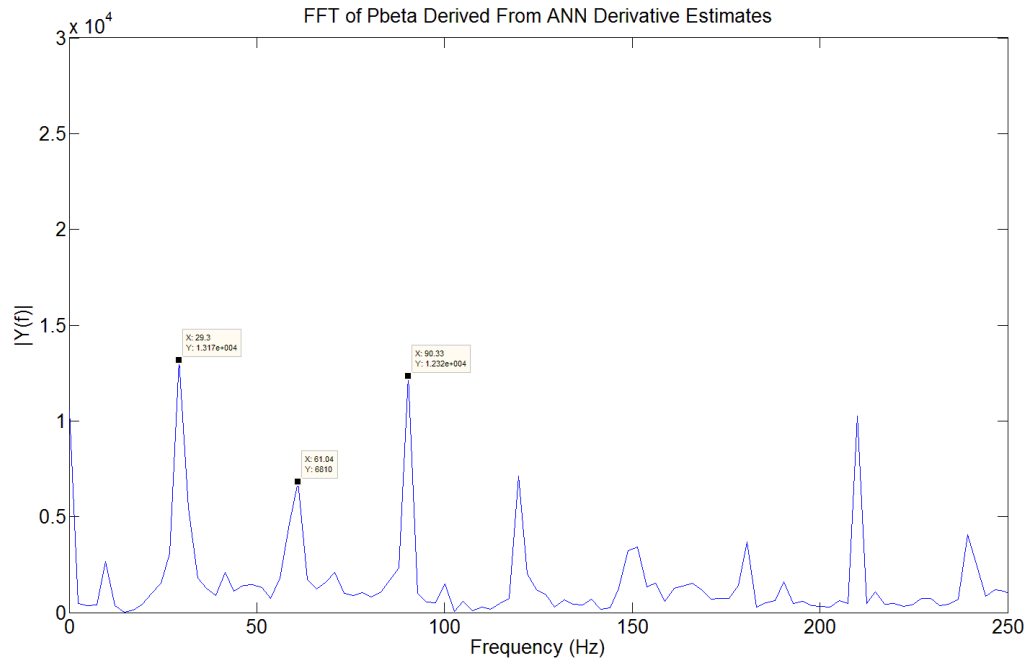


Figure B.77 $t_{\min} = 3\mu\text{s}$, 27% load

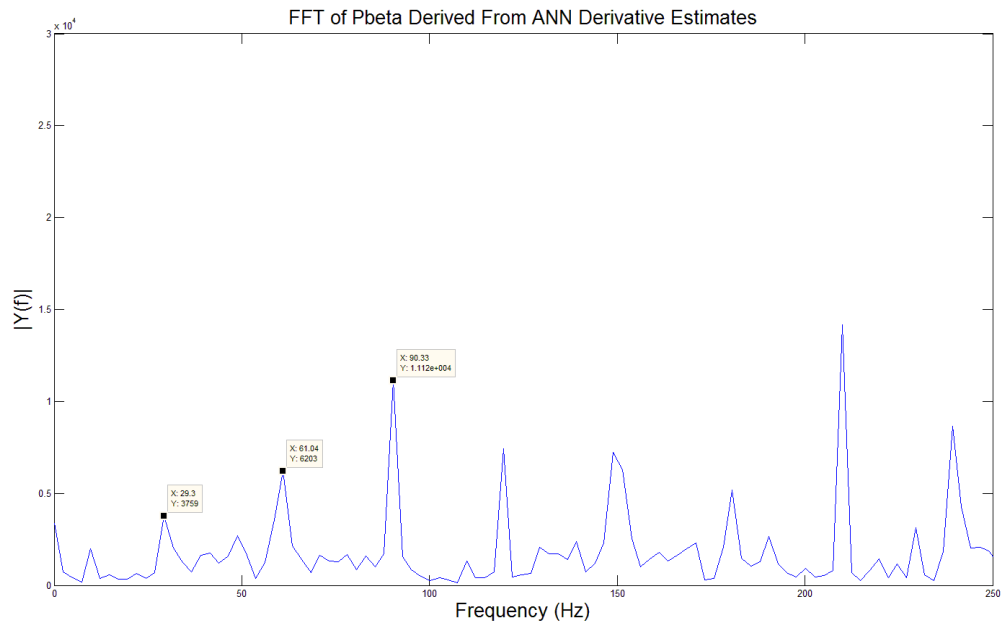


Figure B.78 $t_{\min} = 2.25\mu\text{s}$, 27% load

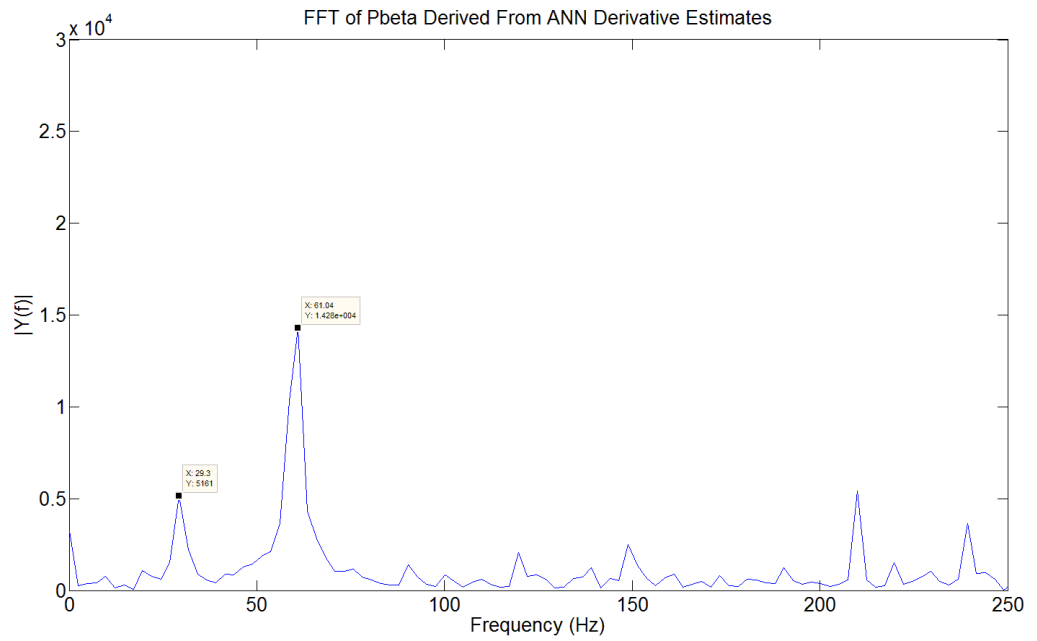


Figure B.79 $t_{\min} = 8\mu\text{s}$, 44% load

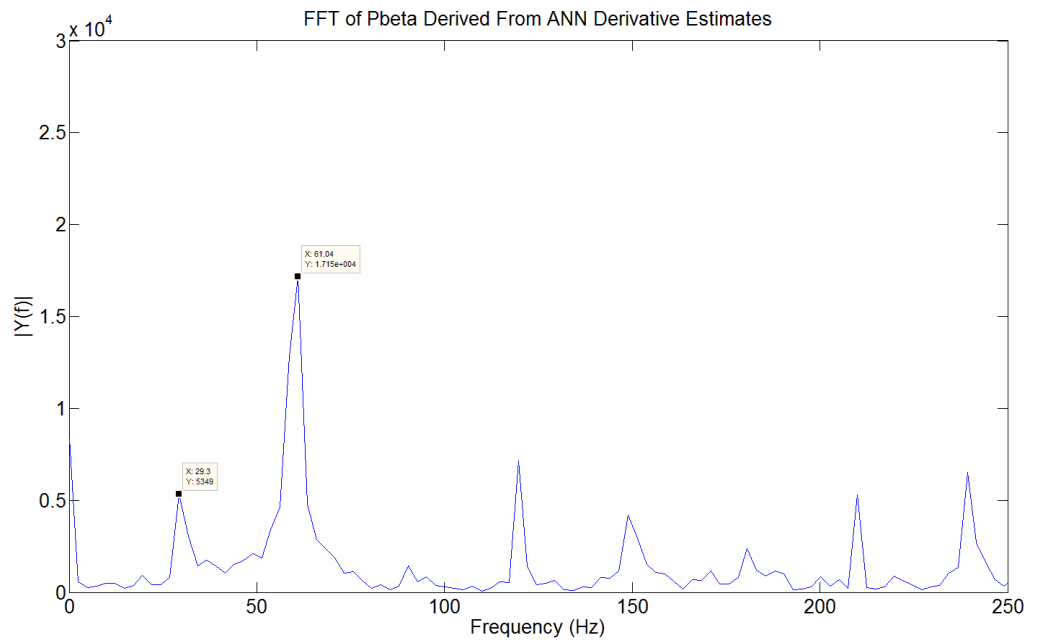


Figure B.80 $t_{\min} = 4\mu\text{s}$, 44% load

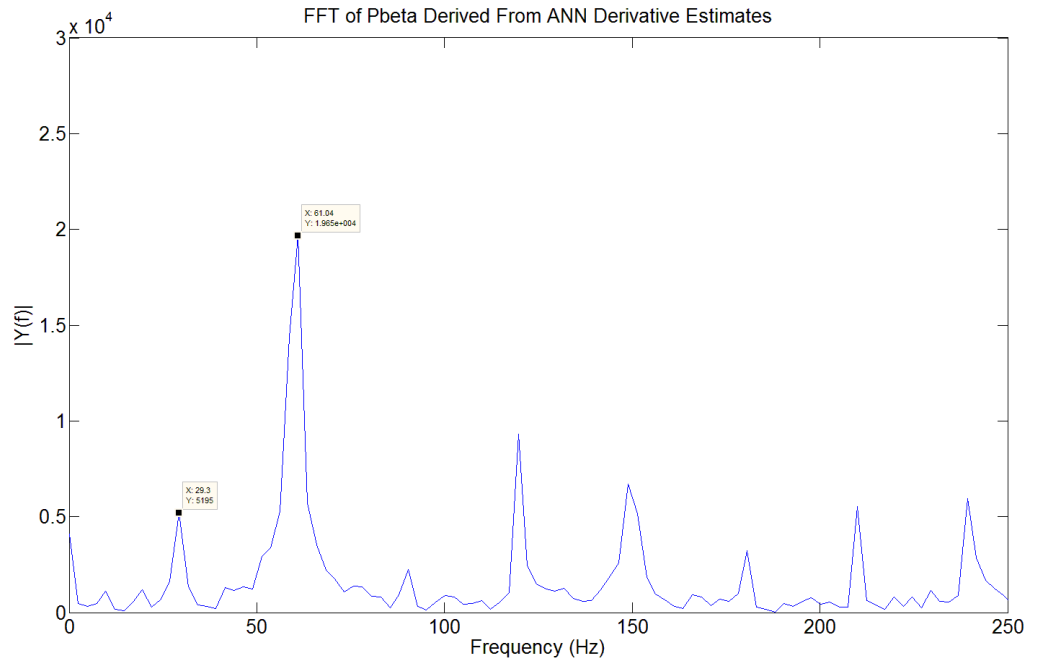


Figure B.81 $t_{\min} = 3\mu\text{s}$, 44% load

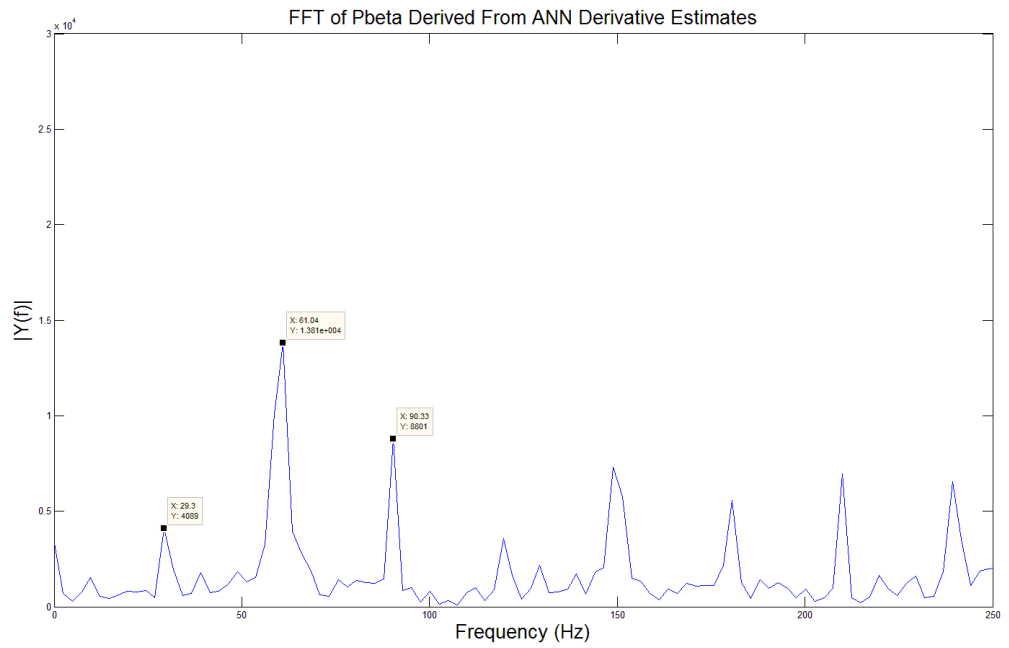


Figure B.82 $t_{\min} = 2.25\mu\text{s}$, 44% load

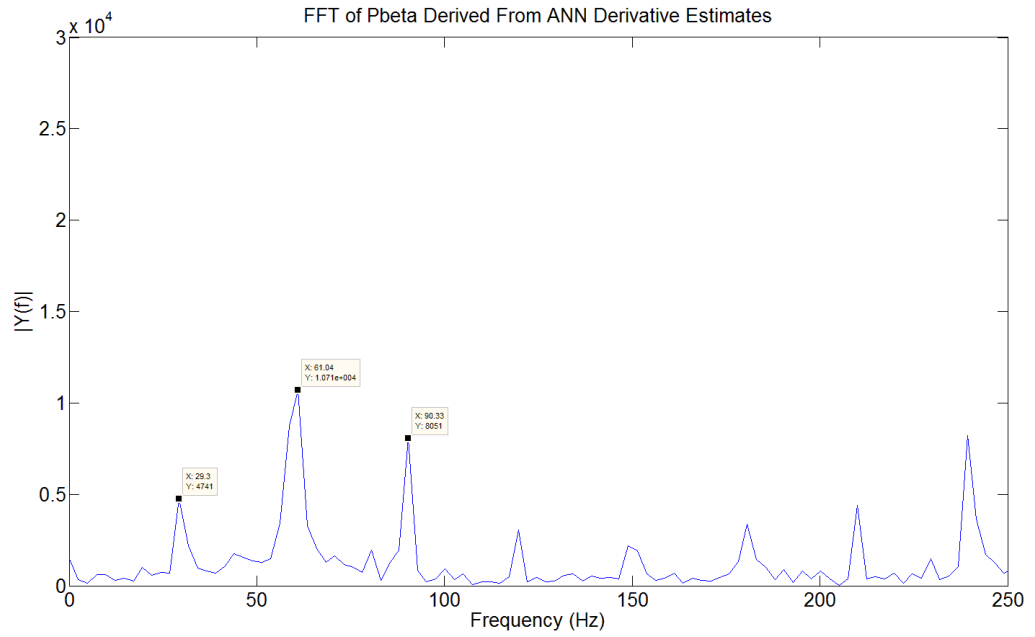


Figure B.83 $t_{\min} = 8\mu\text{s}$, 60% load

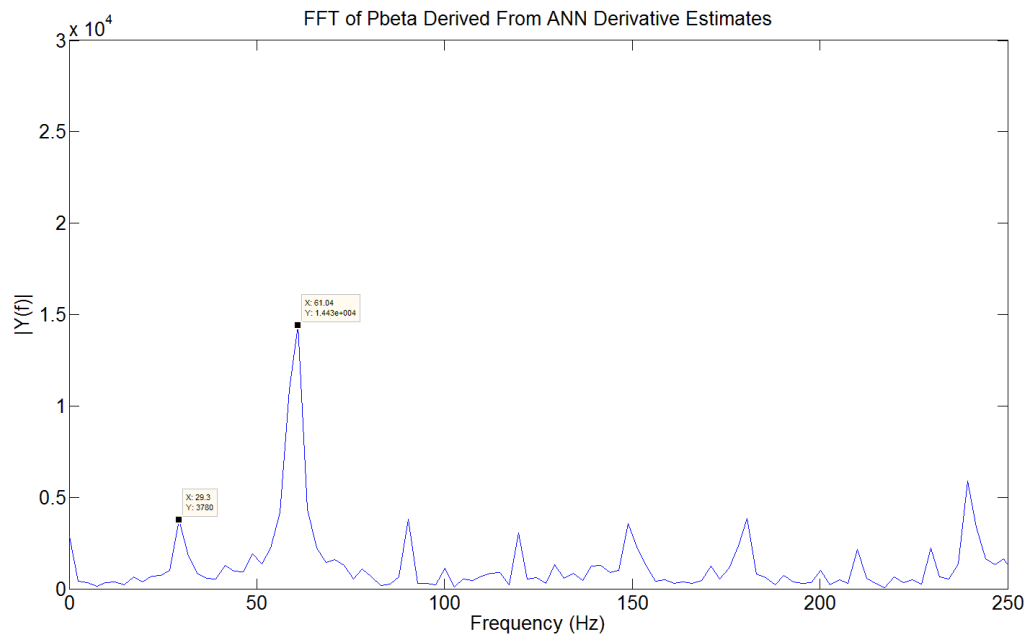


Figure B.84 $t_{\min} = 4\mu\text{s}$, 60% load

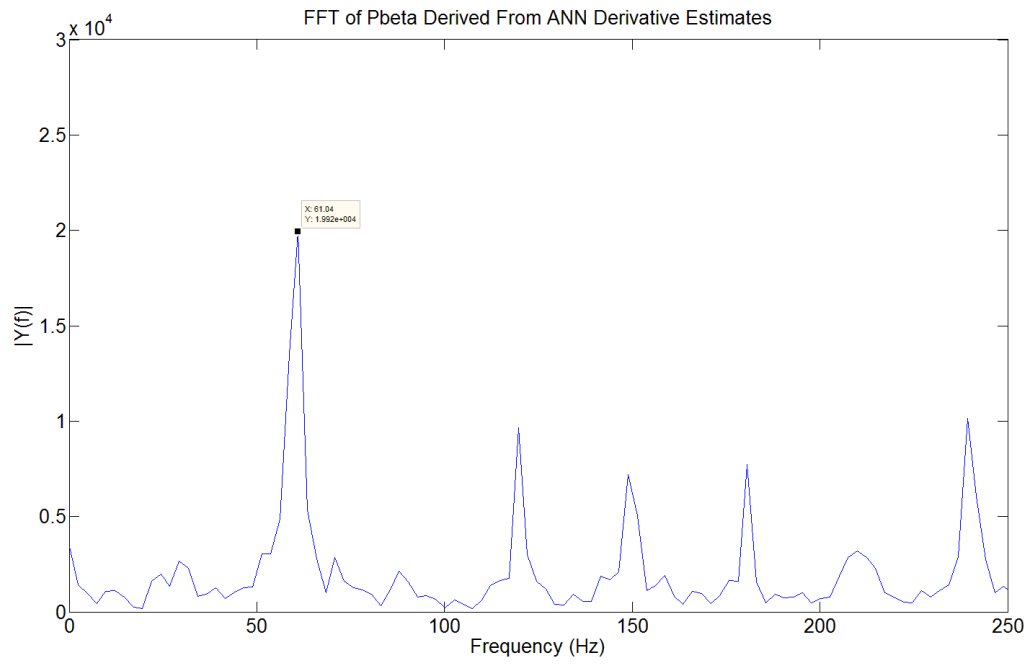


Figure B.85 $t_{\min} = 3\mu\text{s}$, 60% load

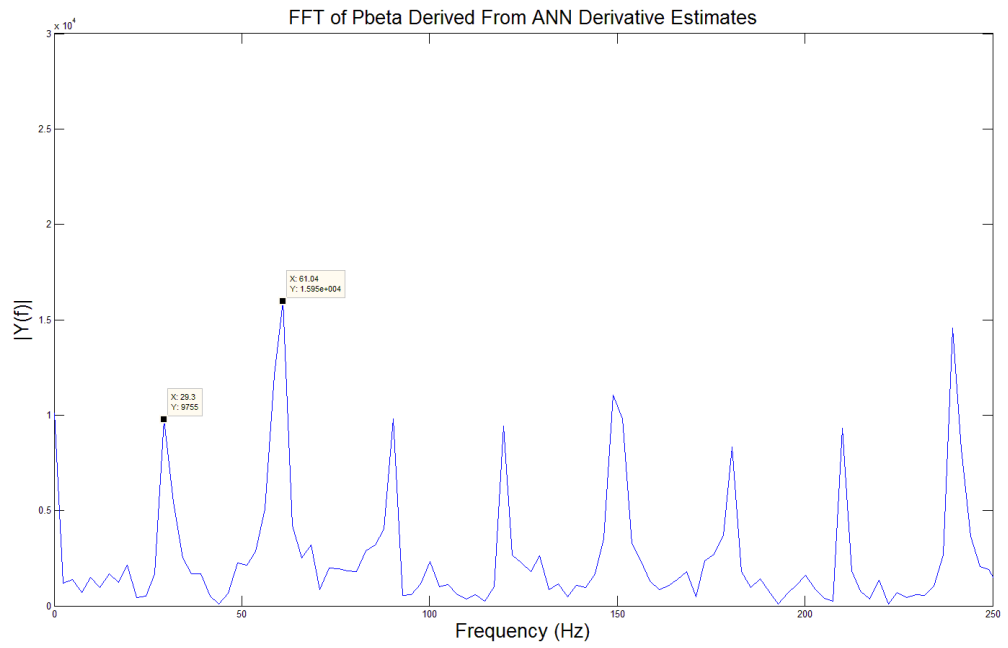
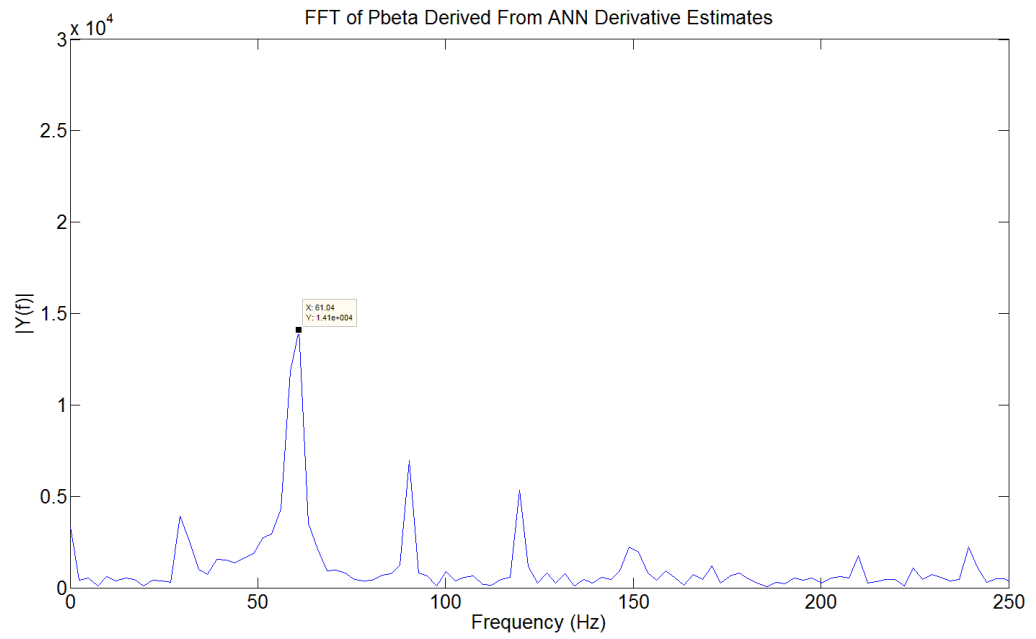
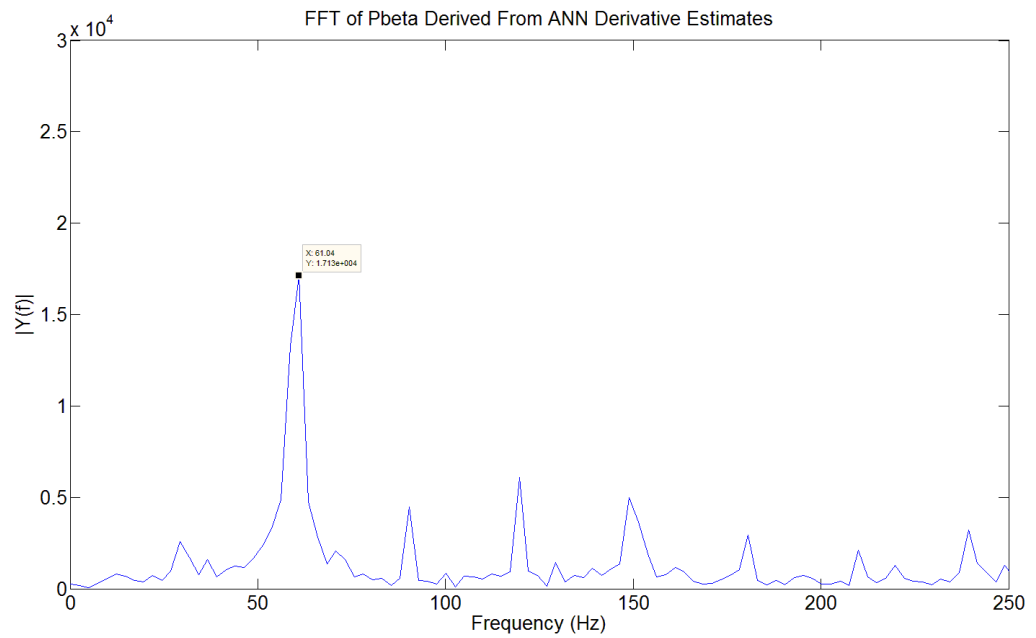


Figure B.86 $t_{\min} = 2.25\mu\text{s}$, 60% load

Figure B.87 $t_{\min} = 8\mu\text{s}$, 73% loadFigure B.88 $t_{\min} = 4\mu\text{s}$, 73% load

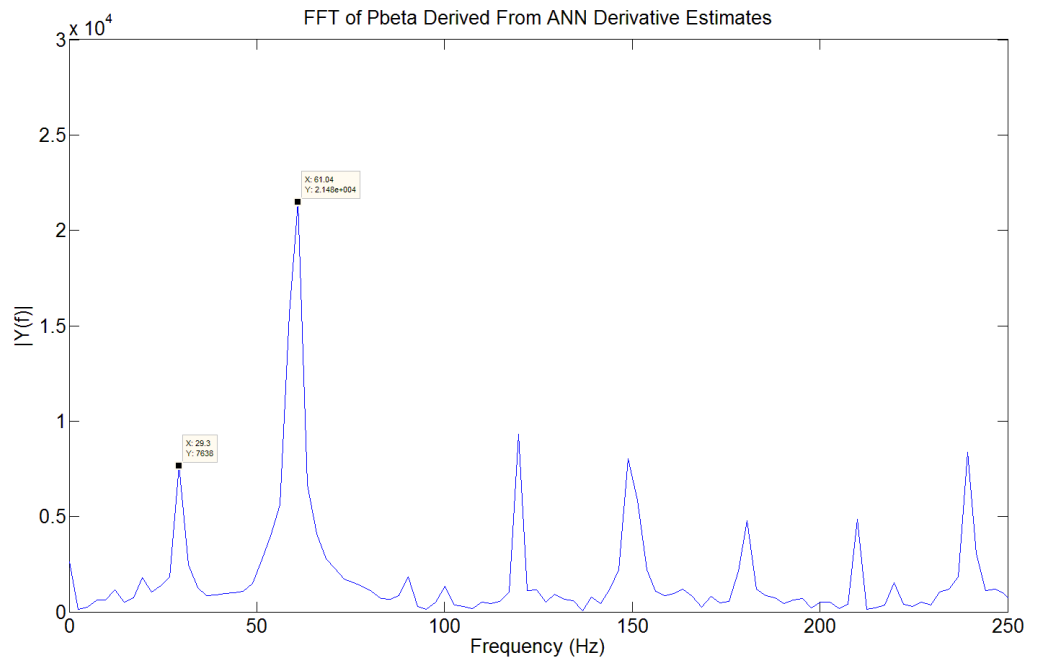


Figure B.89 $t_{\min} = 3\mu\text{s}$, 73% load

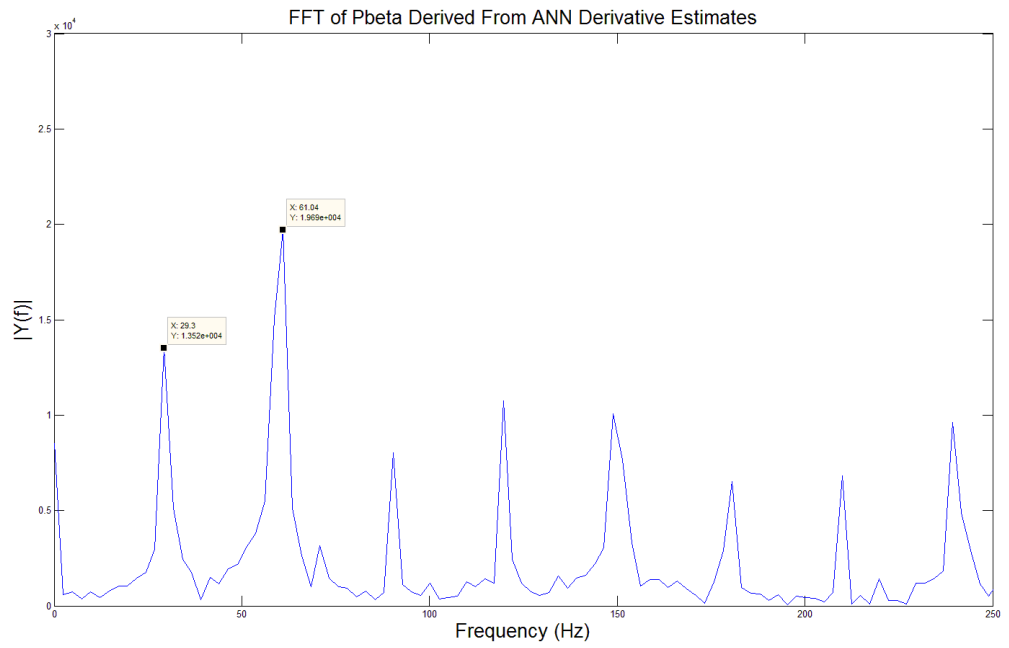
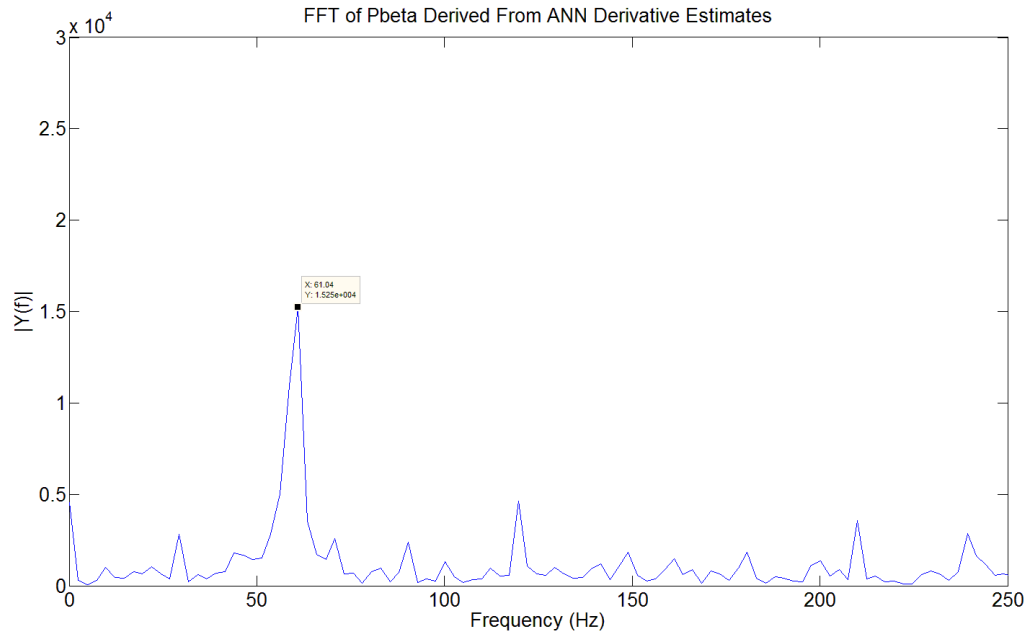
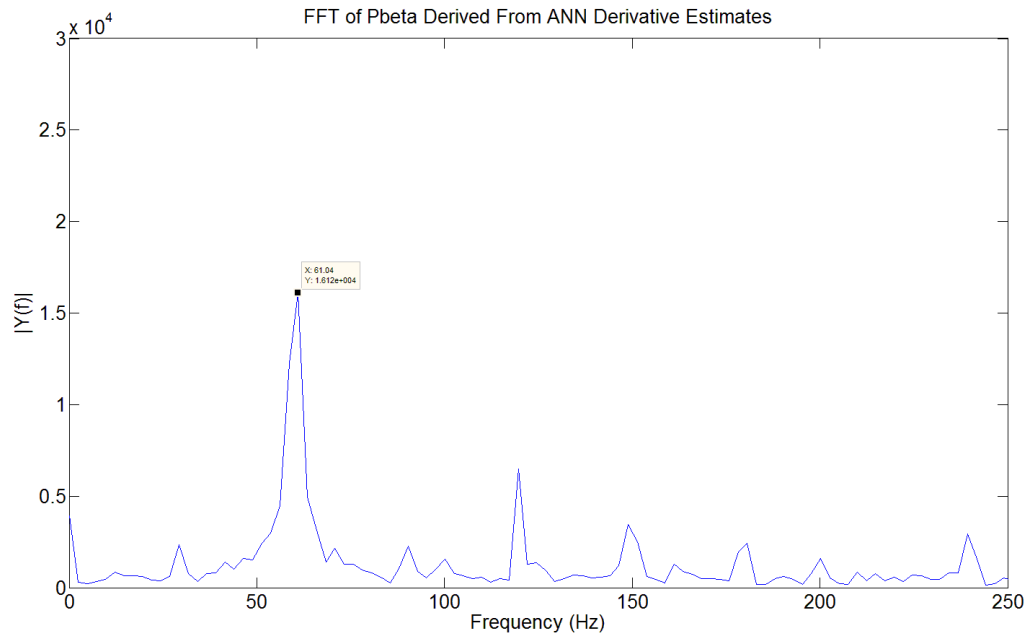


Figure B.90 $t_{\min} = 2.25\mu\text{s}$, 73% load

Figure B.91 $t_{\min} = 8\mu\text{s}$, 83% loadFigure B.92 $t_{\min} = 4\mu\text{s}$, 83% load

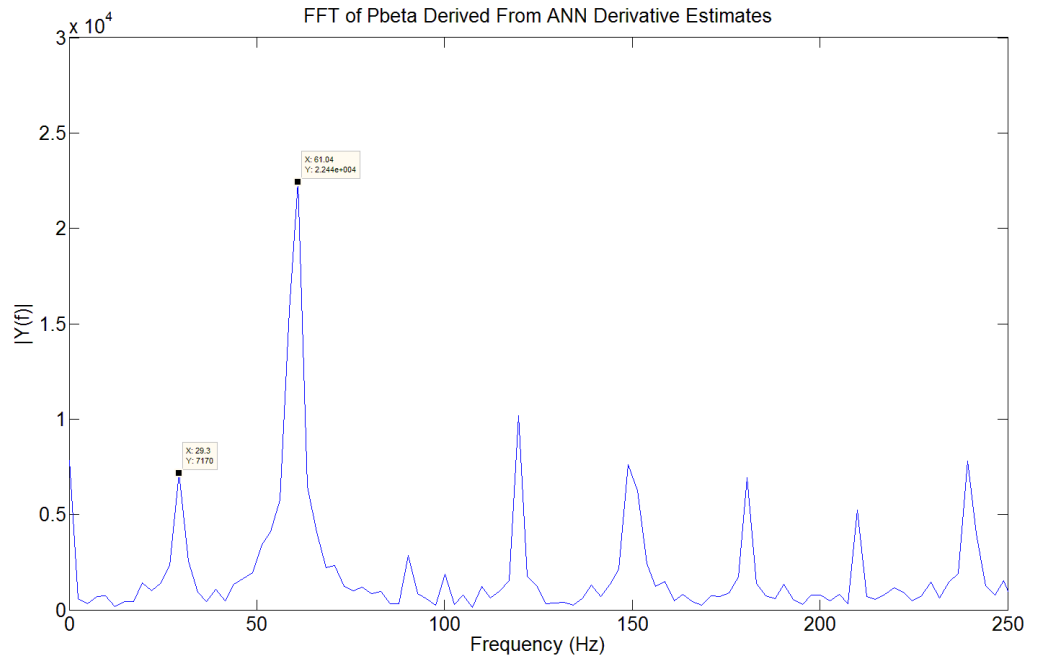


Figure B.93 $t_{\min} = 3\mu\text{s}$, 83% load

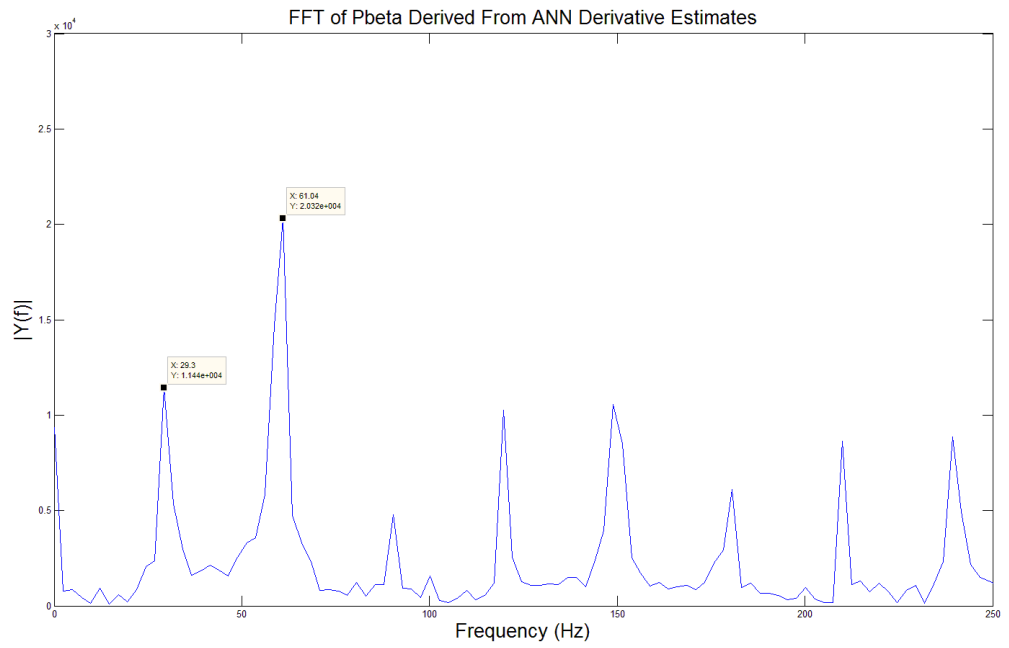
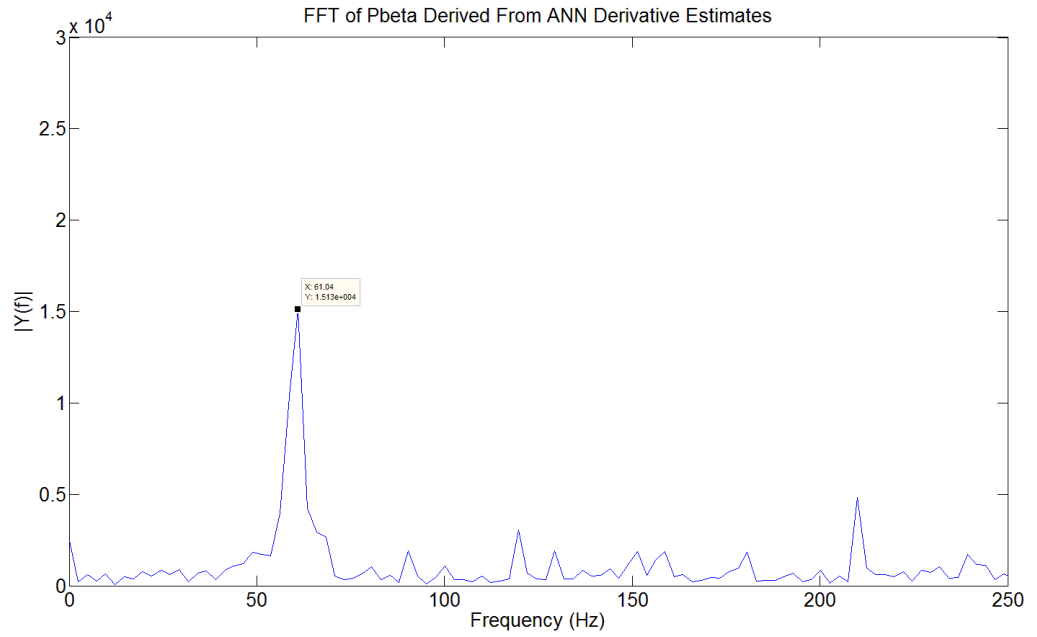
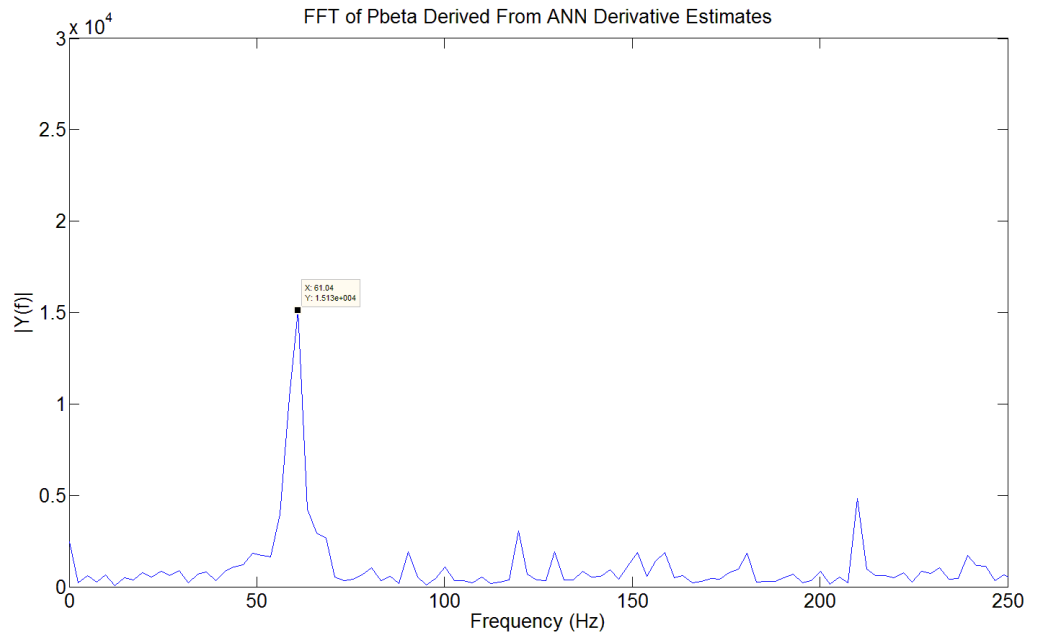
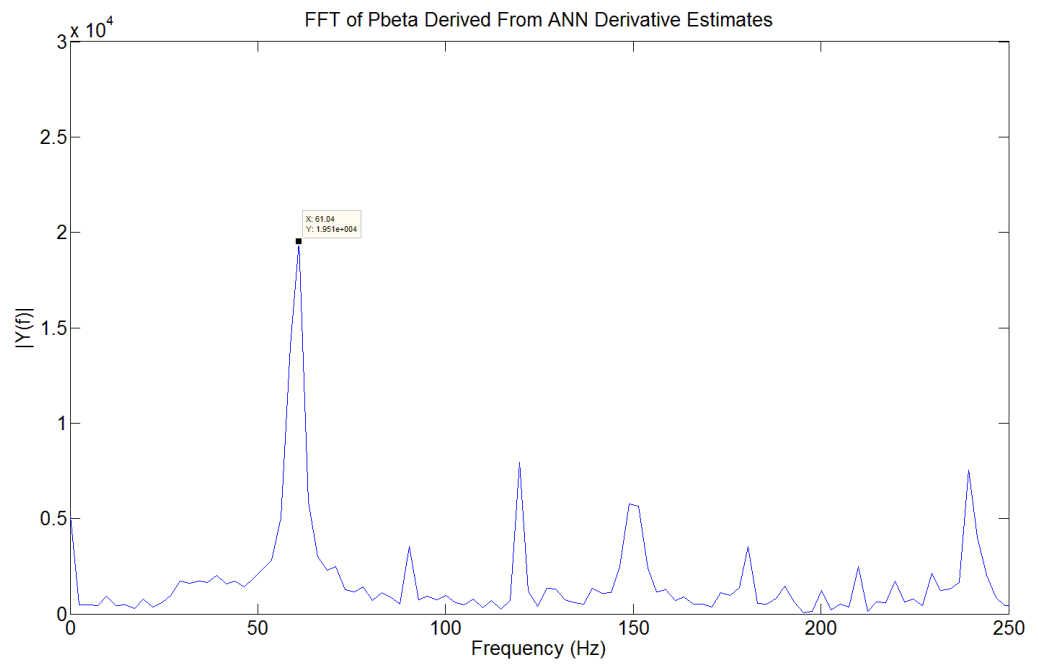
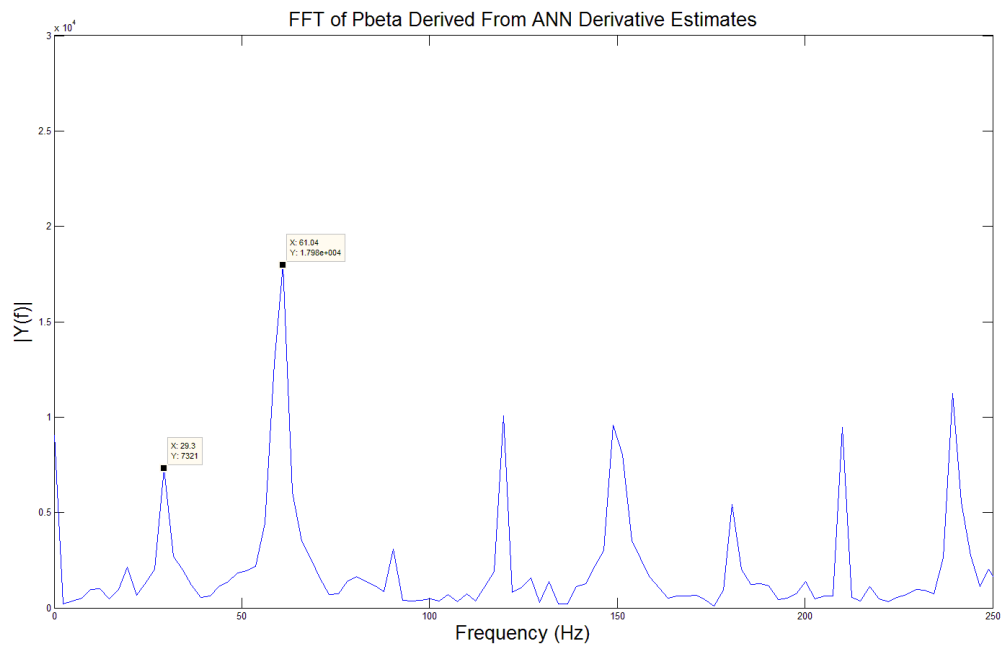


Figure B.94 $t_{\min} = 2.25\mu\text{s}$, 83% load

Figure B.95 $t_{\min} = 8\mu\text{s}$, 91% loadFigure B.96 $t_{\min} = 4\mu\text{s}$, 91% load

Figure B.97 $t_{\min} = 3\mu\text{s}$, 91% loadFigure B.98 $t_{\min} = 2.25\mu\text{s}$, 91% load

Bibliography

- [1] P. Nussbaumer and T. M. Wolbank, "Using switching transients to exploit sensorless control information for electric machines," in *Sensorless Control for Electrical Drives (SLED)*, 2011 Symposium on, 2011, pp. 35-40.
- [2] C. Schauder, "Adaptive speed identification for vector control of induction motors without rotational transducers," *Industry Applications*, IEEE Transactions on, vol. 28, pp. 1054-1061, 1992.
- [3] P. L. Jansen and R. D. Lorenz, "Accuracy limitations of velocity and flux estimation in direct field oriented induction machines," in *Power Electronics and Applications*, 1993., Fifth European Conference on, 1993, pp. 312-318 vol.4.
- [4] G. J. Armstrong, et al., "A comparison of estimation techniques for sensorless vector controlled induction motor drives," in *Power Electronics and Drive Systems*, 1997. Proceedings., 1997 International Conference on, 1997, pp. 110-116 vol.1.
- [5] P. Fang-Zheng and T. Fukao, "Robust speed identification for speed-sensorless vector control of induction motors," *Industry Applications*, IEEE Transactions on, vol. 30, pp. 1234-1240, 1994.
- [6] T. Cao-Minh, et al., "MRAS-based speed sensorless control for induction motor drives using instantaneous reactive power," in *Industrial Electronics Society*, 2001. IECON '01. The 27th Annual Conference of the IEEE, 2001, pp. 1417-1422 vol.2.
- [7] E. Babaei, et al., "Verification of a new method for PI block design of MRAS-based sensorless speed estimators," in *Electrical Machines and Systems (ICEMS)*, 2011 International Conference on, 2011, pp. 1-6.
- [8] B. Karanayil, et al., "Online Stator and Rotor Resistance Estimation Scheme Using Artificial Neural Networks for Vector Controlled Speed Sensorless Induction Motor Drive," *Industrial Electronics*, IEEE Transactions on, vol. 54, pp. 167-176, 2007.
- [9] A. Piippo, et al., "Adaptation of Motor Parameters in Sensorless PMSM Drives," in *Power Electronics and Drive Systems*, 2007. PEDS '07. 7th International Conference on, 2007, pp. 175-182.

-
- [10] H. In-Joong and L. Sang-Hoon, "An online identification method for both stator-and rotor resistances of induction motors without rotational transducers," *Industrial Electronics, IEEE Transactions on*, vol. 47, pp. 842-853, 2000.
- [11] T. G. Habetler, et al., "Stator resistance tuning in a stator-flux field-oriented drive using an instantaneous hybrid flux estimator," *Power Electronics, IEEE Transactions on*, vol. 13, pp. 125-133, 1998.
- [12] D. J. Atkinson, et al., "Observers for induction motor state and parameter estimation," *Industry Applications, IEEE Transactions on*, vol. 27, pp. 1119-1127, 1991.
- [13] J. Holtz and Q. Juntao, "Sensorless vector control of induction motors at very low speed using a nonlinear inverter model and parameter identification," *Industry Applications, IEEE Transactions on*, vol. 38, pp. 1087-1095, 2002.
- [14] Q. Gao, et al., "Sensorless speed operation of cage induction motor using zero drift feedback integration with MRAS observer," in *Power Electronics and Applications, 2005 European Conference on*, 2005, pp. 9 pp.-P.9.
- [15] M. Tursini, et al., "Adaptive sliding-mode observer for speed-sensorless control of induction motors," *Industry Applications, IEEE Transactions on*, vol. 36, pp. 1380-1387, 2000.
- [16] K. Kubota, et al., "DSP-based speed adaptive flux observer of induction motor," *Industry Applications, IEEE Transactions on*, vol. 29, pp. 344-348, 1993.
- [17] C. Lascu, et al., "Very-low-speed variable-structure control of sensorless induction machine drives without signal injection," *Industry Applications, IEEE Transactions on*, vol. 41, pp. 591-598, 2005.
- [18] J. Maes and J. A. Melkebeek, "Speed-sensorless direct torque control of induction motors using an adaptive flux observer," *Industry Applications, IEEE Transactions on*, vol. 36, pp. 778-785, 2000.
- [19] M. Hinkkanen, "Analysis and design of full-order flux observers for sensorless induction motors," in *IECON 02 [Industrial Electronics Society, IEEE 2002 28th Annual Conference of the]*, 2002, pp. 77-82 vol.1.
- [20] Y. R. Kim, et al., "Speed sensorless vector control of an induction motor using an extended Kalman filter," in *Industry Applications*

- Society Annual Meeting, 1992., Conference Record of the 1992 IEEE, 1992, pp. 594-599 vol.1.
- [21] M. A. Ouhrouche, et al., "Application of an extended Kalman filter to rotor speed and resistance estimation in induction motor vector control," in *Electrical and Computer Engineering, 1998. IEEE Canadian Conference on*, 1998, pp. 297-300 vol.1.
- [22] K. S. Saleh, "Sensorless Control of High Power Induction Motors Using Multilevel Converters," PhD, University of Nottingham, 2010.
- [23] Y. Hua, "Sensorless Control of Surface Mounted Permanent Magnet Machine Using Fundamental PWM Excitation," PhD, University of Nottingham, 2009.
- [24] J. Holtz and P. Hangwen, "Elimination of saturation effects in sensorless position controlled induction motors," in *Industry Applications Conference, 2002. 37th IAS Annual Meeting. Conference Record of the*, 2002, pp. 1695-1702 vol.3.
- [25] T. M. Wolbank, et al., "Zero speed sensorless control signals of induction motors with closed rotor slots," in *Power Electronics Specialists Conference, 2002. pesc 02. 2002 IEEE 33rd Annual*, 2002, pp. 997-1002 vol.2.
- [26] Q. Gao, "Sensorless Control of Induction Machines at Zero and Low Frequencies," PhD, University of Nottingham, 2005.
- [27] J. Holtz, "Sensorless position control of induction motors-an emerging technology," in *Industrial Electronics Society, 1998. IECON '98. Proceedings of the 24th Annual Conference of the IEEE*, 1998, pp. 11-12 vol.1.
- [28] P. L. Jansen and R. D. Lorenz, "Transducerless position and velocity estimation in induction and salient AC machines," *Industry Applications, IEEE Transactions on*, vol. 31, pp. 240-247, 1995.
- [29] J. Cilia, et al., "Sensorless position detection for vector-controlled induction motor drives using an asymmetric outer-section cage," *Industry Applications, IEEE Transactions on*, vol. 33, pp. 1162-1169, 1997.
- [30] S. Ovrebo, "Sensorless Control of Permanent Magnet Synchronous Machines," PhD, Department of Electrical Power Engineering, Norwegian University of Science and Technology, 2004.
- [31] Y. Shih-Chin, et al., "Surface permanent magnet synchronous machine design for saliency-tracking self-sensing position estimation at zero

- and low speeds," in Energy Conversion Congress and Exposition (ECCE), 2010 IEEE, 2010, pp. 3493-3500.
- [32] J. F. Gieras, *Permanent Magnet Motor Technology: Design and Applications*, Third Edition: Taylor & Francis, 2011.
- [33] M. Schroedl, "Sensorless control of AC machines at low speed and standstill based on the 'INFORM' method," in Industry Applications Conference, 1996. Thirty-First IAS Annual Meeting, IAS '96., Conference Record of the 1996 IEEE, 1996, pp. 270-277 vol.1.
- [34] Y. Duan, "A Comparison of Saliency Based Sensorless Control Techniques for a PM Machine," PhD, University of Nottingham, 2012.
- [35] F. Blaschke, et al., "Sensorless direct field orientation at zero flux frequency," in Industry Applications Conference, 1996. Thirty-First IAS Annual Meeting, IAS '96., Conference Record of the 1996 IEEE, 1996, pp. 189-196 vol.1.
- [36] H. Jung-Ik, et al., "Design and selection of AC machines for saliency-based sensorless control," in Industry Applications Conference, 2002. 37th IAS Annual Meeting. Conference Record of the, 2002, pp. 1155-1162 vol.2.
- [37] H. Jiang, "Audible Noise Reduction in the High Frequency Injection based Sensorless Torque Control for EPS Applications," PhD, University of Nottingham, 2012.
- [38] H. Jung-Ik and S. Seung-Ki, "Sensorless field-orientation control of an induction machine by high-frequency signal injection," *Industry Applications*, IEEE Transactions on, vol. 35, pp. 45-51, 1999.
- [39] M. S. a. K. S. E. Robeischl, "Improved INFORM measurement sequence and evaluation for sensorless permanent magnet synchronous motor drives," presented at the 10th International Power Electronics and Motion Control Conference, Cavtat and Dubrovnik, Croatia, 2002.
- [40] H. Yahan, et al., "Sensorless Control of Surface Mounted Permanent Magnetic Machine Using the Standard Space Vector PWN," in Industry Applications Conference, 2007. 42nd IAS Annual Meeting. Conference Record of the 2007 IEEE, 2007, pp. 661-667.
- [41] Q. Gao, et al., "Sensorless Control of Induction Machines, including Zero Frequency using only Fundamental PWM Excitation," in IEEE Industrial Electronics, IECON 2006 - 32nd Annual Conference on, 2006, pp. 793-798.

- [42] T. M. Wolbank and J. Machl, "A modified PWM scheme in order to obtain spatial information of AC machines without mechanical sensor," in *Applied Power Electronics Conference and Exposition, 2002. APEC 2002. Seventeenth Annual IEEE, 2002*, pp. 310-315 vol.1.
- [43] Y. Hua, et al., "Improved sensorless control of a permanent magnet machine using fundamental pulse width modulation excitation," *Electric Power Applications, IET*, vol. 5, pp. 359-370, 2011.
- [44] H. Yahan, et al., "Sensorless control for a PM machine with reduced current distortion using space vector PWM excitation," in *Power Electronics and Applications, 2009. EPE '09. 13th European Conference on, 2009*, pp. 1-10.
- [45] D. Q. Guan, et al., "A new high-bandwidth sensorless direct torque controlled IPM synchronous machine drive using a hybrid sliding mode observer," in *Sensorless Control for Electrical Drives (SLED), 2014 IEEE 5th International Symposium on, 2014*, pp. 1-8.
- [46] X. Dan and M. F. Rahman, "Sensorless Direct Torque and Flux Controlled IPM Synchronous Machine Fed by Matrix Converter Over a Wide Speed Range," *Industrial Informatics, IEEE Transactions on*, vol. 9, pp. 1855-1867, 2013.
- [47] C. Silva, et al., "Hybrid rotor position observer for wide speed-range sensorless PM motor drives including zero speed," *Industrial Electronics, IEEE Transactions on*, vol. 53, pp. 373-378, 2006.
- [48] L. Zhongdong, et al., "Hybrid position-sensorless control of PMSM for EV based on EtherLab technique," in *Mechatronic Sciences, Electric Engineering and Computer (MEC), Proceedings 2013 International Conference on, 2013*, pp. 102-106.
- [49] K. Ide, et al., "Hybrid sensorless control of IPMSM Combining high frequency injection method and back EMF method," in *IECON 2010 - 36th Annual Conference on IEEE Industrial Electronics Society, 2010*, pp. 2236-2241.
- [50] M. Tursini, et al., "Sensorless control of an IPM synchronous motor for city-scooter applications," in *Industry Applications Conference, 2003. 38th IAS Annual Meeting. Conference Record of the, 2003*, pp. 1472-1479 vol.3.
- [51] M. Zhixun, et al., "FPGA Implementation of a Hybrid Sensorless Control of SMPMSM in the Whole Speed Range," *Industrial Informatics, IEEE Transactions on*, vol. 9, pp. 1253-1261, 2013.

- [52] W. Gaolin, et al., "DSP-Based Control of Sensorless IPMSM Drives for Wide-Speed-Range Operation," *Industrial Electronics, IEEE Transactions on*, vol. 60, pp. 720-727, 2013.
- [53] P. Landsmann, et al., "Silent and parameter independent hybrid sensorless control for SPMSM based on current oversampling," in *Sensorless Control for Electrical Drives and Predictive Control of Electrical Drives and Power Electronics (SLED/PRECEDE)*, 2013 IEEE International Symposium on, 2013, pp. 1-8.
- [54] J. Luszcz and K. Iwan, "Modelling conducted EMI in inverter-fed AC motor," in *Compatibility in Power Electronics*, 2005. IEEE, 2005, pp. 209-212.
- [55] L. Ran, et al., "Conducted electromagnetic emissions in induction motor drive systems. I. Time domain analysis and identification of dominant modes," *Power Electronics, IEEE Transactions on*, vol. 13, pp. 757-767, 1998.
- [56] M. Schinkel, et al., "Efficient HF modeling and model parameterization of induction machines for time and frequency domain simulations," in *Applied Power Electronics Conference and Exposition*, 2006. APEC '06. Twenty-First Annual IEEE, 2006, p. 6 pp.
- [57] O. A. Mohammed, et al., "Study of High Frequency Model of Permanent Magnet Motor," in *Electric Machines and Drives*, 2005 IEEE International Conference on, 2005, pp. 622-627.
- [58] N. Idir, et al., "High-Frequency Behavior Models of AC Motors," *Magnetics, IEEE Transactions on*, vol. 45, pp. 133-138, 2009.
- [59] Z. Erkuan and T. A. Lipo, "Improvements in EMC performance of inverter-fed motor drives," *Industry Applications, IEEE Transactions on*, vol. 31, pp. 1247-1256, 1995.
- [60] A. F. Moreira, et al., "High-frequency modeling for cable and induction motor overvoltage studies in long cable drives," *Industry Applications, IEEE Transactions on*, vol. 38, pp. 1297-1306, 2002.
- [61] I. Dolezel, et al., "High frequency models of transistor voltage inverter-fed induction motor drives," in *Industrial Technology 2000. Proceedings of IEEE International Conference on*, 2000, pp. 32-37 vol.1.
- [62] A. Boglietti and E. Carpaneto, "Induction motor high frequency model," in *Industry Applications Conference*, 1999. Thirty-Fourth IAS

- Annual Meeting. Conference Record of the 1999 IEEE, 1999, pp. 1551-1558 vol.3.
- [63] W. Liwei, et al., "High-Frequency Modeling of the Long-Cable-Fed Induction Motor Drive System Using TLM Approach for Predicting Overvoltage Transients," *Power Electronics, IEEE Transactions on*, vol. 25, pp. 2653-2664, 2010.
- [64] G. Grandi, et al., "Common- and differential-mode HF current components in AC motors supplied by voltage source inverters," *Power Electronics, IEEE Transactions on*, vol. 19, pp. 16-24, 2004.
- [65] O. Magdun and A. Binder, "The high-frequency induction machine parameters and their influence on the common mode stator ground current," in *Electrical Machines (ICEM), 2012 XXth International Conference on*, 2012, pp. 505-511.
- [66] S. P. Weber, et al., "Modeling induction machines for EMC-Analysis," in *Power Electronics Specialists Conference, 2004. PESC 04. 2004 IEEE 35th Annual*, 2004, pp. 94-98 Vol.1.
- [67] M. Degano, et al., "HF induction motor modeling using genetic algorithms and experimental impedance measurement," in *Industrial Electronics (ISIE), 2010 IEEE International Symposium on*, 2010, pp. 1296-1301.
- [68] L. Arnedo and K. Venkatesan, "High frequency modeling of induction motor drives for EMI and overvoltage mitigation studies," in *Electric Machines and Drives Conference, 2003. IEMDC'03. IEEE International*, 2003, pp. 468-474 vol.1.
- [69] B. Mirafzal, et al., "Determination of Parameters in the Universal Induction Motor Model," in *Industry Applications Conference, 2007. 42nd IAS Annual Meeting. Conference Record of the 2007 IEEE*, 2007, pp. 1207-1216.
- [70] S. Amarir and K. Al-Haddad, "A New High Frequency Modeling Technique of Travelling Waves in Long Cable PWM Drives," in *IEEE Industrial Electronics, IECON 2006 - 32nd Annual Conference on*, 2006, pp. 1119-1124.
- [71] O. A. Mohammed, et al., "High Frequency Modeling Of Permanent Magnet Synchronous Motor Drive," in *Electric Machines & Drives Conference, 2007. IEMDC '07. IEEE International*, 2007, pp. 318-321.
- [72] I. D. Stanislav BARTOŠ, Jakub NEČESANÝ, Jiří ŠKRAMLÍK and Viktor VALOUCH, "Theoretical And Experimental Investigation Of

- Parasitic Effects In Induction Motor Drives Supplied From Semiconductor Inverters," presented at the Acta Electrotechnica et Informatica, 2008.
- [73] A. Kempinski, et al., "Common mode current paths and their modeling in PWM inverter-fed drives," in Power Electronics Specialists Conference, 2002. pesc 02. 2002 IEEE 33rd Annual, 2002, pp. 1551-1556 vol.3.
- [74] G. Busatto, et al., "EMI Characterisation of high power IGBT modules for Traction Application," in Power Electronics Specialists Conference, 2005. PESC '05. IEEE 36th, 2005, pp. 2180-2186.
- [75] C. Winterhalter, et al., "The effect of circuit parasitic impedance on the performance of IGBTs in voltage source inverters," in Applied Power Electronics Conference and Exposition, 2001. APEC 2001. Sixteenth Annual IEEE, 2001, pp. 995-1001 vol.2.
- [76] L. M. Gong and Z. Q. Zhu, "Modeling and compensation of inverter nonlinearity effects in carrier signal injection-based sensorless control methods from positive sequence carrier current distortion," in Energy Conversion Congress and Exposition (ECCE), 2010 IEEE, 2010, pp. 3434-3441.
- [77] C. Jong-Woo and S. Seung-Ki, "A new compensation strategy reducing voltage/current distortion in PWM VSI systems operating with low output voltages," *Industry Applications, IEEE Transactions on*, vol. 31, pp. 1001-1008, 1995.
- [78] R. J. Kerkman, et al., "Effects of parasitics on the control of voltage source inverters," *Power Electronics, IEEE Transactions on*, vol. 18, pp. 140-150, 2003.
- [79] J. M. Guerrero, et al., "Inverter nonlinearity effects in high-frequency signal-injection-based sensorless control methods," *Industry Applications, IEEE Transactions on*, vol. 41, pp. 618-626, 2005.
- [80] R. B. Sepe and J. H. Lang, "Inverter nonlinearities and discrete-time vector current control," in Applied Power Electronics Conference and Exposition, 1992. APEC '92. Conference Proceedings 1992., Seventh Annual, 1992, pp. 494-501.
- [81] P. Yongsoon and S. Seung-Ki, "A novel method to compensate non-linearity of inverter in sensorless operation of PMSM," in Power Electronics and ECCE Asia (ICPE & ECCE), 2011 IEEE 8th International Conference on, 2011, pp. 915-922.

- [82] N. Urasaki, et al., "Dead-time compensation strategy for permanent magnet synchronous motor drive taking zero-current clamp and parasitic capacitance effects into account," *Electric Power Applications*, IEE Proceedings -, vol. 152, pp. 845-853, 2005.
- [83] D. Rendusara and P. Enjeti, "A method to reduce common mode and differential mode dv/dt at the motor terminals in PWM rectifier/PWM inverter type adjustable speed drive systems," in *Applied Power Electronics Conference and Exposition, 1998. APEC '98. Conference Proceedings 1998., Thirteenth Annual, 1998*, pp. 1010-1016 vol.2.
- [84] D. Macdonald and W. Gray, "A practical guide to understanding bearing damage related to PWM drives," in *Pulp and Paper Industry Technical Conference, 1998. Conference Record of 1998 Annual, 1998*, pp. 159-165.
- [85] K. Sung-Jun and S. Seung-Ki, "A novel filter design for suppression of high voltage gradient in voltage-fed PWM inverter," in *Applied Power Electronics Conference and Exposition, 1997. APEC '97 Conference Proceedings 1997., Twelfth Annual, 1997*, pp. 122-127 vol.1.
- [86] P. Shihong and T. M. Jahns, "Flexible dv/dt and di/dt control method for insulated gate power switches," in *Industry Applications Conference, 2001. Thirty-Sixth IAS Annual Meeting. Conference Record of the 2001 IEEE, 2001*, pp. 1038-1045 vol.2.
- [87] K. Saleh, et al., "Low speed sensorless control of an induction motor fed by multilevel converter to reduce current distortion," in *Power Electronics and Applications, 2009. EPE '09. 13th European Conference on, 2009*, pp. 1-10.
- [88] K. Saleh, et al., "Sensorless control of high power induction motors using multilevel converters," in *Power Electronics, Machines and Drives (PEMD 2010), 5th IET International Conference on, 2010*, pp. 1-6.
- [89] K. Saleh, et al., "A novel technique for sensorless control of high power induction motors using multilevel converters," in *Energy Conversion Congress and Exposition (ECCE), 2010 IEEE, 2010*, pp. 492-499.
- [90] K. Saleh and M. Sumner, "Position estimation in a true asymmetric cascade H-bridge multilevel inverter," in *Power Electronics and Applications (EPE 2011), Proceedings of the 2011-14th European Conference on, 2011*, pp. 1-10.

- [91] P. Nussbaumer and T. M. Wolbank, "Saliency tracking based sensorless control of AC machines exploiting inverter switching transients," in *Sensorless Control for Electrical Drives (SLED)*, 2010 First Symposium on, 2010, pp. 114-119.
- [92] P. Nussbaumer and T. M. Wolbank, "Using oversampling techniques to extract ac machine saliency information," in *IECON 2010 - 36th Annual Conference on IEEE Industrial Electronics Society*, 2010, pp. 1035-1040.
- [93] D. Yu and M. Sumner, "A novel current derivative measurement using recursive least square algorithms for sensorless control of permanent magnet synchronous machine," in *Power Electronics and Motion Control Conference (IPEMC)*, 2012 7th International, 2012, pp. 1193-1200.
- [94] P. Landsmann, et al., "Lowering injection amplitude in sensorless control by means of current oversampling," in *Sensorless Control for Electrical Drives (SLED)*, 2012 IEEE Symposium on, 2012, pp. 1-6.
- [95] P. Landsmann, et al., "Silent injection for saliency based sensorless control by means of current oversampling," in *Industrial Technology (ICIT)*, 2013 IEEE International Conference on, 2013, pp. 398-403.
- [96] P. Nussbaumer, et al., "Online detection of insulation degradation in inverter fed drive systems based on high frequency current sampling," in *IECON 2011 - 37th Annual Conference on IEEE Industrial Electronics Society*, 2011, pp. 1954-1959.
- [97] J. Campbell and M. Sumner, "Practical sensorless induction motor drive employing an artificial neural network for online parameter adaptation," *Electric Power Applications, IEE Proceedings -*, vol. 149, pp. 255-260, 2002.
- [98] A. Iqbal and M. R. Khan, "Sensorless control of a vector controlled three-phase induction motor drive using artificial neural network," in *Power Electronics, Drives and Energy Systems (PEDES) & 2010 Power India*, 2010 Joint International Conference on, 2010, pp. 1-5.
- [99] M. Cirrincione, et al., "Sensorless Control of Induction Machines by a New Neural Algorithm: The TLS EXIN Neuron," *Industrial Electronics, IEEE Transactions on*, vol. 54, pp. 127-149, 2007.
- [100] S. M. Gadoue, et al., "An experimental assessment of a stator current MRAS based on neural networks for sensorless control of induction machines," in *Sensorless Control for Electrical Drives (SLED)*, 2011 Symposium on, 2011, pp. 102-106.

- [101] Y. Li and M. Han, "Speed sensorless IM control system based on MRAS and NN flux observers," in *Advanced Computer Theory and Engineering (ICACTE)*, 2010 3rd International Conference on, 2010, pp. V5-163-V5-167.
- [102] P. Garcia, et al., "Automatic Self-Commissioning for Secondary-Saliencies Decoupling in Sensorless-Controlled AC Machines Using Structured Neural Networks," in *Industrial Electronics, 2007. ISIE 2007. IEEE International Symposium on*, 2007, pp. 2284-2289.
- [103] T. M. Wolbank and M. K. Metwally, "Saliency tracking-based sensorless control of induction machines using artificial neural networks," in *Power System Conference, 2008. MEPCON 2008. 12th International Middle-East*, 2008, pp. 377-381.
- [104] T. M. Wolbank, et al., "Combination of signal injection and neural networks for sensorless control of inverter fed induction machines," in *Power Electronics Specialists Conference, 2004. PESC 04. 2004 IEEE 35th Annual*, 2004, pp. 2300-2305 Vol.3.
- [105] Martin T. Hagen, Mark Hudson Beale, Howard B. Demuth. (2013, *Neural Network Toolbox™ User's Guide*, Matlab R2013b. 430.
- [106] Control Techniques, "Unimotor Brochure, Brushless AC Servo Motors," vol. Issue 2 060303, ed, 2002.
- [107] D. H. Q. Si, "A New Implementation of High Frequency, High Voltage Direct Power Converter," PhD, University of Nottingham, 2006.
- [108] TerasIC. (2013, 5/5/2014). Altera DE3 Development System. Available: <http://www.terasic.com.tw/cgi-bin/page/archive.pl?Language=English&CategoryNo=39&No=260&PartNo=3>
- [109] TerasIC. (2013, 5/5/2014). Highspeed AD/DA Card Available: <http://www.terasic.com.tw/cgi-bin/page/archive.pl?Language=English&CategoryNo=73&No=278>
- [110] Tyler Pate, John Miller. (2010, *Driving High-Speed Analog-to-Digital Converters: Circuit Topologies and System-Level Parameters*.
- [111] Analogue Devices, 14-Bit, 20 MSPS/40 MSPS/65 MSPS Dual A/D Converter, AD9248 Datasheet, 2005.
- [112] "Surface Mount RF Transformer Datasheet (Model: ADT1-1WT)."
- [113] LEM, "Current Transducer LA 25-P Datasheet."

-
- [114] LEM. Isolated current and voltage transducers - Characteristics, Applications and Calculations. (*Publication CH 24101 E/US (05.04 • 15/8 • CDH), 3rd Edition*).
- [115] N. Kondrath and M. K. Kazimierczuk, "Bandwidth of Current Transformers," *Instrumentation and Measurement, IEEE Transactions on*, vol. 58, pp. 2008-2016, 2009.
- [116] J. L. Ziyang Zhou. (2010, Artificial Neural Network, DSD Project Final Report.
- [117] J. L. Ziyang Zhou. (2010, FPGA-based Artificial Neural Network. Available: <https://www.ziyang.net/2010/05/fpga-based-artificial-neural-network/>
- [118] S. J. Merrifield. (2008, VHDL SD card interface. Available: <http://stevenmerrifield.com/tools/sd.vhd>
- [119] D. Hind, et al., "Use of an artificial neural network for current derivative estimation," in *Power Electronics and Applications (EPE), 2013 15th European Conference on*, 2013, pp. 1-10.